Exploring physical processes related to past climate proxies: lake sediments and stable water isotopes

Dissertation
zur Erlangung des Grades
“Doktor der
Naturwissenschaften”

am Fachbereich Physik, Mathematik und Informatik
der Johannes Gutenberg-Universität
in Mainz

STEPHAN PFAHL
geb. am 21. Februar 1980
in Bad Schwalbach

Mainz, Juni 2009

Tag der Promotion: 1. Oktober 2009

D77 - Mainzer Dissertation

Contents

Abstract

Proxy data are essential for the investigation of climate variability on time scales larger than the historical meteorological observation period. The potential value of a proxy depends on our ability to understand and quantify the physical processes that relate the corresponding climate parameter and the signal in the proxy archive. These processes can be explored under present-day conditions. In this thesis, both statistical and physical models are applied for their analysis, focusing on two specific types of proxies, lake sediment data and stable water isotopes.

In the first part of this work, the basis is established for statistically calibrating new proxies from lake sediments in western Germany. A comprehensive meteorological and hydrological data set is compiled and statistically analyzed. In this way, meteorological times series are identified that can be applied for the calibration of various climate proxies. A particular focus is laid on the investigation of extreme weather events, which have rarely been the objective of paleoclimate reconstructions so far. In addition, the data set is used for assessing the spatial representativity of these events. Subsequently, a concrete example of a proxy calibration is presented. Maxima in the quartz grain concentration from a lake sediment core are compared to recent windstorms. The latter are identified from the meteorological data with the help of a newly developed windstorm index, combining local measurements and reanalysis data. The statistical significance of the correlation between extreme windstorms and signals in the sediment is verified with the help of a Monte Carlo method. This correlation is fundamental for employing lake sediment data as a new proxy to reconstruct windstorm records of the geological past.

The second part of this thesis deals with the analysis and simulation of stable water isotopes in atmospheric vapor on daily time scales. In this way, a better understanding of the physical processes determining these isotope ratios can be obtained, which is an important prerequisite for the interpretation of isotope data from ice cores and the reconstruction of past temperature. In particular, the focus here is on the deuterium excess and its relation to the environmental conditions during evaporation of water from the ocean. As a basis for the diagnostic analysis and for evaluating the simulations, isotope measurements from Rehovot (Israel) are used, provided by the Weizmann Institute of Science. First, a Lagrangian moisture source diagnostic is employed in order to establish quantitative linkages between the measurements and the evaporation conditions of the vapor (and thus to calibrate the isotope signal). On the one hand, a strong negative

correlation between relative humidity with respect to sea surface temperature in the source regions and measured deuterium excess is found, corroborating results from isotope GCMs. On the other hand, sea surface temperature in the evaporation regions does not correlate well with deuterium excess. This finding contradicts results from other models. Although requiring confirmation by isotope data from different regions and longer time scales, this weak correlation might be of major importance for the reconstruction of moisture source temperatures from ice core data. Second, the Lagrangian source diagnostic is combined with a Craig-Gordon fractionation parameterization for the identified evaporation events in order to simulate the isotope ratios at Rehovot. In this way, the Craig-Gordon model can be directly evaluated with atmospheric isotope data, and better constraints for uncertain model parameters can be obtained. A comparison of the simulated deuterium excess with the measurements reveals that a much better agreement can be achieved using a wind speed independent formulation of the non-equilibrium fractionation factor instead of the classical parameterization introduced by Merlivat and Jouzel, which is widely applied in isotope GCMs. Finally, the first steps of the implementation of water isotope physics in the limited-area COSMO model are described, and an approach is outlined that allows to compare simulated isotope ratios to measurements in an event-based manner by using a water tagging technique. Several case studies are performed, again focusing on isotope fractionation during water evaporation from the sea. The good agreement between model results and measurements at Rehovot demonstrates the applicability of the approach. Because the model can be run with high, potentially cloud-resolving spatial resolution, and because it contains sophisticated parameterizations of many atmospheric processes, a complete implementation of isotope physics will allow detailed, process-oriented studies of the complex variability of stable isotopes in atmospheric waters in future research.

Zusammenfassung

Zur Erforschung von Klimavariabilität auf langen Zeitskalen, für die es keine direkten meteorologischen Beobachtungen gibt, werden Proxydaten verwendet. Der mögliche Nutzen, den man aus einem Proxy ziehen kann, hängst stark davon ab, wie gut die physikalischen Prozesse verstanden sind und quantifiziert werden können, die den zu rekonstruierenden Klimaparameter und das Signal im Proxy-Archiv miteinander verknüpfen. Diese Prozesse können unter heutigen klimatischen Bedingungen untersucht werden. In dieser Arbeit werden dafür sowohl statistische als auch physikalische Modelle verwendet. Dabei stehen zwei spezifische Proxy-Typen im Vordergrund, Seesediment-Daten und stabile Wasserisotope.

Im ersten Teil dieser Arbeit wird die Grundlage für eine statistische Kalibrierung von neuen Proxys basierend auf Seesediment-Daten aus Westdeutschland geschaffen. Ein umfassender meteorologischer und hydrologischer Datensatz wird zusammengestellt und statistisch analysiert. Auf diese Weise werden meteorologische Zeitreihen identifiziert, die für eine Kalibrierung verschiedener Klima-Proxys verwendet werden können. Im Vordergrund stehen dabei extreme Wetterereignisse, die bisher nur selten das Ziel von paläoklimatologischen Rekonstruktionen waren. Zusätzlich wird mit Hilfe des Datensatzes die räumliche Repräsentativität dieser Ereignisse untersucht. Anschließend wird ein konkretes Beispiel für eine Proxy-Kalibrierung vorgestellt. Maxima in der Konzentration von Quartzkörnern in einem Sedimentkern werden mit Windstürmen der letzten Jahre verglichen. Diese Stürme werden mit Hilfe eines neuen Indexes identifiziert, der meteorologische Messdaten und Reanalysen kombiniert. Die statistische Signifikanz der Korrelation zwischen Windstürmen und Signalen im Sediment wird mit Hilfe einer Monte-Carlo-Methode gezeigt. Diese Korrelation kann als Grundlage für die Verwendung eines neuen Windsturm-Proxys basierend auf Seesedimenten dienen.

Der zweite Teil dieser Arbeit befasst sich mit der Analyse und Simulation der Variabilität von stabilen Wasserisotopen in atmosphärischem Wasserdampf auf kurzen Zeitskalen. Ein verbessertes Verständnis der physikalischen Prozesse, die diese Variabilität bestimmen, ist eine wichtige Voraussetzung für die Interpretation von Eisbohrkernen und die Rekonstruktion von vergangenen Temperaturänderungen. Das Hauptaugenmerk liegt hier auf dem Deuterium-Exzess und seiner Beziehung zu den äußeren Bedingungen während der Verdunstung des Wassers vom Ozean. Als Basis für die diagnostische Analyse und zur Beurteilung der Simulationsergebnisse

dienen Isotopenmessungen aus Rehovot (Israel), bereitgestellt durch das Weizmann Institute of Science. Als erstes wird eine Lagrangsche Diagnostik verwendet, um quantitative Zusammenhänge zwischen den Messungen und den Bedingungen während der Verdunstung zu erhalten (und auf diese Weise das Isotopensignal zu kalibrieren). Dabei wird auf der einen Seite eine starke Antikorrelation zwischen Deuterium-Exzess und der relativen Feuchte in der Verdunstungsregion festgestellt. Auf der anderen Seite besteht kein starker Zusammenhang zwischen Deuterium-Exzess und Meeresoberflächentemperatur (im Widerspruch zu den Ergebnissen anderer Modelle). Dieses Resultat muss noch mit Hilfe von Isotopendaten aus anderen Regionen und für längere Zeiträume bestätigt werden, könnte aber von zentraler Bedeutung für die Temperaturrekonstruktion aus Eisbohrkerndaten sein. Als nächstes wird die Lagransche Diagnostik mit einer Craig-Gordon-Parametrisierung für die Isotopenfraktionierung während der identifizierten Verdunstungsereignisse kombiniert, um die Isotopenverhältnisse in Rehovot zu modellieren. Auf diese Weise können das Craig-Gordon-Modell mit atmosphärischen Messungen direkt evaluiert und unsichere Modell-Parameter genauer bestimmt werden. Ein Vergleich mit den Messungen zeigt, dass mit Hilfe eines nicht von der Windgeschwindigkeit abhängigen Nichtgleichgewichts-Fraktionierungsfaktors eine viel bessere Übereinstimmung erreicht werden kann als mit der klassischen Parametrisierung von Merlivat und Jouzel, die normalerweise in GCMs verwendet wird. Schließlich werden die ersten Schritte des Einbaus von stabilen Wasserisotopen in das regionale numerische Modell COSMO beschrieben. Ein Ansatz wird vorgestellt, der es durch Einsatz einer Wasser-Markierungstechnik erlaubt, simulierte Isotopenwerte direkt mit Messungen zu vergleichen. Mehrere Fallstudien werden durchgeführt, wobei der Fokus wiederum auf der Untersuchung der Fraktionierung während der Verdunstung vom Ozean liegt. Die gute Übereinstimmung zwischen Modellergebnissen und Messungen in Rehovot zeigt die prinzipielle Verwendbarkeit des Ansatzes. Da das Modell mit hoher räumlicher Auflösung betrieben werden kann und aufwändige Parametrisierungen von vielen atmosphärischen Prozessen beinhaltet, wird eine komplette Implementierung der Isotopenphysik viele Möglichkeiten für zukünftige detaillierte und prozess-orientierte Studien der komplexen Variabilität von stabilen Wasserisotopen in der Atmosphäre eröffnen.

Chapter 1

Introduction and Objectives

1.1 Proxy data

The historical observation period of the earth's atmosphere with the help of direct meteorological measurements generally covers the last one or two centuries. In the pre-industrial period, hardly any such measurements have been performed. Nevertheless, it is essential for various climatological applications to get information about the state of the atmosphere also in earlier times, often even on time scales of up to several millions of years. For example, in the context of the present climate change debate, it has to be evaluated how the current, observed temperature trend compares with similar trends in the history of the earth's climate system (e.g. with respect to its pace, see *Masson-Delmotte et al.*, 2006). Only by putting the current development into the context of the long-term variability, profound statements can be made on the role of anthropogenic forcing. In order to statistically evaluate changes in the frequency of rare, extreme meteorological events and to study less obvious trends of quantities like precipitation, long time series also must be considered. Furthermore, many processes in the earth system have typical time scales much larger than the historical observation period, for instance the interplay between the orbital configuration and the duration of past (inter-)glacials (*EPICA community members*, 2004). Climate data are required to obtain a principal understanding of these processes. Finally, the numerical models that are used to simulate the (future) evolution of the climate systems (e.g. general circulation models, GCMs) have to be evaluated by comparing their results to measurement data for time periods as long as possible.

Paleoclimatologists try to find a way around this dilemma with the help of proxy data (see *Jones et al.*, 2009, for a recent review on the paleoclimatology of the last millennium). Such proxies are variables that can be measured today and allow to indirectly infer on atmospheric (and other environmental) parameters in past times. A prerequisite for their application is the construction of a suitable age model of the proxy archive. There are many types of proxy data, which are applied for the reconstruction of various climatological quantities on different time scales. Tree

rings are widely used as proxies for temperature and precipitation (depending on the geographical location) during the last few millenia (e.g. *Briffa et al.*, 2004; *Moberg et al.*, 2005). Their largest advantage is the very good age control that can be achieved by counting the annual rings (and cross-correlating data from many different trees). In the ocean, proxies with similar dating accuracy are obtained from corals (e.g. *Correge*, 2006) and mollusk shells (e.g. *Schöne et al.*, 2005); the potential of these archives has been less explored than for tree rings so far. Ice cores are the most popular source for climate reconstruction at high latitudes or altitudes (e.g. *Dansgaard et al.*, 1993; *Thompson et al.*, 1998; *EPICA community members*, 2004). They can be used to deduce the history of local snow accumulation rates, atmospheric trace gas composition (from gaseous inclusions in the ice), temperature (e.g. from stable isotope measurements, see section 1.3), volcanic aerosol load (from ash layers in the core) and many other climate parameters on time scales from decades to several hundred thousands of years (depending on the ice accumulation rate). Geological sediments, e.g. from lakes (see section 1.2), wetlands and oceans (e.g. *Sirocko et al.*, 1993; *Black et al.*, 1999), are applied for the reconstruction of various variables on largely diverging time scales. On the one hand, annual varves in some of these archives allow a precisely dated derivation of climate parameters from the last millennia. On the other hand, geological sediments from the continental crust (e.g. from rocks) often comprise millions of years, albeit with a much lower temporal resolution. Further examples of environmental climate proxies are speleothems (which frequently are annually laminated) and temperature profiles from boreholes (recording the slowly varying component of surface temperature). Another important source of information for the last ca. 1000 years are historical documentary data (see e.g. *Brazdil et al.*, 2005).

The focus of most studies dealing with proxy data lies on the reconstruction of climate parameters on seasonally, yearly or even larger time scales. The most prominent variable, for which many different proxies exist, is average near-surface temperature. Precipitation, drought occurrence, surface pressure, atmospheric composition and various indices that represent large scale patterns of climate variability (e.g. the North Atlantic Oscillation, NAO, and the El Niño-Southern Oscillation, ENSO) are other quantities that frequently are the objective of paleoclimatological reconstructions. There are only few studies focusing on the frequency of rare meteorological events like extreme storms or floods on paleoclimatological time scales (see also section 1.2).

In general, the application of a proxy is based on a physical relationship between a climate parameter and a signal in an archive, which is conserved through time[1]. For example, the growth rate of trees in (semi-)arid regions is mainly controlled by moisture availability (*Cook et al.*, 2004), allowing the reconstruction of drought occurrence from the widths of annual tree rings.

[1]The term “physical” is used in a rather general sense here. Of course, biological or chemical processes may also be important and are implicated in this formulation.

Hence, it should principally be possible to determine a transfer function that quantifies this relationship between proxy and climate parameter using a physical model. This has e.g. been achieved in borehole thermometry, where the relationship between surface and borehole temperature can be specified by parameterizing the thermal conduction in the soil (e.g. *González-Rouco et al.*, 2006). However, for most proxy records a physically based transfer function cannot be (easily) derived. Referring to the example of tree growth and moisture availability, there are many biological and habitat-depending factors influencing the width of a single tree ring that differ from tree to tree and cannot be conclusively quantified. Thus, statistical methods are commonly applied (in addition to a more qualitative idea of the physical relationship) in order to overcome these difficulties. A so-called "calibration" is performed by comparing the proxy signal to direct measurements of the requested climate parameter for periods when both are available. Statistical models are then used for the quantification of the relationship between the two. Nevertheless, also this statistical approach is often related to a variety of challenges:

- The applicability of a proxy variable for recent times might be derogated by human interference.
- The dating method of the proxy material might not be sufficiently accurate.
- Specific proxies, like trees or corals, may respond to several climate parameters at a time.
- Direct measurements of the climate variable at the position of the proxy might not exist, at least not for sufficient periods of time, or might suffer from inhomogeneities and other quality issues. Problems with the meteorological data base are particularly crucial for calibration studies dealing with extreme events, which typically occurred only a few times within the calibration period.
- Certain proxies cannot easily be related to a localized climate signal, but represent the atmospheric circulation in a broader region (e.g. proxies for NAO or ENSO indices) or the integrated history of air masses (e.g. isotope ratios in precipitation, see section 1.3).
- Finally, a problem that is inherent to all calibration efforts is that stationarity in time cannot be assured. If a statistical model fits the data within the calibration period, this does not guarantee that the relationship stays the same when larger time scales or different climate regimes (e.g. the last glacial maximum) are considered. For instance, there are tree ring time series that showed a large covariance with temperature for most of the instrumental record, but have failed to reproduce the strongly increasing trend of the last decade (which might be considered as a shift in climate regime with respect to this aspect) (*Jones et al.*, 2009).

In some cases, the calibration of a proxy record is not possible at all, specifically for climate reconstructions on very long time scales or for periods before the Holocene. Also in these cases,

a more qualitative interpretation of the record based on a basic process understanding or the reconstructions of relative climate changes can often be achieved. For example, the appearance of certain plants or animals, detectable through biological residuals in the proxy archive, may indicate an increase in temperature or moisture availability. In particular, large changes in the climate regime, e.g. glacial-interglacial transitions, can be clearly detected in this way, also if an exact quantification of the corresponding temperature change is not realizable.

Altogether, this discussion shows that the potential value of a climate proxy crucially depends on our ability to understand and quantify the physical processes that relate the corresponding climate parameter and the signal in the proxy archive. This ability can be enhanced by analyzing the respective processes and correlations for present day conditions, for which independent measures of climate variability are available. This is the objective of the present thesis. Two types of climate proxies are explored: data from lake sediments and stable water isotopes. In the former case, the focus is on providing an extensive meteorological data set that can be used for proxy calibration, in particular for the reconstruction of extreme events (see section 1.2 and chapters 2 and 3). For the latter, a more indirect approach is pursued by analyzing isotope measurements in atmospheric water vapor with high temporal resolution. A better understanding of the physical processes determining these isotope ratios is fundamental for a more comprehensive interpretation of water isotope signals from ice cores (see section 1.3 and chapters 4, 5 and 6).

All analyses performed in this study are focused on short, primarily daily time scales. In this way, the atmospheric processes that are most important for the determination of the proxy signals (e.g. the synoptic variability of atmospheric transport) can be properly explored. Moreover, for the analysis of extreme events the application of daily data is essential as these events only last for a few hours or days. However, climate reconstructions usually are performed on much larger time scales, as mentioned before. Hence, particularly with respect to stable water isotopes, the results obtained here contribute to improve our process understanding, but cannot be directly employed for the interpretation of ice core data. Nevertheless, the physical models developed in this thesis will also be applicable on larger time scales in future research (see especially chapters 5 and 6).

1.2 Lake sediments and extreme weather events

Lake sediments are widely used as archives for the reconstruction of past climate, environmental conditions and water properties (e.g. *Last and Smol*, 2001; *Sirocko et al.*, 2005). Therefore, many different proxies are applied. For instance, chemical and isotope analyses of the sediment can be related to the origin of the material and the composition of the lake water (e.g. with

respect to nutrient or oxygen content). The occurrence and concentration of biogenic material, e.g. planktonic organisms (like diatoms and foraminifera) and pollen, are applied as a proxy for air and water temperature, water composition, vegetation in the surroundings of the lake and other environmental factors. Clastic sedimentation rates and grain size distributions also provide information on sediment transport and origin, which can often be linked to climate parameters like the wind regime (*Halfman and Johnson*, 1984; *Brauer et al.*, 2008).

Also for the dating of lake sediments, several methods are widely used. In some lakes, distinct annual layers, also called varves, are present in the sediment. Counting of these varves enables a precise relative age control with annual resolution in specific parts of a sediment core. However, absolute ages can usually not be obtained from varve counting, because the layers are rarely conserved throughout the whole sediment column. Hence, radiogenic methods are often applied for absolute age control. For example, age models for the last century are obtained from measurements of ^{137}Cs and ^{210}Pb; ^{14}C data are used on time scales up to about 50,000 years before present. Further dating methods are the construction of event-based chronologies (e.g. using volcanic ash layers from historical eruption events) and the cross-correlation to other proxy archives (e.g. the comparison of stable isotope signals from lake sediments and ice cores).

The processes that link climate parameters and signals in lake sediments are usually rather complex. Calibration often is an important step in order to apply the sediment data as climate proxy,

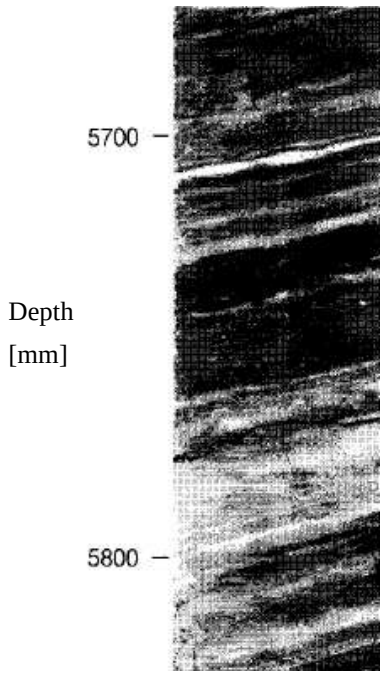

Figure 1.1. *Section of a lake sediment core from the North Island, New Zealand. Pale gray layers represent individual rainstorms (from Eden and Page, 1998).*

as already outlined in section 1.1. For example, proxies from lake sediments have been calibrated for snowmelt and thereby arctic temperature (*Hardy et al.*, 1996; *Hambley and Lamoureux*, 2006), for rainstorms and river floods (*Eden and Page*, 1998; *Nesje et al.*, 2001) as well as for temperature and yearly precipitation amounts (*Trachsel et al.*, 2008). The first objective of this thesis, which is addressed in chapter 2, is the compilation of a comprehensive meteorological and hydrological data set that can be used for a calibration of climate proxies from lake sediments in western Germany. In particular, this data set should have a high, daily time resolution that enables the calibration of proxies of extreme meteorological events (e.g. windstorms, heatwaves, floodings and droughts). To date, lake sediments have mostly been used for reconstructions on climatological time scales, and there are only a few studies dealing with so called "paleoweather" events that last only for a relatively short period of time. Most of these studies have focused on rainstorms and floodings (*Eden and Page*, 1998; *Rodbell et al.*, 1999; *Nesje et al.*, 2001; *Noren et al.*, 2002; *Besonen et al.*, 2008, see also the example in Fig. 1.1). Since extreme events have a very large impact on human society, it is important to know how their frequency has changed during different states of the climate system. Here, the basis shall be established for deducing new proxies of such events from lake sediment data.

In chapter 3, a concrete application of the data set described in chapter 2 is presented. An attempt is made to calibrate number concentrations of quartz grains in a sediment core from a western German maar lake as a proxy of windstorms. Such a calibration may become the basis for the reconstruction of paleo-windstorm records, for which no proxies exist in large parts of the globe up to date. A slightly modified version of this chapter has been accepted for publication in the Journal of Geophysical Research (*Pfahl et al.*, 2009).

1.3 Stable water isotopes

In addition to the most abundant water isotopologue $H_2{}^{16}O$, two stable, heavy water isotopologues (for brevity denoted water isotopes in the following) are widely applied as diagnostic tools in geosciences, HDO (where one of the hydrogen atoms is replaced by deuterium) and $H_2{}^{18}O$ (with oxygen-18 instead of oxygen-16). Their concentrations are usually specified in δ-notation:

$$\begin{aligned} \delta^{18}\mathrm{O} &= \left({}^{18}R / {}^{18}R_{\mathrm{VSMOW}} - 1\right) \cdot 1000, \\ \delta^{2}\mathrm{H} &= \left({}^{2}R / {}^{2}R_{\mathrm{VSMOW}} - 1\right) \cdot 1000, \end{aligned}$$

where R denotes the ratio of molar concentrations of heavy and light isotopes,

$$\begin{aligned} {}^{18}R &= [\mathrm{H_2{}^{18}O}] \,/\, [\mathrm{H_2{}^{16}O}], \\ {}^{2}R &= [\mathrm{HDO}] \,/\, [\mathrm{H_2{}^{16}O}]. \end{aligned}$$

R_{VSMOW} is the isotope ratio of Vienna standard mean ocean water, which is defined as follows (*Araguás-Araguás et al.*, 2000):

$$\begin{aligned} {}^{18}R_{\mathrm{VSMOW}} &= 2.00520 \cdot 10^{-3}, \\ {}^{2}R_{\mathrm{VSMOW}} &= 0.15595 \cdot 10^{-3}. \end{aligned}$$

An important secondary water isotope parameter is the deuterium excess (hereafter called *d*-excess or briefly *d*, measured in ‰), that is defined as $d = \delta^2\mathrm{H} - 8 \cdot \delta^{18}\mathrm{O}$ (*Dansgaard*, 1964).

Stable water isotopes are useful in various ways: they can be applied as tracers in order to improve our understanding of the hydrological cycle (e.g. *Gat*, 1996; *Henderson-Sellers et al.*, 2004), and their concentration in ice cores and other paleo-archives is used to reconstruct past climate variability (e.g. *Dansgaard et al.*, 1993; *Petit et al.*, 1999; *North Greenland Ice Core Project members*, 2004, see also the example in Fig. 1.2). Essential for all these applications are fractionation effects that change the concentration of heavy isotopes with respect to their lighter counterparts at phase transitions of water. Two types of fractionation can be distinguished: Equilibrium effects occur at all phase transitions due to the different bonding energies of the isotopes in the condensed phase, leading to differing water vapor saturation pressures. These processes, according to their quantum mechanical origin, are controlled by temperature (*Gat*, 1996). In addition, the slower diffusion velocities of heavy molecules can lead to fractionation during transport, called non-equilibrium (or kinetic) fractionation. In the atmosphere, the latter occurs mainly during evaporation of water from the ocean (*Craig and Gordon*, 1965).

Measurements of heavy water isotopes in ice cores can be used to infer about past surface temperatures. This reconstruction is based on the so called “temperature effect” (*Dansgaard*, 1964), the linear relationship between surface temperature and isotope ratios in precipitation that is

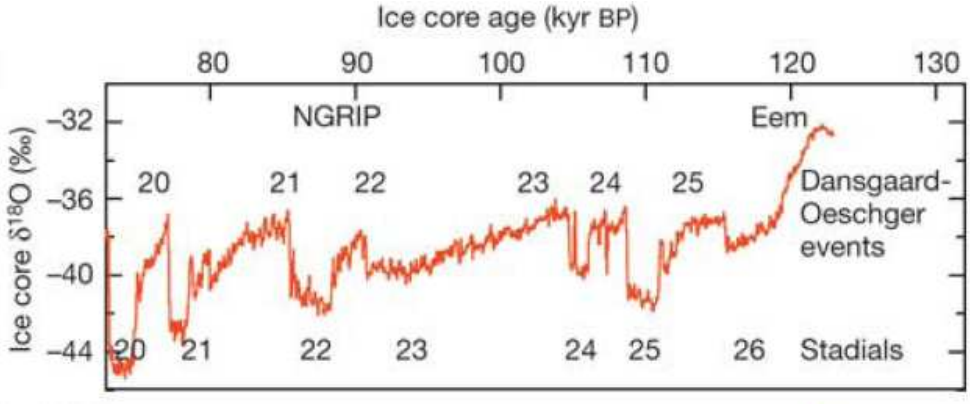

Figure 1.2. *δ^{18}O curve from the NGRIB ice core for the early phase of the last glacial period. Rapid variations are associated with climate shifts (Dansgaard-Oeschger events). Around 120 kyr BP, the transition from the Eem to the glacial period occured (from North Greenland Ice Core Project members, 2004).*

observed in present day climate (see also section 4.1.2). Classically, the spatial slope from this observed relation was widely applied for a calibration of the "isotope thermometer" (e.g. *Johnsen et al.*, 1992), i.e. it was assumed that the spatial relationship can serve as a quantitative indicator for the correlation between temperature and isotope variability in time. More recent studies have shown that this assumption often is not valid (see *Jouzel et al.*, 1997, and references therein), particularly for Greenland ice cores[2]. There are other processes that influence the ice cores' isotopic composition that might lead to a change in the isotope-temperature relationship through time. For example, the seasonality of high-latitude precipitation may change in different climate states, and, probably most important, source conditions of the precipitating water (mainly the temperature during the evaporation of the water from the ocean) may be different. In order to infer about these source conditions, the deuterium excess has been employed (*Vimeux et al.*, 1999, 2002; *Masson-Delmotte et al.*, 2005), since this parameter is thought to be primarily determined during the evaporation process. However, there are hardly any measurements available that allow to analyze this assumed correlation between d-excess and moisture source conditions (see section 4.1.1).

This discussion shows that the d-excess on the one hand is an important parameter for the application of ice core data as temperature proxy. On the other hand, there are several open questions related to the processes and parameters that determine the value of d in atmospheric waters. This imbalance is the main starting point for the research described in the second part of this thesis. In chapter 4, a Lagrangian moisture source analysis is employed in order to detect correlations between measurements of d-excess in atmospheric water vapor (performed by *Angert et al.* (2008) at the Weizmann Institute of Science) and meteorological parameters in the evaporation regions. In this way, a calibration of the d-excess signal can be performed. Isotope data from ice cores cannot be used for this calibration, since they are not available with the temporal resolution that is necessary for a first application and proof of concept of our method (which is based on the identification of moisture sources on synoptic time scales). A modified and edited version of this chapter has been published as *Pfahl and Wernli* (2008).

For the description and understanding of the physical processes determining d, numerical models have to be applied, because these processes are part of the complex, non-linear variability of the atmospheric water cycle (see also chapter 1 in *Sodemann*, 2006). As mentioned above, isotope fractionation during water evaporation from the sea, which is usually parameterized with the help of the Craig-Gordon model (*Craig and Gordon*, 1965), is a particularly important mechanism in this context. In chapter 5, d-excess in water vapor is simulated by combining a parameterization of this fractionation process with the Lagrangian source diagnostic from chapter 4. In this way, the Craig-Gordon model can be directly evaluated with atmospheric measurements, and better constraints for uncertain model parameters can be obtained. A slightly

[2]For Antarctica, *Jouzel et al.* (2003) come to the conclusion that today's spatial slope and the temporal relation agree relatively well if changes at the ocean source are taken into account.

modified version of this chapter has been submitted to the Journal of Geophysical Research (*Pfahl and Wernli*, 2009). Finally, in chapter 6, our modeling framework is expanded and generalized with the help of a mesoscale weather prediction and climate model. The first steps of the integration of stable water isotope physics in this model are described, and an approach is outlined that allows to compare simulated isotope ratios to measurements in an event-based manner by using a water tagging technique. As the model can be run with high, potentially cloud-resolving spatial resolution and contains sophisticated parameterizations of many atmospheric processes (e.g. cloud microphysics), a complete implementation of isotope physics will allow detailed, process-oriented studies of stable isotopes in atmospheric waters in future research. In this way, it will also be possible to simulate the isotope signal in precipitation produced by specific weather systems (mid-latitude cyclones and thunderstorms), which are not accurately represented in GCMs because of the coarse spatial resolution.

As mentioned before, the results obtained for stable water isotopes in the second part of this thesis are not directly applicable for the interpretation of proxy data from ice cores, primarily because the time scales are not commensurable. Nevertheless, the physical models developed here can improve our understanding of the complex physical processes that determine the isotope signals in the cores and thus have an indirect value for the research on paleo-climate proxies.

Chapter 2

Climate and Weather in the Western German Eifel Region

2.1 Introduction

The calibration of climate proxies often is related to a variety of challenges, as outlined in chapter 1. One particular issue is the availability of meteorological data from the region of interest and for a sufficient period of time. These data should be homogeneous in time, and they often have to fulfill certain requirements associated with the specific proxy the calibration is focused on. For example, if extreme meteorological events shall be detected, the data must have a sufficient temporal resolution. Furthermore, in some cases several types of climatological data have to be combined in order to answer specific research questions. If, for instance, a proxy for extreme hydrological events is calibrated using runoff data from river gauges, it might be of additional interest how signals in this hydrological data set are reflected in local precipitation measurements (i.e. in which way the reconstruction of floodings parallels a reconstruction of local-scale rainstorms).

This chapter describes a meteorological and hydrological data set that can be used for the calibration of lake sediment data and that is sufficiently comprehensive to address more specific research questions, as outlined above. In particular, the data presented here have a daily resolution, allowing the analysis of extreme meteorological events. The combination of river runoff data and precipitation measurements can be applied to explore relationships between meteorological and hydrological reconstructions. Reanalysis data are included in order to quantify correlations between local events and atmospheric conditions on larger, synoptic spatial scales. The focus of the work presented in this chapter is on a western German region, roughly between 6° and 7.5°E and between 49.5° and 51°N (see Fig. 2.1). This region is denoted “Eifel region”, referring to the low mountain range that dominates its geography. The Eifel region has been chosen for our analysis because several maar lakes are located there (some of them already dried out), in which

Figure 2.1. *Location of the Eifel region within Europe. For an exact definition of the region, see section 2.2.*

the conditions are favorable for sediment preservation and application as a climate archive (see e.g. *Sirocko et al.*, 2005; *Brauer et al.*, 2008). The Eifel Laminated Sediment Archive (ELSA) is a collection of sediment cores from these lakes that has been compiled at the Institute for Geosciences, University of Mainz (see *Sirocko*, 2009, and further references in section 3.2.1). This archive contains high-quality lake sediment data from the last 150,000 years that can be used as a basis for proxy calibrations, which will prospectively be performed with the help of the data set described in the present chapter (see chapter 3 for an example). Moreover, the Eifel region is well suited for this study since a rather dense network of meteorological surface measurements has been operated in western Germany during the last approximately 60 years.

In section 2.2, the basic data sets are introduced that will be used and further investigated in this chapter. Thereafter, a detailed statistical analysis of the data is presented. This analysis comprises a characterization of the climate in the Eifel region during the investigation period (section 2.3). This characterization may also be helpful for other climatological studies in the future. Section 2.4 deals with the comparison of reanalysis data and meteorological measurements with regard to the temporal variability and the statistical distribution of the data. In this way, the local measurements are integrated in a larger synoptic context. The statistical tools applied here are also useful for the evaluation of climate models in future research. In section 2.5, hydrological extreme events are investigated, focusing on the detection of meteorological droughts and on the comparison between precipitation and runoff. The more specific question of representativity of extreme weather events in the Eifel region on larger spatial scales is investigated in section 2.6 by extending the data base to measurements from other regions in Central Europe. Finally, in section 2.7 some comments are made on the implications of our results for

the calibration of ELSA sediments as proxies for past meteorological conditions and events.

2.2 Data

In order to make the description of climate and weather events in the Eifel region as complete as possible, different data sets are used. The main focus is on direct meteorological measurements, provided by weather stations of the German Weather Service (DWD). In addition, reanalysis data from the European Center for Medium-Range Weather Forecasts (ECMWF) are employed, mainly for investigating the relationship between local phenomena and the atmospheric circulation on larger scales and evaluating the applicability of the reanalysis data as a diagnostic for local meteorological conditions. As our investigation focuses on lake sediment data, which are closely related to hydrological phenomena, runoff time series from several streams in the Eifel region are additionally incorporated in the analysis. In the following, details of these data sets and of the first processing steps are explained.

2.2.1 Station data from the German Weather Service

The basic data set for the analysis in this chapter is provided by weather stations of the DWD. Daily values of several basic meteorological variables for the period 1950-2005 have been obtained from three different types of stations (nomenclature from DWD): mean, minimum and maximum temperature two meters above ground from KL-, precipitation from RR-, mean and maximum wind speed ten meters above ground from FF-stations[1]. Further information on the measurement procedure can be found on the DWD web-page (http://www.dwd.de/). The Eifel region, as shown in Figs. 2.1 and 2.3, is defined as a square of 80 kilometers edge length, centered at 6.9° east and 50.1° north. Data from all stations that lie within or close to that region and provide measurements for an adequate period of time between 1950 and 2005 have been taken into account. In Figure 2.2, the geographical positions of these stations are shown separately for the three station types. The Figure indicates that there are large differences between the three types with respect to the spatial coverage: there are a lot of RR-stations, as the measurement of precipitation is not very complex, but only a few FF-stations. The number of KL-stations is in between. Another critical factor associated with the wind measurements is that most of the FF-stations were introduced in the seventies and for earlier times, almost no wind data are available.

The temporal homogeneity of the data is an important point in climatological studies. The data collected by the DWD are routinely checked for their quality. This check is assumed to be

[1]For simplicity, the measurement height is not specified in the following part of this chapter. Thus, “temperature” always refers to the temperature 2 m above ground, “wind speed” implicates a height of 10 m.

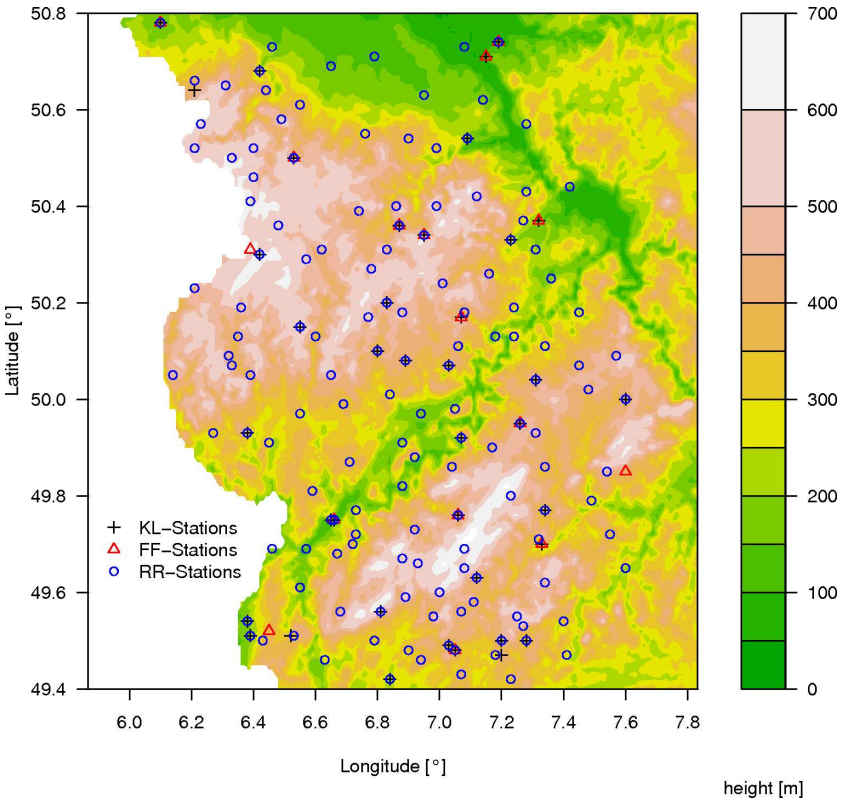

Figure 2.2. *DWD weather stations used in this chapter. Definitions of the different station types are given in the text. Colors show the topography (only shown within Germany).*

adequate for the investigations presented here, also because our study does not include trend analyses, for which homogeneity is particularly crucial. *Hundecha and Bárdossy* (2005) also relied on the DWD routine quality check when performing a trend analysis based on a similar data set. Nevertheless, inhomogeneities as possible error sources have to be kept im mind, especially regarding wind data (see also chapter 3).

For some of the analyses described in the following sections, it is a prerequisite that data from the same base period is used for all stations and that there are as little missing values as possible within this period. Hence, for each station type a subset of stations has been chosen that fulfill this requirement. All RR- and KL-stations with less than two percent missing values between 1969 and 2001 and all FF-stations with less than four percent missing values in 1979-2001 have been extracted. Because of the insufficient coverage of wind measurements, the period for the FF-stations is shorter and the threshold for the missing values less strict than for the other types. Figure 2.3 shows the geographical distribution of all stations selected in this way. The corresponding analysis periods are denoted “restricted base periods” in the following.

In order to compare measurement data from weather stations with output of numerical models

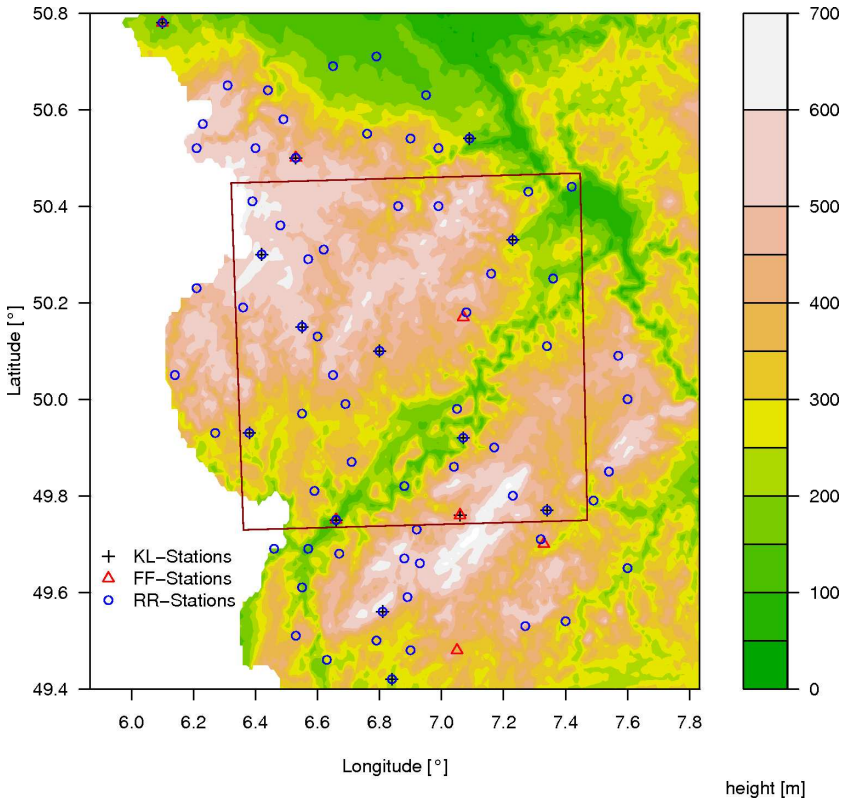

Figure 2.3. *DWD weather stations that are selected for specific statistical analyses in sections 2.3 and 2.4. The red square shows the Eifel region.*

or with analysis data (which are also distributed on a regular spatial grid), there are basically two different approaches. One can either interpolate the gridded model data to the coordinates of the stations (model-to-observation approach) or aggregate the inhomogeneously distributed station data to the regular model grid (observation-to-model approach). Both methods have their advantages, but for a quantity like precipitation, which is highly variable in space and for which the model output represents the average value of a grid cell, the second method leads to a more equitable comparison. Here, average values of all measured variables for the Eifel region, shown as red box in Fig. 2.3, have been calculated. This has been done by interpolating the station data linearly, via a triangulation scheme, to a regular longitude-latitude grid spanning the region. A grid spacing of 0.2° has been chosen. Afterwards, the data have been averaged over the grid. This interpolation method takes the inhomogeneous geographical distribution of the stations into account. It is not necessary to work with a more complicated interpolation scheme here, because the interpolated field is not evaluated at single grid points. Due to the averaging over a rather big area (6400 km^2), small scale spatial differences, which might not be reproduced by the linear method, are averaged out. In this calculation of regional mean time series, the data from all available stations has been used at each time step, i.e. the number of stations contributing to the mean value has varied with time.

For the calculation of the effective drought index from the station data (see section 2.4), precipitation time series without gaps are required. Thus, the missing values in the selected time series from RR-stations during the restricted base period 1969-2001 had to be filled. This has been done in three steps, expanding the approach of *Byun and Wilhite* (1999). For each gap, we have first tried to estimate the missing value by linear interpolation using all available stations. If this was impossible, for example if the station was located outside of the convex hull of the remaining ones, a value has been adopted from one of the five nearest stations, beginning with the closest one. Finally, if all these stations had gaps at the respective date, a climatological value for the calendar day has been used to fill the missing value.

In addition to the analysis of local climate and weather, station data are applied for assessing the representativity of meteorological events in the Eifel region for larger areas in Germany (see section 2.6). Therefore, some additional stations from the DWD are used. These stations are listed in Table 2.1. They have been selected to cover distances of about 100 to 600 km from the Eifel with relatively few stations. As a second condition, their data has been required to be almost complete in the period 1950-1999. The station Trier-Petrisberg, which lies at the border of the above defined Eifel region, is used as a reference for the comparison on larger spatial scales, as it is professionally operated and has very few missing values in the data.

Station	Longitude [°]	Latitude [°]	Distance from Trier [km]
Aachen	6.08	50.78	123
Frankfurt/M-Flughafen	8.58	50.03	142
Karlsruhe	8.35	49.03	146
Würzburg	9.95	49.77	237
Augsburg	10.93	48.42	345
Hannover	9.67	52.45	368
Hof	11.87	50.30	378
Hohenpeissenberg	11.00	47.80	384
Bremen	8.78	53.03	396
Magdeburg	11.58	52.10	434
Hamburg-Fuhlsbüttel	9.98	53.63	491
Berlin-Tempelhof	13.40	52.47	560
Rostock-Warnemünde	12.07	54.02	604
Görlitz	14.95	51.15	608

Table 2.1. *Additional DWD stations used for the correlation analysis on large spatial scales (see section 2.6). The station Trier-Petrisberg is applied as reference for the Eifel region.*

Finally, the DWD provides gridded climatological data of the main variables temperature, precipitation and wind speed (denoted "DWD climate data" in the following) that are used as a reference for the mean climate state in the Eifel region. These data are available on a Gauss-Krüger grid with 1 km grid spacing and with a monthly resolution for the period 1951-2001. They were compiled by the DWD from station measurements with the help of an inverse distance interpolation method; details of the procedure are described by *Walter et al.* (2006).

2.2.2 Reanalysis data from the ECMWF

As a second data set, ERA40 reanalyses from the ECMWF are employed. These reanalysis data are available for the period 1958-2001, with a temporal resolution of six hours and a spectral resolution of T159 in space, which corresponds to a horizontal grid spacing of approximately 125 km. Further details on ERA40 are given by *Uppala et al.* (2005). Two different types of variables from the ERA40 data set are used in this study, starting from 1969. On the one hand, temperature at a height of 2 m and wind speed 10 m above ground are real analysis fields, i.e. they have been produced combining short term model forecasts and meteorological observations with the help of a statistical data assimilation method (3D-var). Note that these variables might be influenced by the specific type of boundary layer parameterization that is used in the numerical model of the ECMWF. On the other hand, precipitation, 10 m gust peak wind speed and 2 m minimum and maximum temperature have been obtained from pure model forecasts without incorporating observations. Here, forecast steps up to 30 hours have been used. For comparison with the station data, all these variables have been interpolated to the coordinates of our reference station Trier-Petrisberg (which is used because of its ensured data quality, as noted above) and to the center coordinates of the Eifel region[2]. Afterwards, daily values have been calculated from the six-hourly time steps.

2.2.3 Hydrological data

Since the geological proxies for which our calibration data set is designed have been retrieved from lakes, they are closely related to hydrological phenomena. In order to take this fact into account, runoff data from some smaller streams in the Eifel region are included in our analyses. Runoff measurements are used instead of gauge heights, because they are thought to be more homogeneous on large time scales. Not all available hydrological stations in the region are employed; a set of several gauges representing the most important streams has been subjectively chosen. These stations are listed in Table 2.2. Runoff data have been provided by the

[2]In fact, we have interpolated the data to several grid points within the Eifel region and subsequently averaged them over the grid, as described for the station data in section 2.2.1. But this does not play a role here because of the coarse ERA40 resolution. It would become important if model data with a higher spatial resolution were used.

"Landesamt für Umwelt, Wasserwirtschaft und Gewerbeaufsicht" (LUWG) in Rheinland-Pfalz. For each station, a normalized runoff time series has been calculated as $\tilde{Q}(t) = (Q(t) - \bar{Q})/\sigma_Q$, where $Q(t)$ denotes the runoff at time t, $\bar{Q}$ is the mean runoff at the station and σ_Q its standard deviation. By averaging these normalized time series from different stations, a value roughly representing the mean regional runoff has been calculated. The stations Daun and Bad Bodendorf have not been included in this averaging, because the Ahr does not flow through the above defined Eifel region in greater parts, and the Lieser should not be incorporated with two stations. For a comparison of hydrological and meteorological drought data (see section 2.5.2), running averages with a seven day window have been computed from the runoff time series, as recommended by *Pfister et al.* (2006).

In addition to local runoff in the Eifel region, we are also interested in the correlation of extreme hydrological events, in particular floods, in this region with corresponding events in Central Europe. An analysis of these correlations is performed with the help of runoff data from some additional stations, again subjectively chosen to represent a few of the most important catchments in Germany and some of its neighboring countries. The data have been provided by the Federal Institute of Hydrology (BfG) and the Global Runoff Data Centre (GRDC) in Koblenz; see the list of stations in Table 2.3. The Finnish station Isohaara has been included because it represents a catchment that is geographically clearly separated from the Eifel region and can thus be used to obtain information on random correlations between flood events.

2.3 Average Eifel climate

In this section, the mean climate state in the Eifel region is characterized. Seasonal cycles of temperature, precipitation and wind speed are described in the first subsection; the second subsection deals with the spatial variability of these variables within the region.

Station	Longitude [°]	Latitude [°]	River
Bad Bodendorf	7.22	50.55	Ahr
Daun	6.83	50.21	Lieser
Kordel	6.64	49.84	Kyll
Nettegut	7.42	50.42	Nette
Peltzerhaus	7.08	50.07	Ueßbach
Platten 2	6.96	49.94	Lieser
Prümzurlay	6.44	49.87	Prüm

Table 2.2. *Hydrological stations in the Eifel region that are used in this study.*

Station	Longitude [°]	Latitude [°]	River
Cochem	7.17	50.14	Moselle
Fremersdorf	6.65	49.41	Saar
Worms	8.38	49.63	Rhine
Düsseldorf	6.77	51.23	Rhine
Steinbach	9.60	50.01	Main
Lauffen	9.16	49.07	Neckar
Ingolstadt	11.42	48.75	Danube
Hofkirchen	13.12	48.68	Danube
Porta	8.92	52.25	Weser
Versen	7.24	52.74	Ems
Treia	9.32	54.51	Treene
Ketzin	12.85	52.48	Havel
Dresden	13.74	51.06	Elbe
Neu-Darchau	10.89	53.23	Elbe
Hohensaaten-Finow	14.14	52.86	Oder
Borgharen	5.72	50.87	Meuse
Lith	5.45	51.82	Meuse
Rheinfelden	7.78	47.56	Rhine
Chancy	5.97	46.15	Rhone
Schaerding	13.44	48.44	Inn
Isohaara	24.55	65.78	Kemijoki

Table 2.3. *Hydrological stations used for the correlation analysis in section 2.6.*

2.3.1 Seasonal variation

In order to describe the mean seasonal variation of temperature, wind speed and precipitation in the Eifel region, monthly values have been calculated from station and ERA40 data, which have been averaged over the region as described in section 2.2. Subsequently, these monthly data, and additionally the monthly values from the DWD climate data set (see section 2.2.1) have again been averaged over the whole analysis period. This period is 1969-2001 for all variables except for the measured wind data, for which the first five years have not been included because too few wind stations were in operation prior to 1974. Furthermore, 95% confidence intervals of the mean values have been estimated. For temperature, a Gaussian distribution can be assumed and thus a t-test has been applied for this estimation. For wind and precipitation, the assumption of a normal distribution is invalid, hence the confidence intervals have been calculated with the help of a non-parametric bootstrap resampling method. An ordinary bootstrap with 999 replicates has been used, based on the 33, respectively 28 mean values for each calendar month, and adjusted

bootstrap percentile (BCa) intervals have been computed from this resampling (see e.g. *DiCiccio and Efron*, 1996). It should be noted here that these confidence intervals represent the variability of monthly means in the analysis period and do not take daily variations of the parameters into account.

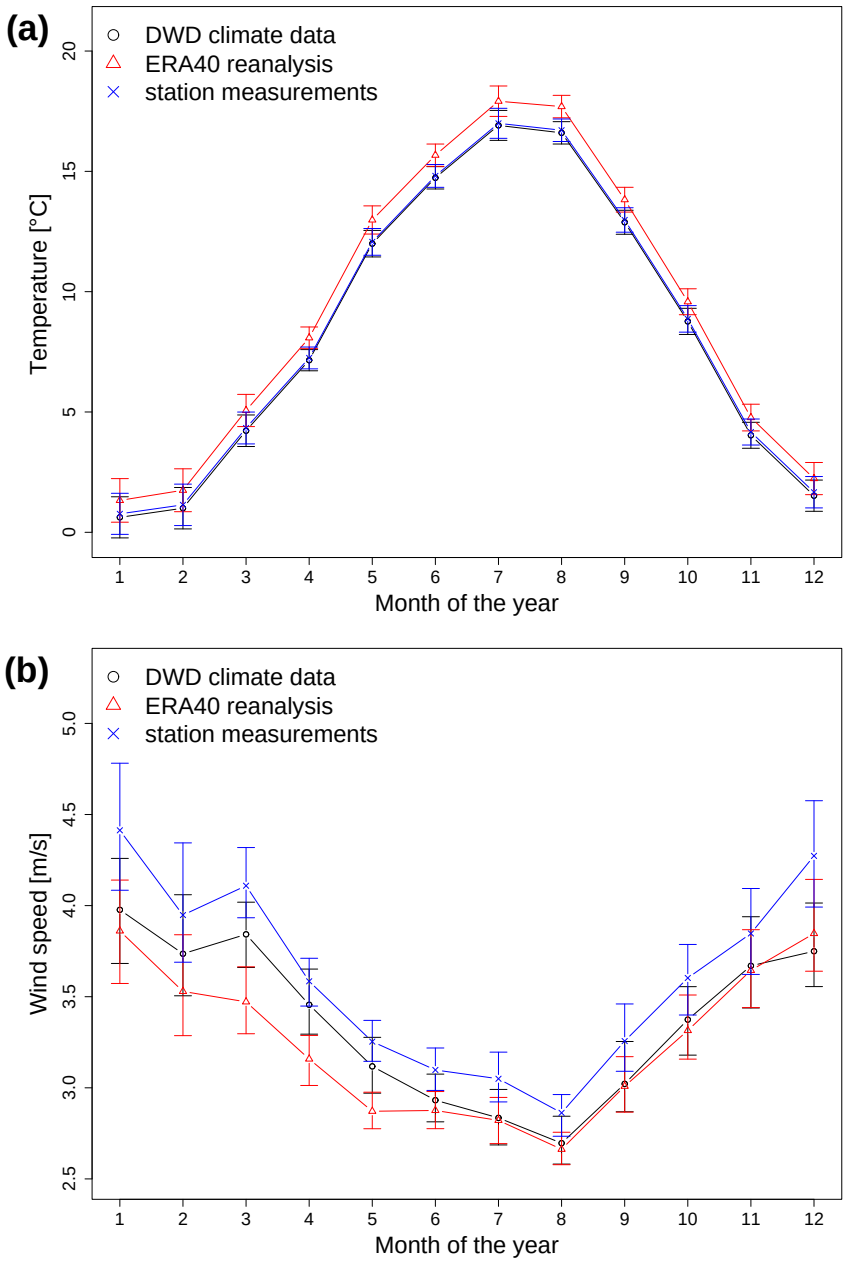

Figure 2.4. *Seasonal variation of temperature at 2 meter height (a) and wind speed at 10 m (b), averaged over the Eifel region and the whole analysis period. Error bars indicate 95% confidence intervals of the monthly means.*

Figure 2.4a shows the seasonal variation of mean temperature. The typical mid-latitude pattern of cold winters and warm summers can be observed. The temperature curves from station and climate data are in perfect agreement, whereas mean ERA40 temperatures show a positive bias between 0.5°C in winter and 1°C in summer. This bias can in great parts be explained with the coarse ERA40 topography, which does not contain local features like the Eifel mountains. Because of this, the average altitude of the Eifel region is about 100 m lower than in reality. Except for this bias, the seasonal variation of temperature is properly represented in the ERA40 data set.
As shown in Fig. 2.4b, the highest mean wind velocities in the region occur in winter, and also the variability of the monthly means is largest for this season. The ERA40 wind speed curve is in good agreement with the climate data during most of the year. Only in spring velocities from the reanalyses are too low. On the contrary, the mean wind speed values obtained from the station data show a distinct positive bias compared to the climate data during the whole year. This bias is only partly due to the somewhat shorter analysis period used for the station data. The insufficient coverage of the Eifel region with wind stations might be another important reason (see again Fig. 2.2). Because of this, an accurate interpolation method is more important for the calculation of the mean value compared to e.g. temperature. The bias may indicate local features in the wind velocity field that are only resolved by the more advanced inverse distance interpolation method used by the DWD, e.g. with the help of the altitude correction included in this method. In particular, the spatial distribution of wind stations might be biased towards high altitudes. Another reason for the deviation between climate and station data may be the fact that not only direct wind measurements were included in the compilation of the climate data set, but also estimates of wind velocity from eye observations (*Walter et al.*, 2006). For these, the measurement error is much greater and could, together with the error from the conversion from Beaufort scale, also lead to a substantial bias. Hence, it is not clear which of the two curves is closer to reality. Nevertheless, except for the bias the seasonal cycle of wind speed is very similar in both station and DWD climate data.

The seasonal variation of precipitation is shown in Fig. 2.5a. No marked seasonal cycle is obvious from the Figure; only for November and December, slightly higher values are observed. The variability of the monthly precipitation means is relatively large, as indicated by the error bars showing the 95% confidence intervals. The curves from station and climate data are in good agreement; the station data only exhibit a small negative bias between 0.07 and 0.15 mm/day that might again be due to differences in the interpolation method. The monthly means from ERA40 precipitation are in very good agreement with those from station data during half of the year, while they are negatively biased during the other half. The differences between these two curves are shown in Fig. 2.5b. A statistically significant difference applying a 95% confidence is marked with a red circle. The significance has been tested with the help of the non-parametric Wilcoxon rank sum test (also known as Mann-Whitney test, see e.g. *Wackerly et al.*, 2002). It is obvious from the Figure that average precipitation in the months November to April is very

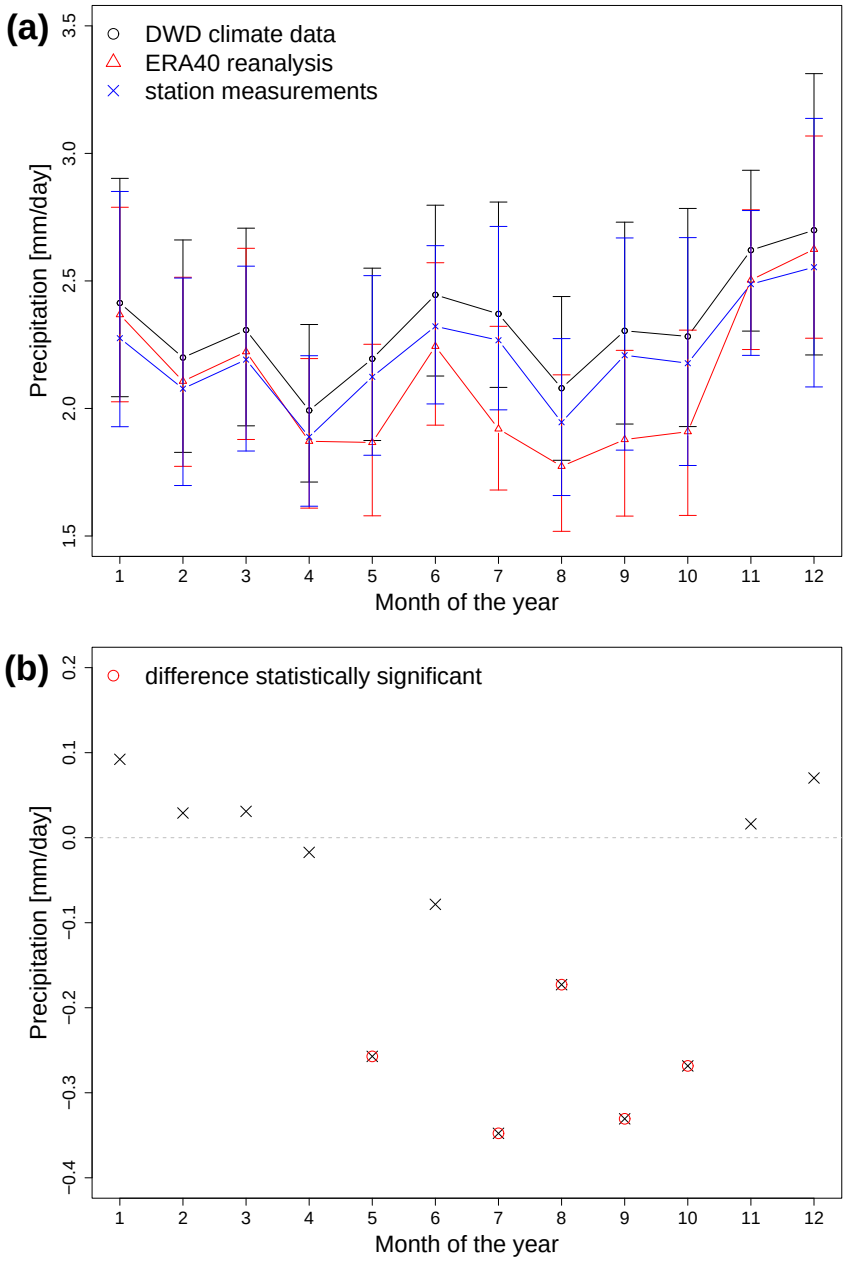

Figure 2.5. *(a) Seasonal variation of precipitation in the Eifel region. Error bars indicate 95% confidence intervals. (b) Difference between precipitation from ERA40 and station data. Statistically significant differences are indicated by red circles.*

well represented in the ERA40 data set. However, from May to October (with the exception of June) values are too small. This discrepancy between the seasons is probably linked to the fact that precipitation in the winter months is mostly stratiform, whereas during summer convection plays a greater role. In a global weather prediction model, which has been used to obtain ERA40 precipitation values, processes leading to the formation of stratiform clouds (e.g. large

scale orographic lifting and mid-latitude cyclonic systems) are directly modeled, whereas convection, which occurs on smaller spatial scales, is only included via a parameterization. This parameterization has been tuned in order to produce correct average precipitation values on continental scales, but it seems to underestimate the magnitude of convective rain in the Eifel region, whose mountainous character is not captured by the rather coarse model orography.

2.3.2 Spatial variability

In the following, the spatial variability of the measured meteorological parameters in the Eifel region is analyzed. As a first step, at the selected stations with almost no missing values during the restricted base periods (see section 2.2 and Fig. 2.3) temporal averages of the main variables temperature, wind velocity and precipitation and of some derivated quantities have been calculated. These derivated quantities are the number of frost days (daily minimum temperature less than 0°C), ice days (daily maximum temperature less than 0°C) and precipitation days (daily precipitation sum exceeds 1 mm) per year. In Fig. 2.6, the average values are plotted against station altitude above sea level. Linear regression lines, obtained with a least square method, and correlation coefficients are also shown in the plots. The Spearman rank correlation coefficient ρ (see e.g. *Wackerly et al.*, 2002), which does not depend on the underlying statistical distribution, has been calculated for all variables to ensure comparability[3].

Figure 2.6a shows that mean temperature decreases linearly with height; the correlation coefficient is close to -1. The average lapse rate from the station data is 0.65°C per 100 m, that is exactly the same value as in the troposphere of the ICAO standard atmosphere. The correlation coefficient for average daily maximum temperatures is -0.996, for daily minimum temperatures it is only -0.75 (not shown). A reason for this difference might be that during daytime, the vertical temperature gradient is, on average, maintained by solar heating of the ground, whereas by night, there is no such external forcing. Hence, in the nighttime the relative importance of additional factors like soil conditions and local features of the landscape is larger than during day, compared to the most dominant influence of station altitude. This difference between night and day is also reflected in the dependence of the number of frost days (medium high correlation) and ice days (very high correlation) on station height (Fig. 2.6c,d).
Mean wind velocity and station height are positively correlated, as shown in Fig. 2.6b; the correlation coefficient is almost 0.9. However, it should be noted that this correlation is not based on a very profound statistic, as the number of stations used to establish the relationship is rather low. The correlation of mean daily gust peaks and altitude is much weaker ($\rho = 0.43$, not shown), probably due to the strong dependence of gusts on local environmental conditions like the orography in the surrounding of the wind mast and on the instruments used for the measurements.

[3]The difference between Spearman and Pearson correlation coefficient is small for these average variables, but can become larger when e.g. correlations between precipitation time series are investigated, see below.

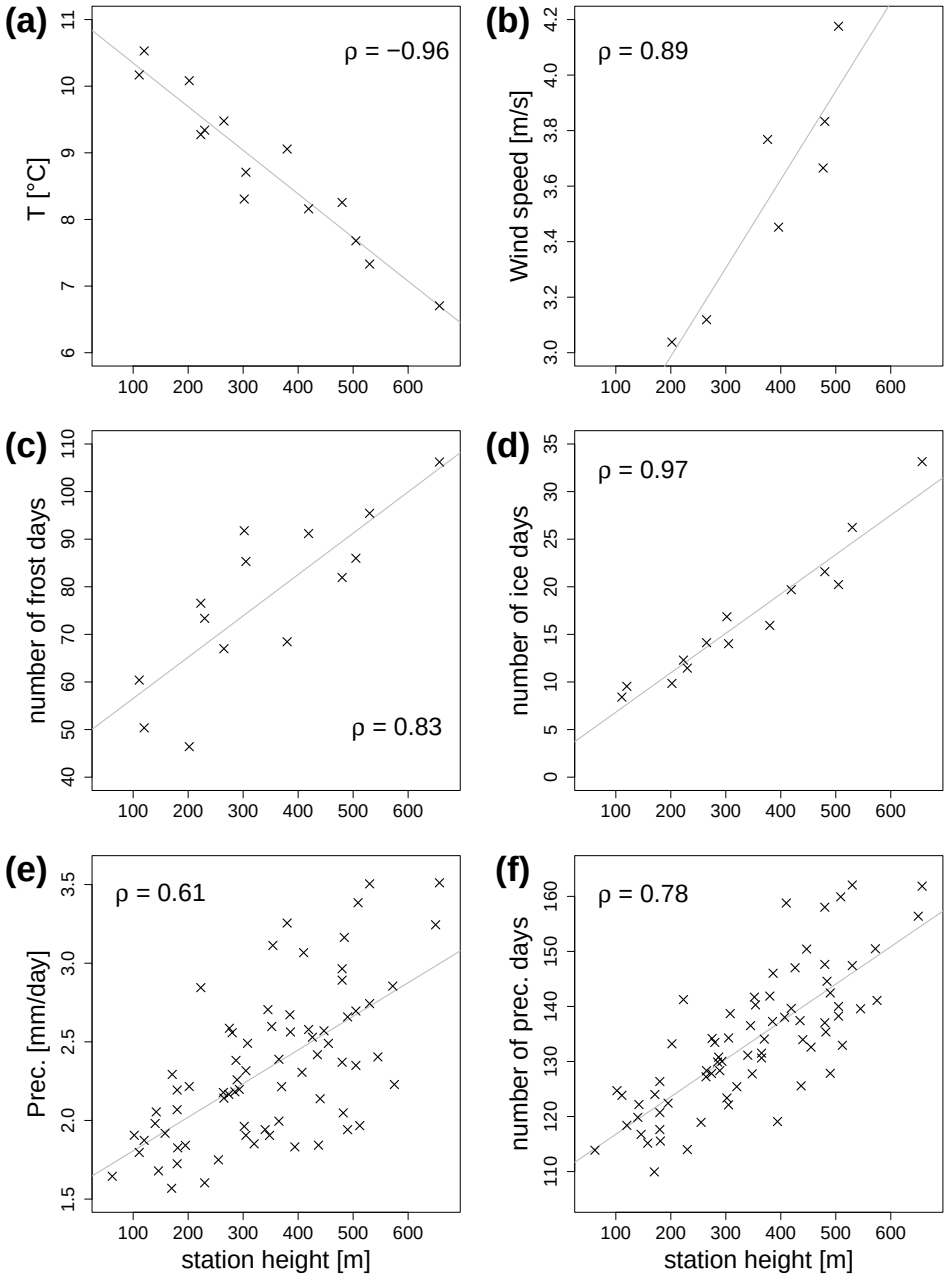

Figure 2.6. *Average values of temperature (a), wind velocity (b), number of frost and ice days per year (c+d), precipitation (e) and number of precipitation days per year (f) for the period 1969-2001 (1979-2001 for wind data). Grey lines show the results of linear regressions. ρ denotes the Spearman rank correlation coefficient.*

Finally, the correlation coefficient between station altitude and precipitation is smaller than for temperature and wind velocity, but a positive correlation can still be observed (Fig. 2.6e). In order to further explore this relationship, the number of precipitation days, i.e. days with more

than 1 mm precipitation, and the average precipitation per precipitation day have been calculated. The former shows a stronger correlation with height (Fig. 2.6f), whereas for the latter the coefficient is only 0.44 (not shown). Hence, the amount of a single precipitation event is, on average, not much influenced by station height, but these events are more frequent at high altitudes compared to low altitude stations.

As a second step for analyzing the spatial variability of the meteorological variables in the Eifel region, correlation maps have been created. This has been done by calculating correlation coefficients of the time series from all available stations with the series from the reference station Trier-Petrisberg and interpolating these coefficients to a regular longitude-latitude grid, using the same triangulation scheme as described in section 2.2. Prior to computing the correlation coefficients, the average seasonal variation has been removed from the time series at each station by subtracting monthly means of the corresponding parameters. The Pearson correlation coefficient has been used for temperature, for which a Gaussian distribution can be assumed. For wind speed and precipitation, Spearman's rank correlation has been applied. It is neither the aim of this method to interprete correlation coefficients at single locations within the Eifel region (otherwise a more advanced interpolation scheme would have been necessary), nor to quantitatively compare the coefficients between different variables. Instead, a qualitative picture shall be presented showing the spatial scales of the representativity of meteorological parameters measured at a single station. This picture is expanded to larger scales in section 2.6 for the special case of extreme events.

Figure 2.7 shows the Eifel correlation map of measured temperature. As can be seen from the Figure, the spatial temperature variability in the region, i.e. on scales of roughly 100 km, is relatively small. The interpolated correlation coefficient is always larger than 0.9, thus temperature measured at the station Trier can be regarded as a good predictor for daily temperature changes in the whole region. Note, however, that there is a bias between the different time series due to the differing station altitudes (see again Fig. 2.6a) that does not affect the correlation coefficient. For wind velocity and precipitation, there is a stronger spatial gradient in the interpolated correlation, as shown in Fig. 2.8. Values down to approximately 0.5 are obtained at the borders of the Eifel region. These fields vary more strongly in space compared to temperature. Precipitation often is a rather local phenomenon, particularly if generated by a thunderstorm. Wind velocity depends crucially on orography and local environmental conditions. Because of this, high correlation coefficients for precipitation are obtained only in a small area around Trier and within the Moselle valley. For wind velocity this area is larger, spanning nearly the whole southern part of the Eifel region, but the correlation at the northern slope of the Eifel mountains, where orography is rather different, is even lower than for precipitation.

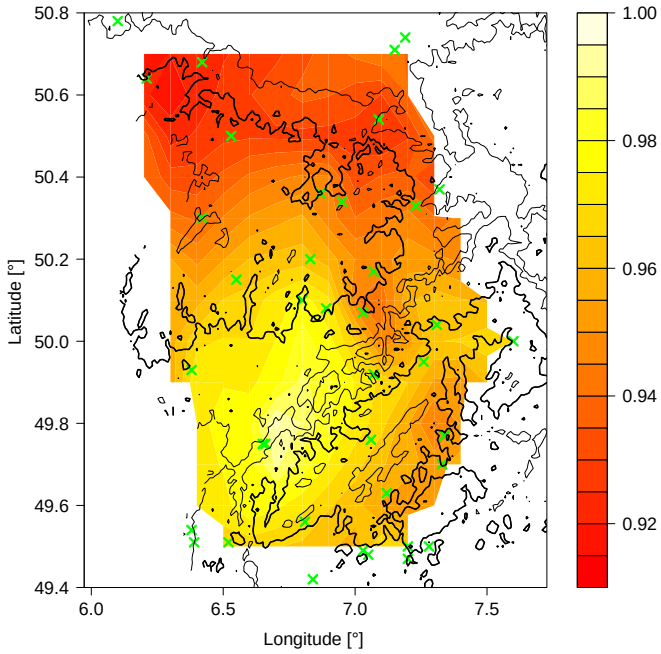

Figure 2.7. *Correlation coefficient of temperature time series with the reference series from Trier-Petrisberg, interpolated in space (color). Green crosses show the stations where temperature has been measured. Solid lines are 200 m, 400 m and 600 m height contours; 400 m contour is printed in bold.*

2.4 Statistical comparison of measurement and reanalysis data

In this section, daily measurement values of meteorological parameters from the Eifel region are compared to ERA40 reanalysis data with the help of statistical methods. In this way, it is evaluated how well the ERA40 data describe local conditions in the region. Furthermore, the relationship between local meteorological events and the large scale synoptic context (represented by the reanalyses) is explored. In the first subsection, ERA40 time series are directly compared to the measurements applying correlation analysis. This comparison would not be possible using output of a (freely running) climate model instead of reanalyses. It allows to assess the performance of the reanalysis data set in not only reproducing the correct statistics, but also the chronology of weather events. The second subsection introduces several methods to compare statistical distributions of parameters from the two data sets. These methods could also be used for the evaluation of climate model simulations. It should be noted here that ERA40 and meteorological station data are not independent (in contrast to climate model data and measurements), because some of the measured values have also been incorporated in the assimilation procedure used to produce the reanalysis. This fact might also lead to differences in the agreement of analysis (e.g. wind velocity) and pure forecast variables (e.g. gust wind speed) between the data sets.

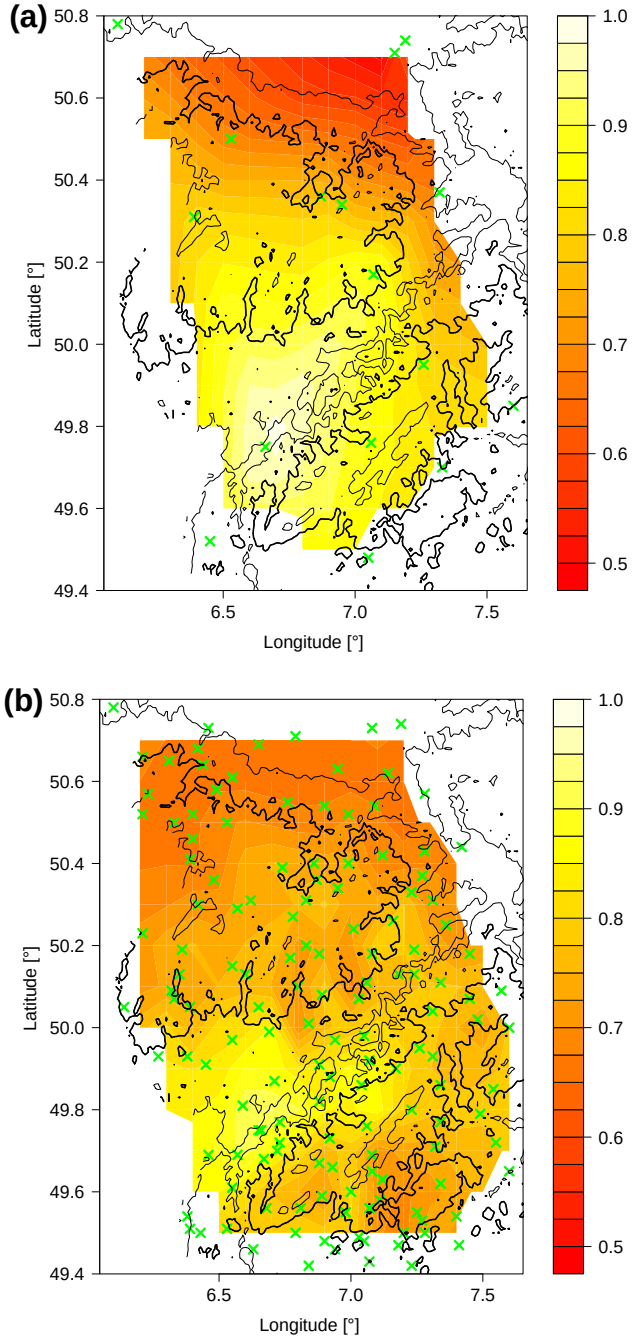

Figure 2.8. *Correlation coefficients of wind velocity (a) and precipitation (b) time series with reference series from Trier-Petrisberg. Symbols as in Fig. 2.7, but note the different ranges of values of the correlation coefficients.*

2.4.1 Time series

Time series from measurements and ERA40 data are compared at the reference station Trier-Petrisberg and for the regional mean. Spearman rank correlation coefficients between time series

from the different data sets, with seasonal variation subtracted as above, have been calculated for the period 1969-2001 (1974-2001 for wind speed). Table 2.4 summarizes the results.

The correlation coefficients for daily mean, minimum and maximum temperature are very high, and there is almost no difference between the coefficients at station Trier and from the regional averages. An example for the very good correspondence between the two time series of daily mean temperature at Trier is shown in Fig. 2.9. The agreement between local measurements and reanalysis data (which have a spatial resolution of more than 100 km) again shows that there is no large variation of near-surface temperature on the spatial scales considered here (cf. section 2.3). The major part of the variance of local temperature fluctuations is controlled by synoptic-scale atmospheric variability, which is described by the ERA40 data. It should be noted here that for $T_{\max}$ and $T_{\min}$ even slightly higher correlation coefficients could be obtained when these parameters were not taken from the ERA40 forecasts, but determined from the six hourly analysis output of the 2 meter temperature. This has been done by fitting a sinus function with a fixed period of 24 hours to the analysis values of each day and adopting the extrema of the range of the function and the six-hourly analyses as daily values for $T_{\max}$ and $T_{\min}$.

For daily precipitation, the correlation coefficients are not as high as for temperature, and there is a large difference between the coefficients at the station and from the regional means. Because of the high spatial variability of precipitation, it is not equitable to compare ERA40 data with values measured at a single location (see again section 2.2.1). Figure 2.10 shows an example of the variability of mean precipitation in the Eifel region. The Figure indicates that the ERA40 data set captures the general characteristics of the measurements, but that there are several precipitation events, particularly those with higher magnitude, that are under- or overestimated. In correspondence with the monthly mean values shown in Fig. 2.5, also in Fig. 2.10 the agreement between reanalyses and measurements is better in winter than in summer.
Correlation coefficients for daily wind speed and gust peaks are in between those for temperature and precipitation (see again Table 2.4). The correlation of the regional mean time series is

	Trier	Region mean
Temp.	0.98	0.99
$T_{\max}$	0.95	0.97
$T_{\min}$	0.94	0.95
Prec.	0.73	0.85
Wind	0.88	0.94
Gusts	0.83	0.90

Table 2.4. *Correlation coefficients between ERA40 and measured time series (daily values) for station Trier-Petrisberg and Eifel region mean. $T_{\max}$ and $T_{\min}$ denote daily maximum and minimum temperature.*

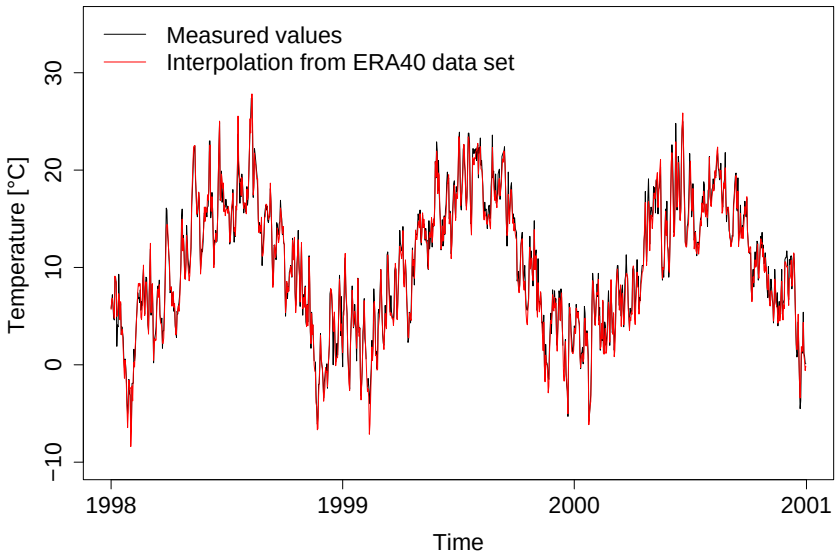

Figure 2.9. *Time series of daily mean temperature at station Trier-Petrisberg from measurements and ERA40 data.*

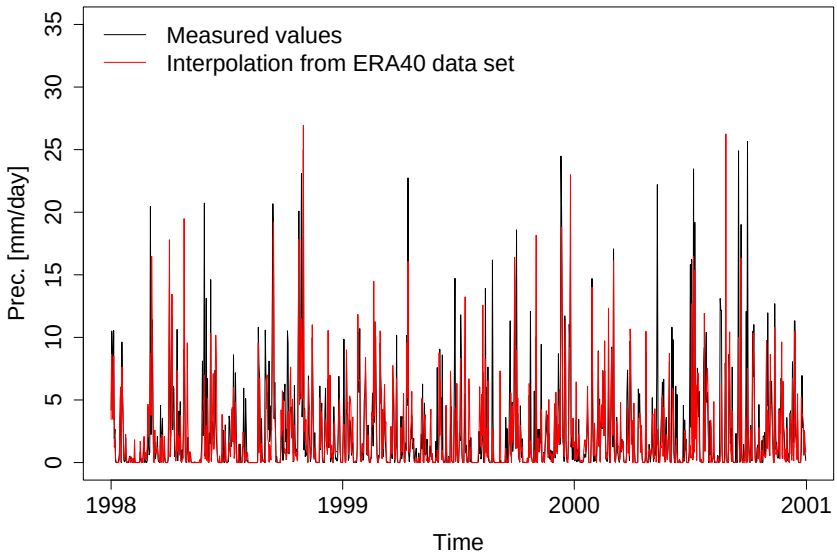

Figure 2.10. *Time series of daily precipitation in the Eifel region from measurements and ERA40 data.*

relatively high; at the station the coefficients are noticeably lower. This fact is again associated with the spatial variability of wind velocity on relatively small scales, which are not resolved in the ERA40 data set. The difference in the correlation coefficients between gusts and mean wind speed points to the positive effect of the data assimilation procedure (note again that the wind gusts used here are pure forecast variables).

2.4.2 Probability density functions and quantiles

For the comparison of statistical distributions from reanalyses and measurements, again data for the period 1969-2001 (1974-2001 for wind) and for both the location of the station Trier-Petrisberg and the Eifel region average are used. Two statistical tools are applied: non-parametric estimators of probability density functions (*pdf*s) and quantile-quantile plots.

The simplest method for estimating pdfs from a set of data is to use histograms. However, this approach has several disadvantages: the resulting approximation of the pdf is not continuous and depends crucially on the breakpoints and the width of the histogram cells. This also leads to some practical drawbacks; it is difficult to produce a large number of histograms automatically, because one has to check the choice of bin-width and breakpoints separately for each histogram. Here, we have avoided most of these disadvantages by applying a kernel density method for the estimation of pdfs of most of the meteorological parameters (see e.g. *Scott*, 1992, for a description of the method). Gaussian kernels have been used, and the bandwidth for each pdf has been objectively chosen with a rule of thumb suggested by *Scott* (1992). This method works well for temperature and wind data. For precipitation, some difficulties occur due to the discontinuity of the pdf at the origin of the coordinate system (precipitation value of 0 mm). It is possible to overcome these difficulties (*Rajagopalan et al.*, 1997), but since this is associated with a considerable complexity, we have decided to use a different approach for precipitation data. After removing days with no precipitation, the logarithmic probability density has been approximated with the help of a log-spline density estimator[4] (*Stone et al.*, 1997).

Figure 2.11 shows the estimated pdfs of several meteorological variables. For precipitation, the difference between the pdfs from station and ERA40 data is rather small, even if local measurements at Trier are compared to the reanalyses (Fig. 2.11a). The reason for this is mostly technical. As shown in the preceding subsection, the two underlying data sets differ substantially, particularly considering events with a high magnitude of precipitation (cf. Fig. 2.10). This is also visible in the pdfs, but does not lead to a large deviation of the two curves, because the statistical weight of such events with high amounts of precipitation is small. The distribution of both data sets is dominated by days with low precipitation around 1 mm. According to this, a direct evaluation of pdfs is not the best method for a statistical comparison of precipitation data from measurements and models. The difference between the distributions becomes much clearer when sample quantiles are taken into consideration (see below).
The pdfs of daily mean wind speed for the Eifel region are shown in Fig. 2.11b. Again, the two data sets are in good agreement. There is only a small negative bias of the ERA40 wind velocities (see also section 2.3), and the density peak between 2 and 3 m/s is slightly overestimated. For daily gust peaks, the match between the two curves is worse (Fig. 2.11d), basically

[4]This log-spline method, on the other hand, has appeared inadequate for fitting densities of wind speed and temperature, because it often undersmooths the pdf, i.e. it produces small-scale, artificial variations in the density. Therefore, it seems necessary to use two different approaches.

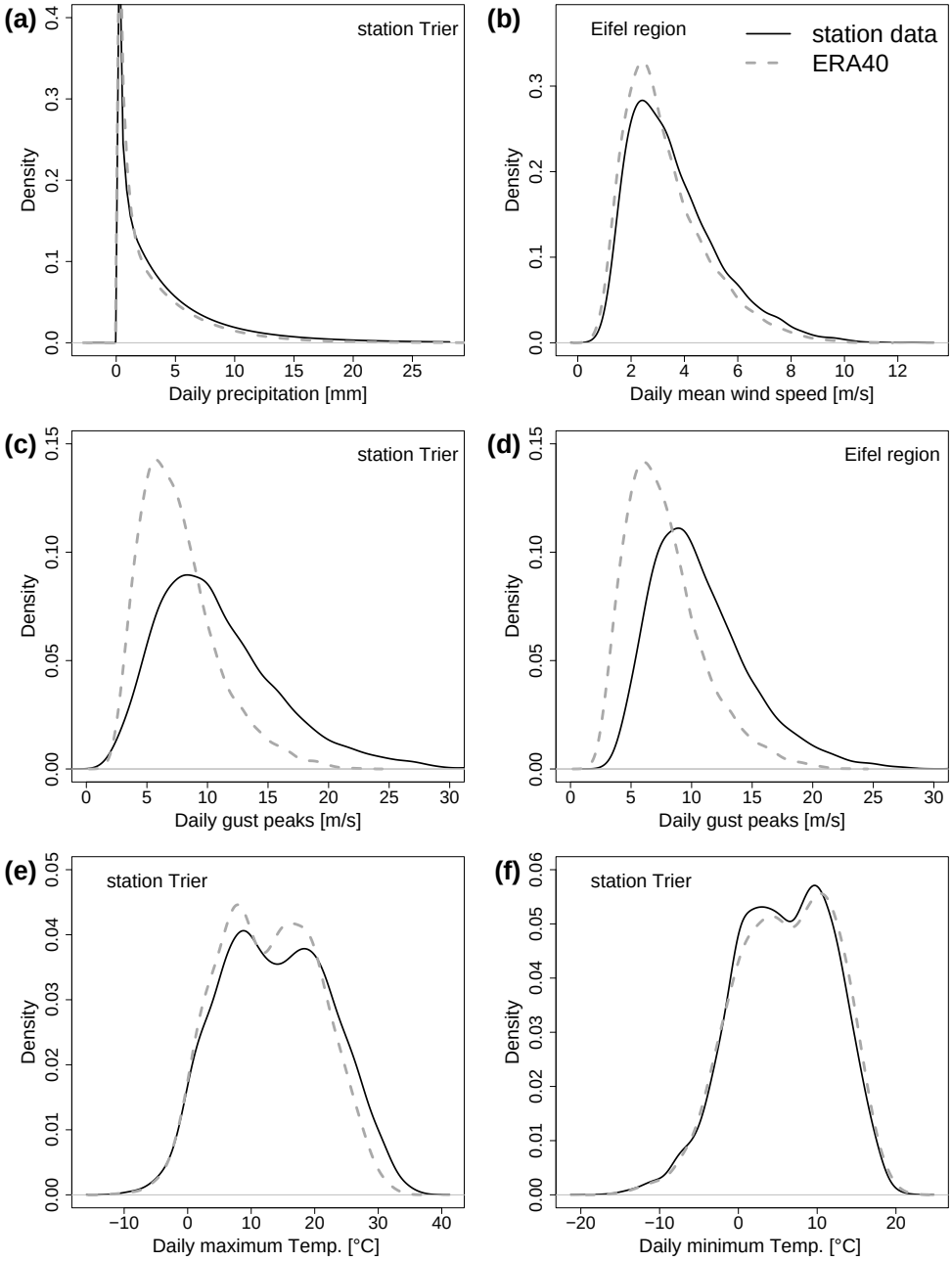

Figure 2.11. *Estimated probability density functions of daily variables from station (solid) and ERA40 data (dashed): precipitation at station Trier (a), regional mean wind speed (b), gust peaks at Trier (c) and for region mean (d), maximum (e) and minimum (f) temperature at Trier.*

because the bias is much larger and the width of the distribution from the reanalyses is slightly too small. Nevertheless, the agreement of the pdfs for regional mean gusts is better than for gusts directly measured at Trier (Fig. 2.11c). For the latter, differences in distribution width and

bias are even larger, indicating that ERA40 gusts, just as precipitation, do not properly represent local measurements, but only regional averages. Recall that, in spite of the deviations between the pdfs shown in Fig. 2.11d, the chronology of ERA40 gusts is in good agreement with the regional mean station data (correlation coefficient of 0.9, see again Table 2.4).
Figures 2.11e and 2.11f show the pdfs of daily maximum and minimum temperature. They are plotted for station Trier, because the station altitude is closer to that of the ERA40 data set than the average altitude of the Eifel region, and thus the temperature bias is smaller[5]. A remarkable feature of the temperature distributions is their bimodality that is clearly visible in both data sets. The pdfs of minimum temperature match almost perfectly. In particular, the left tails of the distributions, representing the coldest nights, have exactly the same shape. For daily maximum temperature, the agreement is slightly worse. The two peaks of the pdf are overestimated in the ERA40 data, and the hottest measured days are not reproduced by the reanalysis.
In Fig. 2.12, pdfs of daily average temperature at station Trier are plotted separately for each meteorological season. Obviously, there is an almost complete match between the curves from the two data sets. The only noticeable difference is a very small underestimation of warm days in summer in the ERA40 data, which is also associated with a peak at around 18°C that is slightly too high compared to the measurements. These seasonal pdfs do not show a bimodality, in contrast to the temperature distribution for the whole year (not shown). Accordingly, the bimodality most probably results from the fact that the Eifel climate is dominated by rather long warm and cold seasons (narrow distributions with clear maxima in winter and summer) and shorter transition periods in between (slightly broader pdfs in autumn and spring).

Another way for comparing the statistical distributions of a variable in two different data sets is to calculate sample quantiles from each set and plot these quantiles against each other in so-called *quantile-quantile plots*. In principle, this can be done using the whole sample, i.e. in our case the whole period 1969-2001, but then high quantiles may be determined by very few extreme events, for example a long lasting heat wave. A more robust statistical quantity is obtained by separately calculating quantiles for each year and subsequently averaging these yearly quantiles over the whole analysis period. Another advantage of this approach is that the uncertainty of the average quantile can be assessed by analyzing the spread in the set of yearly quantiles. Here, this is done with the help of a bootstrap resampling method, as described in section 2.3. For the calculation of the quantiles, an approximately median-unbiased algorithm, independent of the underlying distribution, is used, as recommended by *Hyndman and Fan* (1996). For the sake of completeness, we have also calculated whole sample quantiles, but since the deviations from the average quantiles were always small, they are not shown in the following.

Figure 2.13 shows quantile-quantile plots for precipitation, gust wind speed and daily maximum

[5] Additionally, as already mentioned above, temperature values from reanalysis data can be directly compared to local measurements because of the small spatial variability of the field.

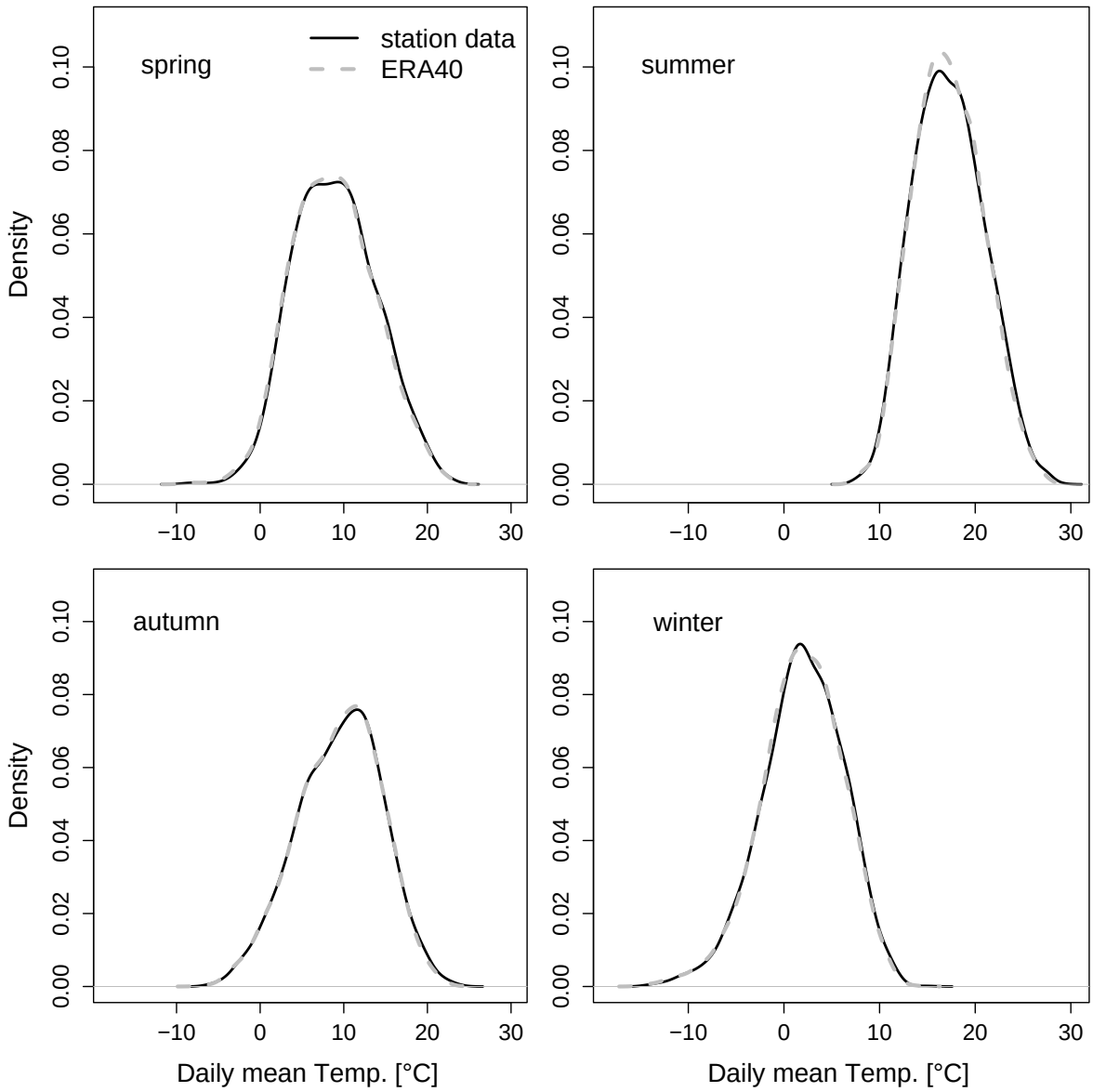

Figure 2.12. *Probability density functions of daily mean temperature at Trier from station (solid) and ERA40 data (dashed), plotted separately for each meteorological season (spring: MAM, summer: JJA, autumn: SON, winter: DJF).*

and minimum temperature. The lengths of the bars indicate the uncertainties of the mean yearly quantiles estimated from resampling. 0.02- (0.1 for precipitation) to 0.98-quantiles are plotted with an increment of 0.02. In Fig. 2.13a, precipitation quantiles at station Trier and for the regional mean are shown. It is again obvious that the agreement between the data sets is much better when regional mean data are considered. For these, quantiles up to 0.9 agree well, only the tail of the distribution, corresponding to strong precipitation events, is underestimated in the

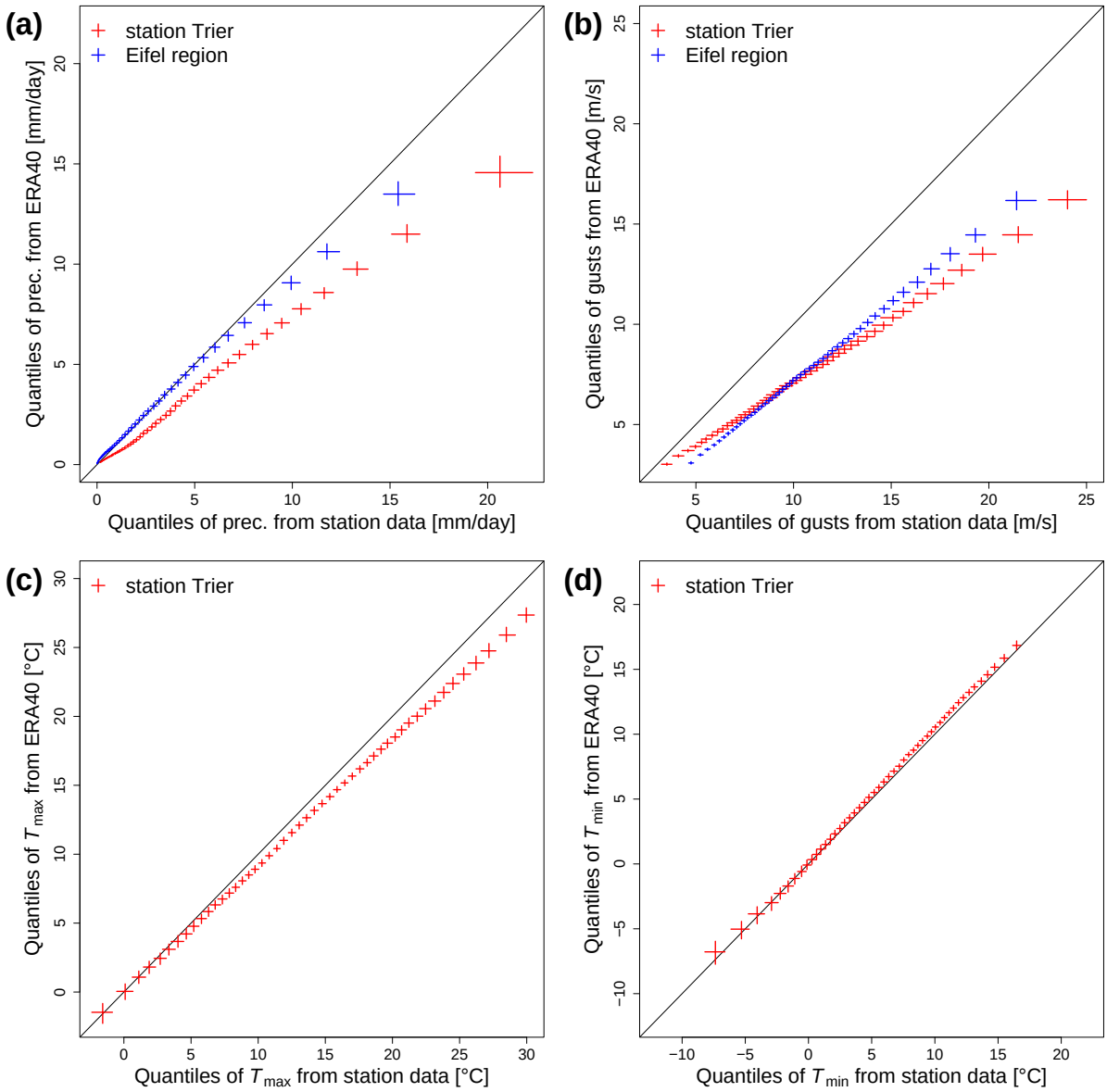

Figure 2.13. *Quantile-quantile plots (ERA40 versus measurement data) of daily precipitation (a), gust peaks (b), maximum (c) and minimum (d) temperature. The vertical and horizontal bars are estimates of the uncertainty of the average yearly quantiles, obtained from bootstrap resampling. The solid black diagonal corresponds to a perfect match. Quantile values from 0.02 (0.1 for precipitation) to 0.98 are plotted, with an increment of 0.02.*

ERA40 data. The rather large deviations obtained in the quantile-quantile plot at station Trier indicate that a direct evaluation of pdfs, as shown in Fig. 2.11a (where the match between the two curves seems to be rather good), is not the best method for comparing statistical distributions of daily precipitation from different data sets. Figure 2.13b shows quantile-quantile plots of daily

gust peaks. As for the pdfs, the agreement is not very good. The slope of the quantiles from regional mean data is closer to 1 compared to the slope of the quantiles at Trier, indicating that the deviations in the former are mainly due to a negative bias. For the latter, also the shape of the distribution differs considerably between reanalyses and measurements (see also Fig. 2.11c). Finally, quantile-quantile plots of daily maximum and minimum temperature at Trier are shown in Figs. 2.13c and d. Again, the match is very good for T_{min}. For T_{max}, quantiles from ERA40 are too small, and the difference is larger for higher temperatures.

In this section it has been shown that there is a good agreement between ERA40 reanalyses and direct measurements of daily temperature variations in the Eifel region. The correlation coefficients between the time series are very high, and also with respect to the statistical distribution, there are almost no differences between the data sets (except for a bias owing to different altitudes). Only the temperature maxima on hot summer days are slightly underestimated in the ERA40 data. This general consistency of temperature variability also leads to a very good agreement of some derivated parameters, e.g. the number of frost and ice days as well as begin and end of the frost period at station Trier (not shown). Taking the variability of wind speed into consideration, daily mean wind velocity and gust speed have to be distinguished. For the former, the temporal correlation and the match between the statistical distributions from ERA40 and measurement data is good; for the latter, the chronology is also well represented in the reanalysis, but there are larger differences in the pdfs. The statistical representation of precipitation in the reanalysis data set is satisfying for regional means, although strong precipitation events are underestimated. This, in addition to other factors (like the more stochastic character of the variability of precipitation on small spatial scales), leads to correlation coefficients slightly lower than for the other variables. The principle consistency between the data sets regarding regional mean precipitation is also reflected in the average number of precipitation days (precipitation larger 1 mm) per year being almost the same (151 for regional mean station data, 153 for ERA40).

2.5 Hydrology

This section focuses on the analysis of hydrological time series from river runoff measurements and their comparison with meteorological precipitation data. It is not the objective of this study to establish quantitative precipitation-runoff relationships in terms of transfer functions, e.g. by using hydrological models (this is beyond the scope of this thesis). Rather, similarities and differences between runoff and precipitation data shall be described. This may, for instance, help to decide which data are more suitable for the calibration of a specific geological proxy. Another objective of our analysis in this section is the detection of droughts. As this detection based on precipitation data is not straightforward, some technical details are explained in the

following subsection. The second subsection describes the comparison of meteorological and hydrological data.

2.5.1 Meteorological droughts

Many different indices have been used for the detection of droughts on the basis of meteorological, hydrological and agricultural data (see e.g. *Keyantash and Dracup*, 2002). For our purposes, a meteorological index shall be employed that is solely based on precipitation, because firstly, other parameters like the properties of the soil, which are often used in addition, are not available here. Second, we intend to clearly separate meteorological and hydrological variables. In addition, the drought index shall be applicable with daily precipitation data, because in this way onset and duration of droughts are detected more precisely, and in particular a statistical comparison of drought lengths from different data sets can be performed in a much better way than using monthly data. An index that fulfills these criteria is the *effective drought index* (EDI), introduced by *Byun and Wilhite* (1999). This index is not considered in the comparison study by *Keyantash and Dracup* (2002), but in another comparison by *Morid et al.* (2006) it shows the best overall performance.

The calculation of the EDI is based on the concept of *effective precipitation* (EP). EP is a measure for the accumulated precipitation over a pre-defined period, multiplied with a weight function representing the decreasing contribution of precipitation events further backward in time. *Byun and Wilhite* (1999) give several alternative formula for the calculation of EP. In this work, the following equation has been chosen:

$$\mathrm{EP} = \sum_{n=1}^{\mathrm{DS}} \left(\frac{\sum_{m=1}^{n} P_m}{n} \right) = P_1 + \frac{P_1 + P_2}{2} + \frac{P_1 + P_2 + P_3}{3} + \ldots, \tag{2.1}$$

where P_m denotes the daily precipitation m days ago and DS is the *duration of summation*. This DS is a crucial parameter and has to be determined as a first step of the calculation. In order to do this, EP is calculated first with a dummy value of DS $= 365$ days, as proposed by *Byun and Wilhite* (1999), because this is the most dominant precipitation cycle. Subsequently, a mean EP value is calculated for each calendar day by averaging this quantity over the whole analysis period and applying a five day running mean. The deviation of EP from this mean (denoted DEP in the following) is then used as a basis for the calculation of DS: For each day in the analysis period, DS is defined as the sum of dummy DS (here 365 days) and the number of consecutive past days with negative DEP, i.e. days dryer than average[6]. Then, equation (2.1) is applied once again with this new DS, and averaging is performed as above to obtain DEP. Finally, the

[6]For example, if DEP < 0 between July 1 and 15, but > 0 before that and afterwards, then DS $= 379$ for July 15 and DS $= 365$ for July 17. This calculation takes into account that e.g. the residence time of water in the soil varies between dry and wet periods.

effective drought index is defined as follows:

$$\mathrm{EDI} = \frac{\mathrm{DEP}}{\sigma_{\mathrm{DEP}}}, \tag{2.2}$$

where σ_{DEP} is the standard deviation of each day's DEP, again smoothed with a five day running mean. Because of the normalization contained in equation (2.2), the EDI does not depend on the climatological characteristics of a specific location.
In order to capture the impact of a drought, both its severity and duration are important. In the following, a drought is defined as a period of consecutive days with EDI lower than minus one, where days with negative EDI in between those drought peaks are included (see again *Byun and Wilhite*, 1999). For each drought, duration and minimum of the EDI during the period are used for estimating the event's impact.

In order to asses the occurrence of meteorological droughts in the Eifel region, the EDI has been calculated for each precipitation station with almost complete data during the restricted base period 1969-2001. Missing values in the time series have been filled as described in section 2.2. Additionally, the EDI has been computed from regional mean precipitation and from ERA40 data (again at station Trier-Petrisberg and at the center of the Eifel region).

When the occurrence of droughts at different stations in the Eifel region is compared (not shown), some similarities can be observed, particularly on large time scales. For example, at almost all stations the years 1971-1973 were rather dry, whereas in the beginning of the 1980s nearly no droughts occurred. Nevertheless, there are also several remarkable differences between the stations with regard to the appearance and duration of single drought events. This is surprising, because droughts are usually thought to affect relatively large areas. The main reason for the spatial variability discovered here is that the EDI is solely based on spatially highly inhomogeneous precipitation measurements. This might be a weakness of the index, but it is not clear to which degree it might overestimate the spatial variability of drought occurrence. This issue shall not be addressed further in this work, but it could be interesting for other studies, also because the EDI has not been used before in an area with such a high density of rain gauges as in the Eifel region. Another interesting starting point for future studies might be to explore the coherence of droughts on larger time scales and the linkage to atmospheric circulation modes like the NAO.
In order to avoid problems with spatial inhomogeneity, the EDI has also been calculated from regional mean precipitation, as mentioned above. It should be noted here that the index was developed for an application with directly measured precipitation data and this is, to our knowledge, the first test using regional means and reanalyses. Table 2.5 shows the most intense and long lasting droughts from regional mean station data. The average daily precipitation during all these droughts was around 1 mm, that is less than half of the long term mean in the region (cf. Fig. 2.5a). The general characteristics that have appeared in the comparison of droughts at

different stations are fairly well reproduced by the regional mean time series (not shown). At the beginning of the 1980s, only very few dry periods occurred in the Eifel region. On the contrary, there were many droughts during the first years of the 1970s and 1990s.

An example for the comparison between measurement and ERA40 data with respect to the EDI and the occurrence of droughts (again for the regional mean) is shown in Fig. 2.14. There are several similarities between the two EDI time series (the correlation coefficient is 0.66), but also certain differences, for example the offsets in the second half of the year 2000 or in the last months of 1997. These offsets can lead to the identification of droughts in one data set that are not detected using the other. They are presumably caused by the over- or underestimation of single, strong precipitation events, as the fluctuations of the EDI on smaller time scales during the offset periods seem to be fairly well correlated. A rather unphysical feature is the sudden decline of the index from ERA40 data at the end of 1997 (such drops infrequently occur in the EDI calculated from station data too, not shown). This decline is due to a drop in the DS on this day and not related to the start of a drier period[7]. The occurrence of such features seems to be a drawback of the EDI, but we think that this does not substantially influence the detection of droughts, firstly because of the rareness of these drops, secondly because the EDI does not fall beneath minus one in most of the cases.

One way for statistically comparing drought data from the two data sets is to look at the statistical distributions of drought lengths. These distributions have been estimated with the kernel density method described in section 2.4 and are shown in Fig. 2.15 for regional mean precipitation data. In general, the two curves agree rather well. Only the main peak is overestimated and smaller peaks at around 50 and 110 days are not contained in the reanalysis data set. Nevertheless, the small peak between 150 and 200 days is captured, albeit shifted a little bit towards shorter durations.

This section has demonstrated that the detection of droughts with a meteorological, precipitation-based index can be complicated and depends strongly on the underlying data set. The EDI

[7] In fact, original EP, calculated with the dummy DS, even increased at this date. This led to the DEP growing positive and to the termination of a long period of EP lower than average.

Begin	End	Duration [d]	Minimum EDI	Aver. prec. [mm/day]
1953-09-01	1954-02-24	177	-2.09	1
1972-12-15	1973-04-01	108	-2.08	1
1963-12-11	1964-03-23	104	-1.91	0.9
1991-03-26	1991-09-24	183	-1.88	1.3

Table 2.5. *Droughts with minimal EDI and a duration of at least 100 days in the Eifel region, calculated from regional mean station data for the period 1950-2005.*

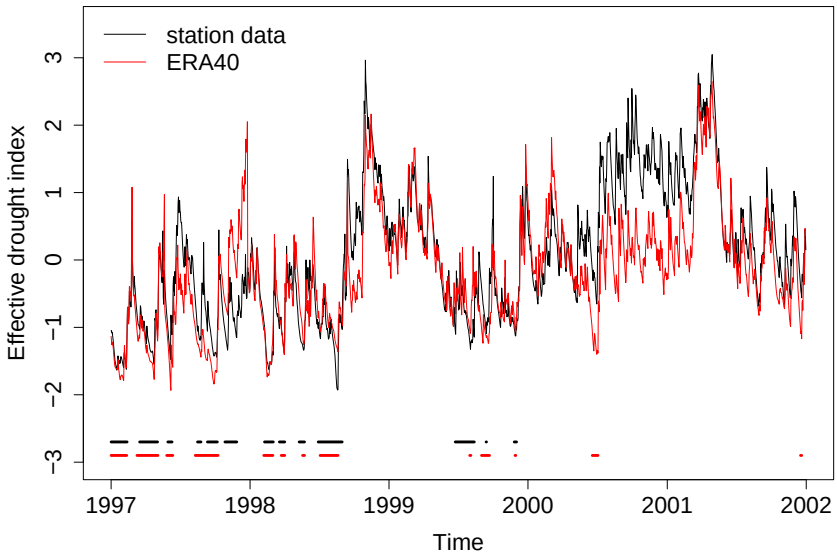

Figure 2.14. *Example time series of the EDI, calculated from regional precipitation means. Horizontal lines at the bottom show the diagnosed droughts.*

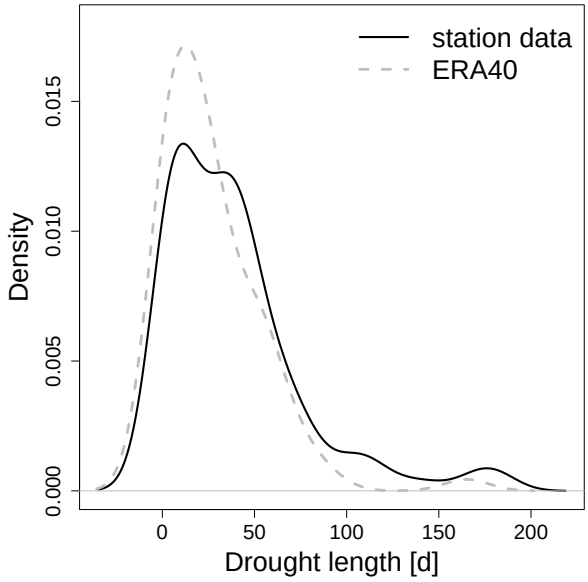

Figure 2.15. *Estimated pdfs of drought length in the Eifel region during the period 1969-2001.*

applied here has several advantages, but because it is a relatively new index and has not been widely used so far, there are some open questions related to its applicability and spatial representativeness. Nevertheless, it has been outlined that the index can consistently be used with regional mean precipitation data. Its application to reanalysis data has to be handled with care. In spite of the good agreement with results from measurement data on a statistical basis (see again Fig. 2.15), there are some difficulties in detecting particular droughts, because the index

is very sensitive to single, strong precipitation events, which are not properly captured by the ERA40 data in many cases (cf. section 2.4).

2.5.2 River gauges

As a first step, runoff and precipitation data are compared qualitatively, focusing on extreme events with high runoff and/or strong precipitation. Figure 2.16 shows measurements of both variables from station Daun for a 3-year period starting in summer 1992. A fact that complicates a direct comparison of such time series is that precipitation is sampled at a single location and for a constant period of time (here one day), whereas a runoff measurement integrates the water from a catchment area and a changing and unknown period. In the case of Daun, the catchment area of the stream Lieser is comparatively small (42.2 km^2). Hence, the error introduced by this integration should also be small, although it cannot be totally neglected because of the inhomogeneity of precipitation also on such relatively small spatial scales. An apparent feature of the runoff time series shown in Fig. 2.16 is the very strong seasonal cycle, which does not appear in the precipitation data, at least not with such a high amplitude (see again section 2.3.1). During summer, evapotranspiration from soil and plants is large, soils are in general drier, and there are more plants absorbing the precipitating water. Owing to this, a much smaller percentage of rainfall is transported to and by streams compared to wintertime, and even strong precipitation events only lead to small peaks in river runoff (e.g. the fourth highest precipitation peak in Fig. 2.16 in summer 1994). On the contrary, during winter most of the maxima in stream flow are directly related to heavy precipitation events. For example, seven of the ten daily maxima in runoff (including the top four) measured at station Daun in the period 1978-2006 were caused by very strong precipitation events that can also be detected in the data from close-by rain gauges or in the regional mean precipitation time series[8]. However, it is difficult to put this relationship into quantitative terms, because also during winter factors like the soil condition have a strong influence on the development of a flood event.

In order to quantify the seasonal cycle in the correlation of daily runoff and precipitation, Spearman correlation coefficients have been calculated separately for each month. An estimate of the runoff roughly representing all streams included in this study has been obtained as described in section 2.2.3 and correlated with the regional mean precipitation time series from station measurements for the period 1973-2005. The result is shown in Fig. 2.17. All correlation coefficients are relatively low, because firstly, as mentioned above, there are other processes apart from precipitation influencing river runoff. Secondly, the correlation method used here is very simple and does not take into account any temporal offsets between the time series, which, however, typically are in the order of one to a few days. Additionally, our estimate of the average regional

[8]The five maximum events from four nearby rain gauges and the ten daily and five-daily maxima from Eifel mean precipitation were taken into account for this comparison.

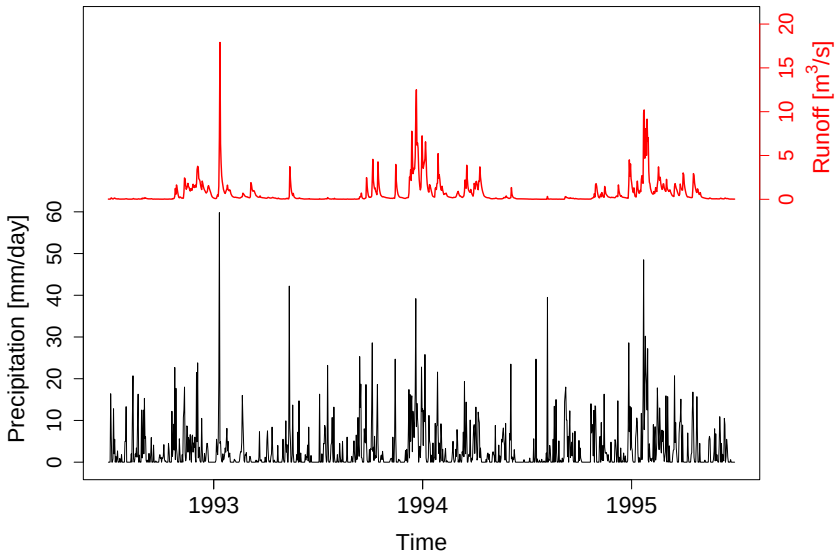

Figure 2.16. *Daily measurements of precipitation (black, bottom row) and runoff (red, top row) from station Daun.*

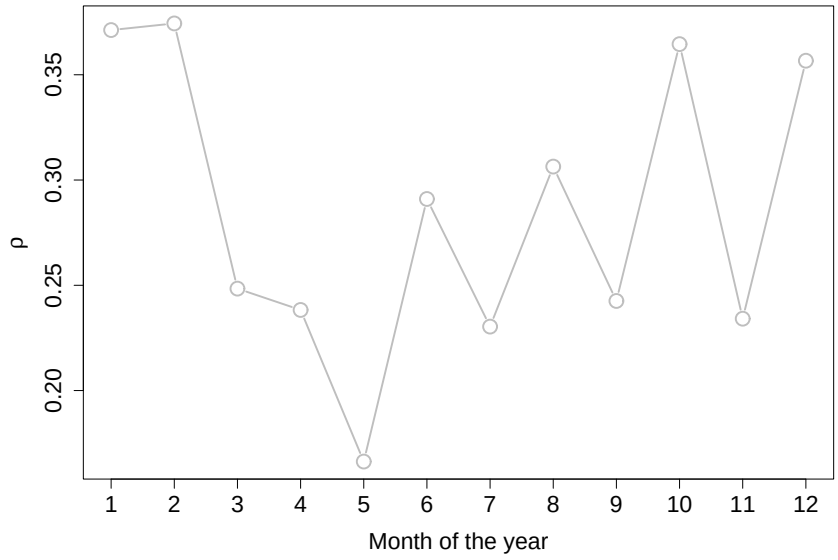

Figure 2.17. *Monthly correlation coefficients of daily regional mean runoff and precipitation (compiled from measurements) for the period 1973-2005.*

runoff is rather crude. In spite of these drawbacks and the temporal fluctuations of the monthly correlation coefficients, a seasonal cycle with minimum in May and maximum in the winter months can be observed in Fig. 2.17. However, particularly the low correlation in November and the increase from May to June cannot be easily understood. These features might also be related to oversimplifications in the method.

In the second part of this subsection, runoff is compared to meteorological drought data, obtained with the help of the EDI as described in section 2.5.1. Therefore, runoff time series have been smoothed with a seven day running average, as outlined in 2.2 and recommended by *Pfister et al.* (2006). Figure 2.18 shows an example of this comparison for the river gauge at Daun and the precipitation station Oberstadtfeld[9]. Droughts diagnosed from the precipitation time series are highlighted in red. In general, there is a good agreement between the two data sets. Most of the meteorological droughts coincide with comparably low runoff values. One has to keep in mind that the EDI measures the deviation of effective precipitation from a calendar day mean, i.e. the runoff values during a winter drought have to be compared with average winter conditions and may, according to this, be higher than in summer. Particularly for the first years shown in Fig. 2.18, the correspondence is very good; the index selects almost exclusively the periods with the lowest river discharge values. Later, there are some deviations, e.g. the low runoff values during summer 1995 and winter 1996 are not detected as drought (just as in summers 1988 and 1994). A reason for this may be that the index is still influenced by the very large amount of precipitation that occurred in winter 1995. This might indicate that the time scale used to calculate effective precipitation, i.e. the dummy DS of 365 days, is too large when the results are compared to river runoff data. This could also explain the pronounced droughts detected in winter 1996/97, which seem to be delayed in some degree.

[9]The rainfall station at Daun only provides data from 1985 to 2000, thus station Oberstadtfeld has been used here, which lies at a distance of 6 km from the river gauge.

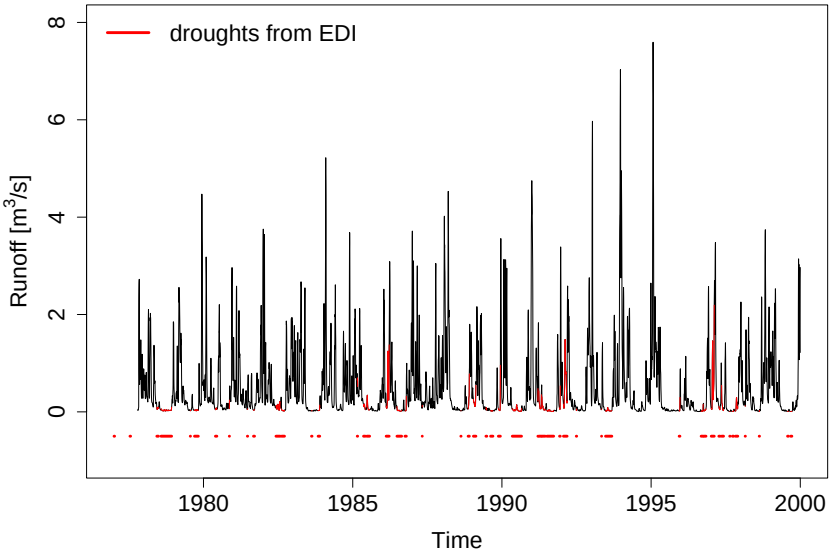

Figure 2.18. *Runoff from station Daun, smoothed with a 7 day running mean. Periods highlighted in red and shown with a red line at the bottom are droughts detected from precipitation measurements at station Oberstadtfeld with the help of the EDI.*

In summary, high runoff values, that is floods in small Eifel streams, are related to local heavy precipitation events in most of the cases. The reverse conclusion is often invalid, there are many strong precipitation events not leading to river floods. A reason for this is the strong seasonal cycle in river discharge, which is influenced by many other factors, e.g. the soil conditions. Owing to this, it is not straightforward to determine quantitative transfer functions linking runoff and precipitation.
The EDI appears to be an appropriate tool for the detection of droughts, also when compared to river runoff data (taking the seasonal cycle in discharge into account). Differences between the two data sets indicate that the time scale used here for the EDI calculation might be too large. In general, one has to keep in mind the integrating effect of river runoff and its temporal delay with respect to precipitation when comparing these quantities.

2.6 Spatial correlation of extreme events

A major objective of this chapter is to provide meteorological data that can be used for a calibration of Eifel lake sediments as proxies of extreme weather events (see section 2.1). In this context, it is an additional, more specific question how representative these local extremes in the Eifel region are for larger areas in Central Europe. This question could be addressed by using proxies at other locations, but this is not easy to achieve, also because the Eifel maar lakes are a relatively unique geological archive. Alternatively, it can be investigated by comparing the occurrence of recent weather extremes in the Eifel region (based on our meteorological calibration data set) with measurements from other locations.

In order to analyze the simultaneous occurrence of extreme events at different stations, it is not sufficient to calculate correlation coefficients between the time series, because these correlations are not substantially influenced by rare extreme events. Instead, a method has been developed using average yearly quantiles of the time series (cf. section 2.4). Based on these quantiles, which have been separately calculated for each station listed in Table 2.1 as well as for the Eifel stations Deuselbach and Trier-Petrisberg as reference, the following extreme events are defined:

- *hot days*: daily maximum temperature exceeds its average yearly 99%-quantile,
- *cold nights*: daily minimum temperature falls below its average yearly 1%-quantile,
- *strong precipitation*: daily precipitation exceeds its average yearly 99%-quantile,
- *strong gusts*: daily gust peak exceeds its average yearly 99%-quantile.

For every station, the number of extreme events has been counted that occurred simultaneously with an extreme event at the reference station Trier. A five day window around the date of the

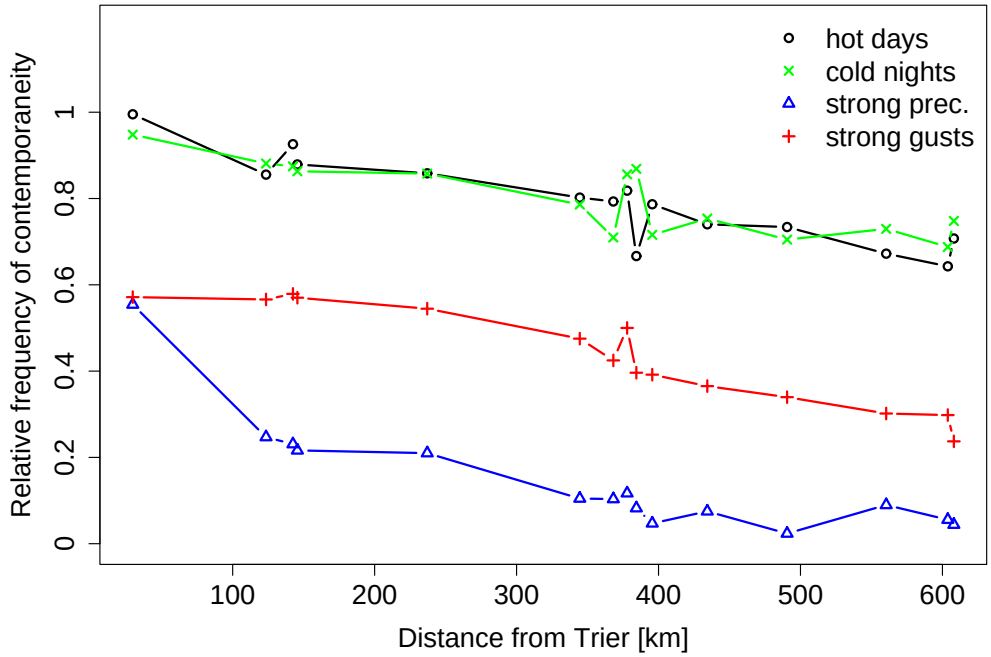

Figure 2.19. *Relative frequency of a simultaneous occurrence of extreme meteorological events at the German weather stations listed in Table 2.1 (plus the Eifel station Deuselbach) and extremes at station Trier-Petrisberg. The reference period is 1971-1999 for wind data and 1950-1999 for all other parameters.*

event at Trier has been applied for the definition of contemporaneity in order to incorporate time lags between its appearance at different locations.

Figure 2.19 shows the frequencies of such simultaneous events (relative to the total number of extreme events at the station) as a function of the station's distance to Trier. The four curves decline rather constantly with distance from Trier; small fluctuations can be attributed to the restriction to one spatial dimension in this plot. Differences between the meteorological variables are obvious in the Figure. Temperature extremes occur simultaneously on large spatial scales; at a distance of 600 km still around 70% of hot days and cold nights happen at the same time as in Trier. For the contemporaneity of extreme gusts, the decrease with distance is comparable to that for the temperature variables, but on a lower level, showing that around 40% of the strong wind events occur on a very local scale. On the other hand, up to a distance of about 300 km more than 50% of these events happen at the same time as in Trier. Precipitation extremes are the most localized events. There is a steep decline of the curve on the first 100 km (for a more detailed description of the local scale, see section 2.3). For distances of more than about 350 km, no coherence between extreme precipitation events can be found.

A similar approach has been adopted for exploring the spatial representativity of flood events, detected in the Eifel region with the help of river runoff data. An extreme flood has been defined

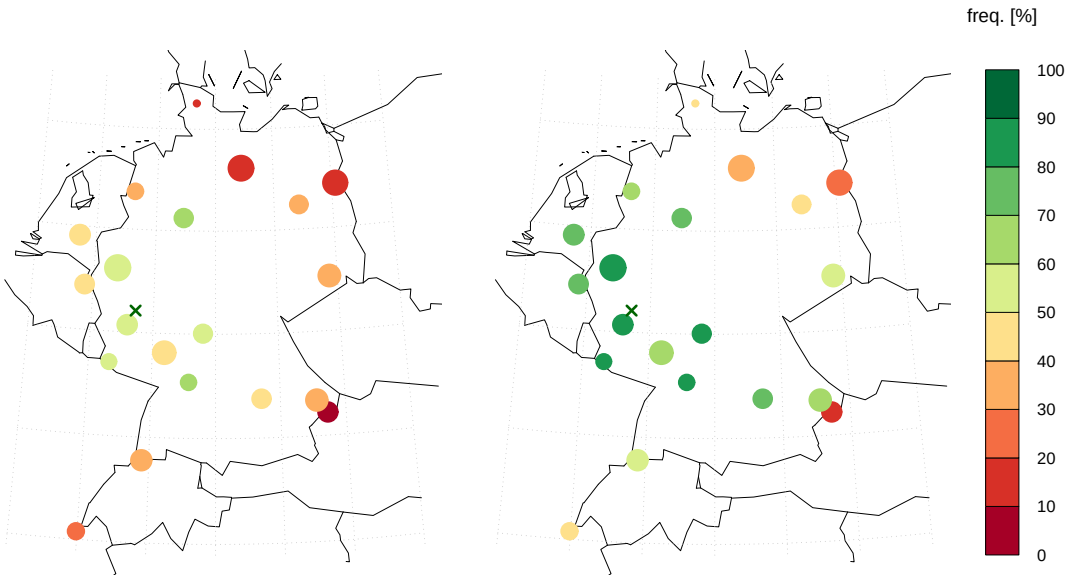

Figure 2.20. *Frequencies of extreme floods (exceeding the average yearly 99%-quantile in runoff) at station Nettegut (Eifel stream Nette, location marked with a green cross), for which simultaneous extreme floods (left panel) or strong floods (exceeding the 95%-quantile; right panel) have been detected at the respective river gauges, listed in Table 2.3. The size of the symbols is a measure for the size of the river's catchment represented by the station. The reference period is 1970-2000.*

as an exceedance of the average yearly 99%-quantile of daily runoff. All stations listed in Table 2.3 have been used, the gauge at Nettegut serves as a reference for the Eifel. The time window for the definition of contemporaneity has been enlarged to eleven days, since the different catchment areas can lead to varying time lags for floods at the stations. As the average 99%-quantile of runoff at Nettegut has been exceeded only infrequently (compared to the other stations), the relative frequencies of simultaneous events have been normalized in a different way than for the meteorological variables. All these frequencies have been computed relative to the number of extreme events at the reference station[10]. Figure 2.20a shows the frequencies of simultaneous extreme flood events, the location of Nettegut is marked with a green cross. Frequencies of more than 50% can be found at the rivers Moselle, Main, Saar, Neckar, Weser and at the lower reaches of the Rhine. In a large part of the displayed region, the values are larger than 30%. Only in northern Germany and in the Alpine region, lower values occur. This shows that a considerable fraction of extreme floods in the Eifel happened at the same time as extreme floods in a large area in Central Europe. If the threshold for the definition of extreme events at the river gauges

[10]For a normalization relative to the number of events at each station, even a very good agreement does not lead to a high frequency because of the low number of events at Nettegut.

is reduced to the average yearly 95%-quantile, referring to “strong” instead of “extreme” floods, but the higher threshold (99%-quantile) is still used at Nettegut, the frequencies of contemporaneity are even larger, as shown in Fig. 2.20b. This large spatial representativity of flooding events in the Eifel region is surprising, particularly taking into account the localized character of extreme precipitation events (see Fig. 2.19).
The consistency of our method for the detection of simultaneous flood events has been checked by including the Finish station Isohaara. For floods at this station, no physical relation to events in the Eifel region is assumed owing to the large distance between the river catchments. The frequency of simultaneous extreme floods at Nettegut and extreme (strong) floods at Isohaara is 2% (5%). These numbers indicate the fraction of simultaneous events that occur only by chance. They are much lower than the frequencies obtained in central Germany, confirming the applicability of the method and the significance of the results. An additional check has been made using a different reference station in the Eifel region, Kordel at the river Kyll. The results obtained with this station have been very similar to those shown here.

Altogether, this analysis shows that the spatial representativity of extreme events in the Eifel region depends strongly on the type of the event. Temperature extremes likely occur simultaneously in a large region in central Europe. Extreme wind gusts may be very localized, but in the majority of the cases they also affect areas of more than 100 km in diameter (and are thus related to synoptic-scale windstorms, cf. chapter 3). Most precipitation extrema are very local events, only about 20% occur simultaneously on distances of more than 100 km. Nevertheless, flood events often affect different rivers with remote catchment at the same time. This is most probably due to the integrating effect of river discharge, because owing to this, only precipitation events with a certain spatial extent lead to floodings in larger rivers. Also, the seasonality of river discharge plays a role in this context: During summer, when floods are rare, precipitation events are often localized; in winter, when most of the floodings occur, precipitation is frequently triggered by a synoptic-scale storm and affects larger areas.

2.7 Proxy calibration

The calibration process of a specific proxy from lake sediments depends crucially on the climatological parameter this process focuses on. Moreover, factors like the location and limnology of the lake are important. Hence, it is not possible to exactly specify the meteorological data necessary for calibrating an arbitrary proxy in the Eifel region. These data have to be selected from the comprehensive data set provided through this thesis according to the needs of a specific calibration task. An example for such an approach is given in chapter 3. Nevertheless, as a conclusion of the present chapter we would like to make some more general comments on the usefulness of the various climatological parameters described in the previous sections with respect to proxy calibration and give a few examples of meteorological times series that might

be applied in this context.

When a proxy of extreme weather events shall be calibrated, the occurrence of these events at a specific location has to be deduced from the meteorological time series. Typically, only a rather small number of extreme events can be detected in the top part of an ELSA sediment core, which represents the calibration period of circa 50 years, owing to the limited temporal resolution (for instance, in chapter 3 six peaks in the grain number concentration of the core are compared to recent windstorms). The selection of such a small number of extremes from meteorological data is often associated with additional complexity, since e.g. the temporal homogeneity of the data might be important in this case. Another general difficulty of the calibration process is that in most of the cases no meteorological measurements are available directly at the location of the proxy. Thus, the spatial variability of the climatological target parameter is crucial, which differs a lot between the various variables (see sections 2.3 and 2.6).

A calibration of proxies for temperature variability or extremes is the least problematic, because, as shown in the previous sections, temperature does not vary a lot on spatial scales comparable to the whole Eifel region. Moreover, there are many stations in the region that provide temperature measurements of good quality and homogeneity in time. All daily temperature variables are very well represented in the ERA40 data set (see section 2.4), and a local temperature reconstruction can be considered representative for synoptic-scale conditions. Figure 2.21 shows an example of a time series that might be applied for such a calibration. Running temperature averages over 30 days have been calculated from the daily means at the station Trier-Petrisberg. This station has again been chosen because of its ensured data quality, and it is representative for conditions in the whole region, as outlined above. The maxima of the 30-day mean temperature time series represent summer heat waves, which might, for example, have caused increased calcium deposition in a maar lake (this is of course just a hypothesis, which could be tested in a detailed calibration study in future research). The most prominent heatwaves at Trier occurred in the

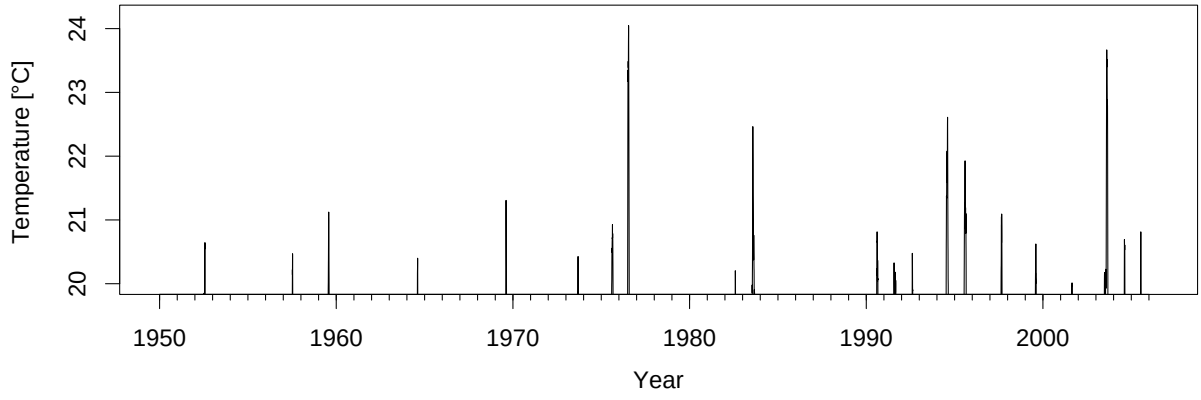

Figure 2.21. *Maxima in 30-day average temperature at station Trier-Petrisberg.*

years 1976 and 2003, the latter was related to a very pronounced, record-breaking temperature maximum in large parts of Europe (*Schär et al.*, 2004). It may also be inferred from Fig. 2.21 that the number of heat waves has slightly increased during the analysis period, but this is not the objective of the present study.

Calibration studies focusing on wind speed or direction usually are more complex. There are many spatial fluctuations in the near-surface wind field, both in a stochastic sense and associated with local environmental conditions as e.g. the slope of orography or the surface roughness. This variability makes it difficult to estimate the wind velocity at a location where no measurements are available. In addition, time series from wind stations are often affected by larger inhomogeneities. In chapter 3, we try to overcome these problems by using a statistical method that combines direct wind measurements and reanalyses.

Section 2.5 has shown that it might be important to distinguish between sediment signals caused

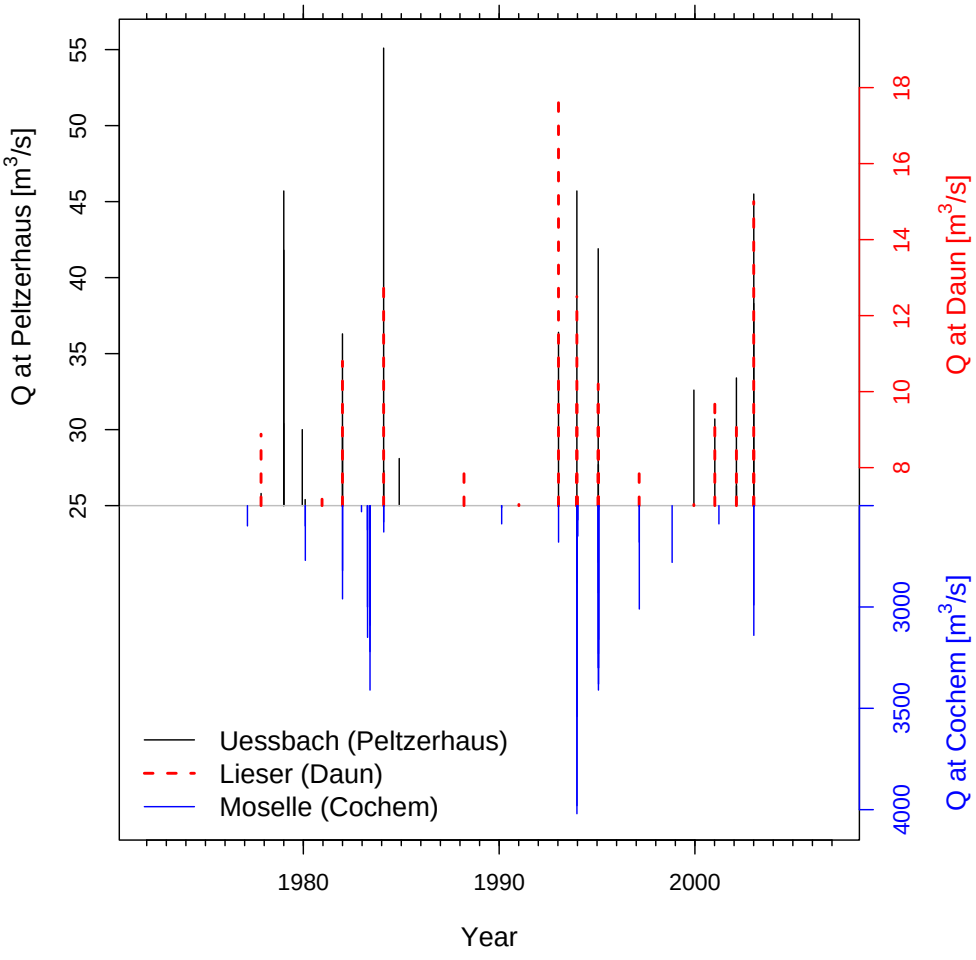

Figure 2.22. *Maximum runoff values Q at two Eifel gauges and at Cochem (Moselle). Data from Daun is only available since 1978.*

by stream flow (for example if the material is transported in this flow, see *Nesje et al.* (2001)) and those directly linked to precipitation (e.g. through erosion, see *Eden and Page* (1998)), because extreme events in both do not necessarily coincide. The high spatial variability of precipitation makes the calibration process difficult, in spite of the very dense network of rain gauges in the Eifel region. When considering extreme floodings, the results from section 2.6 indicate that the spatial coherence of these events is surprisingly high. Nevertheless, there are also certain differences between the runoff maxima of streams in the Eifel region, as shown in Fig. 2.22. Hence, the event-based calibration of a proxy for river floods can be best performed if runoff data are available from a close-by catchment. In a statistical sense, reconstructions obtained from such a proxy are then representative for larger regions in space. This fact is also illustrated by the similar distributions of the maxima in Fig. 2.22 (e.g. many flood events in the middle of the 1990s and almost none during the late 1980s).

A calibration of a proxy for droughts based on precipitation data and the effective drought index is also complex due to the high spatial variability. Figure 2.23 shows the minima in the EDI and the duration of major droughts in the Eifel region. These have been deduced from regional mean precipitation data and are thus thought to represent regional scale events (cf. section 2.5.1). According to the Figure, the most intense droughts occurred in the winters 1953/54 and 1972/73; in 1991, there was a very long lasting dry period. However, additional challenges may arise when these data shall be related to signals in the ELSA sediment. For example, if the sediment signals are associated with variations in the lake's water level, they are not determined by precipitation alone, but also by evaporation of water and thus by temperature changes, which are not taken into account for the calculation of the EDI. This fact is also obvious in Fig. 2.23: In summer 2003, the extreme heat also led to very dry conditions in Central Europe, but precipitation in the Eifel region was not particularly low, thus no remarkable drought has been diagnosed for this year. This example shows that proxy calibrations may be extremely complex if more than one

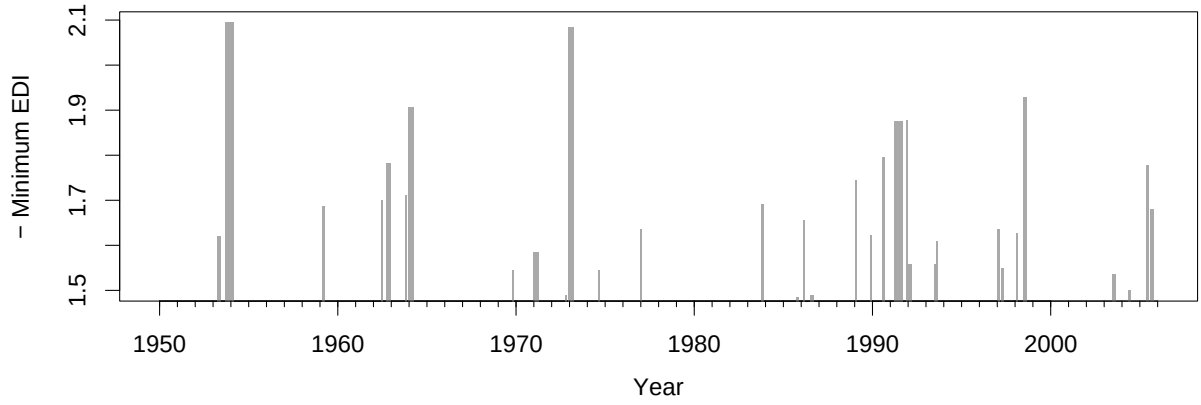

Figure 2.23. *Minimum EDI values (shown at the inverted vertical axis) and duration (widths of the gray bars) of major droughts in the Eifel region, calculated from regional mean precipitation time series.*

climatological parameter influences the sediment signal. In these cases, a more quantitative process understanding is essential. For instance, a more sophisticated model of lake level variability would be necessary in order to calibrate a drought proxy for the example outlined above.

Chapter 3

A new Windstorm Proxy from Lake Sediments[1]

3.1 Introduction

Extreme windstorms are among the natural disasters with the highest impact on human society. The losses from single storm events can amount to several hundred millions of Euro for a country like Germany (*Klawa and Ulbrich*, 2003). In order to estimate variations in the frequency and intensity of windstorms in a changing climate, it is essential to improve our knowledge about these parameters in past times. However, extreme events by definition are rare and the time period for which direct measurements of wind speed are available is relatively short. Hence, it is very important to prolong this period by integrating proxy data, which enable us to infer about windstorm occurrence in past times. A few studies have addressed this question, mainly focusing on the northern European coastal regions. Some of these investigations relied on coastal dunefields (e.g. *Pye and Neal*, 1994; *Clemmensen et al.*, 2001; *Wilson et al.*, 2001) and cores from peat bogs (*Björck and Clemmensen*, 2004; *de Jong et al.*, 2006). However, for large parts of the globe there are no windstorm proxies available.

There are only few investigations that apply lake sediment data for the reconstruction of paleoweather events, as outlined in section 1.2. In all of these studies focusing on past storms (*Eden and Page*, 1998; *Rodbell et al.*, 1999; *Nesje et al.*, 2001; *Noren et al.*, 2002; *Besonen et al.*, 2008), the sedimentation mechanism has been related to erosion after strong rainfall or river floods. Hence, the detected storms have been characterized by extreme precipitation, but not necessarily by strong winds. In a statistical sense, the frequency of storms with heavy rain

[1] A slightly modified version of this chapter has been accepted for publication as *Pfahl et al.* (2009). Copyright 2009 American Geophysical Union.

might be linked to the frequency of severe windstorms, but looking at isolated events, one has to distinguish between the two. Lake sediments have not been used as proxies for the identification of single extreme windstorms so far, but there are several studies that make inferences about the general wind climate based on lake sediments (e.g. *Halfman and Johnson*, 1984; *Brauer et al.*, 2008). It is well documented that high winds influence sedimentation by inducing water currents and waves (*Larsen and MacDonald*, 1993). Waves mobilize sediment grains in the littoral and sublittoral zone of the lake, where coarse grained minerogenic and biogenic particles (mainly plant remains) get in suspension and are then transported into the inner parts of the lake by surface or bottom currents, depending on the density of the suspension fluid. Coarse-grained sand particles are removed gravitationally over the slope, but smaller silt grains have a potential to reach a few hundred meters offshore. Wave height and current speed are a function of wind velocity, with surface currents being near to 2% of the wind speed (*Larsen and MacDonald*, 1993).

When a proxy for past windstorms shall be calibrated, the quality of meteorological data constitutes an additional challenge. Almost all multi-decadal time series of wind measurements suffer from inhomogeneities, caused for instance by changes of instruments or changes in the surroundings of the site where measurements are performed (*WASA-Group*, 1998; *Bärring and von Storch*, 2004). Such inhomogeneities are particularly problematic for the detection of extreme storms within long time periods and prevent the direct use of the measured time series. In addition, the high spatial variability of wind speed has to be taken into account if, as it is typically the case, no measurements are available at the location of the proxy data. In many studies, indices deduced from pressure records have been applied to overcome the difficulties related to inhomogeneity (see again *WASA-Group*, 1998; *Bärring and von Storch*, 2004), but they cannot be used to detect single storms in an event-based manner. In this chapter, we introduce a new index of storminess calculated from a combination of reanalysis data and wind measurements and compare it with sediment core data.

This study can be regarded as a pilot study, in the sense we assess the requirements for establishing a connection between severe windstorms and signals in lake sediment, focusing on the last 50 years, for which detailed meteorological surface measurements and reanalysis data are available. The calibration approach proposed in this chapter can be subsequently applied also for the interpretation of long records, beyond the time period of meteorological measurements, and it provides the basis for the application of a new windstorm proxy in all regions where suitable lakes with similar sediment records can be found.

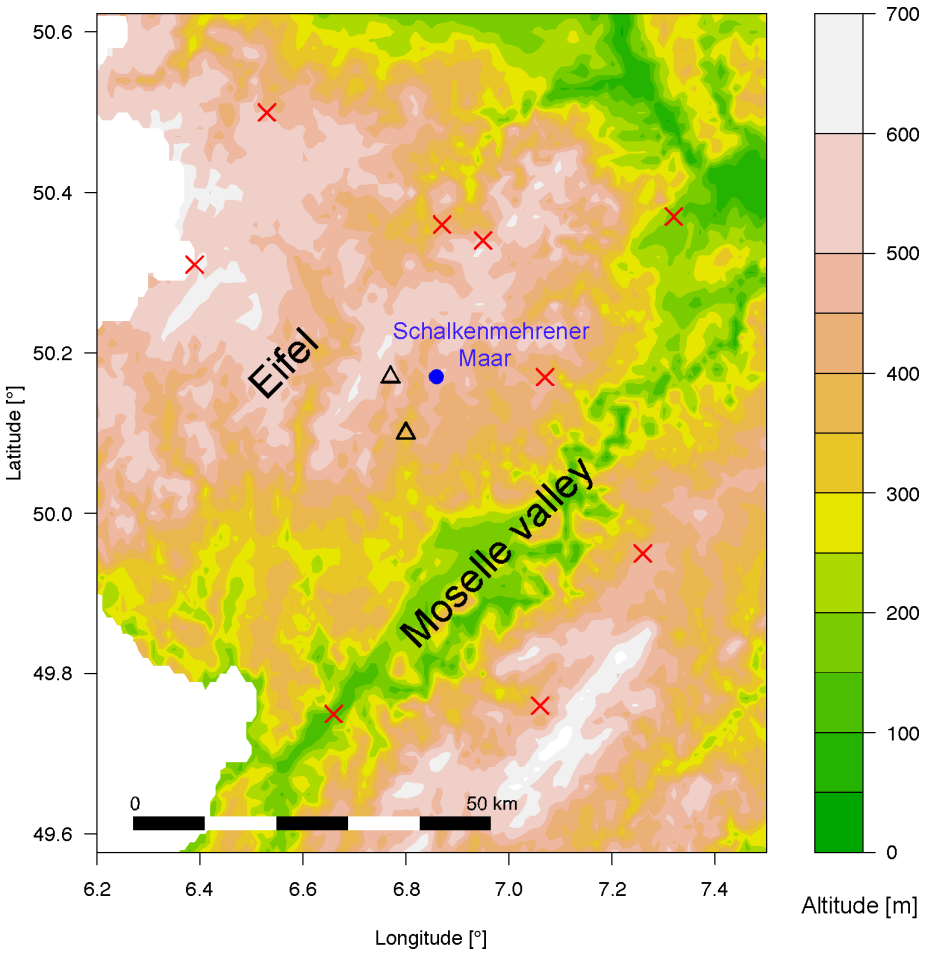

Figure 3.1. *Topography of the Eifel region (colors, only shown within Germany). The position of the Schalkenmehrener Maar is labeled with a blue circle. Red crosses denote locations of DWD stations with wind measurements used in this chapter (cf. Table 3.1); black triangles denote the positions of the two stations with precipitation measurements, Mehren and Oberstadtfeld.*

3.2 Sediment data and analysis

3.2.1 Sediment core

The core used for this study is part of the Eifel Laminated Sediment Archive (ELSA), a collection of sediment cores (from freeze cores to Seilkern cores of 150 m length) that have been retrieved from 30 maar lakes in the western German Eifel region (7° E/50° N; see Fig. 3.1). These cores constitute a continuous record of sediment data in Central Europe for the last 150.000 years (e.g. *Sirocko et al.*, 2005; *Schaber and Sirocko*, 2005; *Seelos and Sirocko*, 2007; *Sirocko*, 2009). Here, we use a freeze core from the Schalkenmehrener Maar lake (SMf; see Figures 3.1, 3.2,

3.3). The almost circular maar has a diameter of circa 550 m and is 21 m deep. Its surface area is 219,000 m^2 and the catchment area amounts to $1.2 \cdot 10^6 m^2$. The lake is dimictic, with mixing in spring and fall and strong summer stratification; the depth of the thermocline varies between 4 and 8 m in May and between 6 and 10 m in September. Several deep cores have been obtained from the maar (see again *Sirocko*, 2009), but SMf, which was taken close to the center, is the only freeze core. Freezing technology (see http://www.uni-mainz.de/FB/Geo/Geologie/sedi/) allows to retrieve the water saturated top layers of the core, which represent recent times. Figure 3.3a shows a photo of the core directly after drilling. The lower part of the core is continuously laminated, whereas there is no visible lamination of the top part due to the eutrophication of the lake, which began around 1860. The sediments have been transformed to petrographic thin sections of 10 cm length, and a quartz grain size analysis has been performed up to micrometer resolution with the RADIUS method (*Seelos and Sirocko*, 2005) at the Institute for Geosciences, University of Mainz, in the group of F. Sirocko. Particularly important for the detection of storm signals is the number of grains per area in the coarse silt fraction, i.e. with grain sizes between 20 and 63 μm. Peaks in the silt fraction curve (Fig. 3.3b) mark distinct layers (details of such a layer are shown in Fig. 3.4), which share the following attributes:

- average layer thickness of circa 1 mm (Fig 3.4a),
- sharp quartz grain size distribution with clear Gaussian shape and a mean value of ca. 18 μm, as shown in Fig. 3.4b (i.e. the distribution is clearly shifted to larger grain sizes with respect to the distribution of the background sediment, exemplarily shown in Fig. 3.5),
- no gradation (i.e. no variation of grain sizes within the layer),
- high amount of relatively large organic material, e.g. pieces of plant debris (not shown),
- high concentration of carbonate grains (slightly smaller mean grain size than quartz particles, Fig. 3.4c).

3.2.2 Age model

An age model for the SMf core has been developed from ^{137}Cs and ^{210}Pb activities in the sediment, measured by direct gamma assay, in the Liverpool University Environmental Radioactivity Laboratory. Figure 3.6 displays the ^{137}Cs activity. The curve shows a distinct peak at a depth of 9.5 cm, marking the Chernobyl fallout in 1986. A second maximum at a depth of 16.5 cm is also visible, probably recording the fallout maximum from atmospheric nuclear weapon tests in 1963. However, this second peak is much less pronounced than the first one, indicating that the ^{137}Cs activity has been diluted in the respective depth. Since a similar dilution occurred for the ^{210}Pb activity (see appendix A), the ratio ^{137}Cs/^{210}Pb, peaking at 17.5 cm, has been considered

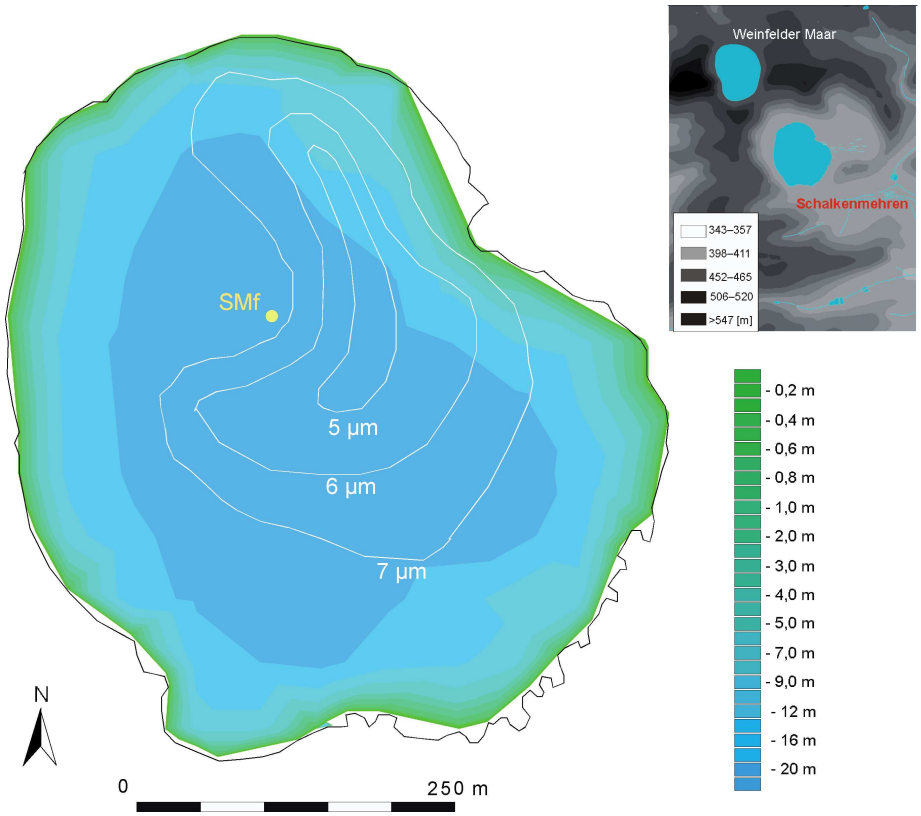

Figure 3.2. *Bathymetry (color) and average grain size distribution of the floor (white contours; determined from sediment sampling) for the Schalkenmehrener Maar. The yellow dot gives the position of the freeze core SMf. The inlet shows the topography in the environment of the maar. The location of the village Schalkenmehren (SM) is indicated in red. The Weinfelder Maar is another maar lake located to the northwest of SM. (from K. Seelos)*

as a better marker for the 1963 fallout maximum.

The constant rate of supply (CRS) dating model (*Appleby and Oldfield*, 1978) has been applied to calculate raw dates from the ^{210}Pb measurements (measured ^{210}Pb activities are provided in appendix A). These raw dates have appeared to be clearly too old compared to the ^{137}Cs peaks. Likely reasons for this discrepancy are moderate variations of the ^{210}Pb supply rate during the last decades and an incomplete recovery of the ^{210}Pb record in deeper sections of the core. In particular, a hiatus in the sediment record most probably occurred at a depth of more than 20 cm, which represents the time of World War II when large amounts of weapons and ammunition have been dumped in the maar causing sediment redeposition from the upper slope to depth. This influences the CRS dating model, but does not affect the inferences of this study, which is based on data from the uppermost 20 cm. In order to overcome these discrepancies and to obtain a final chronology for the SMf core, the CRS model has been recalculated with the 1963

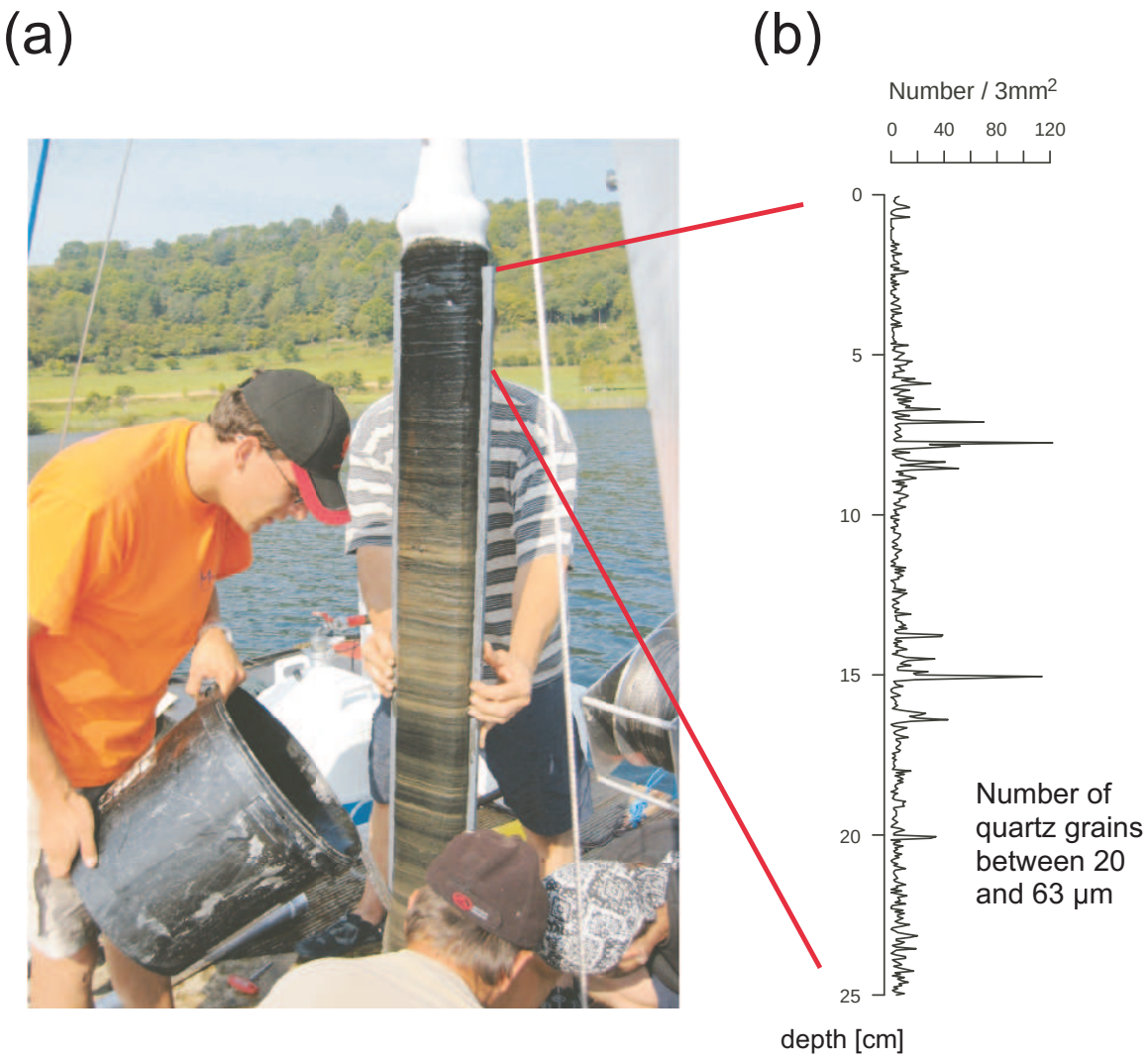

Figure 3.3. *(a) Photo of the SMf core directly after drilling (from Sirocko (2009)). (b) Measured number concentration of coarse silt particles in the top part of the core.*

$^{137}Cs/^{210}Pb$ marker as a reference, using the method described by *Appleby* (2001). The resultant chronology is shown in Fig. 3.7. The correspondence with the 1986 ^{137}Cs maximum is very good for this curve. However, the uncertainties of the age model are rather large, especially for greater depths (between ± 1 years for small and ± 6 years for large depths), owing to the problems described above (e.g. dilution of the activity signals).

3.2.3 Sedimentological windstorm identification

In many cases, deposition of coarse quartz grains in lake sediments is related to fluvial erosion processes (e.g. *Eden and Page*, 1998; *Noren et al.*, 2002). However, in the case of the Schalken-

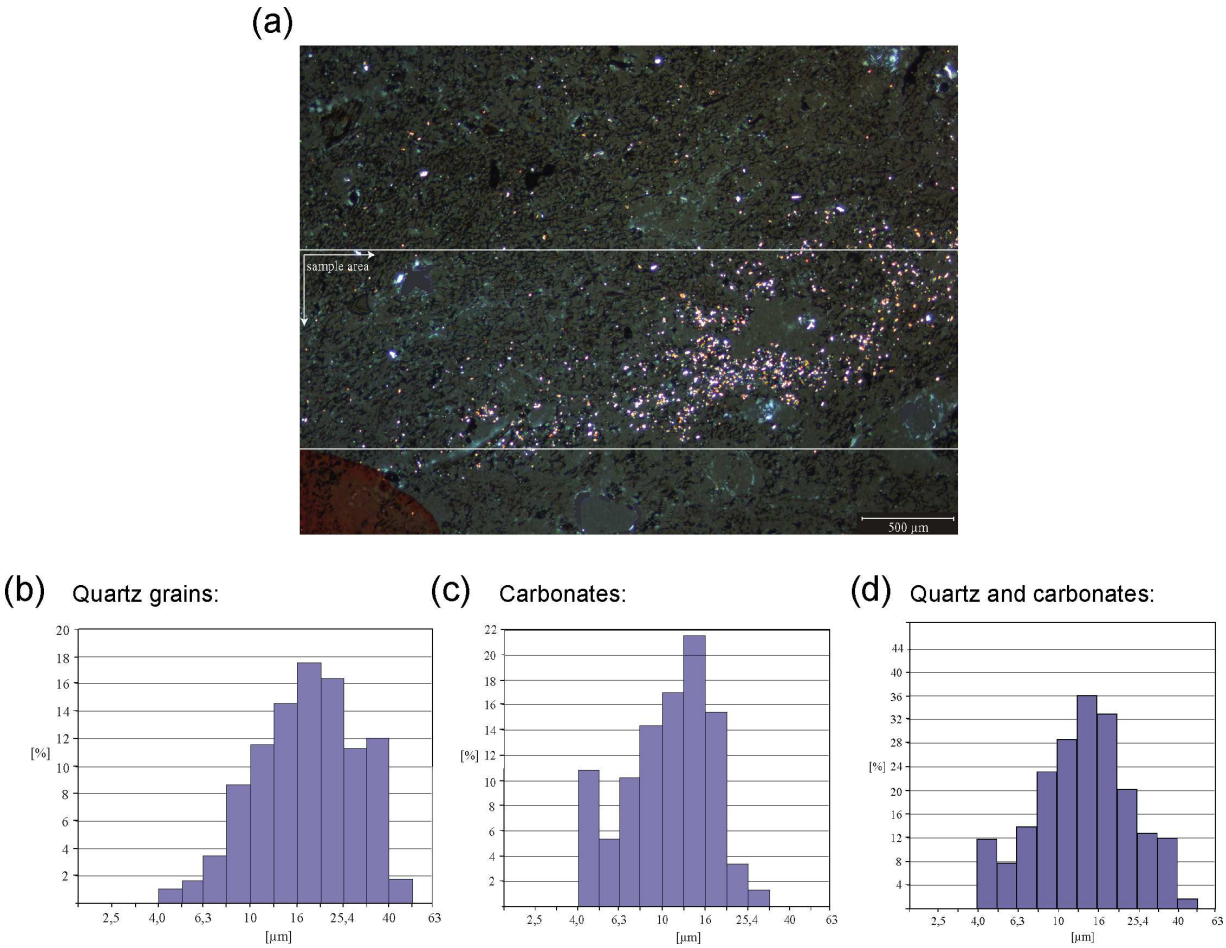

Figure 3.4. *(a): Polarized microscope image (magnification: 25x) of the SMf core sequence 7.62-7.89 cm (corresponding to the windstorm labelled 5 in Fig. 3.10), showing the sample area (1.0 x 3.6 mm) and the layer with white (quartz) and reddish (carbonate) particles. (b): Grain size distributions (diameter in µm) of quartz grains in the layer (1/3 phi classification). 569 quartz particles have been detected. (c): Grain size distribution of carbonate particles (792 detected particles). (d): Combined distribution of quartz and carbonates. (from K. Seelos)*

mehrener Maar, no riverine sediments have entered the lake since around 1950, when the basin and delta of the creek feeding the maar in earlier times were artificially transformed into a vegetation covered swamp that acts as a sediment sink. Moreover, there are no steep hills surrounding the lake (in contrast to the lakes sampled e.g. by *Noren et al.* (2002)), hence the inflow of rainwater from strong precipitation events is comparably small. Accordingly, it is unlikely that the layers of enhanced silt grain fractions observed in the SMf core are caused by fluvial erosion processes, i.e. reflecting precipitation events. An alternative mechanism is that these layers were formed during windstorms by wave erosion at the shore and subsequent current transport. High wave activity leading to erosion at the shore is intrinsically related to high wind velocity (*Larsen*

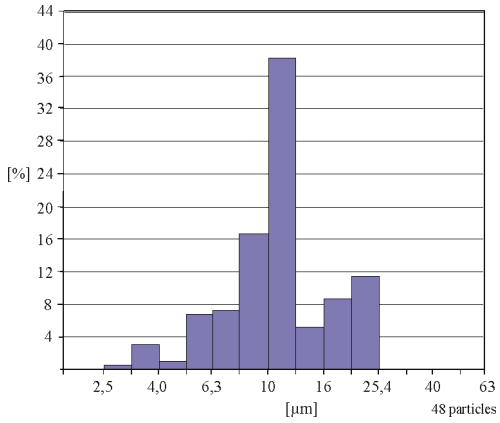

Figure 3.5. *Example for the quartz grain size distribution in the background sediment (no storm layer). The sample has been taken from SMf in a depth of 11 cm. Only 48 quartz particles have been detected in the sample area (again 1.0 x 3.6 mm). (from K. Seelos)*

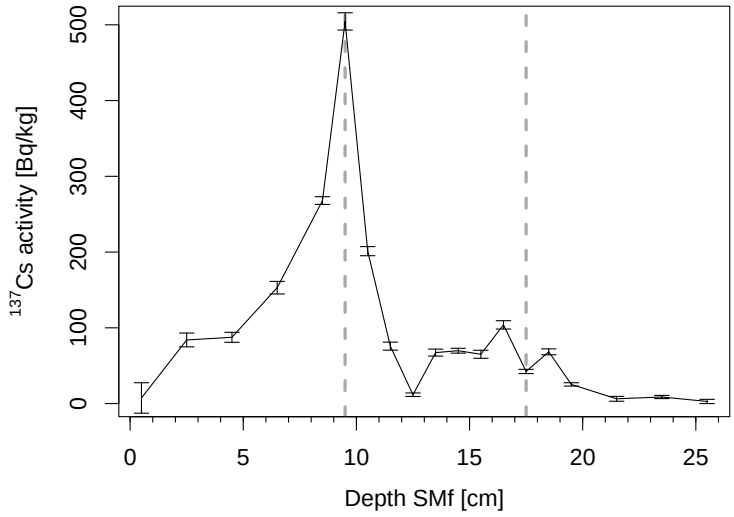

Figure 3.6. *Measured* ^{137}Cs *activity from the SMf core. The vertical dashed lines give the positions of the Chernobyl fallout in 1983 and the fallout maximum from atmospheric nuclear weapon tests in 1963 (note that the maximum of the ratio* ^{137}Cs$/^{210}$Pb *has been used as indicator for the latter).*

and MacDonald, 1993). In order to create a distinct layer in the sediment core, quartz grains eroded during strong wind events have to be transported to the centre of the maar. This transport can proceed in several ways: If the stratification of the lake is rather weak, the sediment loading of the waters close to the shore can generate a density current that transports the grains along the lake floor (*Middleton*, 1966; *Pharo and Carmack*, 1979). The rather steep slope of the lake bottom close to the shore might support such a current. However, in cases of strong stratification a density current is unlikely. In this case, grains can be transported by currents within the wa-

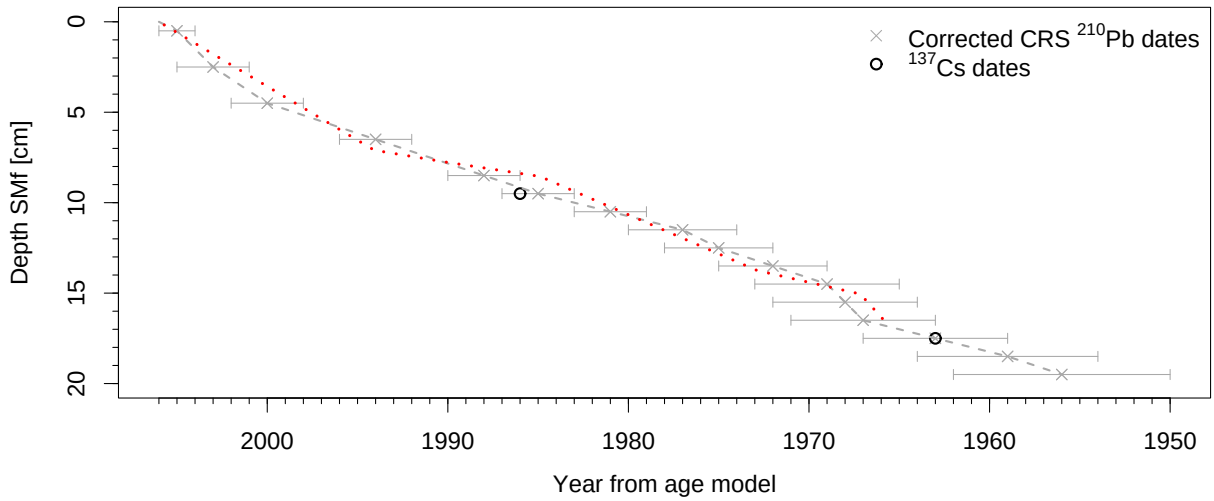

Figure 3.7. *Corrected CRS age models for SMf. Black circles give the dates derived from the* ^{137}Cs *activity maxima. The dotted red line shows an age model obtained from the storm layer allocation given in Figure 3.11.*

ter body (*Elçi et al.*, 2007; *Marti and Imberger*, 2008). In laboratory experiments and with the help of a linear model, *Stevens and Imberger* (1996) showed that in stratified waters under wind stress, a return flow in upwind direction can establish in the thermocline, and the flow velocities in this return current can be of the same order as the friction velocity at the lake surface. Because of the relatively small settling velocities of the silt particles (in the order of 1 mm/s), grains of 60 μm diameter can reach the maar centre within this return flow. However, the three-dimensional flow in a real lake depends on many factors, and the exact form and velocity of the return current in the Schalkenmehrener Maar cannot be determined here.

Two observations of storm events support the argumentation given above (F. Sirocko, *pers. comm.*, 2008). First, for an extreme thunderstorm in August 2006 it was observed that wave-generated silt particles were dispersed in near surface currents. The particles were sampled 100 m offshore at the top of the thermocline, two hours after the thunderstorm event. Waves during this thunderstorm were 30 cm high and the entire surface water down to the thermocline was highly turbulent with visible sediment load. In Figure 3.8, an image of a smear slide produced from the sample and the corresponding grain size distributions are shown. These distributions have the same shape as the distributions from the SMf storm layer (Fig. 3.4), supporting the idea that the particles originated from the same transport process. However, although the thunderstorm sample was taken closer to the shore (compared to the location of SMf), its mean grain sizes are clearly smaller than those shown in Fig. 3.4. The likeliest reason for this shift is that the thunderstorm did not continue long enough to erode a substantial amount of material at the shore (it lasted about 30 minutes). This shows that, in order to form a visible storm layer in the

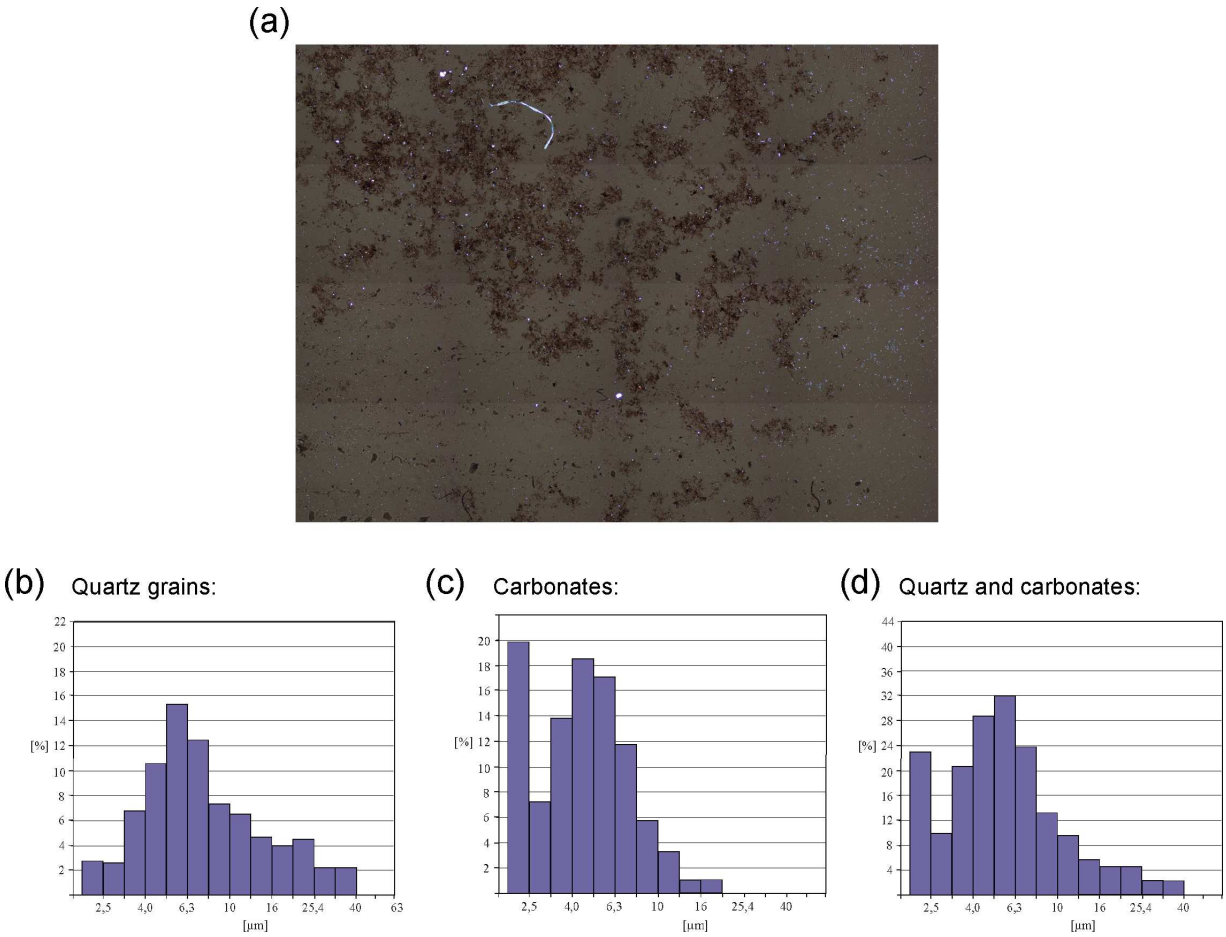

Figure 3.8. *(a): Polarized microscope image (magnification: 40x) of a smear slide sample, taken from the Schalkenmehrener Maar (ca. 100 m offshore) after a thunderstorm in August 2006, showing quartz and carbonate particles as in Figure 3.4, together with a lot of organic debris (darker regions). (b): Grain size distributions (diameter in µm) of quartz grains in the sample (1/3 phi classification). (c): Grain size distribution of carbonate particles. (d): Combined distribution of quartz and carbonates. (from S. Dietrich)*

core, it is necessary that high winds persist for a longer period of time, at least one or two hours. This is usually the case for a large-scale storm (e.g. a typical mid-latitude winter storm), but not for a more local event like a thunderstorm.

Second, a windstorm in the early morning on 1 March 2008 also induced waves on the maar that were high enough to erode a substantial amount of material, leading to a visible turbidity of the near-shore waters persisting for about two hours. This event was among the strongest windstorms in the winter half-year 2007/08, and the only one that generated visible turbidity in the Schalkenmehrener Maar. At the DWD weather station Nürburg-Barweiler (see Table 3.1 and Fig. 3.1), gusts of more than 28 m/s were reported during the storm.

From the characteristics of the layer shown in Fig. 3.4, there is additional evidence that the respective material has been transported from the littoral zone to the position of the sediment core. The layers contain both large organic particles of littoral origin and carbonates, which have been formed by sublittoral macrophytes in the shallow, warm littoral water. The almost perfect Gaussian shape of the combined histogram of quartz and carbonates shown in Fig. 3.4d gives evidence that both particle classes have originated from the same transport process. In addition, the absence of large amounts of fine particles and of gradation within the layers indicates that these layers have not been formed by turbidites.

3.3 Meteorological windstorm identification

3.3.1 Construction of a windstorm index from meteorological data

In order to validate the relationship between windstorms and sedimentation of coarse quartz particles at the location of the freeze core, which has been outlined in the previous section, a meteorological storm index has been constructed combining monitored winds from surface weather stations of the DWD and ERA40 reanalysis data from the ECMWF (see also section 2.2). The ERA40 data set (*Uppala et al.*, 2005) contains parameterized gust peaks in ten meters height for 3-hourly time periods, calculated from twice daily short-term forecasts. To avoid model spin up effects, 3-15 hour forecasts have been used to compute daily gust peaks at the maar during the period 1958 to 2001. ERA40 data have a horizontal resolution of about 100 km and linear interpolation has been applied to obtain gust values at the location of the maar. ERA40 gust peaks are biased low compared to local measurements, however they provide valuable information about the relative severity of storms on a spatial scale of about 100 km (cf. chapter 2). In addition, daily gust peaks from nine DWD weather stations with automatic wind measurement within a radius of 50 km from the maar have been selected from the data set described in chapter 2. The geographical positions of these stations are shown in Fig. 3.1 and listed in Table 3.1. Since only between 1965 and 2001 measurements from at least two stations have been available, the investigation has been restricted to these years. For nearly all stations, there are known inhomogeneities within this period, related to instrument changes. They have been taken into account by splitting each time series into parts without any known inhomogeneity and analyzing every partition separately. As mentioned before, the large variability of the station data prompts the combined use of temporally homogeneous large-scale information from ERA40 analyses with local measurement data in a statistical sense. This fact is visualized in Fig. 3.9, where the 150 strongest daily gusts between 1965 and 2001 are shown exemplarily for the two stations with the longest records, Trier-Pertrisberg and Büchel. As can be seen from the Figure, the correlation between the two time series on long time scales is rather poor. In addition, the influence of the

inhomogeneities related to instrument changes, which are shown as dashed vertical lines, is also visible, in particular in Fig. 3.9b, but also for the first inhomogeneity in Fig. 3.9a. In spite of the large spatial variability of wind gusts, the sediment signals from SMf are thought to represent large scale storms, because it is not only the amplitude of wind gusts, but also their temporal duration that is recorded in the core, as outlined in section 3.2.3.

The construction of the storm index started with the identification of the 99 days with maximum ERA40 gust peaks at the maar (Fig. 3.10; ERA40 gust wind speed is given on the vertical axis). For each of these days, the number of DWD stations that indicate an extreme storm has been counted. For all stations and parts of the time series without known inhomogeneities, a threshold value that defines an extreme event has been determined. This has been done by calculating the 99.8%-quantile of the daily maximum wind speed for each year and averaging this quantile over the respective part of the time series. For the calculation of the quantiles, the same algorithm as in section 2.4 has been used. The averaging process eliminates the influence of the different lengths of the time series partitions and makes sure that the threshold value is not completely determined by single extreme events. Next the number of stations n_{ex} for which the threshold has been exceeded within a 5-day-window around the 99 strongest ERA40-storms has been counted. The relative frequency n_{ex}/N (where N denotes the total number of stations measuring at the given time) is shown with colors in Fig. 3.10. Together with the ERA40 wind speed, it provides a two-dimensional storm index that represents large scale and local wind velocity features. Figure 3.10 indicates that from a multitude of large-scale storms, those specifically relevant for the local surroundings of the maar can be identified by our method.

Name	Longitude [°]	Latitude [°]	Altitude [m]
Nürburg-Barweiler	6.87	50.36	485
Roth bei Prüm	6.39	50.31	593
Hahn	7.26	49.95	497
Kall-Sistig	6.53	50.50	505
Nürburg	6.95	50.34	627
Trier-Petrisberg	6.66	49.75	265
Deuselbach	7.06	49.76	480
Mendig	7.32	50.37	181
Büchel (Flugplatz)	7.07	50.17	477

Table 3.1. *Geographical locations and altitudes of DWD stations with wind measurements (see also Fig. 3.1).*

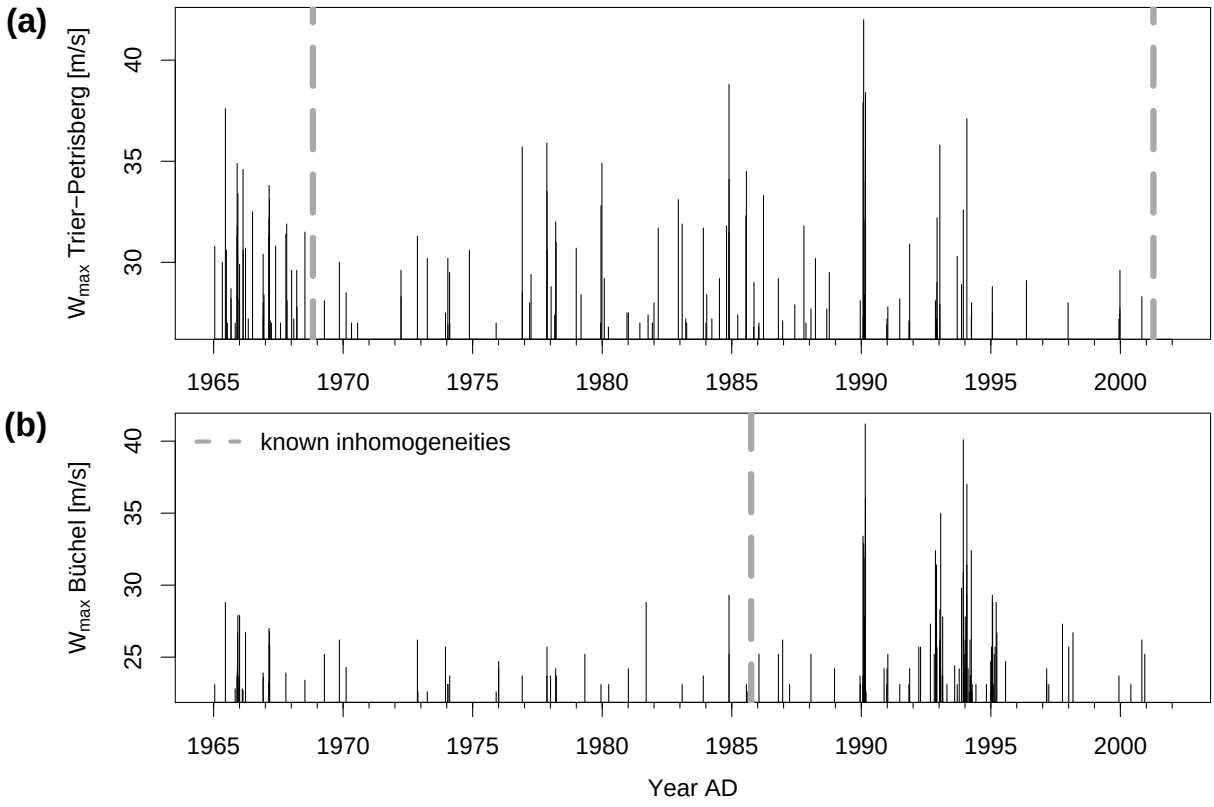

Figure 3.9. *Time series of daily gust peaks from stations Trier-Petrisberg (a) and Büchel (b) (for station coordinates see Table 3.1). For each station, the 150 highest daily gusts are shown. Dashed vertical lines indicate known inhomogeneities from instrument changes.*

3.3.2 Allocation of windstorms to peaks in the silt curves

In the following, the windstorm record shown in Fig. 3.10 is compared to the silt fraction curve of SMf. The abscissa of the silt curve has been transformed to a time axis using linear interpolation based on the age model shown in Fig. 3.7. Because of the uncertainties of this model, it cannot be expected that the resultant time axis matches real time exactly. The largest peaks in the silt curve have been allocated to the largest storm events. In order to give a quantitative estimate of the quality of such an allocation, a root mean square error (RMSE) has been calculated as follows:

$$\mathrm{RMSE} = \sqrt{1/M \sum_{i=1}^{M} \left(t_i^{\mathrm{storm}} - t_i^{\mathrm{silt}}\right)^2}, \tag{3.1}$$

where M labels the number of allocated peaks, t_i^{storm} the date of the i-th allocated windstorm and t_i^{silt} the age model date of the respective silt fraction peak.

Figure 3.11a shows all windstorms from Fig. 3.10 with a relative frequency of storm detection at

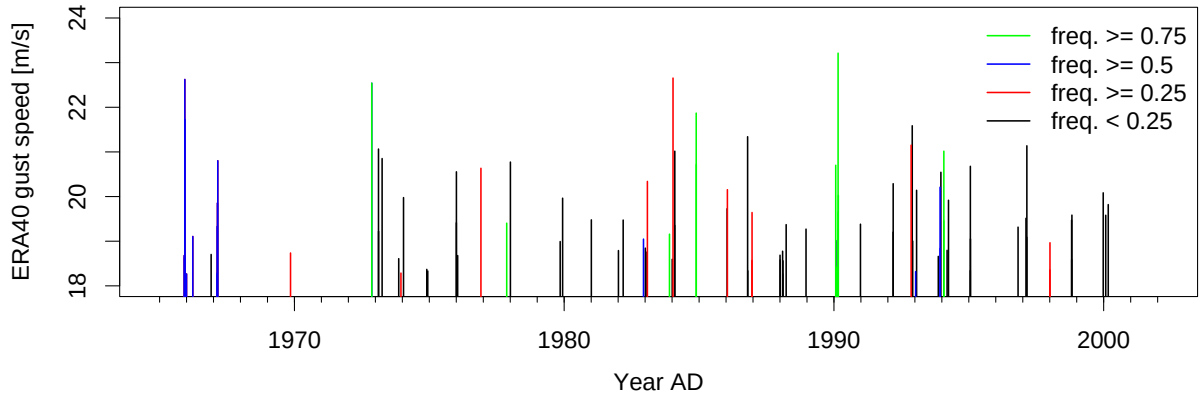

Figure 3.10. *Storm index, combining gust peak wind speed from ERA40 data (vertical axis) and relative frequency of storm detection n_{ex}/N at weather stations (color) for strongest windstorm events. Note that the absolute values of ERA40 gust velocities are biased low compared to direct measurements of wind gusts.*

the weather stations n_{ex}/N larger than 0.5. Only these particularly relevant storms are used for the allocation. The transformed silt fraction curve from the SMf core is shown in Fig. 3.11b. The positions of several years from the age model are exemplarily given on the horizontal axis and their uncertainties are shown as gray bars (a complete overview of the age model dates can be obtained from Fig. 3.7). The red numbers in Fig. 3.11 indicate an allocation of the six strongest windstorms (maxima in ERA40 gust speed) to the six largest separate peaks in the silt curve. This allocation has been performed in chronological order. The best concurrence of the peaks is obtained for storm number 5; for number 4, the dating mismatch is largest. The RMSE of this windstorm allocation is 1.7 years.

The consistency of the windstorm allocation with the uncertainty estimates of the age model can be checked by plotting the storm dates (which are known from the meteorological record) as a function of the core depth of the associated silt peaks. The red dotted line in Figure 3.7 shows that almost everywhere this alternative event-based age model lies within the uncertainty range of the CRS model; only in the middle of the 1980s, very small deviations occur (it just turns out that the 1986 ^{137}Cs peak falls in this period of worst concurrence; a possible explanation might be a wrong allocation of storm number 4). Altogether, the windstorm allocation can thus be considered as successful within the range of age model uncertainty, as corroborated in the next subsection, where a statistical technique is applied in order to quantify the significance of the allocation.

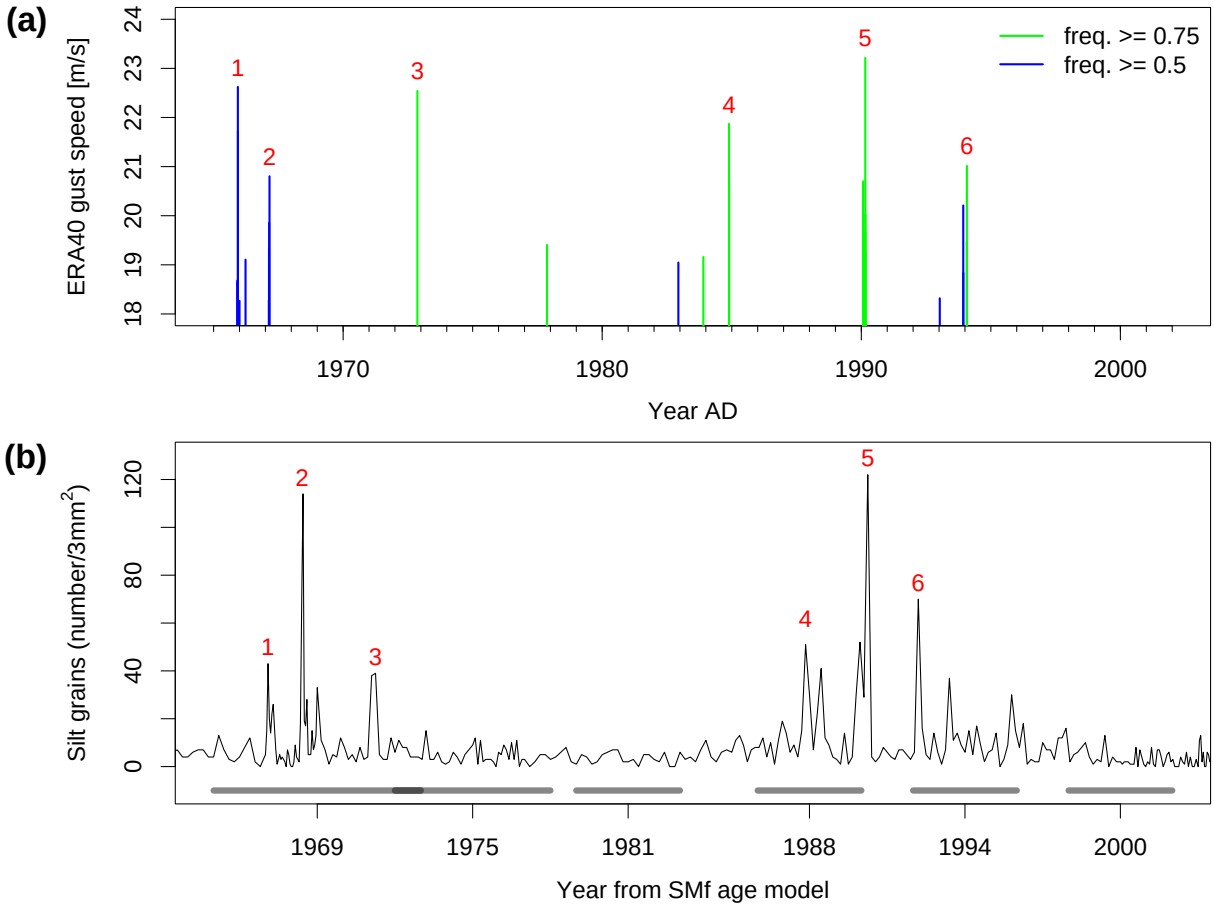

Figure 3.11. *(a): Storms from Fig. 3.10 with n_{ex}/N larger or equal 0.5. (b): Coarse silt fraction curve (number concentration of quartz grains between 20 and 63 µm) for the upper part of SMf. Red numbers indicate a mapping of the peaks on the storms shown in (a). The corrected CRS age model was used to linearly transform the horizontal axis from depth to time. The positions of several selected age model years are given at the horizontal axis; grey horizontal bars show the uncertainty of these ages, darker gray indicates an overlap of the uncertainty bars. See Figure 3.7 for a complete overview of the dates that were used for the axis transformation.*

3.3.3 Different peak allocations

While geological arguments rather support a wind-driven sedimentation mechanism for the SMf core, as described in section 3.2.3, the possibility of a relation between extreme rain events and the silt peaks in the core is evaluated in this section. Data from two DWD weather stations with daily precipitation measurements, Mehren (1.8 km distance from SM; see Fig. 3.1) and Oberstadtfeld (6.4 km distance) have been analyzed. Because of the proximity of these stations to the maar, their measurements are supposed to be representative for the precipitation at Schalkenmehren. Data from Mehren has only been available since 1971, thus this station

is used for the period 1971-2006, and Oberstadtfeld for earlier times. Figure 3.12a shows the most intense precipitation events (daily rainfall larger than 40 mm) for the period 1950-2006. In Fig. 3.12b, the transformed silt fraction curve from SMf is displayed again. The numbers indicate a possible mapping of the silt fraction peaks on the precipitation events. It is apparent that this mapping does not lead to an adequate result. During periods with strong precipitation events, e.g. the late seventies and early eighties, no signals are present in the core, and on the other hand around 1970 and 1990, no extreme rain events occurred. Accordingly, the RMSE for the allocation indicated by the red numbers is 7.4 years, i.e. much higher than the value of 1.7 years obtained for the windstorm allocation described in section 3.3.2. Omitting the two events with the largest mismatch (numbers 4 and 5) only leads to a moderate improvement (RMSE of 6.0 years). This result corroborates our hypothesis that silt sedimentation in the Schalkenmehrener Maar is much more likely determined by wind-induced processes than by erosion due to precipitation and runoff.

Although the allocation of the silt peaks to windstorms shown in Fig. 3.11 leads to much smaller errors than for precipitation (Fig. 3.12), the match between the curves is not perfect. As mentioned above, this is thought to be mainly due to uncertainties in the age model. Nevertheless, it is important to statistically estimate the reliability of the established relationship. In order to do this, we have performed a Monte Carlo experiment. The age model dates of the six largest peaks in the SMf silt fraction curve (labeled with red numbers in Fig. 3.11b) have been compared to six randomly chosen dates in the period 1965-2001. The earliest random date has been allocated to peak number 1, the second earliest to peak number 2 and so on. This experiment has been repeated 999 times, and for each iteration, the RMSE has been determined according to equation (3.1). With this approach, we are able to determine the likelihood that a similar match as found between silt peaks and windstorms (RMSE $= 1.7$ years) occurs purely by chance and thus estimate the significance of the windstorm allocation. The resultant distribution of RMSEs has a median of 6.9 years; first and third quartiles are 5.6 years and 9.0 years, respectively. Only 0.6% of the random samples lead to a RMSE smaller than 1.7 years, the value obtained from the windstorm allocation shown in Fig. 3.11a,b. On the contrary, 57% of the random samples have a smaller RMSE than the mapping of the silt peaks to precipitation events given in Fig. 3.12.

This statistical analysis indicates that it is very unlikely that the correspondence between windstorms and peaks in the SMf silt fraction curve detected in this study has appeared randomly. Using the RMSE as a quantitative measure of success, the windstorm allocation is statistically significant with respect to a 99% confidence level. In addition, the analysis shows that the allocation of silt peaks and precipitation events is statistically not significant and confirms that the peaks are not caused by pure precipitation events.

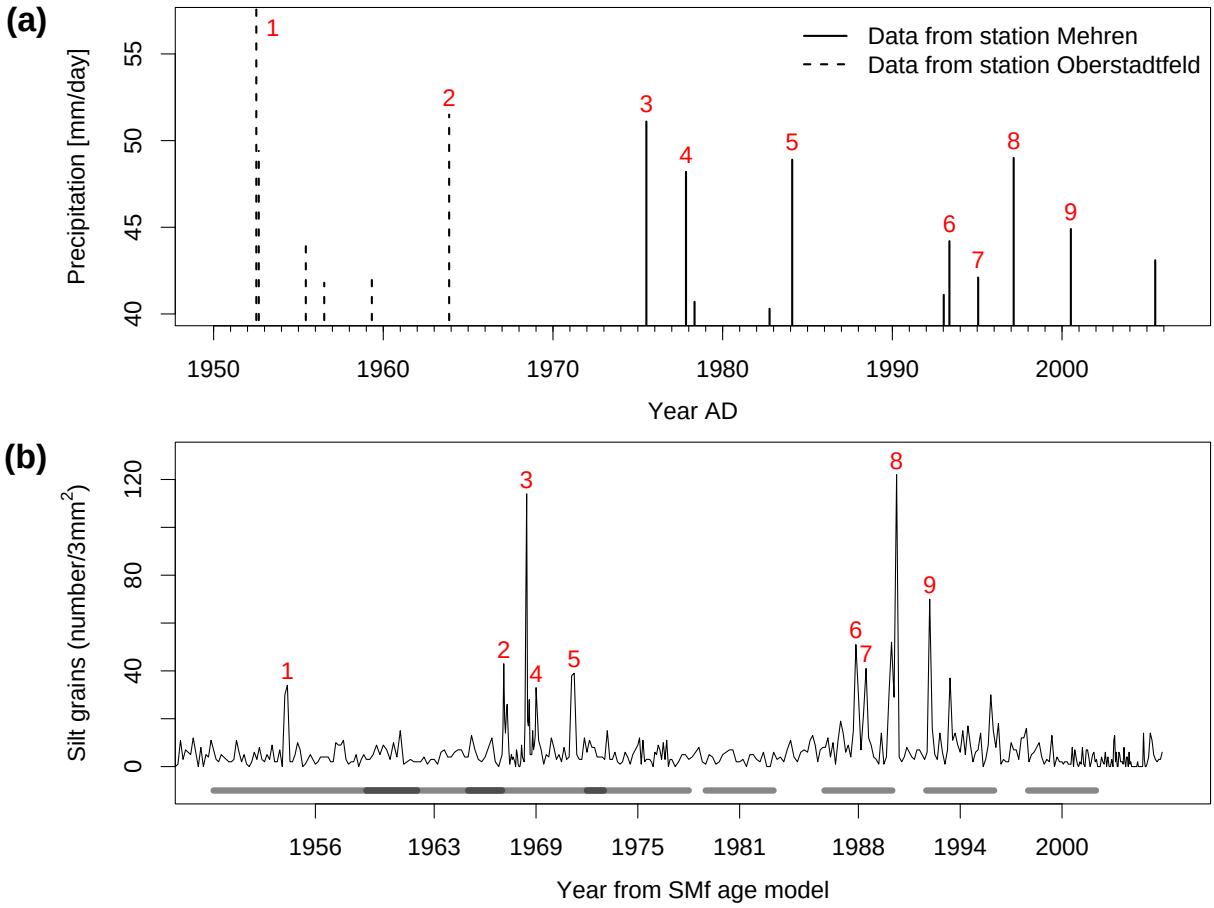

Figure 3.12. *(a) Extreme precipitation events (daily rainfall larger than 40 mm) from two DWD weather stations. Before 1971, data from Oberstadtfeld is shown, after 1971 data from Mehren. The rainfall amount of the event with label 1 is 70.6 mm (not shown). (b): Silt fraction curve for SMf, as in Fig. 3.11b. Numbers indicate a statistically non-significant mapping of the peaks on the precipitation events shown in (a).*

3.3.4 Grain transport within the lake

As outlined in section 3.2.3, several transport mechanisms for the silt grains from the shore to the center of the maar are conceivable. These mechanisms are strongly influenced by the lake's density stratification. Eifel maar lakes typically are dimictic, with mixing in spring and fall and strong summer stratification. All major storms shown in Fig. 3.11a occurred between the middle of November and the beginning of March, i.e. in a period of rather weak stratification. However, it is difficult to estimate the exact stratification of the lake at a given point of time from the available data. Because temperature is one of the main influence factors, temperature data from the DWD weather station Manderscheid (9 km distance from SMf) has been analyzed, showing that average temperatures in the two weeks before the storms varied between 1°C and

8°C. Particularly for the November storm (number 3 in Fig. 3.11a), relatively warm temperatures have been detected, pointing to a possibly stronger stratification. Altogether, we are unable to determine which transport mechanism within the lake has been the dominant one, though a transport via density currents seems more plausible because the storms occurred during winter or late fall.

3.4 Conclusions

In this chapter, an attempt has been made to identify recent windstorms in a lake sediment core based upon a calibration applying a combination of meteorological data sets. It has been shown that such an attempt is challenging since several requirements have to be fulfilled in order to enable the conservation and detection of windstorms layers:

- A suitable study site has to be chosen. It is most important that the lake does not have a riverine inlet, as fluvial inflow would dominate the sedimentation. In case of the Schalkenmehrener Maar that has been studied here, also several other morphological and bathymetric factors have facilitated the identification of windstorms: a) the deep water of the lake is seasonally anoxic, preventing bioturbation, b) the bottom of the lake is flat, preventing sediment focusing, c) the lake is exposed to the wind and with 550 m diameter large enough to allow wave generation, d) with a transport distance of maximal 300 m grains can be transported to the site of coring by wind generated current activity. In addition to these lake characteristics, meteorological wind measurements must be available in the vicinity of the lake over several decades.

- An age model of the sediment core has to be constructed, which allows a quantification of the dating uncertainties. Here, this age model has been based on measurements of ^{137}Cs and ^{210}Pb activities.

- A basic physical understanding of the sedimentation processes in the lake should be obtained. For windstorms, the processes connecting the meteorological event and the sediment signal are complex and less straightforward compared to, e.g., a strong precipitation event leading to a direct transport of sediment material into a lake.

- Information on extreme windstorm events at the location of the geological site during recent years has to be inferred from meteorological data. In this study, a novel windstorm index has been developed combining homogeneous large-scale wind data from reanalyses with non-homogeneous time series from in-situ observations.

- The likelihood of the identification of windstorm layers in the sediment has to be assessed using statistical means. Here, this has been done with the help of a Monte Carlo method

and based on the calculation of root mean square errors.

Comparing the meteorological windstorm record to peaks in the silt fraction curve from the SMf core, six major storm events of the period 1965-2001 have been allocated to specific layers in the sediment. These layers are characterized by a sharp Gaussian grain size distribution with enhanced mean grain sizes compared to the background sediment. Among the allocated windstorms, the "Niedersachsen Orkan" in 1972 and the consecutive gales "Daria", "Vivian" and "Wiebke" in 1990 caused the probably biggest damages in Germany during the whole analysis period (*Klawa and Ulbrich*, 2003). This indicates that the most extreme storm events that affect Central Europe on a larger spatial scale can be recovered in the SMf sediment.

However, there are of course some uncertainties in the mapping of windstorms on sediment signals presented above. First, these uncertainties are due to the relatively inaccurate age model of the sediment, which is also reflected in an imperfect visual match between the peaks in the meteorological and geological time series (see again Fig. 3.11). Nevertheless, the allocation of storm layers is statistically highly significant, as shown with the help of a Monte Carlo method. Another severe problem, which often occurs in calibration studies for recent times (e.g. *Pye and Neal*, 1994), is the mostly unknown human interference in the sedimentation process. Effects of this interference can never be totally eliminated. We think that in the case of the Schalkenmehrener Maar they are reduced to a minimum, because the lake is effectively shielded from external sediment input.

It would be highly desirable to extend the present approach to other sediment cores covering the last decades and to apply the methods introduced in this study (novel windstorm index; statistical test of peak allocations) in order to further test the feasibility of windstorm identification. It may then be possible to use the detailed characterization of the storm layers given in section 3.2.1 for identifying similar layers in sediment cores from other lakes and extended time periods, presumed that these lakes fulfill the morphological requirements stated above. If the layers are preserved throughout the Holocene, they may be used as a new proxy for the reconstruction of the paleo-windstorm record.

Chapter 4

Air Parcel Trajectory Analysis of Stable Isotopes in Water Vapor in the Eastern Mediterranean[1]

4.1 Introduction

4.1.1 Non-equilibrium fractionation and deuterium excess

As outlined in section 1.3, fractionation effects are essential for various applications of stable water isotopes in climatology, meteorology and hydrology. Whereas equilibrium fractionation is well understood theoretically (*Bigeleisen*, 1961) and in laboratory experiments (*Majoube*, 1971; *Horita and Wesolowski*, 1994), the situation for non-equilibrium effects is less clear. In particular, there are several models describing evaporation of water from the sea (*Craig and Gordon*, 1965; *Merlivat and Jouzel*, 1979), based upon the theory of one-dimensional advective-diffusive systems (*He and Smith*, 1999), but there is only very little isotope data available which can be used to validate these models. Hence, it is not clear if some of the assumptions are oversimplified and if all critical physical processes are properly represented. For instance, newer lab measurements by *Cappa et al.* (2003) showed that surface cooling due to evaporation, which is not included in the standard models, might play an important role. Under realistic atmospheric conditions, additional factors like sea spray evaporation in the case of strong winds come into play (*Gat et al.*, 2003), and feedbacks between the isotopic composition of the evaporation flux and the ambient air have to be taken into account (*Gat and Bowser*, 1991). Difficulties in quantifying these various processes arise not only from the paucity of isotope measurements on short time scales ($<$ 1 day), which are required for establishing direct linkages to the involved mech-

[1] A modified and edited version of this chapter has been published as *Pfahl and Wernli* (2008). Copyright 2008 American Geophysical Union.

anisms, but also from the complexity of the interpretation of these measurements.

For evaporation under equilibrium conditions from ocean water with isotopic composition equal to that of VSMOW, the ratio $\delta^2\mathrm{H}/\delta^{18}\mathrm{O}$ is approximately 8, thus the d-excess (see again section 1.3) is a measure for non-equilibrium fractionation. In addition, the equilibrium ratio for the liquid-vapor transition slightly depends on temperature, hence equilibrium fractionation can also lead to small changes in d[2]. The global average value of d in meteoric waters is 10‰ (*Craig*, 1961), indicating that atmosphere and ocean typically are out of thermodynamic equilibrium.

The dominating effect that determines the d-excess on a global scale is non-equilibrium fractionation during water evaporation from the ocean (*Craig and Gordon*, 1965; *Merlivat and Jouzel*, 1979). Other non-equilibrium effects, as re-evaporation of rain drops under the cloud base in unsaturated air (*Steward*, 1975; *Gedzelman and Arnold*, 1994) and the formation of ice clouds, when supersaturation is possible (*Jouzel and Merlivat*, 1984) are thought to be important on local to regional scales (*Jouzel et al.*, 2007). From theoretical evaporation models, it can be deduced that d is primarily determined by relative humidity, measured with respect to saturation at the sea surface temperature ($\mathrm{RH_{SST}}$), temperature, isotopic composition of the ocean and, to a lesser degree, the wind regime at the evaporation site (*Merlivat and Jouzel*, 1979; *Johnsen et al.*, 1989) (the global closure assumption made in these studies is not crucial for this general conclusion, but can affect the quantitative relationships (cf. *Jouzel and Koster*, 1996; *Armengaud et al.*, 1998)). Simulations with isotope GCMs, in which parameterization of the evaporation flux is based on the theoretical model described by *Merlivat and Jouzel* (1979) without global closure, show the same governing factors for d of water vapor over the sea (*Jouzel and Koster*, 1996). Furthermore, simple Rayleigh-type isotope models indicate that the information about the evaporation conditions is at least partially conserved along the subsequent trajectory of the vapor until rainout (*Johnsen et al.*, 1989; *Petit et al.*, 1991; *Ciais et al.*, 1995), as supported again by results from GCM simulations (*Armengaud et al.*, 1998). Based on these findings, d-excess records from ice cores have widely been used to reconstruct source region conditions of precipitation in past climates, thus providing information that cannot be derived from $\delta^2\mathrm{H}$ or $\delta^{18}\mathrm{O}$ alone (e.g. *Vimeux et al.*, 1999, 2001, 2002; *Uemura et al.*, 2004; *Masson-Delmotte et al.*, 2005; *Jouzel et al.*, 2007). However, these studies restrict their analysis on the reconstruction of source temperature, not taking into account the dependence on relative humidity. The authors justify this focus on temperature with the decreasing influence of source RH moving inland in Antarctica as seen in simple Rayleigh-type models, the weak glacial-interglacial changes of RH in GCM simulations and, as the main argument, the linear relationship between sea surface temperature (SST) and RH in the overlying air observed in GCMs (*Vimeux et al.*, 1999, 2001, 2002; *Armengaud et al.*, 1998). This relationship is used to include the dependence of d from RH in

[2] However, at the transition from vapor to ice, even large changes in d can occur, also under equilibrium conditions.

the coefficient of the temperature relation.

4.1.2 Interpretation of atmospheric stable isotope data

There is a large number of observations of stable isotopes in precipitation with a monthly time resolution all over the globe. The largest data collection, the Global Network for Isotopes in Precipitation, is operated by the International Atomic Energy Agency and the World Meteorological Organization (see e.g. *Araguás-Araguás et al.*, 2000). The climatological isotope patterns obtained from these measurements are usually interpreted in terms of different isotope effects (*Dansgaard*, 1964), e.g. the latitude and altitude effects. These are not related to single physical processes, but reflect a complex sequence of fractionation during the phase transitions of water from evaporation to precipitation. For instance, isotope distillation via rainout, the temperature dependence of equilibrium fractionation factors and the increasing fraction of solid precipitation with latitude contribute to the poleward decrease of the concentration of heavy isotopes. Since this effect is particularly important for the calibration of the isotope-temperature relationship used for temperature reconstruction from ice cores (see section 1.3), a better physical understanding of the individual processes is required to overcome uncertainties resulting from variations of the relation in space and time (*Jouzel et al.*, 1997, 2000; *Noone and Simmonds*, 2002; *Helsen et al.*, 2007; *Sodemann et al.*, 2008a).

In order to improve our understanding of fractionation processes under atmospheric conditions, measurements on short time scales in the order of days to hours are needed, as mentioned above. Only few of these measurements are available, though the number has increased during the last years (*Gat et al.*, 2003; *Lawrence et al.*, 2004; *Anker et al.*, 2007; *Strong et al.*, 2007; *Tian et al.*, 2007; *Barras and Simmonds*, 2008). Their physical interpretation is complicated, because a single isotope value reflects the integrated phase transition history of the respective water. Several studies tried to deduce transport histories from meteorological considerations (*Tian et al.*, 2007) or with the help of trajectory calculations (*Rindsberger et al.*, 1983; *Gat et al.*, 2003; *Lawrence et al.*, 2004; *Anker et al.*, 2007; *Strong et al.*, 2007; *Barras and Simmonds*, 2008). However, in all these studies relationships between isotope data and water history could only be given in qualitative terms.

GCMs fitted with water isotope processes have been used to model stable isotope patterns on the global scale (e.g. *Joussaume et al.*, 1984; *Hoffmann et al.*, 1998; *Noone and Simmonds*, 2002). These models are able to reproduce climatological patterns of δ^2H and δ^{18}O in precipitation, however their representation of d-excess is not yet satisfying (*Werner et al.*, 2001; *Jouzel et al.*, 2007). Also, there are first hints that they do not capture the annual cycle of isotopes in water vapor on local scales (*Angert et al.*, 2008). In spite of their high suitability to explore stable isotopes on climatological time scales, it is more difficult to use them for simulating single

meteorological events (e.g. to compare with measurements from a specific storm), not least because of their coarse spatial resolution (see also chapter 6).

Recently, several studies have been conducted that modeled stable isotope ratios in high latitude precipitation using a combined approach (*Helsen et al.*, 2004, 2006, 2007; *Sodemann et al.*, 2008a). As a first step, backward trajectories were calculated from the precipitating airmass with the help of (re-)analysis data, representing realistic water transport paths. Parameters like temperature, pressure and specific humidity were extracted from the analysis data along the trajectories and used as input for a Rayleigh-type isotope model, which calculated fractionation along the (in *Sodemann et al.* (2008a) idealized) transport paths. In these studies, no event-based comparison with measured isotope ratios has been performed (except for *Helsen et al.* (2004)), due to the focus on climatological interpretations. *Helsen et al.* (2004, 2006, 2007) initialized the Rayleigh-type model with three-dimensional, monthly averaged isotope fields from a GCM without explicitely considering moisture source regions. *Sodemann et al.* (2008a) extracted evaporation regions from the backward trajectories quantitatively. In order to initialize the isotope model, which had the diagnosed moisture source regions as the starting points, GCM isotope fields at the lowest model level have been applied.

In this chapter, a backward trajectory diagnostic based on the algorithm of *Sodemann et al.* (2008b) is used to detect moisture sources for a set of isotope measurements in water vapor in Rehovot (Israel). Unlike *Sodemann et al.* (2008a), we do not use these diagnosed regions to initialize an isotope model, but try to establish a direct, quantitative link between the measured isotope ratios and meteorological quantities in the source regions. A special focus is laid on the *d*-excess as a measure for non-equilibrium fractionation.

4.2 Data and method

4.2.1 Measurements of isotopes in water vapor

Non-equilibrium fractionation in water evaporation regions can be best explored with the help of isotope measurements in water vapor, because the additional isotopic signal due to condensation can be excluded more easily compared to measurements in precipitation. Another advantage of measuring isotopes in vapor is that it is possible throughout the year, independent of the synoptic situation and not limited to rain days. On the other hand, there are also potential problems related to the measurement of isotopes in water vapor, because technically, the sampling procedure is more difficult than for liquid water. For future applications, new approaches to determine isotope ratios in vapor from remote sensing might be used in addition to surface in situ measurements (see e.g. *Worden et al.*, 2006; *Payne et al.*, 2007; *Worden et al.*, 2007).

From 1998 till 2006, measurements of stable isotopes in water vapor were performed at the Weizmann Institute of Science in Rehovot, Israel (31.9°N, 34.8°E, 76 m above sea level). The sampling site was on a rooftop, about 6 meters above the ground. Samples were taken roughly twice a week, with some bigger gaps in between. Altogether, 433 measurements were conducted up to July 2006. In this study we only use measurements since October 2000 (265 measurements), because not all ECMWF data necessary for the analysis are available previous to this date (see section 4.2.2). The water vapor collection time usually was around 8 hours, but there are some exceptional cases with times between 3 and 24 hours. After collection, the water was analyzed with the help of a Finnigan MAT 250 mass spectrometer. The precision of the analysis was 0.1‰ for ^{18}O and 1‰ for ^{2}H. Technical details about the analysis procedure are described by *Angert et al.* (2008).

Stable isotopes in precipitation have been studied to a large extent in the entire eastern Mediterranean region (cf. *International Atomic Energy Agency*, 2005; *Lykoudis and Argiriou*, 2007) and particularly in Israel (e.g. *Rindsberger et al.*, 1990; *Gat et al.*, 1994). Compared to other coastal regions, the isotopic composition of rainwater in the Mediterranean, due to the geographical location, is particularly strongly influenced by the interaction of continental air with the sea surface, leading to rather high values of and large variations in *d*-excess (*Gat and Carmi*, 1970). Hence, the measurement site is not representative for coastal conditions worldwide, but provides the possibility to explore the diversity of meteorological conditions that lead to a large spectrum of *d*-excess values.

4.2.2 Moisture source diagnostic

For each day with isotope measurements in water vapor at Rehovot, moisture source regions have been identified. In order to do this, we have used a Lagrangian diagnostic, introduced by *Sodemann et al.* (2008b), with some minor modifications. The diagnostic is based on the calculation of air parcel trajectories using analysis data. Trajectories have been started at Rehovot and calculated 10 days backward in time. Several meteorological variables have been traced. In order to concentrate on evaporation processes and transport in cloud-free conditions, trajectories have been clipped to exclude clouds or rain from above. The change in specific humidity along the trajectories has been used to detect moisture uptake. In particular, uptake in the oceanic boundary layer can be directly related to evaporation from the sea. Only those measurement days have been taken into account for which sources can be attributed to a substantial fraction of the measured vapor with our method. Finally, a weight has been assigned to each uptake according to its contribution to the final humidity, and different meteorological quantities have been averaged over the uptake regions of a specific date, weighted with the respective contributions. From this, it has been possible to explore statistical relationships between measured

isotope ratios and average moisture source conditions. The following paragraphs describe each technical step of the analysis procedure in full detail.

Analysis data and principles of trajectory calculation

Three-dimensional, kinematic backward trajectories (*Wernli and Davies*, 1997) have been calculated, using wind fields and other meteorological variables from operational analysis data of the European Centre for Medium-Range Weather Forecasts (ECMWF). These data are available every six hours, with a spectral resolution of T511 and 60 vertical levels until February 2006. Thereafter, the model resolution corresponds to T799 and 91 vertical levels. The data has been interpolated on a horizontal grid with a spacing of 0.75°. Along the trajectories, several variables have been recorded, including specific humidity, temperature, cloud liquid water and ice content, sea surface temperature (SST) at the respective horizontal position and boundary layer height (which is calculated by the boundary layer parameterization scheme of the ECMWF model according to *Troen and Mahrt* (1986)). In time, linear interpolation between the analysis steps has been applied. The spatial interpolation used to obtain all the variables at a specific trajectory position has been linear in the vertical and bilinear in the horizontal. SST is not defined over the continents, hence there are points close to the shore where a bilinear interpolation is not possible. Thus, the following scheme has been applied at these locations: In the presence of one continental point at one of the four adjacent grid points, the value has been estimated with linear interpolation using the three oceanic points. If there were two continental points, linear interpolation has been applied ignoring the variation of the SST field perpendicular to the direction given by the two remaining oceanic points. Finally, if three of the adjacent grid points have been located over land, the SST at the trajectory location has been set to the value of the fourth oceanic point. This special interpolation scheme is necessary, because otherwise SST cannot be determined for a lot of humidity uptake points close to the continental shore. Furthermore, precipitation has been estimated along the trajectories by averaging the 6-hourly accumulated prognostic ECMWF field (sum of large-scale and convective precipitation) over the respective trajectory section. To this end, forecast steps between 6 and 18 hours have been used from forecasts started at 00 and 12 UTC. Because of the relatively low temporal resolution, this averaging provides only approximate values. Also, precipitation estimates from model forecasts have to be handled with care as they are affected by spin-up and forecast errors. Finally, because the vertical position of the trajectories is calculated in pressure coordinates, the pressure at the top of the boundary layer (BLP) has to be calculated. Therefore, the ECMWF boundary layer height (in meter) has been multiplied with a factor of 1.5 and then converted to pressure by linear interpolation in logarithmic pressure. The factor 1.5 has been introduced because of the uncertainties of the boundary layer parameterization and in order to address the fact that a lot of moisture uptake occurs close to the boundary layer top (see *Sodemann et al.*, 2008b).

Specific trajectory setup

Backward trajectories have been started every hour during a measurement period. As horizontal positions of the starting points, the coordinates of Rehovot and four additional points, displaced by 0.25° in longitude or latitude, have been chosen. In the vertical, starting coordinates have been taken as the pressure values of the uneven model levels $1, 3, \ldots, 15$, if they were located within the diagnosed boundary layer at the respective horizontal position and point of time (linear interpolation in time has been applied). The trajectories have been calculated ten days backwards, about the maximum time scale on which integrity of the traced air parcel can be assumed. Calculations have been performed for every measurement date between October 2000 and July 2006, excluding days when rain was detected at the measurement site. These days have been excluded because re-evaporation of rain drops might bring moisture into the boundary layer at Rehovot that cannot be diagnosed by our method. (Since 2004, no appropriate precipitation data have been available at Rehovot during the measurement periods. Hence, an explicit exclusion of rain days has only been performed up to December 2003. For later times, rain days have been excluded implicitly, see below.) Altogether, about 50,000 trajectories have been calculated for 238 measurement days with a total measurement duration of circa 1900 hours. As an example, all trajectories for a specific date, the 17 May 2001, are shown in Fig. 4.1a. The air that reached Rehovot at this date originated from Northern Europe. In a northerly flow, very dry air was transported towards the Eastern Mediterranean. After a relatively fast descent to levels primarily below 900 hPa, humidity was taken up over the eastern Mediterranean Sea during the last two days of transport.

Precipitation and cloud formation during transport alter the isotopic composition of the moisture along the trajectories. Because in this study the focus is on relationships between measured isotope values and the moisture source conditions, trajectory segments where these additional processes occur should be excluded. This has been done by detecting, for each trajectory, the first point (starting from Rehovot and going backwards in time) where either interpolated precipitation exceeds 1 mm (per 6 hour time step) or the sum of cloud liquid water and ice is larger than 0.1 g/kg. Only the trajectory section in between this point and Rehovot has been kept for further analysis (see Fig. 4.1b for an example). In section 4.3.3, the influence of this criterion on the results will be explored.

Moisture uptake

The key parameter used to diagnose moisture sources along a trajectory is the change of specific humidity q within one trajectory time step:

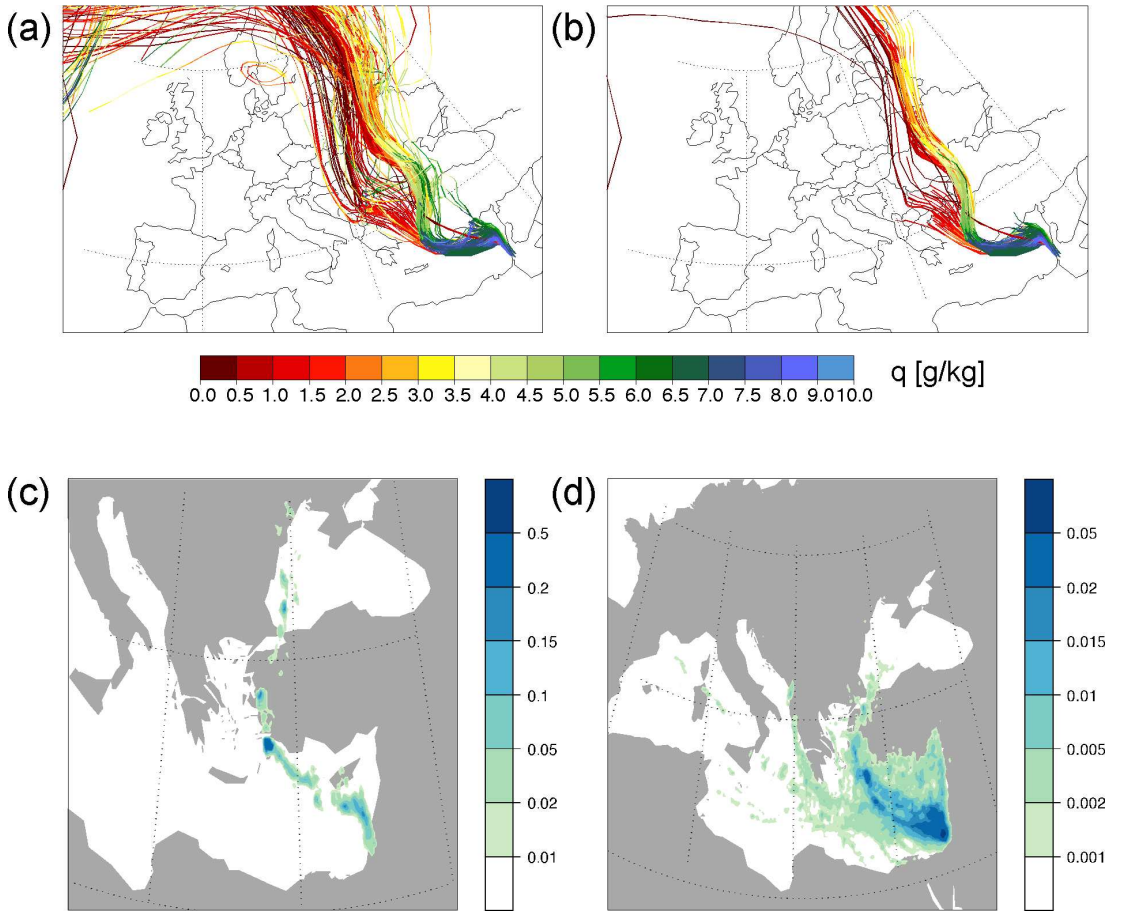

Figure 4.1. *(a) 10 day backward trajectories calculated for the isotope measurements at Rehovot on 17 May 2001. Colors indicate specific humidity along the trajectories. (b) Parts of the trajectories for which no clouds and no rain from above were detected. Only these parts are considered for the further analysis. (c) Moisture source regions for the 17 May 2001, deduced from the trajectories shown in (b). Note the non-linear scale. Units are percent of the final humidity at Rehovot, accumulated over all backward trajectories, per square kilometer. Altogether, 62 % of the final humidity can be attributed to these moisture sources. (d) Moisture source regions for all measurement days with* $\mathrm{Ra} > 0.6$*. Units as in c. Altogether, 68 % off the accumulated humidity at Rehovot can be attributed to these sources.*

$$\Delta q(t) = q(\vec{x}(t)) - q(\vec{x}(t - 6\mathrm{h}))\,, \tag{4.1}$$

where $\vec{x}(t)$ denotes the position of the air parcel at time t (*Sodemann et al.*, 2008b). When this parameter is positive, humidity is taken up by the air parcel. Different types of uptakes can be distinguished; especially important for this study is humidity uptake within the oceanic boundary layer (OBL). This is associated with mixing of the advected air with moisture that has locally evaporated from the sea at the respective position. Turbulent fluxes, not explicitely resolved by

the coarse model, are responsible for this mixing. In order to detect such OBL uptake, average values of BLP and air parcel pressure for the respective uptake have been calculated, i.e. averages of the quantities at t and $t-6$h. If this averaged air parcel pressure is larger than the respective BLP, the uptake is supposed to be located in the boundary layer. The second criterion for OBL uptake is that at least one of the trajectory positions at t and $t-6$h is located over the sea. If both conditions have been fulfilled, the average trajectory position during the six hour interval has been considered as a moisture source location. All other uptakes that occur over the continents or above the boundary layer cannot be attributed to a specific oceanic source. The former is related to water recycling, i.e. evaporation from soils and transpiration from plants, the latter can occur e.g. due to processes like convection, small scale turbulence and re-evaporation of precipitation, which are not resolved by the model, as well as due to numerical errors and inconsistencies in the analysis data set.

After detecting all moisture sources along a trajectory, the relative contribution of each source to the final humidity of the air parcel has been determined. A weight has been assigned to each uptake according to this relative contribution. However, the weight of a specific moisture source has been reduced if humidity has been lost later along the trajectory (for details, see again *Sodemann et al.*, 2008b). A measure for the total amount of water vapor gathered at Rehovot during a measurement period (q^{final}) has been estimated by averaging first for each hour the specific humidities at all trajectory starting points and then the hourly values over the entire measurement period (this two-step-process is necessary because the boundary layer height and thereby the number of starting points vary in time). The total weighted humidity for a specific date for which uptakes can be identified in the oceanic boundary layer, q^{obl}, has been obtained following the same averaging process. The ratio of these quantities, denoted Ra, corresponds to the fraction of measured water vapor for which sources can be attributed with our method. Figure 4.1c shows the weighted source regions for the example trajectories shown in Fig. 4.1b. Colors indicate the percentage of final humidity per square kilometer which is taken up at the respective position. For this example, two major uptake spots can be identified, one close to the Turkish coast, the other just before the arrival in Israel.

4.2.3 Statistical analysis

In the following, only those measurement dates are kept for further analysis for which sources have been attributed for at least sixty percent of the water vapor collected at Rehovot, i.e.

$$\text{Ra} \equiv \frac{q^{\text{obl}}}{q^{\text{final}}} > 0.6\,. \tag{4.2}$$

This criterion is fulfilled for only 45 of the 238 days. The main reason for this low percentage exceeding the Ra threshold is the strict exclusion of cloudy trajectory sections. The exclusion of the majority of measurements seems necessary, because reliable statements about the relationship between isotope ratios and moisture source conditions are solely possible if sources can be detected for the greater part of the measured water vapor. In section 4.3.3 the sensitivity of the results with respect to this exclusion criterion will be investigated. The moisture source regions for all measurement days with Ra > 0.6 are shown in Fig. 4.1d. Humidity uptake takes place almost exclusively over the eastern Mediterranean Sea, corresponding to a transport duration of two days or less from the evaporation to the measurement site. A clear domination of a north-westerly vapor transport path, associated with uptake close to the Turkish coast, is also visible from the Figure. It should be kept in mind that these uptake regions do not necessarily represent the climatological average of water vapor sources for Israel, but are surely biased by our approach (e.g. the trajectory clipping to avoid clouds and the selection of trajectory starting times solely during measurement periods).

For the remaining 45 dates, in addition to the variables mentioned above, the following quantities have been determined at the moisture source regions:

- relative humidity with respect to the temperature at the air parcel position, $\mathrm{RH}(\vec{x}) = q(\vec{x})/q_{\mathrm{sat}}(T(\vec{x}))$, and with respect to saturation at the sea surface, $\mathrm{RH}_{\mathrm{SST}}(\vec{x}) = q(\vec{x})/q_{\mathrm{sat}}(\mathrm{SST}(x,y))$ (where T denotes temperature and $\vec{x} = (x,y,z)$ position in space),
- wind velocity at the air parcel position,
- evaporation flux (as parameterized by the ECMWF model)
- 2-meter temperature and dew point as obtained from the ECMWF boundary layer parameterization, and derived relative humidity RH2M and relative humidity with respect to sea surface $\mathrm{RH2M}_{\mathrm{SST}}$ (defined analogously to $\mathrm{RH}_{\mathrm{SST}}$), and
- wind velocity at 10 meter height (from the ECMWF boundary layer parameterization).

All these variables have been interpolated linearly to the uptake position, i.e. they have been averaged between two trajectory time steps. If only one of the trajectory positions at t and $t-6$h is located over the sea, the variables have been analyzed at this position (for air parcels that move from land to sea or vice versa within one time step, the uptake over the ocean is assumed to be dominating). Finally, all available variables have been averaged over the humidity sources, weighted with the contribution of the specific uptake to the final humidity at Rehovot (see section 4.2.2). Mean values for each measurement day have been obtained by averaging over the trajectories as described for water vapor in the previous section.

Correlation analysis and linear regression have been used to explore the statistical relationships between measured isotope values and diagnosed water vapor source conditions. Assuming Gaussian distributions for all variables, we have used the Pearson correlation coefficient (denoted with r) and a least square method to calculate regression lines. Additionally, Spearman rank correlation coefficients, independent of the underlying distribution, have been calculated to ensure universality of the results (in a statistical sense) (see e.g. *Wackerly et al.*, 2002). In the following, only Pearson coefficients are specified, because the differences between the two methods appeared to be small. As a second step, multiple linear regression (with two independent variables) has been applied to investigate connections between different combinations of source condition parameters and the isotope measurements.

4.3 Results and interpretation

In the following section, the results of our correlation analysis are described. In the first subsection, correlations of d-excess measured at Rehovot with various meteorological parameters determined at the moisture source regions are shown. Additionally, the influence of surface wind velocity is examined, and a definition of an adjusted deuterium excess is presented, which describes non-equilibrium during water evaporation more precisely. In the second subsection, results of the correlation analysis of δ^2H and δ^{18}O are shown. Finally, in the third subsection we explore the sensitivity of the results to parameter settings in the analysis.

4.3.1 Correlation analysis of d-excess with meteorological parameters

Correlation with $\mathrm{RH2M_{SST}}$

Figure 4.2a shows the measured d-excess, plotted against averaged relative humidity at 2 meters height above ground, calculated with respect to saturation at the respective sea surface temperature ($\mathrm{RH2M_{SST}}$). The two parameters show a strong negative correlation ($r = -0.82$, as indicated in the plot). A linear regression leads to the following equation: $d = 48.3‰ - 0.53‰/\% \cdot \mathrm{RH2M_{SST}}$. The standard errors for intercept and slope are $3‰$ and $0.06‰/\%$, respectively. This substantial correlation indicates that information from the source region, particularly about relative humidity, is preserved along the water vapor trajectories and can be measured in terms of d.

A similarly negative, but slightly less significant correlation ($r = -0.74$, not shown) has been found between d-excess and relative humidity with respect to sea surface temperature at the trajectory level ($\mathrm{RH_{SST}}$). The height of the trajectories at humidity uptake, averaged for all uptakes during a measurement day, varied between circa 250 and 1000 m above ground. Hence

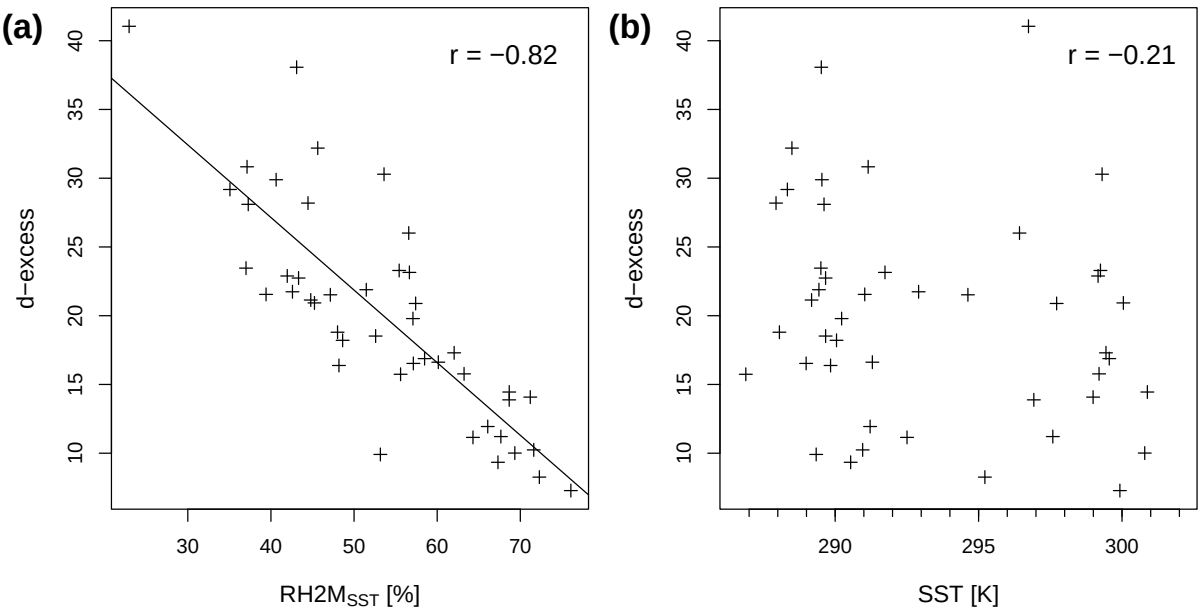

Figure 4.2. *Measured deuterium excess at Rehovot, plotted against (a) relative humidity at a height of 2 m with respect to saturation at the sea surface (*$\mathrm{RH2M_{SST}}$*) and (b) sea surface temperature (SST), averaged over the identified water vapor source regions. Pearson correlation coefficients and a linear regression line (in a) are also given in the plots.*

it is reasonable that the correlation with $\mathrm{RH_{SST}}$ is lower than with $\mathrm{RH2M_{SST}}$, because the conditions close to the surface are most important for the isotopic composition of the evaporation flux. Nevertheless, the relation with $\mathrm{RH_{SST}}$ is still highly significant, showing that the humidity deficit, which determines d, is a property of the whole air column in the boundary layer and not just the surface layer. According to this result, it is evident that the value of d in the evaporation flux is not only determined by surface quantities, but might also crucially depend on properties of advected air within the boundary layer (as incorporated in simple theoretical models in terms of a constant upper boundary condition, (cf. *He and Smith*, 1999)). It is important to note that the calculation of relative humidity with respect to saturation at the sea surface is essential for our results. Calculation of RH relative to the local temperature at the trajectory level does not lead to a significant correlation ($r = 0.05$), showing that the gradient of relative humidity within the air column at the evaporation site is indeed the critical quantity.

Correlation with SST

In Fig. 4.2b, measured d-excess is plotted against averaged sea surface temperature (SST) at humidity uptake. The plot shows that the correlation between these variables is rather weak ($r = -0.21$). With a multiple statistical model with SST and $\mathrm{RH2M_{SST}}$ as independent variables,

70% of the variance in d can be explained, that is only 2% more than with the model based on $\mathrm{RH2M_{SST}}$ only. Thus, SST at the humidity source is not the appropriate quantity to explain the variability in measured d-excess in this data set. Implications of these results, i.e. the low correlation of d with SST and the strong negative correlation with $\mathrm{RH2M_{SST}}$, are discussed in section 4.4.

Correlation with other quantities

Correlations with d have also been calculated for all other parameters listed in the previous section and for some derived quantities (see Table 4.1). The derived quantities include the time that an air parcel was situated within the boundary layer after humidity uptake. The latter potentially has an influence on the isotopic composition of the air parcel by mixing with surrounding water vapor without net moisture uptake. However, this potential influence does not lead to a substantial correlation coefficient. A larger negative correlation is obtained for the average evaporation flux at the uptakes ($r = -0.69$). This is in agreement with our previous findings, because the flux, as parameterized in the ECMWF model, directly depends on the vertical humidity gradient above sea surface.

Another quantity that shows a strong negative correlation with d-excess is the difference between temperature at a height of 2 meters (T2M) and SST (i.e. the temperature gradient in the surface layer) at humidity uptake, as shown in Fig. 4.3a ($r = -0.82$). The main reason for this

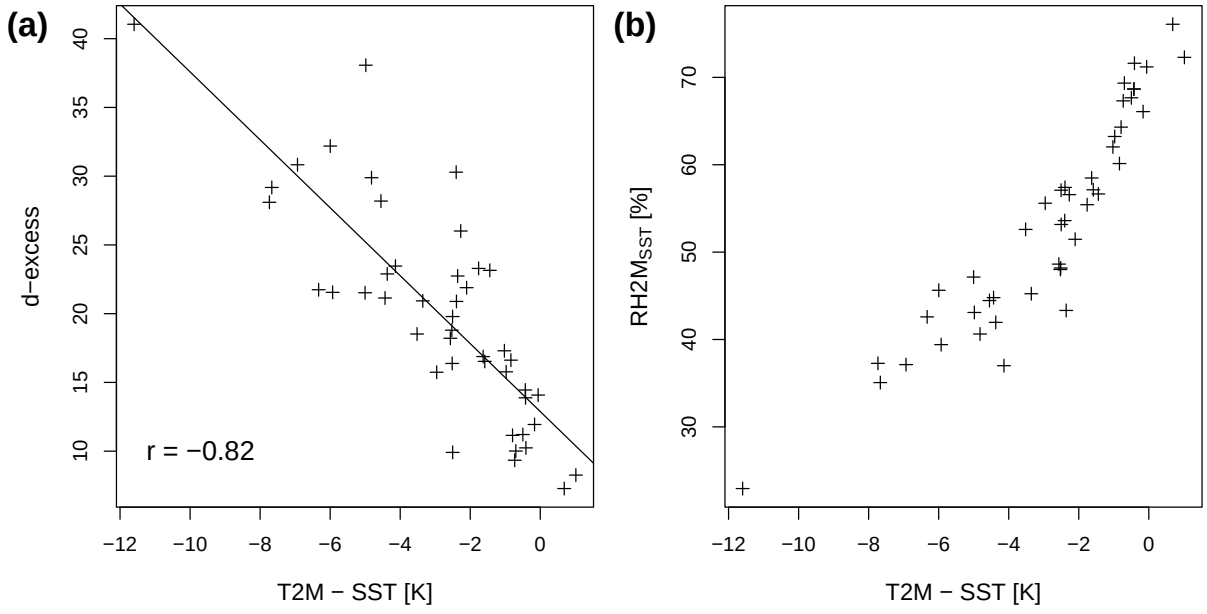

Figure 4.3. *Deuterium excess (a) and* $\mathrm{RH2M_{SST}}$ *(b) as functions of the difference between temperature at 2 m (T2M) and SST. Again there is one entry per measurement day.*

Source variable	Correlation coefficient
$RH2M_{SST}$	-0.82
RH2M	-0.64
RH_{SST}	-0.74
RH	0.05
SST	-0.21
T2M	-0.52
T	-0.55
T2M – SST	-0.82
T – SST	-0.77
VEL	0.29
VEL10M	0.37
Δp	0.34
$\Delta q/q$	0.14
Evaporation flux	-0.69
Time in OBL after uptake	-0.21

Table 4.1. *Correlation coefficients of different diagnosed moisture source parameters with measured deuterium excess.* VEL *denotes wind velocity,* VEL10M *wind velocity at 10 meter height.* Δp *indicates the difference between surface pressure and pressure at the trajectory level.* $\Delta q/q$ *is the uptake of specific humidity, divided by the total humidity in the air parcel, and OBL denotes the oceanic boundary layer.*

correlation is the clear functional relation between this temperature difference and $RH2M_{SST}$, as indicated in Fig. 4.3b. Physically, this functional relation indicates that humidity uptake generally occurs in relatively cool air compared to SST, e.g. in continental air moving over a warm sea surface. This results in a negative temperature difference as shown in Fig. 4.3b on the horizontal axis. (Note as an aside that positive temperature differences at the humidity uptakes do not occur, since they would imply an inversion layer just above the surface, which hampers mixing and humidity uptake by overlying air.) The functional relation between T2M-SST and $RH2M_{SST}$ occurs because RH2M is limited by the saturation vapor pressure at T2M, and therefore, a large difference between T2M and SST implies a low value of $RH2M_{SST}$, i.e. of RH2M with respect to the warmer sea surface. In contrast, if the temperature of the overlying air is not much lower than the SST, its water vapor capacity is larger, leading on average to higher values of $RH2M_{SST}$. Besides this physical mechanism, the observed functional relation might partly be generated by the boundary layer parameterization scheme of the ECMWF model (note that both T2M and RH2M are not explicitely calculated model variables). However, the functional dependence shown in Fig. 4.3b is still present if using temperature and RH at the trajectory level instead of the 2 meter quantities, corroborating the physical explanation given above. Addition-

ally, the correlation between temperature difference and d (Fig. 4.3a) also occurs if temperature is considered at the trajectory level ($r = -0.77$). Also T and T2M are both negatively correlated with d, but the absolute values of the coefficients are distinctly smaller than for the temperature differences (T-SST and T2M-SST). These correlations are mainly due to the same physical effect as described above and the fact that SST varies much slower in time than air temperature. This implies that the high frequency part of the correlations of the temperature differences with d is generated by variations in T2M and T. Nevertheless, the absolute values of the correlation coefficients show that the temperature gradient and by this the humidity gradient in the surface layer is the most important quantity for understanding variations in d.

In addition, multiple linear statistical models have been specified with d as dependent and all pairwise combinations of the source parameters as two independent variables. The highest values for the explained variance appear in models including $\mathrm{RH2M_{SST}}$, but none of these is substantially larger than 70%, i.e. no significant increase in explained variance can be obtained compared to the model based on $\mathrm{RH2M_{SST}}$ alone.

Influence of surface wind velocity

In their model, *Merlivat and Jouzel* (1979) found that isotopic fractionation during evaporation from the sea depends on the roughness regime of the sea surface, which is in turn related to the mean wind speed at a height of 10 m. They defined a smooth regime for wind speeds below and a rough regime for velocities above 7 m/s. In order to compare this finding with our data, linear models for the dependence of d on $\mathrm{RH2M_{SST}}$ have been defined separately for the two regimes, using the diagnosed ECMWF 10-meter wind velocity, averaged over all uptake points, as indicator for surface roughness. The slopes of the two regression lines differ significantly ($-0.5‰/\%$ for low, $-0.73‰/\%$ for high wind speeds, not shown), confirming the dependence of the relation on surface roughness. However, this conclusion is preliminary and might be misleading due to several reasons: Firstly, by averaging the wind velocity and applying the threshold for the roughness regime afterwards, an intrinsically non-linear process is treated as linear, what might introduce distinct errors. Secondly, there are only 11 measurement days with diagnosed mean wind speeds larger than 7 m/s, and for none of these days $\mathrm{RH2M_{SST}}$ is much larger than 60%; hence, this regression is not based on a profound statistic.

Adjusted d-excess

As already mentioned in section 4.1.1, d is not an exact measure of non-equilibrium fractionation, because the equilibrium ratio $\delta^2\mathrm{H_{eq}}/\delta^{18}\mathrm{O_{eq}}$ slightly depends on temperature. An adjusted deuterium excess d_{adj}, which takes this temperature dependence into account, can be calculated

as follows:

$$d_{\mathrm{adj}} = \delta^2\mathrm{H} - \frac{\delta^2\mathrm{H}_{\mathrm{eq}}(T)}{\delta^{18}\mathrm{O}_{\mathrm{eq}}(T)} \cdot \delta^{18}\mathrm{O}\,. \tag{4.3}$$

Here, T denotes the temperature at the evaporation site and has been taken as the average value of T2M derived from our moisture source diagnostic. Assuming no further fractionation during water vapor transport, d_{adj} measures non-equilibrium fractionation at evaporation exactly. Equilibrium values $\delta^2\mathrm{H}_{\mathrm{eq}}(\mathrm{T2M})$ and $\delta^{18}\mathrm{O}_{\mathrm{eq}}(\mathrm{T2M})$ have been calculated from the fractionation factors given by *Majoube* (1971), assuming Vienna standard mean ocean water. From this equilibrium values and the measured isotope ratios $\delta^2\mathrm{H}$ and $\delta^{18}\mathrm{O}$, d_{adj} has been computed according to (4.3). Figure 4.4 shows d_{adj} plotted against mean $\mathrm{RH2M}_{\mathrm{SST}}$. The correlation ($r = -0.88$) is even more significant than for standard d-excess ($r = -0.82$), indicating that the adjusted excess is more directly related to non-equilibrium fractionation, and thereby to $\mathrm{RH2M}_{\mathrm{SST}}$, than d. Overall, almost 80% of the variance in d_{adj} can be explained with the variation of mean $\mathrm{RH2M}_{\mathrm{SST}}$ in the moisture source regions.

4.3.2 Correlation analysis of oxygen and deuterium isotopes

Additionally to the results for d-excess shown in the previous section, correlations between the directly measured isotope ratios $\delta^2\mathrm{H}$ and $\delta^{18}\mathrm{O}$ and the diagnosed moisture source conditions have been calculated. Figure 4.5 shows these isotope ratios, together with source SST (horizontal axis) and $\mathrm{RH2M}_{\mathrm{SST}}$ (color). Also shown are linear regression lines for all points and for

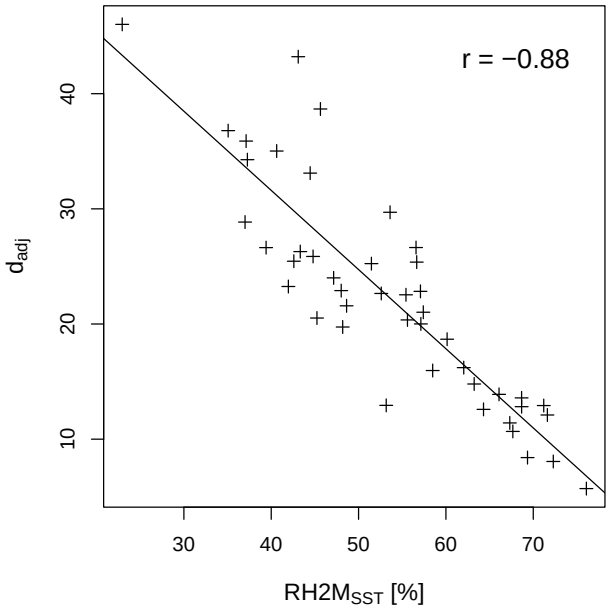

Figure 4.4. *Adjusted d-excess, as calculated from equation (4.3), plotted against* $\mathrm{RH2M}_{\mathrm{SST}}$. *See text for details.*

points with RH2M $> 62\%$, as well as theoretical equilibrium lines, calculated based on equilibrium fractionation factors given by *Majoube* (1971). The correlation coefficients for δ^2H versus SST and RH2M$_{SST}$ are $r = 0.47$ and $r = 0.43$, respectively. Also with respect to all other source variables, no correlations with absolute values larger than 0.5 are obtained for δ^2H, and the multiple statistical models using two independent variables do not lead to a substantial increase in explained variance. These rather low correlations indicate that the imprint of source conditions on δ^2H directly is lower than for d. Equilibrium fractionation during transport, not materially affecting d, can distinctly change the isotope ratio itself. Such fractionation, as mentioned above, can occur e.g. during sub-grid scale cloud formation. Apart from these transport effects, the correlation between source SST and δ^2H, which would be one in idealized thermodynamic equilibrium, is diminished by non-equilibrium effects during evaporation. This becomes clear when looking only at points with relatively high source RH2M$_{SST}$ (larger than 62%). For these points, non-equilibrium fractionation is less pronounced (as indicated by the results in section 4.3.1 and discussed further in section 4.4), and the correlation coefficient between SST and δ^2H increases to 0.57. Using d as a more explicit measure for non-equilibrium, the increment in correlation is even a bit larger ($r = 0.60$ for all points with $d < 16‰$). However, these increases are statistically not very robust because of the low number of data points in the reduced cases. Despite the relatively low correlation coefficients, the correspondence between both regression lines shown in Fig. 4.5a and the theoretical equilibrium line is surprisingly good. The deviations of points to both sides of this equilibrium line indicate that transport effects dominate in the generation of these deviations (contrasting the increase in correlation described above), because non-equilibrium effects during evaporation solely cause larger depletion than in equilibrium. It is not clear if the balance of these deviations, determining the correspondence of regression and equilibrium lines, is just a coincidence in this data set.

The correlation coefficient between source SST and δ^{18}O is even a bit lower than for δ^2H ($r = 0.44$), whereas the correlation to RH2M$_{SST}$ is very high ($r = 0.81$). All other correlations are smaller, and the multiple models do not lead to substantial gains, as described for d in section 4.3.1. The similarly large correlation of δ^{18}O and d with RH2M$_{SST}$ implies a correspondence between these variables, which is due to the fact that the relative importance of non-equilibrium effects is much larger for δ^{18}O than for δ^2H (see *Jouzel et al.*, 2007). This is manifested in the negative deviation of all points in Fig. 4.5b from the equilibrium line and the decrease of δ^{18}O with increasing RH2M$_{SST}$, as also indicated by the positioning of the regression lines. Due to the bad correlation, these regressions can certainly be regarded as rough estimates only. For δ^{18}O, omitting points with low RH2M$_{SST}$ does not lead to a better correlation with SST ($r = 0.33$ for points with RH2M$_{SST} > 62\%$). Most probable, this is again caused by the strong influence of non-equilibrium fractionation, also for high RH2M$_{SST}$.

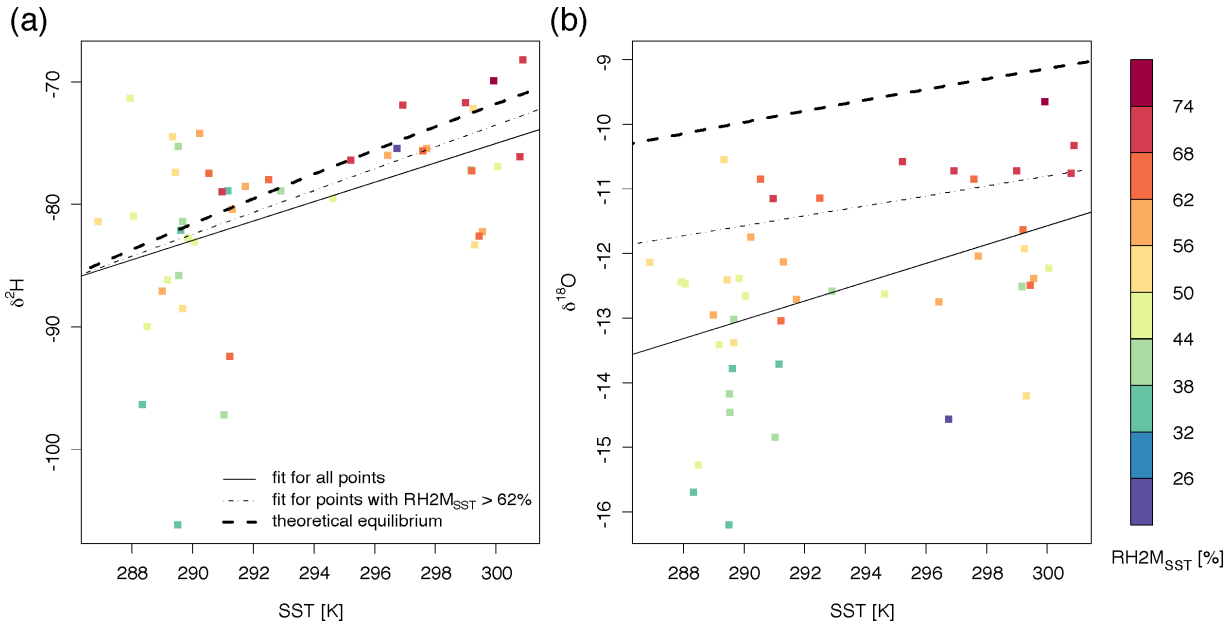

Figure 4.5. *Measured δ^2H (a) and δ^{18}O (b, both given in ‰) plotted against average SST at humidity uptake. Colors indicate diagnosed* $\mathrm{RH2M_{SST}}$ *in the uptake regions. Linear regression lines for all points (solid lines) and for points with* $\mathrm{RH2M_{SST}} > 62\%$ *(dash-dotted lines) are also shown. The gray dashed lines represent thermodynamic equilibrium isotope ratios, calculated from equilibrium fractionation factors given by Majoube (1971).*

4.3.3 Sensitivity of the results to parameter settings in the analysis

The most important result from the previous paragraphs is the strong correlation between d and $\mathrm{RH2M_{SST}}$. This result is based on moisture uptake regions diagnosed from trajectories that have been cut at the first point, going backwards in time, where rain from above or cloud water larger than a given threshold have been detected. The reason for this trajectory clipping is to exclude, as strictly as possible, other fractionation processes apart from evaporation. Now, the influence of this clipping on our correlation result is explored. Figure 4.6 shows d-excess plotted against $\mathrm{RH2M_{SST}}$, identified from trajectories for which this clipping criterion has been moderated (a) or totally omitted (b). For Fig. 4.6a, clipping has been performed only at rain points, i.e. condensation and clouds have been allowed along the trajectories. In this case, there are of course more measurement days for which Ra exceeds 60% than with the full clipping (59 instead of 45). The correlation coefficient remains the same, indicating that cloud formation during transport from the evaporation site to Rehovot has no substantial influence on d. The reason for this is most probably that in the region and altitudes considered here, almost no ice clouds occur and warm clouds are assumed to condense in thermodynamic equilibrium, which does not materially affect d. Figure 4.6b shows that, if rain is also allowed along the trajectory (116 days with $\mathrm{Ra} > 0.6$), the correlation decreases only slightly. Rain from above can influence d of the trajectory's water

vapor in two ways: Firstly, through equilibration the vapor adapts to the isotopic signature of the water that falls into the air parcel from higher levels, which in general has different uptake regions and a different d-excess. Secondly, the evaporation of raindrops in unsaturated air itself is a non-equilibrium process, changing d of the vapor. The small reduction of r in Fig. 4.6b, compared to Figs. 4.2a and 4.6a, shows that the influence of these processes is small, at least for the present data set in the Eastern Mediterranean. Indeed, this reduction might also be caused by the fact that the source regions in the no clipping case are, on average, at a larger distance from Rehovot (not shown), possibly introducing larger uncertainties of the trajectory approach, e.g. due to sub-scale mixing. Hence, it is not possible to estimate more quantitatively the impact of rain re-evaporation in this study.

Another parameter, in addition to the thresholds for clouds and rain, which has been chosen subjectively is the threshold for Ra, the fraction of collected water vapor of which sources can be attributed. In Fig. 4.7, d is plotted against $\mathrm{RH2M_{SST}}$ for the original threshold value of 0.6 and for reduced values, 0.4 and 0.2. The absolute value of the correlation coefficient decreases slightly when adding measurements with lower Ra, but unexpectedly remains large ($r = -0.77$). Even most of the points with $\mathrm{Ra} < 0.4$ can be found in the same range as the original points with $\mathrm{Ra} > 0.6$. Several reasons for this high correlation of d with source $\mathrm{RH2M_{SST}}$ at days with low

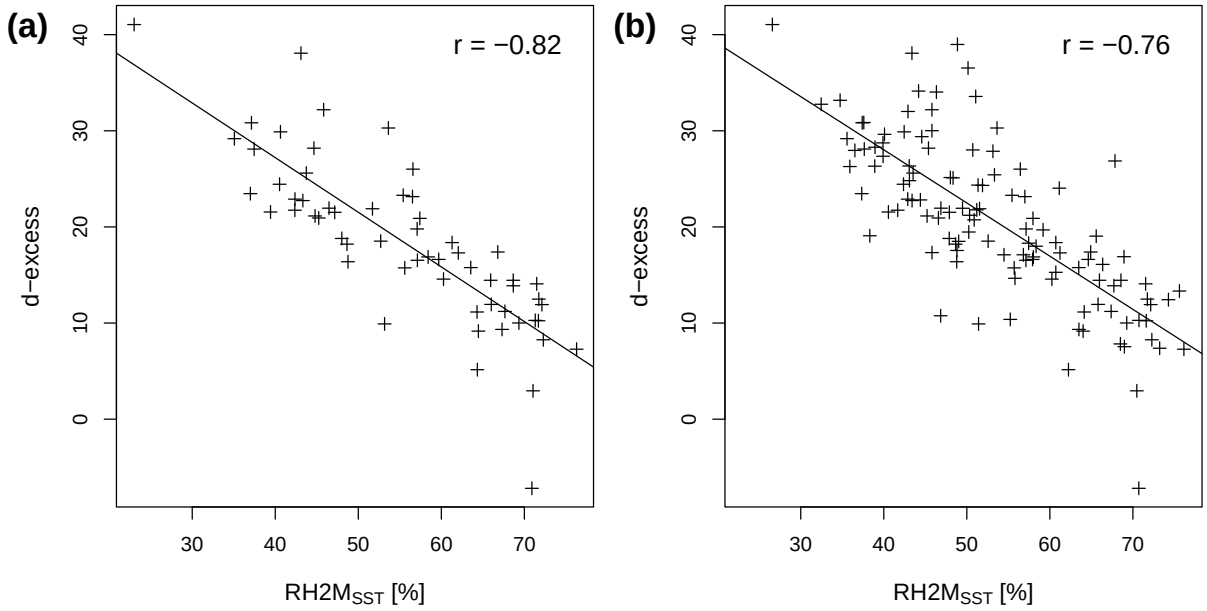

Figure 4.6. *Plots of d-excess against* $\mathrm{RH2M_{SST}}$ *for varying clipping criterions for the trajectories. In (a), trajectories have been cut at the first point, going backwards in time, where rain from above (larger than 1 mm in 6 hours) has been detected, not taking into account cloud liquid water and ice. In (b), no clipping has been performed at all.*

fractions of attributable water vapor are conceivable. Firstly, our source diagnostic might underestimate the contribution of local moisture sources close to the Israeli coast. Since the algorithm detects local sources also in cases with low Ra, these sources might explain a larger fraction of measured isotope ratios than estimated from the humidity increase along the trajectories. Secondly, the meteorological conditions in the diagnosed uptake regions are possibly representative for larger areas at the respective time instant. Thus, the uptake conditions (e.g. the relative humidity) might be similar at locations where uptake takes place in reality, but which are not identified by our method. All together, the results shown in Fig. 4.7 indicate that the method introduced in this study might also yield useful results in cases with low values of Ra.

In addition to the correlation coefficients, also the linear regression lines shown in Figs. 4.6a,b and 4.7 do not differ significantly from the original results given in section 4.3.1. Consequently, the relationship between d and $\mathrm{RH2M_{SST}}$ is very robust, i.e. it does not depend quantitatively on the clipping criterion and the threshold for Ra.

Finally, the sensitivity of the correlation results with respect to the degree of sophistication of the source region attribution has been explored. Therefore, as a simpler alternative to using the relative humidity at the exact moisture uptake regions determined with the Lagrangian method described in section 4.2.2, we averaged $\mathrm{RH2M_{SST}}$ over the whole Eastern Mediterranean Sea (defined as all Mediterranean ocean grid points in the ECMWF analysis data east of 24°E and south of 40°N). This region has been assumed to be the main water source region for Israel. For each measurement day, the temporal average of this domain-mean relative humidity has

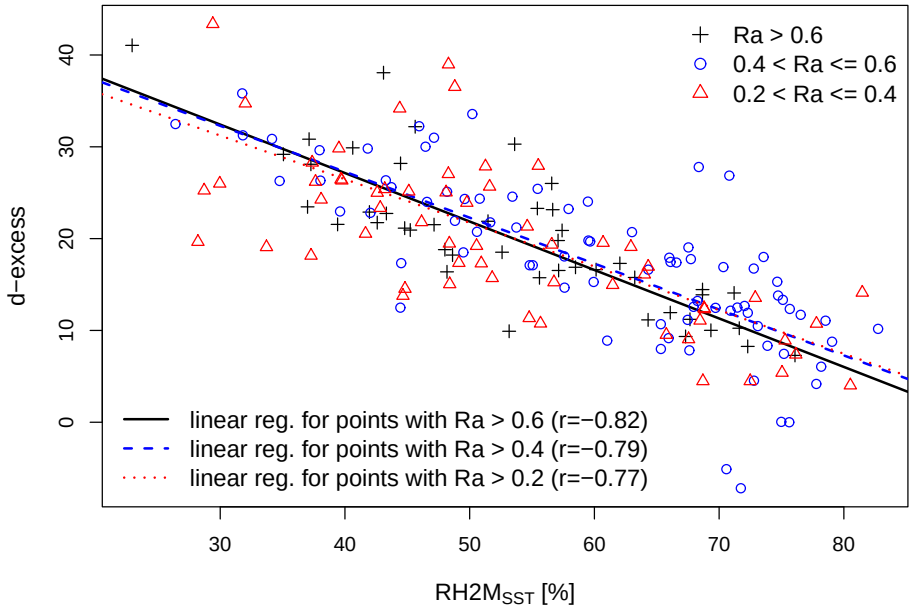

Figure 4.7. *Deuterium excess and* $\mathrm{RH2M_{SST}}$ *for different thresholds for* Ra.

been calculated over 48 hours prior to 6 UTC at the respective day and correlated with the measured deuterium excess. The correlation coefficient obtained from this analysis is $r = 0.69$. This correlation is surprisingly high, showing that the distribution of $RH2M_{SST}$ in the Eastern Mediterranean region is rather representative for the respective conditions at the actual evaporation sites of the water transported to Rehovot. For days included in the original analysis (i.e. days with $Ra > 0.6$), the reason for this is that almost all detected source regions are located over the Eastern Mediterranean Sea (cf. Fig. 4.1d). In spite of the good results that can be obtained with such a simple (Eulerian) approach, which is based upon averages over a large region that is considered as representative for the actual water origins, a detailed (Lagrangian) analysis of moisture source regions is still meaningful and rewarding due to the following reasons: (i) The correlation coefficient is substantially larger with the Lagrangian method, showing that detected source conditions represent actual evaporation conditions in a better way. (ii) Without a detailed knowledge of source regions, one can hardly be sure whether a subjectively chosen region of average origin adequately represents reality. This might be relatively simple for Israel and the Mediterranean, but for other locations an a priori assumption is less straightforward. (iii) Detailed source regions can be used as starting points for Lagrangian modeling in future research, as pointed out in section 4.5.

4.4 Discussion

In section 4.3, we have demonstrated a strong negative correlation between deuterium excess in water vapor measured at Rehovot, Israel and the relative humidity in the water evaporation regions, defined with respect to saturation at the sea surface. This result is physically very plausible, because the importance of non-equilibrium effects during evaporation is basically determined by the humidity gradient above the ocean surface. The strong influence of relative humidity on non-equilibrium fractionation and, by this, d-excess is documented in several studies (e.g. *Craig and Gordon*, 1965; *Merlivat and Jouzel*, 1979; *Gat et al.*, 2003). Furthermore, the preservation of source region information along water trajectories in the atmosphere and its measurability in terms of d has also been deduced from Rayleigh type models and isotope GCMs (see section 4.1.1).

In the following paragraphs, we discuss some aspects of the results presented in the previous section in more detail. First, we compare our data with other data sets from the literature, addressing the quantitative commensurability of the relationships deduced with the help of our method. Second, some implications of the low correlation of d with source SST found in this study for the interpretation of d as temperature proxy are discussed. Finally, possible error sources of our method are addressed, and an example is given illustrating the possibility of modeling d-excess as an application of our results.

4.4.1 Quantitative comparison with other d-excess data

Unfortunately, measurements of stable isotopes in water vapor over the sea that can be used to directly validate our results are very rare. *Gat et al.* (2003) performed such measurements for vapor collected during a cruise in the Mediterranean Sea in winter 1995. In Fig. 4.8, d-excess from these measurements is plotted against locally measured RH_{SST} (not taking into account the advection of moisture from other sources in this case) together with the Rehovot data already shown in Fig. 4.2a. Only measurements are included for which no rain occurred in the vicinity of the ship during sampling. It should be noted that the relative humidity applied for the cruise data is based on measurements at mast height, i.e. 27.9 m above the waterline, in contrast to the diagnosed values of RH at 2 m altitude used for the Rehovot data. The red dotted line shown in the plot is a linear regression line for the ship data. Overall, the agreement between the two data sets is surprisingly high. All points lie in the same range, and the regression lines do not differ significantly. Hence, the values of $RH2M_{SST}$ during evaporation, obtained from reanalysis data with the help of our moisture source diagnostic, are quantitatively commensurable to measured RH_{SST} over the ocean. Furthermore, this agreement confirms that relationships between measured isotope values and diagnosed source parameters can also be interpreted in quantitative terms. The correlation coefficient for the ship data is $r = -0.73$, i.e. lower than for the Rehovot data set. The reason for this is that for the latter multiple moisture sources are considered which contribute to the local signal by mixing of advected air, whereas for the ship data only the vapor that has evaporated locally, under the measured RH_{SST} conditions, is taken into account. This local evaporate dominates water vapor at a height of circa 20 m over the ocean, but advection of moisture obviously cannot be neglected in this situation.

The red, dashed line in Fig. 4.8 has been taken from *Jouzel and Koster* (1996). It shows results from an isotope GCM. For all pure open ocean grid points of the model, average isotope values of water vapor and RH near the surface for the months June, July and August were derived for two years of a last glacial maximum simulation. The line in Fig. 4.8 is the result of a linear regression based on these data. In spite of the different time scale and climate conditions, the modeled relationship is in line with the measurement results discussed before. This might lead to the conclusion that the processes which relate RH and the isotopic ratio of the evaporation flux are properly represented in the GCM. In addition, it gives a first hint that the results found in this study for the Mediterranean might be generalized to global scales. However, these conclusions are very preliminary due to the different time scales used for the analysis of the measured and GCM data (synoptic vs. climatological scales).

Finally, the blue dashed-dotted line is the result of a theoretical evaporation model, derived from a global closure assumption (i.e. assuming the identity of the isotopic composition of evaporation flux and water vapor on a global scale) and for a temperature of 25°C. It shows data from

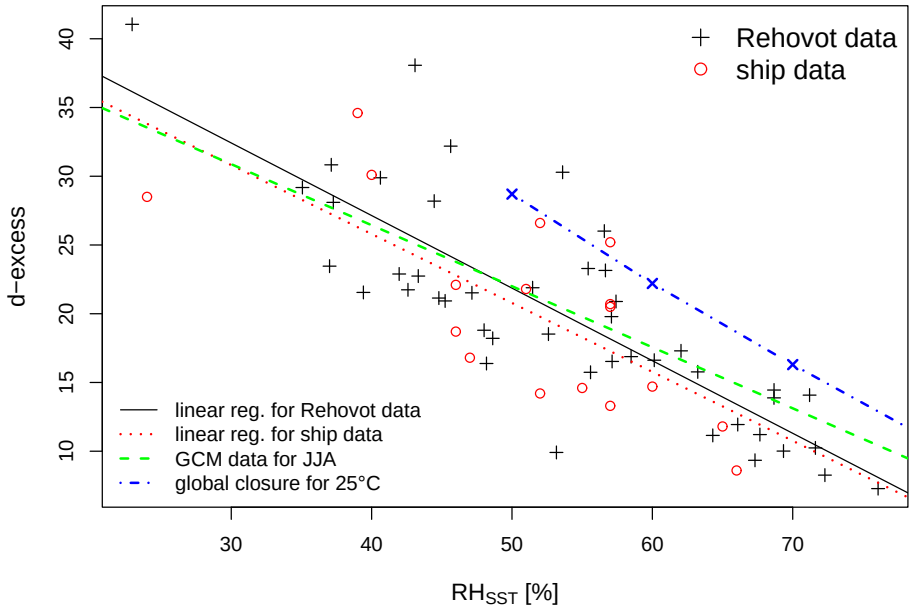

Figure 4.8. *Comparison of the deduced relationship between d-excess and* $\mathrm{RH2M_{SST}}$ *with other data sets. Black crosses and solid regression line are as in Fig. 4.2a. Red circles and the dotted regression line stem from ship measurements by Gat et al. (2003). The green dashed line was derived from climate model data by Jouzel and Koster (1996) (see text for details). The blue dash-dotted line is the result from a theoretical evaporation model and a global closure assumption for a temperature of* 25°C *(Merlivat and Jouzel, 1979).*

Table 1 in *Merlivat and Jouzel* (1979). A comparison with our data is not totally fair, because assumptions on temperature and surface wind speed were made in this paper, which do not necessarily match local conditions in the Eastern Mediterranean. Furthermore, *Merlivat and Jouzel* (1979) defined the d-excess in a somewhat different way (with slopes in the δ^{18}O-δ^{2}H space slightly departing from 8). However, an offset of these results from the other data in the plot is obvious, corroborating that the global closure assumption can lead to wrong results on the local scale, as already pointed out by *Jouzel and Koster* (1996).

4.4.2 Implications for the interpretation of *d* as temperature proxy

A positive correlation between *d*-excess and SST observed in GCM simulations is the major fundament of source temperature reconstructions from ice cores (see again section 1.3)[3]. However, there is little to no confirmation of such a correlation from measurements. In this context,

[3] In fact, source and site temperatures are often estimated in parallel using multivariate statistical models based on *d* and either δ^{18}O or δ^{2}H; nevertheless, *d* is assumed to describe the major part of source temperature variability in these models.

it might be important that the analysis performed in this study and the ship measurements by *Gat et al.* (2003) disagree with the GCM simulations at this point: there is a negative and weak correlation between d and SST in our data (cf. Fig. 4.2b) and a stronger negative correlation in the ship data ($r = -0.53$, not shown). Also, T and T2M are negatively correlated with d in data presented here. The positive correlation between d and SST observed in GCMs is related to the fact that RH is itself negatively correlated with SST in these models (*Jouzel and Koster*, 1996; *Armengaud et al.*, 1998). This correlation in turn is positive in our data ($r = 0.42$ for $\mathrm{RH2M_{SST}}$ against SST), as it is in the ship data ($r = 0.31$).

At this point, it is not clear if the parameterization of isotope fractionation or the simulation of mean humidity and temperature fields in the GCMs is responsible for the observed discrepancies. This might be a starting point for future research, comparing correlations between modeled humidity and temperature with observations. Nevertheless, the deviations might also be due to the different time scales and the restriction on moisture uptake points in the Mediterranean in this study and in the study of *Gat et al.* (2003).

Of course, the results presented here alone are not sufficient to put the validity of source temperature reconstructions with the help of the d-excess into doubt. The main reason for this is the local character of our data set and the different time scales involved. Ice core data are interpreted on scales from decades to glacial-interglacial cycles, while our analysis operates on diurnal scales. The fact that correlations are absent or present on these short time scales does not automatically imply the same for longer scales. There is a need for clarification of these issues within future research, and the present study can serve as a starting point for such an undertaking.

4.4.3 Modeling d-excess

Relying on the linear relationship between d and $\mathrm{RH2M_{SST}}$ deduced above and the moisture source diagnostic, it is possible to model 3-dimensional fields of deuterium excess, also at locations where no measurements are available. This is demonstrated in an example for the Mediterranean region on 18 November 2001, the day with the highest measured d-excess at Rehovot for which Ra is larger than 0.6. At 12 UTC on this day, backward trajectories have been started from grid points of the four lowest model levels of the ECMWF analysis data set in the region from 10° W - 40° E, 30° N - 50° N with a horizontal grid spacing of 0.75°. For all these horizontal grid points, the moisture source diagnostic has been performed as described in section 4.2.2, for each point based on the four trajectories from slightly different vertical levels. Average $\mathrm{RH2M_{SST}}$, derived from the moisture sources of each grid point separately, has then been used to calculate d via the linear relationship given in section 4.3.1. Figure 4.9 shows the resulting

spatial pattern of *d* on the lowest ECMWF model levels (i.e. at about 980 hPa). Values are only shown for points where Ra is larger than 0.6. A very strong gradient in *d* is visible from the very east of the Mediterranean (with high values, as measured at Rehovot at this date) to its western part. Such a gradient, albeit less pronounced, can also be found in the climatological pattern of *d* in precipitation (*Lykoudis and Argiriou*, 2007). At the western shore of the Mediterranean sea, close to the Strait of Gibraltar, *d* increases again to relatively high values (see Fig. 4.9). It is also apparent from the Figure that the method can be applied more easily to locations over or close to the sea. For these points, Ra in general is higher. Reducing the threshold for Ra or omitting the trajectory clipping can improve the applicability over continental areas, and both does, according to section 4.3.3, not substantially lower the accuracy of the method.

4.4.4 Methodical error sources

Certainly, there are also some drawbacks related to our moisture source diagnostic that might influence the deduced correlations between source parameters and measured isotopic values (cf. *Sodemann et al.*, 2008b). The Lagrangian scheme applied here assumes coherence of an air parcel on time scales up to ten days, in accordance with the results of *Stohl and Seibert* (1998). But

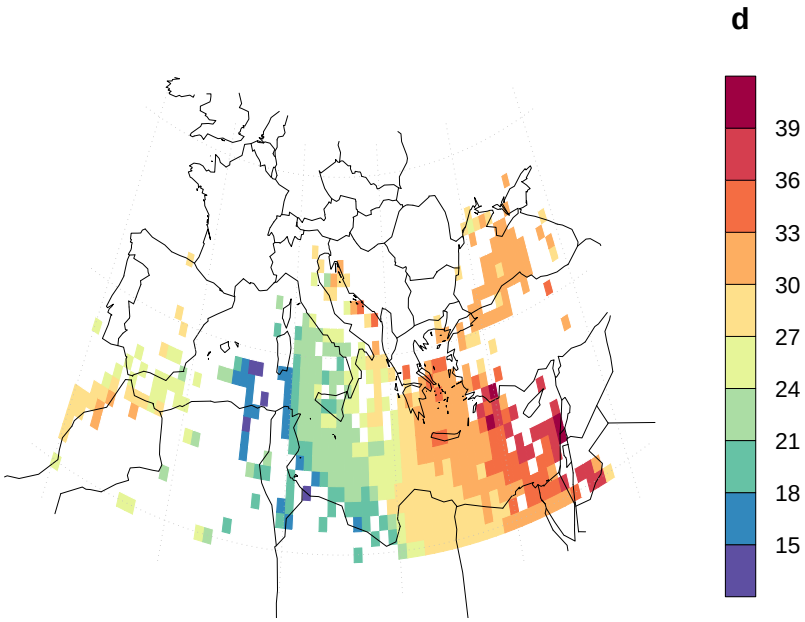

Figure 4.9. *Modeled d-excess at about 980 hPa in the Mediterranean region at 12 UTC, 18 November 2001. Only points are shown for which sources can be attributed to more than sixty percent of the final water vapor (*Ra $>$ 0.6*).*

of course, the time scale of this coherence depends on various parameters and varies from case to case. Besides, there are many small scale processes, like convection and turbulence, which are not resolved by the model and might lead to undetected moisture transport. The moisture content of air parcels along a trajectory in the model world is additionally altered by non-physical factors like numerical diffusion. However, these effects obviously do not affect the source diagnostic strongly enough to prevent the detection of physically reasonable and quantitatively meaningful correlations between source parameters and isotope measurements.

More specifically, one can ask the question if shortcomings of the method are the reason that potential correlations between *d*-excess and SST, which might exist in nature, are not observed here. However, we think that this is very unlikely because (i) for $RH2M_{SST}$, a strong correlation has been detected, and (ii) the SST field shows less spatial variation than RH. In order to give a more quantitative estimate of the difference in spatio-temporal variability of these fields, for each measurement day the range of source parameter variation that accounts for 90% of the humidity uptake has been calculated. For $RH2M_{SST}$, the mean value of this daily source variability is 22%, for SST it is 4 K. Relative to the entire range of source parameter variation (i.e. the difference between maximum and minimum of all daily ranges), this average daily variability is 31% for $RH2M_{SST}$, but only 18% for SST. Hence, it should in fact be easier to detect source SST properly with our method, and errors due to averaging in space and wrong attribution of source regions should be smaller.

4.5 Conclusions

In order to link isotope measurements at Rehovot with the transport history and particularly the meteorological conditions at the source regions of the respective water vapor, a Lagrangian moisture source diagnostic has been applied. With the help of this diagnostic, it has been possible to establish quantitative relationships between the source conditions and the measured isotope ratios. The significance of these relations has been analyzed by calculating correlation coefficients. Establishing such linkages enhances our understanding of stable isotopes in the atmospheric water cycle in several ways. Firstly, it is a first step towards a quantitative interpretation of isotope measurements on short time scales in terms of their very complex transport and fractionation history. So far, this history was comprised qualitatively in such an interpretation by several studies (*Rindsberger et al.*, 1983; *Gat et al.*, 2003; *Anker et al.*, 2007; *Strong et al.*, 2007). However, an estimation of the effects of many different processes during water transport requires their quantification. In this context, our work can be seen as a starting point, which can be expanded by integrating processes like cloud formation more directly and exploring other measurement data sets, specifically measurements of isotopes in precipitation. In addition, it might be very interesting to include measurements of $\delta^{17}O$ in the analysis, because recent studies showed that

the ^{17}O-excess (defined with respect to ^{18}O) is also related to moisture evaporation conditions (*Barkan and Luz*, 2007; *Landais et al.*, 2008). Secondly, the methodology applied here can be used in the context of Lagrangian modeling of water isotopes. In chapter 5, the moisture source diagnostic, together with a parameterization of the isotopic composition of evaporation fluxes, is used to test predictions of the Craig-Gordon model (*Craig and Gordon*, 1965). Thirdly, the diagnosed relationships can, of course, be used for further applications, e.g. the interpretation of ice core data or modeling of d-excess fields in time and space, as shown in section 4.4.3. Another interesting application of the relationship might be the determination of water source regions from isotope measurements in terms of footprint analyses. *Yamanaka et al.* (2002) performed such an analysis for Japan, based on the theoretical relation deduced by *Merlivat and Jouzel* (1979) with the help of a global closure assumption.

In principle, connections between the isotopic composition of the evaporation flux and the local meteorological conditions can be measured directly over the ocean. Our method shall not replace these direct measurements, but complements and extends results from such measurements by incorporating transport effects. Furthermore, the paucity of isotope measurements over the sea requires to implement more advanced techniques to investigate the local isotopic composition of the atmosphere there.

In section 4.3.1 it has been shown that a major part of the variance of measured deuterium excess can be explained with varying relative humidity at a height of two meters at the moisture uptake, calculated with respect to saturation at the sea surface. The correlation coefficient between the two parameters is -0.82 and becomes even more significant taking into account the temperature dependence of the equilibrium ratio $\delta^2\mathrm{H}/\delta^{18}\mathrm{O}$. The deduced relationship is very robust when varying different thresholds of the diagnostic. Besides, a comparison with similar relations from ship measurements and GCM data shows a very good correspondence. Finally, it has been demonstrated that the relationship can be used to model d in water vapor for regions where no measurements are available with high spatial and temporal resolution.

In contrast to results from isotope GCMs, no significant correlation between source SST and d-excess could be detected in this study. A possibly spurious correlation of these quantities in GCMs might be induced by a likewise questionable anti-correlation of SST and RH in the models. Due to the fact that source temperature reconstruction from ice cores is basically founded on such correlations observed in GCMs, the work presented here might also have important consequences in this context. However, in this study we have just looked at an isotope data set from a single location, and the global applicability of the results still has to be examined. Furthermore, the time scale of our data set differs substantially from the scales important for ice core interpretation (see again chapter 1).

Correlations between meteorological source conditions and the isotope ratios δ^2H and δ^{18}O have also been explored. Whereas δ^{18}O has been shown to be mainly determined by non-equilibrium fractionation during evaporation, as it is the case for *d*, δ^2H depends more strongly on equilibrium effects during vapor transport. These transport effects have not explicitely been considered in this study. As mentioned above, this might be another starting point for future research.

Chapter 5

Lagrangian Modeling of Stable Isotopes in Water Vapor[1]

5.1 Introduction

Our understanding of the variability of stable isotope concentrations in atmospheric waters is to a large extent based on theoretical and numerical models. The complexity of these models varies from dynamically relatively simple, one-dimensional Rayleigh models (e.g. *Petit et al.*, 1991; *Sodemann et al.*, 2008a) to isotope equipped GCMs (e.g. *Joussaume et al.*, 1984; *Hoffmann et al.*, 1998; *Yoshimura et al.*, 2008). One important and critical aspect of the models is the parameterization of isotope ratios in the evaporation flux over the ocean (see also section 4.1.1). The concurrence of equilibrium and non-equilibrium fractionation processes makes this parameterization relatively complex. As outlined in chapter 4, the value of the deuterium excess in atmospheric water vapor is mainly determined by fractionation processes during water evaporation. Hence, measurements of the d-excess can be used to validate the models' parameterization of isotope fractionation during evaporation. Several studies showed that there are some deficiencies in the performance of GCMs in modeling d-excess on climatological time scales (e.g. *Werner et al.*, 2001; *Jouzel et al.*, 2007). Moreover, in chapter 4 it has been shown that also correlations between d and sea surface temperature might be inaccurately simulated by the models. The observational data set of d-excess in water vapor from Rehovot and the sophisticated moisture source diagnostic presented in chapter 4 open new opportunities for a direct comparison of modeled and measured d-excess values on short time scales, and finally for an improvement of the fractionation parameterization in GCMs and other models.

Isotope ratios in the evaporation flux over the ocean are classically parameterized with a linear

[1] A slightly modified version of this chapter has been submitted for publication as *Pfahl and Wernli* (2009).

resistance model, as introduced by *Craig and Gordon* (1965). By now, there are various formulations of similar models, and most of them are principally based on the following equation (e.g. *Merlivat and Jouzel*, 1979; *Gat*, 1996; *Horita et al.*, 2008):

$$R_E = k \cdot \frac{\alpha R_L - h R_A}{1-h}, \tag{5.1}$$

(which is often written in δ-Notation, see *Gat* (1996) for the respective transformation). Here, R_E is the isotope ratio in the evaporate (see section 1.3); R_L and R_A give the isotope ratios in the ocean and in atmospheric vapor, respectively. h denotes the relative humidity of the atmosphere, defined with respect to saturation at the sea surface, α is the equilibrium fractionation factor between vapor and liquid at the surface, and finally k denotes a non-equilibrium (diffusive) fractionation factor. Equation (5.1) can be derived from simple one-dimensional advection-diffusion equations based on Fick's law (*He and Smith*, 1999) (where, in the present formulation, perfect mixing of the liquid with respect to water isotopes is assumed, which is a good approximation for open water bodies). The non-equilibrium parameter k probably is the least well known quantity in this formula. It depends on the molecular diffusivities D of the different water isotopes and most certainly also on the wind regime. In GCMs, k is usually parameterized after *Merlivat and Jouzel* (1979) (in the following referred to as MJ79), who calculated the parameter as a function of 10 meter wind speed $u_{10\mathrm{m}}$, based on the theoretical evaporation model of *Brutsaert* (1975) and wind tunnel experiments by *Merlivat* (1978a). Their formulation differs fundamentally between a smooth and a rough wind regime, with k exhibiting a discontinuity at the transition of the two regimes at $u_{10\mathrm{m}} = 7\mathrm{m/s}$ (see Figure 5.1). In other, dynamically simpler models, k is often assumed to be independent of the wind velocity (see again *Gat*, 1996). For the parameterization of k, the molecular diffusivities measured by *Merlivat* (1978b) are commonly used. However, these diffusivities differ from those predicted by the kinetic theory of gases. In a more recent study, *Cappa et al.* (2003) suggested that this deviation results from neglecting surface cooling effects due to evaporation in the interpretation of the measurements by *Merlivat* (1978b). Such surface cooling can amount to several K under laboratory conditions. In the ocean, cooling usually is not that large owing to more dynamic conditions compared to the laboratory; values of up to 0.6 K have been observed by *Wick et al.* (1996). Based on their own measurements, *Cappa et al.* (2003) suggested to use the diffusivities predicted by kinetic theory, that is $D_{\mathrm{H_2{}^{18}O}}/D_{\mathrm{H_2O}} = 0.969$ and $D_{\mathrm{HDO}}/D_{\mathrm{H_2O}} = 0.984$.

In Rayleigh-type isotope models, fractionation usually is calculated along more or less idealized trajectories of air parcels with a single, prescribed moisture source (e.g. *Petit et al.*, 1991). In order to initialize the model at the source, a so called "global closure assumption" was widely used in the past, as introduced by MJ79. Thereby, the isotopic composition of atmospheric vapor and of the evaporation flux are assumed to be equal on a global scale. Setting $R_A = R_E$ in

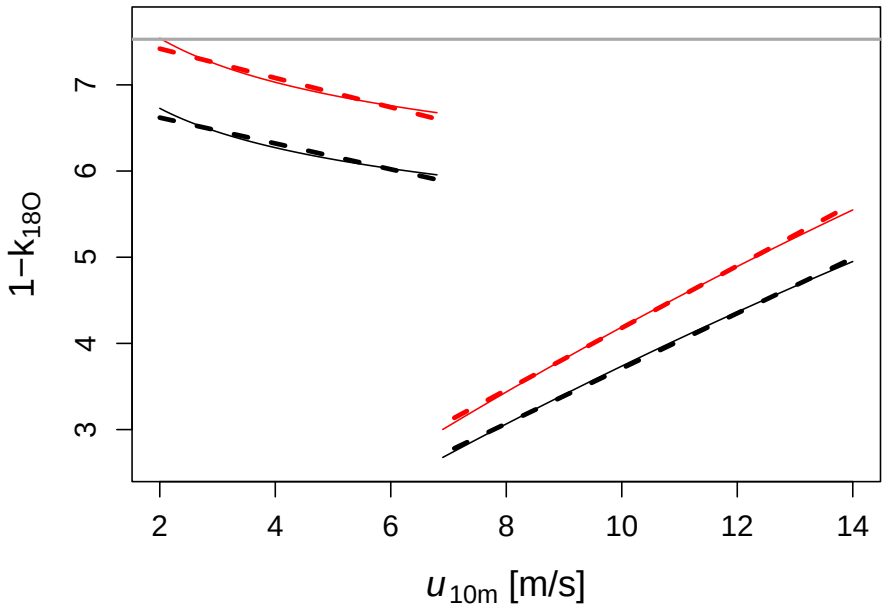

Figure 5.1. *Non-equilibrium fractionation factor for* $H_2{}^{18}O$ *($1-k$, in ‰). Solid lines show the exact values from MJ79 (see equation (11) and the paragraph below in their paper, but note that k here is defined as $1-k$), dashed lines are linear approximations applied in this study. The black curves have been obtained using molecular diffusivities measured by Merlivat (1978b); for the red curves, diffusivities from Cappa et al. (2003) have been used (cf. section 5.1). The gray solid line ($1-k = 7.5‰$) shows the constant value used for the new parameterization introduced in this study.*

equation (5.1) thus leads to

$$R_E = \frac{\alpha k}{1-h(1-k)} \cdot R_L. \tag{5.2}$$

However, *Jouzel and Koster* (1996) showed that this assumption might not be valid on local scales. Hence, in recent studies, which model the isotopic composition of precipitation along realistic trajectories calculated from atmospheric analysis data, the global closure assumption has not been used (*Helsen et al.*, 2007; *Sodemann et al.*, 2008a). Instead, the models have been initialized with climatological isotope ratios of water vapor obtained from GCM simulations, as recommended by *Jouzel and Koster* (1996).

In this chapter, we model the isotopic composition of water vapor at Rehovot by applying equation (5.1) in the evaporation regions of the vapor, which have been determined in chapter 4. The results are compared to the measurement data set that has also been used for the diagnostic analyses in the previous chapter. In this way, a direct evaluation of the Craig-Gordon model with atmospheric data in an event-based manner can be performed, and different parameterizations of the non-equilibrium fractionation factor can be tested.

5.2 Data and method

The model for calculating the isotope ratios in water vapor at Rehovot introduced here is based on the Lagrangian moisture source diagnostic described in chapter 4 as well as the meteorological parameters extracted from ECMWF analyses in the evaporation regions. Because only isotope fractionation during evaporation from the ocean is modeled, air masses that experience precipitation and cloud formation are excluded from the diagnostic by clipping the backward trajectories at the respective points. As in the previous chapter, modeling is only done for days for which sources have been attributed to at least sixty percent of the water vapor at Rehovot. On these 45 days, modeled isotope ratios and in particular the modeled d-excess d_{mod} are compared to the measurements d_{meas} used in chapter 4 and described in detail by *Angert et al.* (2008).

In the following paragraph, the simulation approach is described in detail for a single backward trajectory started at Rehovot, and an illustrative example is presented. Subsequently, the calculation of average isotope ratios for each measurement day is outlined.

In order to model the isotopic composition of the evaporation flux in the moisture source regions, every backward trajectory started at Rehovot is treated separately. At all moisture uptake locations along the trajectory, equation (5.1) is applied. Therefore, several parameters are needed:

1. The relative humidity with respect to saturation at the sea surface h is calculated from the diagnosed specific humidity q_{ll} on the lowest model level of the ECMWF analysis data at the uptake location and the diagnosed SST:

$$h = \frac{q_{\mathrm{ll}}}{q_{\mathrm{sat}}(\mathrm{SST})}, \tag{5.3}$$

   where $q_{\mathrm{sat}}(T)$ denotes the saturation humidity for temperature T.

2. The equilibrium fractionation factor α is obtained from the SST using the parametric equations given by *Horita and Wesolowski* (1994):

$$\begin{aligned} \ln\alpha_{18\mathrm{O}} &= 0.35041\cdot 10^{6}\cdot \mathrm{SST}^{-3} - 1.6664\cdot 10^{3}\cdot \mathrm{SST}^{-2} + 6.7123\cdot \mathrm{SST}^{-1} \\ &\quad -7.685\cdot 10^{-3}, \\ \ln\alpha_{2\mathrm{H}} &= 2.9992\cdot 10^{6}\cdot \mathrm{SST}^{-3} - 161.04\cdot 10^{-3} + 0.79484\cdot 10^{-3}\cdot \mathrm{SST} \\ &\quad -1.6201\cdot 10^{-6}\cdot \mathrm{SST}^{2} + 1.1588\cdot 10^{-9}\cdot \mathrm{SST}^{3}. \end{aligned}$$

3. For the isotopic composition of the ocean water, constant values of $\delta^{18}\mathrm{O}_L = 1.7‰$ and $\delta^{2}\mathrm{H}_L = 8.2‰$ are used, reflecting the results of measurements in the eastern Mediterranean by *Gat et al.* (1996). Since particularly the measured $\delta^{2}\mathrm{H}_L$ values are slightly unusual compared to other measurements and model results (*Schmidt et al.*, 2007), sensitivity experiments will be performed setting $\delta^{2}\mathrm{H}_L = 11.6‰$ (i.e. the d-excess is increased from -5.4‰ to a more common value of -2‰).

4. In order to define the upper boundary condition for the model, i.e. the atmospheric isotope ratio R_A, we can take advantage of the fact that in almost all cases multiple moisture sources are detected along a trajectory by the source diagnostic (contrasting the single source prescribed for the classical Rayleigh models). Hence, for most of the moisture uptakes R_A is set to the weighted mean of the composition of the evaporate R_E from previous uptakes along the same trajectory:

$$R_{A,N} = \sum_{i=1}^{N-1} w_i R_{E,i}\,,\; N > 1, \tag{5.4}$$

   where N denotes the number of the respective moisture uptake (counting forward in time, beginning at the first uptake detected along the trajectory), and w_i is the weight of the i-th previous uptake. This weight is calculated as the relative contribution of the previous uptake to the trajectory's humidity at the current position N (see *Sodemann et al.* (2008b) for details about the algorithm). Only for the first uptake of each trajectory, i.e. for $N = 1$, R_A has to be defined independently[2]. This is implemented in two possible ways: First, the global closure assumption can be applied at the first uptake point and equation (5.2) can be used. Second, isotope ratios in water vapor from the lowest vertical level of a GCM simulation can be employed for $R_{A,1}$. Because we compare with measurements in an event-based manner, the best possible choice for this GCM data is to use a historical simulation, in which the large scale atmospheric circulation is constrained to reanalysis data with the help of a nudging technique. The only historical isotope simulation published to date has been performed by *Yoshimura et al.* (2008), using the Scripps ECPC GSM model equipped with isotope physics (IsoGSM). Isotope ratios from the lowest vertical output level from this simulation are used to initialize R_A and also as a benchmark for the evaluation of our model. The data (IsoGSM version 1), which are available with a spectral resolution of T62 and 17 vertical levels, are linearly interpolated to the locations of the moisture uptake (and to the location of Rehovot for comparison with the measurements).

5. Finally, the value of the non-equilibrium fractionation factor k has to be set. This is also done in several possible ways. First, the classical parameterization of MJ79 is used, where k is defined as a function of diagnosed wind velocity at 10 m altitude at the uptake locations. Linear approximations of the exact formula given by MJ79 are applied, as shown in Figure 5.1 for ^{18}O, which is also commonly done in GCMs. Second, k is parameterized independently of the wind speed. The following empirical equation introduced by *Cappa et al.* (2003) is employed:

$$k = \left(\frac{D_h}{D_{\mathrm{H_2O}}}\right)^m, \tag{5.5}$$

[2]It should be noted here that the contribution of this first uptake to the final water vapor at Rehovot is small in almost all cases.

where D_{H_2O} is the diffusion coefficient of standard water, D_h the coefficient of one of the heavy isotopes (either $H_2{}^{18}O$ or HDO) and $0 \leq m \leq 1$. The tuneable parameter m controls the ratio of diffusive over turbulent transport of water molecules. If $m = 0$, then $k = 1$ and the transport is solely turbulent, without any non-equilibrium fractionation. For $m = 1$, there is purely diffusive transport. This empirical formulation can be shown to be approximately equivalent to the parameterization given by *Gat* (1996): From (5.5), we get $k \approx 1 - m \cdot \left(\frac{D_{H_2O}}{D_h} - 1\right)$. On the other hand, from equations (5a) and (6b) in *Gat* (1996), it follows that $k \approx \left(1 + n\theta \cdot \left(\frac{D_{H_2O}}{D_h} - 1\right)\right)^{-1} \approx 1 - n\theta \cdot \left(\frac{D_{H_2O}}{D_h} - 1\right)$, since $n\theta \cdot \left(\frac{D_{H_2O}}{D_h} - 1\right) \ll 1$. Thus, we can identify $m \approx n\theta$, where n denotes the exponent of the diffusion coefficient in the expression for the molecular resistance of the water molecules, and θ is the ratio of molecular over total resistance (see again *Gat* (1996) or *Horita et al.* (2008) for details). The molecular diffusion coefficients in equation (5.5) can be chosen either from *Merlivat* (1978b) or from *Cappa et al.* (2003) (see section 5.1).

Using equation (5.4) in order to average over previous moisture uptakes, isotope ratios in water vapor can be calculated at every location along an air parcel trajectory succeeding the first uptake. Figure 5.3 gives an example for the simulated isotope variation along a backward trajectory started from Rehovot at 07 UTC on 10. August 2005 shown in Fig. 5.2. Within 10 days, the modeled air parcel moves from the Norwegian coast over the North Sea, Central Europe, Italy and the eastern Mediterranean. The main moisture uptakes are located over the North and the Mediterranean Sea, as shown by the increase of specific humidity along the trajectory in

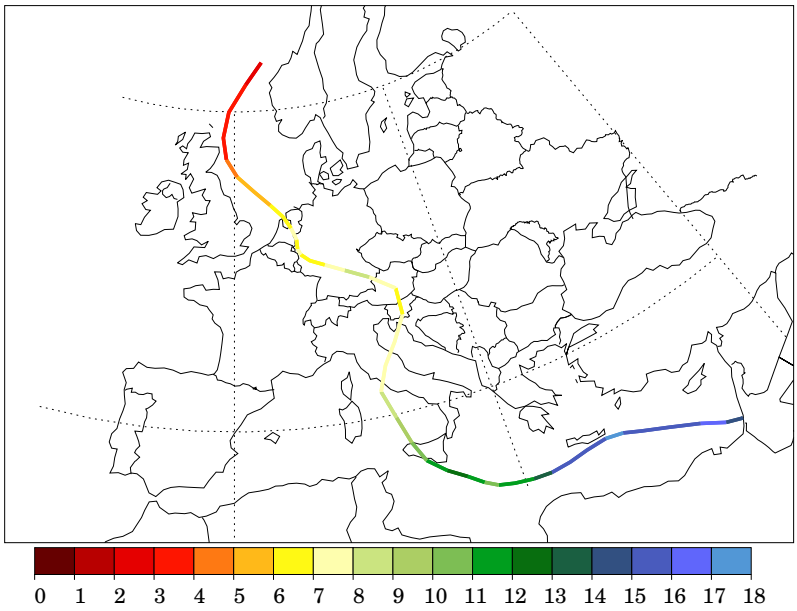

Figure 5.2. *Example 10-day backward trajectory, started from Rehovot at 07 UTC on 10. August 2005. Colors give the specific humidity along the trajectory in g/kg.*

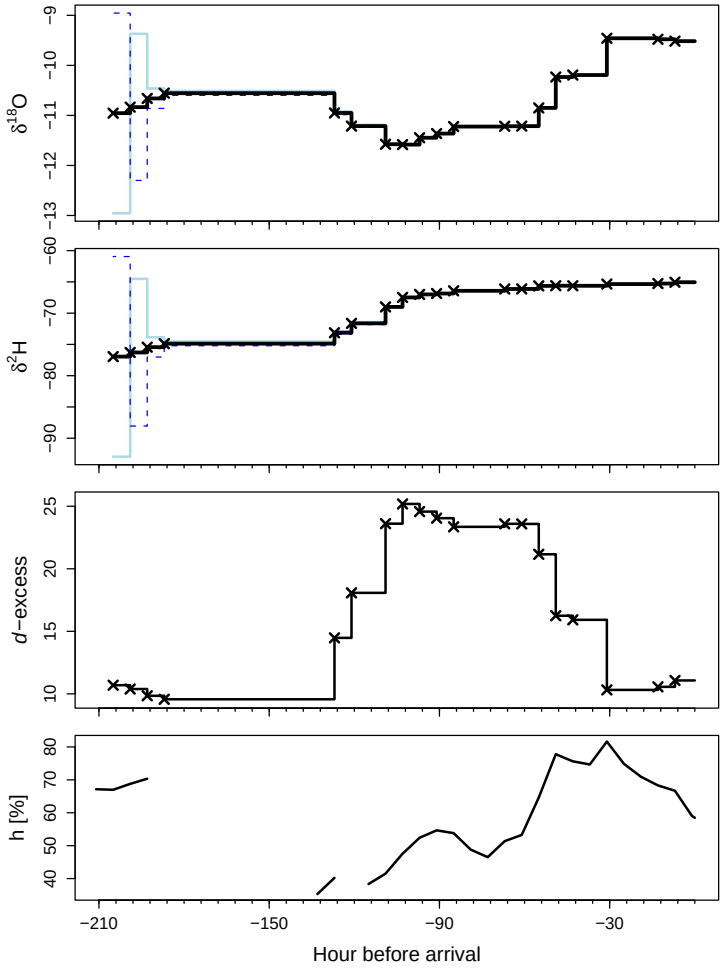

Figure 5.3. *Evolution of modeled isotope ratios in water vapor (δ^{18}O, δ^{2}H and d-excess), computed using equations (5.4) and (5.1), and diagnosed relative humidity h (on the lowest ECMWF model level, calculated relative to SST with equation (5.3)) along the example trajectory shown in Figure 5.2. The non-equilibrium fractionation factor has been parameterized with equation (5.5), using diffusion coefficients from Cappa et al. (2003), and the initial boundary condition has been determined with equation (5.2). Black crosses denote diagnosed moisture uptake locations in the oceanic boundary layer. h is only shown over the sea (where SST is defined). The blue solid (dashed) lines show modified model results for which the isotopic composition of the atmosphere after the first humidity uptake was decreased (increased) by* 2‰ *for* δ^{18}O *and* 16‰ *for* δ^{2}H.

Fig. 5.2 (note again that uptakes over the continent are not taken into account by the source diagnostic). Figure 5.3 shows that there are rather large changes in the isotope ratios along the trajectory for this sample case, which are only due to variations in the isotopic composition of the evaporate from the ocean (recall that no cloud processes are taken into account). It should be

noted here that these isotope ratios just represent the fraction of the air parcel's water vapor that is captured by the previously identified humidity uptakes along the trajectory. This fraction is small in the beginning, but increases with time. It becomes larger than 60% 85 hours before the arrival at Rehovot and finally reaches 78%. The simulated variability of δ^2H is mainly driven by changing SSTs. Over the North Sea, SSTs are rather cold, leading to a large equilibrium fractionation factor α and therefore strongly depleted values of δ^2H. In contrast, the warmer SSTs of the Mediterranean Sea result in a smaller depletion of δ^2H. For δ^{18}O, also variations in the humidity conditions play an important role. The modeled variability of d-excess is primarily controlled by the relative humidity h with respect to saturation at SST, as indicated in the two lower panels of the Figure (see also chapter 4). For the first humidity uptakes located over the North Sea, h is high, leading to small d values. When the air parcel moves from the European continent to the Mediterranean, it is relatively dry compared to saturation at the warm sea surface. Hence, the d-excess for the subsequent moisture uptakes is large, leading to an increase of d along the trajectory. Finally, when the air parcel approaches Rehovot, it becomes more humid and the simulated d-excess decreases. The blue lines in Fig. 5.3 show that the model results, at least in this particular case, are very stable with respect to variations in the initial value of the isotopic composition of atmospheric vapor.

With the help of equation (5.4), isotope ratios at Rehovot can be calculated for each trajectory. Then, as mentioned above, for each of the 45 measurements days for which more than 60% of the moisture at Rehovot can be traced back to its evaporation region by our method, mean isotope ratios are calculated by averaging over all backward trajectories started during the measurement period (typically 8 hours). Altogether, average isotope ratios at Rehovot are obtained from the isotope ratios of the evaporation flux at the moisture uptake locations as follows:

$$\overline{R} = \sum_{j=1}^{M} \sum_{i=1}^{N_j} \tilde{w}_{ij} R^j_{E,i}. \tag{5.6}$$

Here, M is the number of backward trajectories started within the measurement period, N_j denotes the number of moisture uptake points for trajectory j, and $R^j_{E,i}$ is the modeled isotope ratio in the evaporation flux of the i-th uptake point of this trajectory, computed from equation (5.1). The modified weights $\tilde{w}_{ij}$ incorporate the relative contribution of the i-th uptake to the final moisture content (as the weights w_i in equation (5.4)), but additionally account for the temporal variation of the specific humidity at Rehovot and of the number of trajectories calculated per hour (which depends on the boundary layer height, see again chapter 4). Finally, the weighted mean isotope ratios $\overline{R}$ are transformed to δ-notation and compared to the isotope measurements. Therefore, correlation coefficients (r), root mean square errors (RMSE) and regression lines between measured and modeled isotope composition are calculated.

It is important to note that the isotope values modeled with equation (5.6) only represent the fraction of the vapor at Rehovot to which sources can be attributed by our Lagrangian approach.

This fraction is larger than 60% for all measurements used here. On the other hand, this means that up tp 40% of the moisture is unaccounted, and its isotopic composition cannot be modeled with our approach. Hence, it is possible that this unaccounted part of the moisture introduces a bias to the comparison of model and measurements (see the discussion in section 5.4.1).

5.3 Results

Lagrangian simulations with different parameterizations of non-equilibrium fractionation have been performed for each of the 45 measurement days, as described in section 5.2. For the most important model settings, the results for *d*-excess are displayed in Fig. 5.4, and statistical measures of the model performance are given in Table 5.1.

In Figure 5.4, deuterium excess at Rehovot, modeled with our Lagrangian approach and using the parameterization of MJ79, is plotted against measured *d*-excess as black circles. The black dashed line shows the result of a linear regression. This model setup leads to a correlation coefficient of 0.53 and a RMSE of 10.7‰. Here, equation (5.2) has been applied to compute R_A at the first uptake location of each trajectory. If instead IsoGSM data are used to initialize R_A, this does not lead to a substantial change in the statistics ($r = 0.48$, RMSE $= 10.7$‰). Also, using the diffusion coefficients given by *Cappa et al.* (2003) (instead of *Merlivat* (1978b)) with the MJ79 parameterization (cf. Fig. 5.1) gives only a moderately lower RMSE of 8.4‰ and almost no change in *r* (0.54). Since the diagnosed ERA40 10 meter wind velocities are subject to significant uncertainties, simulations have also been performed with modified 10 meter winds. When these are reduced or increased by 20%, there is little change in the correlation coefficient and the RMSE. Finally, if the the deuterium content of the ocean water $\delta^2\mathrm{H}_L$ is changed from 8.2‰ to 11.6‰ (cf. section 5.2), the correlation coefficient stays the same and the RMSE is reduced to 8.4‰.

When, instead of the parameterization by MJ79, the wind speed independent parameterization of *k* given in equation (5.5) is used, *m* is a free parameter. Therefore, the model has been applied for various values of *m*. Using this approach, the correlation coefficient between measured and modeled *d*-excess at Rehovot has a fairly constant value of 0.8 for *m* between 0.2 and 1, no matter whether diffusion coefficients from *Cappa et al.* (2003) or *Merlivat* (1978b)) are used. When IsoGSM data are applied at the first uptakes instead of equation (5.2), the correlation coefficients change only marginally. The optimal value of *m* has been determined by minimizing the RMSE. This leads to values of $m = 0.24$ for diffusion coefficients from *Cappa et al.* (2003) and $m = 0.28$ for coefficients from *Merlivat* (1978b) (with equation (5.2) as initial boundary condition). These two settings result in almost identical *d*-values and a RMSE of 4.6‰. In the following, the parameterization with $m = 0.24$, diffusion coefficients from *Cappa et al.* (2003)

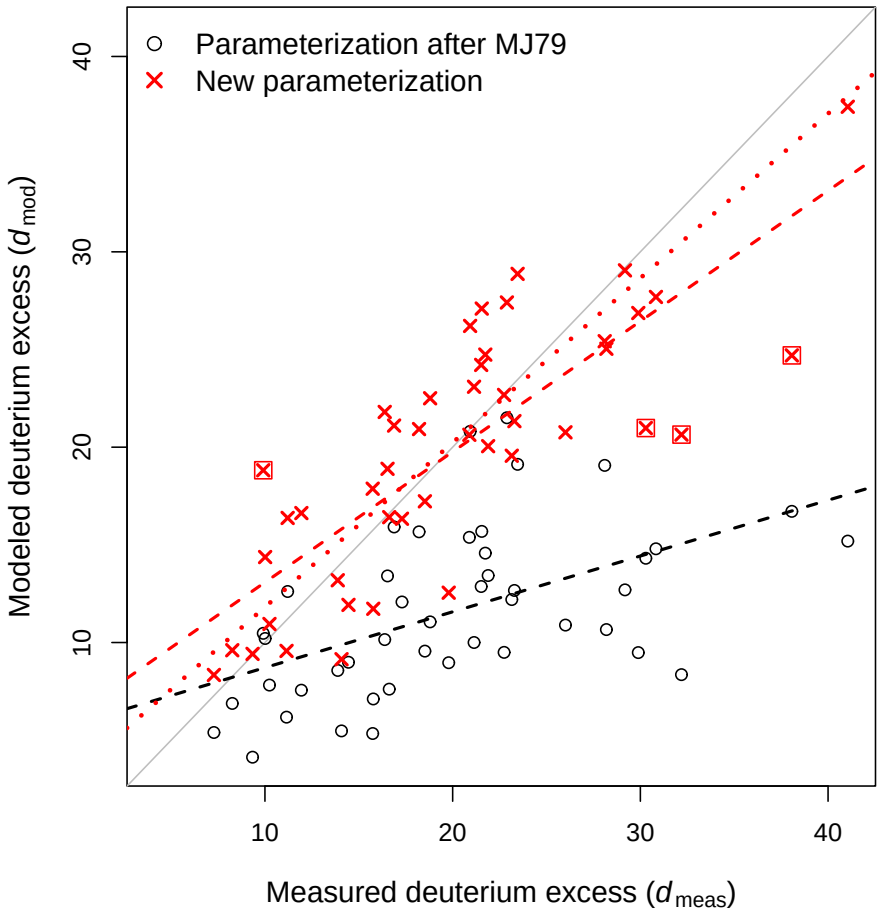

Figure 5.4. *Modeled d-excess using a Lagrangian technique (d_{mod}) plotted against d measured at Rehovot (d_{meas}). The solid gray diagonal corresponds to a perfect match. Black circles are obtained from the classical parameterization of non-equilibrium effects with wind dependent fractionation by MJ79, red crosses show the result of the new parameterization without wind dependence. The black dashed line shows the result of a linear regression for the MJ79 data, the red dashed line for the new parameterization results. The red dotted line also shows a linear regression for the new parameterization data, but here the 4 points with the largest mismatches ($|d_{mod} - d_{meas}| > 8$, marked by red squares) have been omitted.*

and equation (5.2) as initial boundary condition, referred to as “new parameterization”, will be further investigated. The results from the Lagrangian model using this new parameterization are shown as red crosses in Fig. 5.4, its statistics are again listed in Table 5.1. The red dashed line in Fig. 5.4 is a linear regression line for the results obtained with this new parameterization, which are much closer to the observed d values compared to the results using the MJ79 parameterization.

Model	Parameterization	Correlation coef.	RMSE [‰]	Slope of regression line
Lagrangian	MJ79	0.53	10.7	0.29 (0.07)
Lagrangian	new (this study)	0.80	4.6	0.67 (0.08)
IsoGSM	MJ79	0.49	9.0	0.24 (0.07)

Table 5.1. *Comparison of deuterium excess measured at Rehovot with results from different models and parameterizations. Correlation coefficients, root mean square errors and slopes of regression lines (along with their standard errors) between measured and modeled d-excess are given. The trajectory approach introduced in this study is termed Lagrangian model. MJ79 denotes the parameterization of Merlivat and Jouzel (1979), the new parameterization is based on wind speed independent fractionation (see text for details). Both Lagrangian simulations have been initialized using equation (5.2). In the third row, results from the historical GCM simulation with the IsoGSM model by Yoshimura et al. (2008) are given for comparison.*

Cappa et al. (2003) suggested that surface cooling may have a non-negligible effect on isotope fractionation, also under realistic oceanic conditions. Because there are still large uncertainties related to the deduction of skin temperature from the bulk temperature of the ocean top layer (which is included as SST in ECMWF analyses), we explore the effect of surface cooling with the help of a sensitivity experiment (instead of explicitely calculating skin temperature). All SST values used for the calculation of α and h are reduced by 0.5 K, which is in the order of the maximum observed surface cooling by *Wick et al.* (1996). Applying the new parameterization with this reduced SST, almost the same d-excess values can be obtained when the parameter m is slightly modified ($m = 0.25$ instead of 0.24 leads to the same statistics as given for the new parameterization in Table 5.1). Hence, the effect of surface cooling on the model results is very small.

Modeled isotope ratios can also be compared directly to the measured values of δ^{18}O and δ^{2}H. There is a large difference in the resultant correlation coefficients: for δ^{18}O, which is strongly influenced by non-equilibrium fractionation processes, the coefficient obtained from the new parameterization is of the same order as for d-excess ($r = 0.81$); for δ^{2}H, for which non-equilibrium fractionation is much less important, it is much lower ($r = 0.51$). When IsoGSM boundary data are used instead of equation (5.2), the coefficients are lower (0.75 for δ^{18}O, 0.34 for δ^{2}H). The correlation of δ^{2}H is hardly influenced by the different parameterizations described above ($r = 0.52$ for the parameterization after MJ79), whereas for δ^{18}O it is lower using the MJ79 parameterization ($r = 0.70$). A parameterization without any non-equilibrium processes (just equilibrium fractionation during water evaporation) leads to correlation coefficients of 0.44 and 0.47 for δ^{18}O and δ^{2}H, respectively. Figure 5.5 displays the model results obtained with the MJ79 and the new parameterization. For δ^{2}H, hardly any difference between

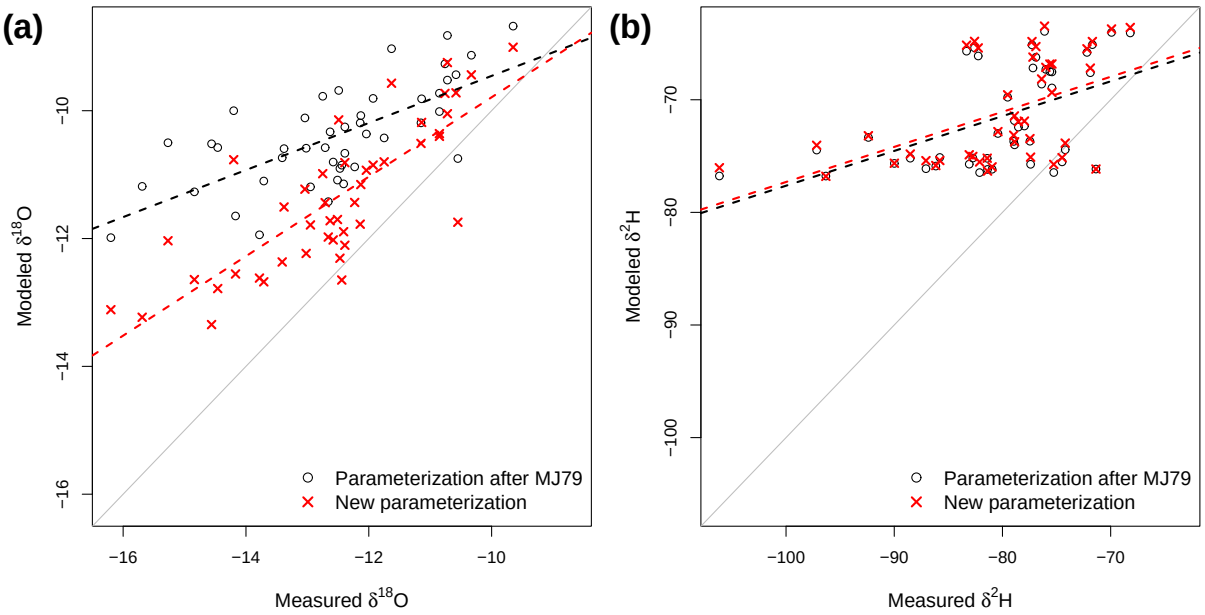

Figure 5.5. *Modeled δ^{18}O (a) and δ^{2}H (b), plotted against the corresponding measurements. Symbols are the same as in Fig. 5.4.*

the two parameterizations can be observed; the slope of the regression lines is 0.31 in both cases. For δ^{18}O, the slope of the regression line from the new parameterization (0.62) is considerably larger than from the MJ79 parameterization (0.37).

5.4 Discussion

In this section, the performance of the Lagrangian model and its different parameterizations for non-equilibrium fractionation effects is discussed in more detail, and the limitations of our modeling approach are outlined. Furthermore, the results are compared to simulations from an isotope enabled GCM, and the numerical estimate of the tuning parameter *m* obtained here is compared to data from other studies, in particular to isotope measurements from the Southern Ocean. Finally, the possibility of detecting a more subtle wind speed dependence of non-equilibrium fractionation with the help of the measurement data set used here is discussed.

5.4.1 General implications and limitations of the approach

As shown in section 5.3, a much better agreement between Lagrangian model results for *d*-excess and observations at Rehovot can be obtained using a wind speed independent parameterization of non-equilibrium fractionation during evaporation, compared to the parameterization given by MJ79 (see again Fig. 5.4 and Table 5.1). In particular, for wind velocities larger than

7 m/s, non-equilibrium fractionation is clearly underestimated with the MJ79 parameterization, leading to d-excess values that are too low. This underestimation is specifically relevant when measured d values become large, as shown by the slope of the black dashed regression line in Fig. 5.4. The new parameterization, in addition to improving the correlation coefficient and the RMSE, leads to a distinctly larger slope of the regression line for d_{mod} vs. d_{meas}. However, this slope is still lower than 1. When the days with the largest mismatches between modeled and measured d are removed from the linear regression (4 points with $|d_{\mathrm{mod}} - d_{\mathrm{meas}}| > 8$), there is further improvement of the regression line (dotted red line in Fig. 5.4, slope of 0.84), showing that the badly modeled days introduce a bias to the relationship. Noting that on these 4 days also the largest deviations from the diagnostic relationship between d and relative humidity occurred in chapter 4, it is possible that the respective mismatches result from limitations of the moisture source diagnostic and are not related to errors in the fractionation parameterization.

Based on the statistical evaluation performed above, using diffusion coefficients from *Cappa et al.* (2003) and $m = 0.24$ in equation (5.5) leads to the best model performance (new parameterization). In this case, $k_{\mathrm{H_2{}^{18}O}} = 0.9925$ and $k_{\mathrm{HDO}} = 0.9961$. Similar results can be obtained with diffusion coefficients from *Merlivat* (1978b) and $m = 0.28$. Then, $k_{\mathrm{H_2{}^{18}O}}$ is almost identical (0.9922) and $k_{\mathrm{HDO}} = 0.9931$ is a bit lower. However, this difference has very little effect on the model performance, because the simulated δ^2H values are almost insensitive to changes in the parameterization of non-equilibrium effects (see again Fig. 5.5b). The difference in the correlation coefficients of modeled and measured δ^2H between any type of Craig-Gordon model and a simple equilibrium fractionation model is small.

Surface cooling has almost no effect on the results of the fractionation model. This might be due to the fact that possible impacts are masked by the relatively large variability of relative humidity and thereby d-excess in the eastern Mediterranean or by additional variability induced by drawbacks of the moisture source diagnostic. However, the result that surface cooling effects can be neglected is in agreement with a GCM sensitivity experiment by *Schmidt et al.* (2005).

A limitation of our model approach is the fact that isotope fractionation during cloud formation is not taken into account. As the focus lies on the analysis of the Craig-Gordon model for water evaporation from the ocean, only those measurement days have been used for which the major moisture sources could be attributed without significant cloud and precipitation occurrence during humidity transport from the evaporation sources to Rehovot (see again chapter 4). Furthermore, our main conclusions have been based on the analysis of d-excess, which is less influenced by equilibrium fractionation in clouds than δ^2H and δ^{18}O. Nevertheless, when the model results of these isotope ratios are directly evaluated, the effects of cloud processes become obvious. Almost all of the measured δ^2H values are more depleted than the modeled ratios, and

the slope of the regression line in Fig. 5.5b is much smaller than 1. The same is true for δ^{18}O, but the deviations are less pronounced. This greater depletion may result from fractionation within small scale, convective clouds that are not resolved by the rather coarse ECMWF analyses and thus not detected along the trajectories that we use for the moisture source analysis. Another effect that is not properly accounted for is the turbulent small scale mixing of (usually more depleted) air from aloft into the air parcel. Finally, it is well possible that the part of the water vapor at Rehovot that is not traced back to its evaporation region by our source diagnostic (recall that this unaccounted part amounts up to 40%) is more depleted in δ^{2}H owing to the removal of heavy isotopes by cloud formation and precipitation. On the contrary, it is unlikely that the unaccounted moisture introduces a bias to the d-excess values that could be responsible for the underestimation of d by the MJ79 parameterization, because also the correlation coefficient, which should not be influenced by such a bias, is considerably improved with the new parameterization. Moreover, d-excess values in the unaccounted moisture would have to be unrealistically high in order to compensate this underestimation of d. One possible way to mitigate these difficulties owing to cloud processes (which are not resolved or not incorporated in the Lagrangian simulations) would be to test the fractionation parameterizations within a more complex model, e.g. a global or regional climate model that contains parameterizations for all these processes. This approach, though associated with other complexities, will be pursued in future research. It should, however, be noted that the Lagrangian method applied in this study, although limited with respect to the considered processes, provides a very direct way for evaluating the Craig-Gordon model with measurement data.

Another process that is not accounted for in the current model setup is the evaporation of sea spray, which constitutes an additional moisture flux from the ocean into the atmosphere that is not considered in the Craig-Gordon parameterization (e.g. *Gat et al.*, 2003). An assessment of the isotopic composition of this flux might be difficult, at least if the sea spray droplets do not completely evaporate. The contribution of sea spray to the total oceanic evaporation flux strongly depends on wind speed. Hence, we have calculated the 95% percentile of the distribution of wind speed at the moisture sources for each measurement day (velocities have again been weighted with the contribution of the corresponding moisture uptake to the humidity at Rehovot). All these percentiles are smaller than 15 m/s. Thus, the bulk of evaporation occurs at relatively low wind speeds, for which the contribution of sea spray is very small (see e.g. Fig. 1 in *Perrie et al.*, 2005). This estimation indicates that sea spray evaporation most probably does not have an impact on the general conclusions obtained in this study.

5.4.2 Comparison with GCM data and results from other studies

The d-excess from the IsoGSM model, interpolated to the location of Rehovot, can serve as a benchmark for the evaluation of the Lagrangian model. Table 5.1 shows that the performance of the GCM is comparable to the trajectory model with the MJ79 parameterization, but much worse than with the new parameterization. The problems of IsoGSM are also similar to those of the Lagrangian model with the MJ79 parameterization: high d-excess values are underestimated, leading to a slope of the regression line that is much too low. Of course, it is not totally fair to compare GCM data, which have a relatively low spatial resolution, with measurements at a single location. However, the fact that both IsoGSM and the MJ79 trajectory model have similar problems with high d-excess values might indicate that this issue is in both cases related to deficiencies in the parameterization of non-equilibrium fractionation, which is the same in both models. Another reason for the low correlation and high RMSE of the IsoGSM data may be its low spatial resolution that, for instance, hampers a proper representation of the large spatial humidity gradients occurring in the eastern Mediterranean coastal regions. The correlation coefficient between IsoGSM isotope ratios and measurements of δ^{18}O is lower than for the trajectory model with the new parameterization ($r = 0.71$, compared to $r = 0.81$), for δ^{2}H it is higher ($r = 0.67$, compared to $r = 0.51$). This shows once more that equilibrium fractionation during transport, which is parameterized by IsoGSM, but not by the trajectory model, is more important for δ^{2}H than for δ^{18}O.

The values of m obtained in this study are in the same order as those given by *Gat* (1996) for the eastern Mediterranean region: With $m \approx n\theta$ (see section 5.1) as well as $n = 0.5$ and $\theta = 0.5$, we get $m = 0.25$. The value of $n = 0.5$ given by *Gat* (1996) is based on theoretical considerations; θ was estimated by *Gat et al.* (1996) from the comparison of relative humidity from shipboard measurements with the humidity in advected continental air masses on seasonal time scales[3]. Considering the totally different data, method and time scale used in the study of *Gat et al.* (1996) and in this work, the agreement between the numerical estimates is surprisingly good.

In a recent field campaign, *Uemura et al.* (2008) measured isotope ratios in water vapor over the Southern Ocean. The authors showed that a large part of the variance of d-excess in their data ($r = 0.85$) can be explained with the help of a simple Craig-Gordon model similar to equation (5.2), applying a global closure assumption and using local temperature and humidity data from the measurement location (note that they calculated relative humidity with respect to local air temperature and not to SST, as done here). For the non-equilibrium fractionation factor k, *Uemura et al.* (2008) used values from *Araguás-Araguás et al.* (2000), independent of the

[3] In fact, these estimates from *Gat* (1996) are even somewhat lower than 0.5, being more consistent with the value of $m = 0.24$ obtained here with the *Cappa et al.* (2003) diffusion coefficients.

wind velocity. The high correlation obtained with this simple model shows that ocean surface conditions at the measurement locations did not differ much from the conditions in the actual evaporation regions of the sampled water, i.e. these conditions were relatively homogeneous over a larger area in the Southern Ocean (at least compared to the variability in the Mediterranean). Therefore, we do not think that an explicit calculation of vapor source regions with our diagnostic would lead to substantially larger correlation coefficients. Nevertheless, the measurements of *Uemura et al.* (2008) can be used to explore the parameter tuning of the new parameterization of the non-equilibrium fractionation factor with an independent data set (note that no wind velocities are reported by *Uemura et al.* (2008), so that the MJ79 parameterization cannot be tested with their data). Applying equations (5.2) (with h relative to SST, taken from local measurements reported in the paper, and $R_L = R_{\mathrm{VSMOW}}$) and (5.5) (with diffusion coefficients from *Cappa et al.*, 2003), we have calculated the optimal value of m for this independent measurements by minimizing the RMSE, as done for the Mediterranean data. The resultant value of $m = 0.22$ leads to a slightly improved correlation coefficient ($r = 0.87$), and a slope of the regression line of 0.91, that is much closer to 1 compared to the model of *Uemura et al.* (2008) (slope of 0.70; the relatively high value of this original slope compared to the MJ79 parameterization for the Mediterranean data results from the fact that *Uemura et al.* (2008) also use a wind speed independent formulation of k, as mentioned before). It should be noted here that this value of m might be biased by the global closure assumption, which neglects the advection of moisture from remote sources, as already pointed out by *Jouzel and Koster* (1996) and *Uemura et al.* (2008). Nevertheless, the proximity of the optimal values of this tuning parameter for the two data sets from very remote regions ($m = 0.24$ for the Mediterranean, $m = 0.22$ for the Southern Ocean) may indicate that the variability of the parameter on global scales is relatively small. However, this conclusion has to be validated with additional measurements and different models in the future.

5.4.3 Influence of wind velocity

We do not think that the non-equilibrium fractionation factor k in principle is independent of wind velocity. On the contrary, it depends on the ratio of diffusive over turbulent transport of water molecules from the ocean to the atmosphere, and there is clear physical reasoning that this ratio may depend on the turbulence regime and thus on wind speed. In order to find out if our method and the measurement data set from Rehovot allow to make an inference about the character of this wind dependence, the following, slightly more sophisticated experiment has been performed. The non-equilibrium fractionation factor k has been parameterized with equation (5.5), but the exponent m has been varied as a function of 10 meter wind speed. Four wind velocity bins have been defined ($u_{10\mathrm{m}} \leq 4\mathrm{m/s}$, $4\mathrm{m/s} < u_{10\mathrm{m}} \leq 7\mathrm{m/s}$, $7\mathrm{m/s} < u_{10\mathrm{m}} \leq 10\mathrm{m/s}$, $10\mathrm{m/s} < u_{10\mathrm{m}}$), and for each of these bins, various values of m have been used ($m \in \{0.12, 0.16, 0.18, 0.2, 0.22, 0.24, 0.26, 0.28\}$, corresponding to $(1 - k_{\mathrm{H_2{}^{18}O}}) \in$

$\{3.8, 5.0, 5.7, 6.3, 6.9, 7.5, 8.2, 8.8\}$ ‰, cf. Fig. 5.1). For every possible combination of these values, a Lagrangian model simulation has been performed (i.e. the model has been run with 4096 different configurations) and for each configuration the correlation coefficient and RMSE between modeled and measured *d*-excess have been calculated. The optimal configuration obtained with this experiment only leads to a very small improvement of the performance statistics compared to the new parameterization with constant $m = 0.24$. Setting $m = (0.24, 0.22, 0.26, 0.24)$ (for the four wind speed bins defined above), the correlation coefficient is 0.81 (compared to 0.80 for constant *m*) and the RMSE equals 4.55 (compared to 4.61). When assessing this small enhancement, it also has to be kept in mind that there is a larger number of degrees of freedom in the extended experiment. Figure 5.6 shows an example of the RMSEs obtained from several model runs as a function of the non-equilibrium fractionation factor for δ^{18}O in the third wind velocity bin (i.e. for $7\text{m/s} < u_{10\text{m}} \leq 10\text{m/s}$). For each value of $k_{H_2{}^{18}O}$, results are shown from the 5 simulations with lowest RMSE (varying the value of *m* in the three remaining bins). The Figure indicates that the best agreement between modeled and measured *d*-excess is obtained when $k_{H_2{}^{18}O}$ is a bit larger than the "new parameterization" value of $1 - k_{H_2{}^{18}O} = 7.5$‰, although the difference in the RMSEs is very small (as already mentioned before). This is the most significant and systematic effect that can be observed in the extended experiment (compared to the influence of *k* in other wind velocity bins). On the contrary, RMSEs are substantially larger for lower values of $1 - k_{H_2{}^{18}O}$. Hence, values of the non-equilibrium fractionation factor $1 - k_{H_2{}^{18}O}$ lower than 5‰ for wind velocity between 7 and 10 m/s, as used in the MJ79 parameterization (see again Fig. 5.1), lead to a degradation of the model performance, no matter how the values of *k* are chosen for smaller or larger velocities.

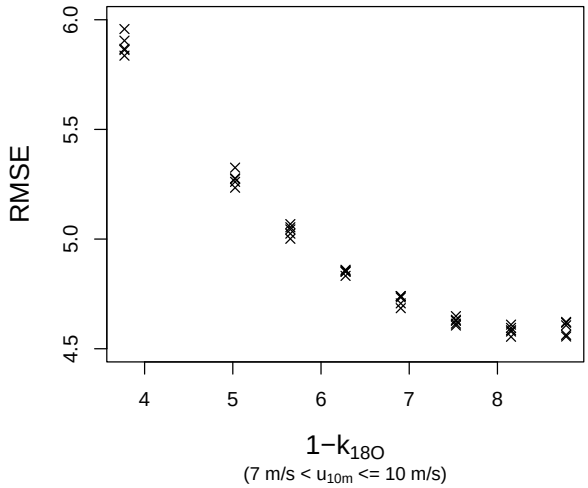

Figure 5.6. *Root mean square errors of several Lagrangian model simulations with varying settings of m (in 4 different wind bins), shown as a function of the non-equilibrium fractionation factor $k_{H_2{}^{18}O}$ in the third velocity bin (see text for details). For each value of $k_{H_2{}^{18}O}$, results are shown from the 5 model runs with lowest RMSE.*

Altogether, this series of numerical experiments shows that the agreement between Lagrangian model results and measurements of d-excess cannot be significantly improved by incorporating a possible wind speed dependence of the non-equilibrium fractionation factor in the parameterization. Thus, this wind dependence either is relatively small (at least in the wind velocity range considered here, i.e. for $u_{10\mathrm{m}}$ primarily smaller than 15 m/s), or it cannot be detected with our diagnostic owing to some more fundamental complexity. For instance, the number of observations might be too small, there might be too many constraints due to the requirements of the moisture source analysis, the uncertainty related to this analysis might be too large or the influence of wind velocity might be masked by the accumulation of moisture from multiple sources on each measurement day.

In future research, two main issues will have to be addressed in order to establish an appropriate description of the dependence of the non-equilibrium fractionation factor k on wind velocity (or, alternatively, to show in a more definite way that this dependence is negligible). First, more measurements of isotope ratios in atmospheric water vapor should be made available that allow to test newly developed parameterizations of k. As isotope ratios in the evaporation flux cannot be measured directly, complex models, which include processes like the advection of water vapor (e.g. GCMs or the Lagrangian approach used here) have to be applied to compare theoretical predictions from a Craig-Gordon model with measurements. Second, more recent parameterizations of water evaporation from the ocean (see e.g. *Fairall et al.*, 2003) might provide the theoretical basis for the description of k. These parameterizations have the advantage that they are grounded on measurement data in a much stronger way than the mostly theoretical Brutsaert model applied by MJ79. However, they usually do not contain an explicit formulation of molecular diffusion, but subsume the properties of the diffusive surface layer in a parameter called moisture roughness length, which is then parameterized with an empirical equation. Basically, the moisture roughness length can also be expressed in terms of a diffusion coefficient or Schmidt number (and thus calculated for the different water isotopes) (cf. *Liu et al.*, 1979; *Brutsaert*, 1982). But, owing to its empirical formulation, it is not straightforward to employ these more recent parameterizations of evaporation for the deduction of the isotope fractionation factor. In our opinion, this issue will have to be addressed with the help of a comprehensive experimental (e.g. wind tunnel) study analyzing the dependence of the moisture roughness length on the Schmidt number, extending the work of *Merlivat* (1978a).

5.5 Conclusions

In this chapter, isotope ratios in water vapor at Rehovot (Israel) have been modeled with the help of a trajectory approach and different types of Craig-Gordon like parameterizations of isotope fractionation during water evaporation from the ocean. The performance of the model depends

critically on the form of the non-equilibrium fractionation factor. With the classical parameterization of MJ79, which is commonly used in GCMs, the agreement with observations has been substantially worse than with a wind speed independent formulation. The latter has led to a correlation coefficient of 0.8 between modeled and measured values of deuterium excess. Optimal results have been obtained using the following values for the non-equilibrium fractionation factors:

$$\begin{aligned} k_{\mathrm{H_2{}^{18}O}} &= 0.9925, \\ k_{\mathrm{HDO}} &= 0.9961. \end{aligned}$$

Here, the uncertainty for k_{HDO} is larger than for $k_{\mathrm{H_2{}^{18}O}}$. However, this larger uncertainty is not really serious, because non-equilibrium effects play only a minor role in the determination of δ^2H. Altogether, the success of the Lagrangian model corroborates that the physics of isotope fractionation during evaporation are properly described by a linear resistance model, as introduced by *Craig and Gordon* (1965). Limitations of our approach are, in addition to uncertainties in the fractionation parameterization, related to the neglect of cloud processes and sea spray evaporation, the precision of the trajectory calculation and the spatial resolution of the analysis data, as also described in chapter 4.

The methodology introduced in this chapter may be used to obtain the initial conditions for Rayleigh-type isotope fractionation models, calculated along air parcel trajectories, in a more explicit way than in previous studies (cf. *Helsen et al.*, 2007; *Sodemann et al.*, 2008a). Moreover, the new parameterization of the non-equilibrium fractionation factor k may also be applied in other models, in particular GCMs, instead of the formulation of MJ79. In future research, it should be tested with the help of sensitivity experiments if this new parameterization leads to an improvement of GCM modeled isotope fields, particularly deuterium excess, for which the performance of current GCMs is not optimal (see again *Werner et al.*, 2001; *Jouzel et al.*, 2007; *Uemura et al.*, 2008).

Chapter 6

Water Isotopes in the COSMO Model

6.1 Introduction

6.1.1 Motivation

The isotopic composition of atmospheric waters is determined by a variety of dynamical and microphysical processes like moisture transport, evaporation from ocean and land, cloud formation and many more. In order to comprehensively describe these processes and the non-linear interactions between them, complex numerical models have to be applied. To this end, a popular choice has been to use global circulation models equipped with the physics of stable water isotopes (e.g. *Joussaume et al.*, 1984; *Hoffmann et al.*, 1998; *Noone and Simmonds*, 2002; *Lee et al.*, 2007). Many different studies have been performed with these GCMs up to date, primarily focusing on climatological and paleoclimatological applications. In principle, GCMs can also be used on shorter, synoptic time scales, and the potential in applying these models for more process-oriented studies has recently been recognized (*Schmidt et al.*, 2005). However, such approaches are constrained by the limited spatial resolution of the global models and the simplicity of some of their physical parameterizations (e.g. considering cloud microphysics) and numerics (e.g. with respect to tracer advection). These difficulties can be moderated by using regional climate or weather forecast models, which can be run with higher spatial resolutions. Currently, there is one regional climate model capable of simulating isotope physics, the REMO_{iso} (*Sturm et al.*, 2005), which so far has been utilized for long-term, climatological simulations (*Sturm et al.*, 2007a,b).

In this work, the first steps of an implementation of stable water isotope physics in the COSMO model are performed. The COSMO model (*Steppeler et al.*, 2003) is the operational limited-area weather prediction model of, e.g., the German Weather Service DWD and can also be used for regional climate simulations (*Jacob et al.*, 2007). Compared to the REMO, which is based on

an older weather prediction model of the DWD, the COSMO has several advantages: First, it is non-hydrostatic and thus allows simulations with very high resolutions down to 1 km (compared to the maximum resolution of REMO that is limited to approximately 15 km due to the hydrostatic approximation). Simulations with a resolution of 1-3 km are able to explicitly represent the dynamics of high cumulus convection. Second, the COSMO model contains a positive definite, mass conserving and more accurate advection scheme (see section 6.2.2) and more sophisticated parameterizations of land surface processes, atmospheric turbulence (section 6.2.3) and cloud microphysics (section 6.2.5). Technical details of the COSMO model and its utilization are given by *Doms and Schättler* (2002), *Doms et al.* (2005), *Schättler et al.* (2008) and references therein.

The main goal of the development of a new limited-area dynamical water isotope model, named $COSMO_{iso}$ is to provide a tool that allows the simulation and interpretation of the variability of isotopes in atmospheric waters on short, synoptic time scales. With the help of this model, it should be possible to quantify the various processes that contribute to this variability and to improve our physical understanding of these processes, for instance with the help of sensitivity experiments and by directly comparing model results to measurements on short time scales. The Rehovot data set of isotopes in water vapor that is used in chapters 4 and 5 illustrates this variability, which is not well captured in isotope GCMs (see chapter 5 and *Angert et al.*, 2008). Once $COSMO_{iso}$ will be completed, it will also be possible to simulate the isotope signal in precipitation produced by particular weather systems, e.g. extratropical cyclones (e.g. *Rindsberger et al.*, 1990; *Gedzelman and Lawrence*, 1990; *Coplen et al.*, 2008) and mesoscale convective systems (*Rao et al.*, 2008), and to explore the relationship between the isotope variability and the dynamics of these systems. Such studies to date have only been done with dynamically relatively simple Rayleigh-type (e.g. *Smith*, 1992) or two-dimensional bulk cloud microphysical models (*Gedzelman and Arnold*, 1994). They can hardly be performed with a GCM, which represents the structure and dynamics of weather systems with limited accuracy because of the coarse spatial resolution.

6.1.2 Implementation approach

In general, $REMO_{iso}$ and all isotope GCMs to date have been used for climate simulations. Therefore, their results can be compared with measured isotope data only on a statistical basis, but not with respect to distinct synoptic events and historic variability (the historical isotope simulation by *Yoshimura et al.* (2008), which has also been used in chapter 5, is an exception). However, in order to improve our process understanding of isotope physics, it is essential to directly compare modeled and measured isotope ratios on an hourly or daily basis and to evaluate the simulation of the isotope signal from specific weather systems with measurement data.

Therefore, the new $COSMO_{iso}$ (at least in its development phase) shall not be used in "climate", but in "weather forecast" mode. That is, only a few consecutive days are simulated within one model run, and meteorological analyses are used for the model initialization and as boundary data. In this way, the simulated meteorology is never far from reality. On the other hand, simulating stable water isotopes in forecast mode leads to some difficulties regarding the initial and boundary data for these isotopes: There is no isotope analysis available to date, and the only historical isotope simulation (*Yoshimura et al.*, 2008) for several reasons cannot be used to drive the COSMO model directly. First, it is only available on a very coarse grid, and an indirect application of the isotope ratios from this simulation together with other meteorological variables from ECMWF analyses would lead to large inconsistencies (because water vapor fields from both data sets are not consistent, for example). Second, the accuracy of the isotope fields from the historical simulation is limited, in particular regarding water vapor, the most important initial and boundary field for the isotopes (see chapter 5 and *Uemura et al.*, 2008, for example). If these fields were used, it would be very hard to distinguish if deficiencies in the performance of $COSMO_{iso}$ were related to shortcomings in its own model physics or in the initial and boundary data. The last point illustrates that, if one wants to evaluate the performance of a regional isotope model, one has to make sure that the crucial physical processes are simulated within the model domain and that the simulated isotope signal is not diluted by boundary data from global models, whose quality cannot easily be controlled.

In order to address these difficulties, a novel approach is introduced in this study: the implementation of isotope physics in the COSMO model is combined with an explicit water tagging. Such tagging methods have been used in GCMs to quantify the contribution of different predefined moisture source regions to the precipitation in a given target area (e.g. *Joussaume et al.*, 1986; *Koster et al.*, 1986; *Delaygue et al.*, 2000; *Werner et al.*, 2001). Recently, the same approach has been applied in the regional climate model CHRM (*Sodemann*, 2006; *Sodemann et al.*, 2009). In the COSMO model, we tag water that evaporates from the ocean. Concurrently, the isotopic composition of the evaporate can be determined using a Craig-Gordon parameterization (see chapter 5 and *Craig and Gordon*, 1965). Afterwards, the respective water (tagged H_2O as well as $H_2{}^{18}O$ and HDO) is traced through the model water cycle. In this way, it is possible to determine the fraction of tagged water (i.e. water that has evaporated from the ocean during the simulation) and the isotopic composition of this water at every grid point and model time step. At the beginning of the model run, this fraction of tagged water is zero; during the simulation it grows to a hopefully substantial magnitude, at least at the location where isotope ratios are supposed to be interpreted or compared with measurements. Using this method, the problem of defining initial and boundary data for the water isotopes can be avoided (these are set to zero), and it is assured that all physics that determine the modeled isotope ratios are simulated by $COSMO_{iso}$. The fraction of tagged water allows to quantify the relative amount of water for which the regional isotope model results are meaningful.

In this study, isotope fractionation is parameterized only at the ocean surface. For all other phase transitions, the heavy water isotopes are treated in the same way as normal water (i.e. without fractionation). This can be seen as a starting point, other isotope effects will be incorporated in the model in future work. Nevertheless, on days with little clouds and rain in the Mediterranean region, isotope ratios modeled by this preliminary version of $COSMO_{iso}$ can be compared to the Rehovot data set of isotopes in water vapor (see chapter 4). This procedure has the advantage that there is an optimal comparability between $COSMO_{iso}$ and the trajectory model introduced in chapter 5. Furthermore, the first step in the model water cycle, evaporation from the sea, can be best explored, without being masked by further fractionation effects.

In the next section, some technical details of the implementation of water tagging in the COSMO model are given. There is no specific focus on stable isotopes in this section, because the tagging approach is independent of isotope physics; all isotopes are traced through the model water cycle in the same way (at least in this first implementation step). The following section describes the parameterization of isotope fractionation during evaporation from the ocean. Subsequently, in section 6.4 results are presented from several case studies with the new model. Finally, the last section of this chapter contains some concluding comments and an outlook on the further development of $COSMO_{iso}$.

6.2 Water tagging

6.2.1 General aspects of the COSMO model and the tagging implementation

The basis for the water tagging implementation is version 4.2 of the COSMO model. There are many different configurations of this model, and the user can chose between these configurations with the help of namelist parameters that have to be provided as model input. The tagging implementation and the development of $COSMO_{iso}$ has been based on and only tested for one specific configuration. Technically, this means that several namelist switches controlling the model numerics are fixed when $COSMO_{iso}$ is used. Only this specific configuration is described in the following.

The COSMO model is a limited-area numerical weather forecast and climate model, based on the primitive thermo-hydrodynamical equations describing the flow of moist air in the earth's atmosphere (*Doms and Schättler*, 2002). These equations are formulated on a regular longitude-latitude grid, which is rotated in order to place the model area close to the equator and to avoid the convergence of coordinate lines at the poles. In the vertical, a general terrain following coordinate is applied. For the time integration of the equations of motion, a two time level, second

order, time-splitting Runge-Kutta scheme (*Wicker and Skamarock*, 1998) is used in the present model setup; second order finite differences and staggering on an Arakawa C-grid are used for the spatial discretization. In the COSMO setup applied here, the following prognostic model variables are employed: horizontal and vertical wind components, pressure perturbation (from a predefined base state, representing a dry, stratified atmosphere), temperature, specific humidity of water vapor, cloud liquid content, cloud ice content, specific water content of rain and snow (see also section 6.2.5). Many physical processes are represented in the model by different parameterization schemes, e.g. sub-grid scale turbulence, surface layer fluxes, cloud microphysics, moist convection, radiation and soil processes (*Doms et al.*, 2005). One important assumption that is generally applied during the numerical solution of the COSMO model equations is that these equations can be split into different terms, which are successively solved within one model time step. For instance, for the different water species the advection equation is solved before the tendencies due to cloud microphysical processes are calculated (the latter based on the new model variables, updated due to advection). This procedure, called Marchuk splitting method, is also reflected in this document, where all processes affecting water tagging are described separately in the following subsections (and not in terms of a single equation of motion). Some details of the numerics and parameterizations of these processes that are important for the tagging implementation are outlined there.

In many aspects, the implementation of water tagging in the COSMO model performed in this study follows the work of *Sodemann* (2006). A parallel tagged water cycle has been introduced in the model, without any feedback on or change to the normal model behavior, that is as a purely diagnostic tool. For this parallel water cycle, all processes that modify the atmospheric water content have to be taken into account. For example, if clouds are formed during a simulation, this process has to be mimicked for the tagged water in the parallel cycle. On the other hand, no changes are required in the radiation scheme, which is influenced by atmospheric moisture (e.g. acting as greenhouse gas or through cloud cover), but does not directly feed back on water content. In contrast to the work of *Sodemann* (2006), who has focused on different tracer initialization (i.e. tagging of water in different regions), here the only source for the secondary water cycle is evaporation from the ocean, as mentioned above. Since the land surface parameterization scheme has not yet been included in the tagging approach in this study[1], tagged water is lost when it is removed from the atmosphere by rain or snow reaching the surface; thus, precipitation is the only sink for the secondary water cycle.

Several additional variables have been added to the COSMO model. For each prognostic water field (vapor, cloud water, cloud ice, rain and snow; also called “total” water in the following),

[1]Reasons for this are, among other things, that the parameterization of isotope fractionation, e.g. during evapotranspiration, and the rather long renewal time scale of soil moisture pose additional problems, which need to be addressed later.

a new prognostic tagged field has been introduced with the same unit as the original variable, i.e. as specific water content. Moreover, some new diagnostic variables have been added (cf. section 6.2.7). For in- and output of these variables in GRIB format, a new GRIB table (with GRIB table number 206) has been defined. A complete description of this table and the new variables is given in appendix B. In order to control the simulation of tagged (and isotope) water fields, a main control switch (called liso) and an additional namelist is used, details are also given in appendix B.

For the simulations presented in this study, the COSMO model has been run with a spatial resolution of 7 km in the horizontal and 40 vertical layers. Operational analyses from the ECMWF have been used as initial and boundary data. Because the model results are compared with measurements from Rehovot, a model area that comprises the eastern Mediterranean sea and the surrounding countries has been chosen, as shown in Figure 6.1.

6.2.2 Tracer advection

For any water quantity, represented by its specific humidity q_x (where $x \in \{v, c, i, r, s\}$, and v stands for water vapor, c for cloud water, i for cloud ice, r for rain and s for snow), the advective

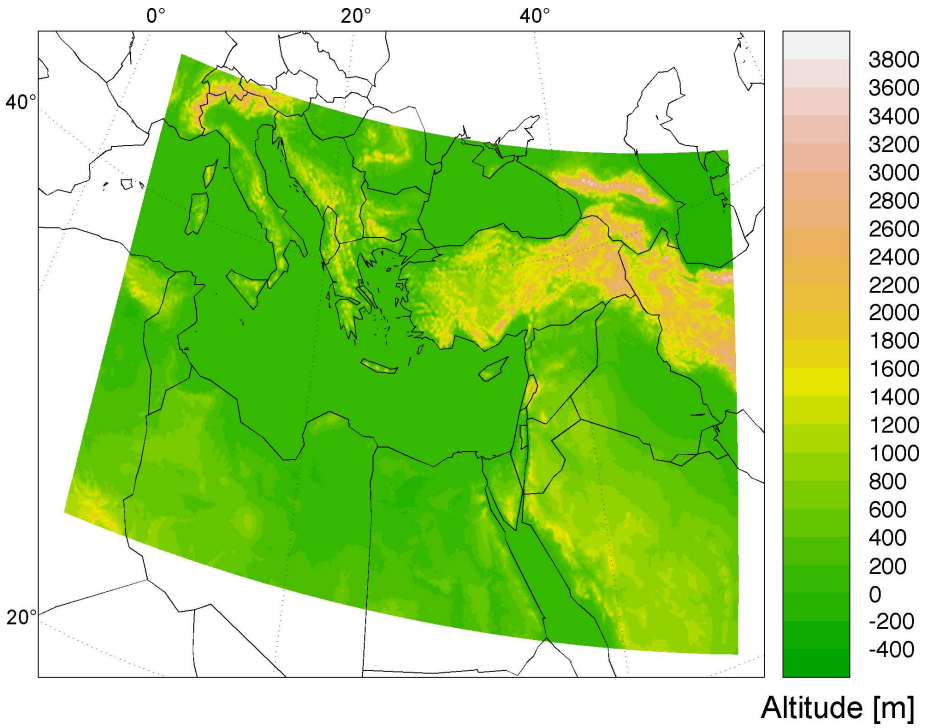

Figure 6.1. COSMO *model area and topography (colors) used in this study.*

transport equation in a flow field defined by the wind velocity $\vec{u}$ can be written in flux form[2]:

$$\left(\frac{\partial(\rho q_x)}{\partial t}\right)_{\text{adv}} = -\nabla\cdot(\vec{u}\rho q_x)\,, \tag{6.1}$$

where t denotes time, ρ is the total density of the air mixture and ∇ denotes the three-dimensional gradient operator (which has to be expressed in the specific coordinate system of the model). In the present setup of the COSMO model, the solution of equation (6.1) is based on the numerical scheme introduced by *Bott* (1989). Within this scheme, water fluxes (i.e. the right hand side of equation (6.1)) are estimated by fitting polynomials to the field ρq_x. Here, we use polynomials of fourth order, thus the algorithm is called "4th order Bott scheme". Afterwards, the fluxes are normalized and limited by upper and lower bounds. The resulting advection equation is solved using a simple forward Euler step in time. This Bott scheme, due to its flux limitation, is positive definite and conserves water mass. Moreover, it generates less numerical diffusion compared e.g. to a simple upstream scheme, and using 4th order polynomials makes it rather accurate. Note, however, that the scheme is not monotone, that is there might occur over- and undershoots of the transported field. A monotone version is principally available (*Bott*, 1992), but has not yet been implemented in the COSMO model.

The transport equation of a tagged water field is obtained by replacing q_x in equation (6.1) with the tagged specific humidity q_x^t. Hence, exactly the same numerical routine as for total humidity can be applied for the advective transport of tagged water. This routine requires a three dimensional moisture field as input and provides the transformed field after advection over one time step as output.

In the CHRM model, which has been used for water tagging simulations by *Sodemann* (2006), humidity fields are advected with a simple Leapfrog algorithm that is not positive definite and does not conserve mass. These deficiencies have led to large problems with the transport of tagged water, which often exhibits large spatial gradients and for which mass conservation is an essential feature. Therefore, *Sodemann* (2006) decided not to use this Leapfrog algorithm, but the more appropriate MPDATA scheme (*Smolarkiewicz and Grabowski*, 1990; *Smolarkiewicz and Margolin*, 1998) for the advection of tagged humidity fields. This approach, on the other hand, leads to inconsistencies between the transport of total and tagged humidity[3]. The COSMO model has the advantage that the Bott scheme has similar characteristics as MPDATA with regard to positivity and mass conservation. Hence, total and tagged water can be transported with the

[2]Recall that, due to Marchuk splitting, in the model this equation is solved independently from other source and sink terms.

[3]Such inconsistencies also occur if the same scheme is used for total and tagged water and if the numerical characteristics of the scheme are scale-dependent (as it is usually the case), since typically the spectra of the two fields differ.

same numerical scheme, reducing inconsistencies compared to the CHRM. The benefit of this fact in terms of the total mass conservation of the tagged fields will be further explored in section 6.2.8.

6.2.3 Turbulent transport and evaporation from the ocean

The tendency of any non-sedimenting humidity field q_x due to sub-grid scale turbulent transport is given by the divergence of its turbulent flux $\vec{F}_x$ (for rain and snow, turbulent transport is neglected in the COSMO model):

$$\rho \left(\frac{\partial q_x}{\partial t} \right)_{\text{tur}} = -\nabla \cdot \vec{F}_x.$$

When Reynolds decomposition is used (that is the decomposition of q_x in a temporal average value $\overline{q}_x$ and a rapidly varying part q'_x, $q_x = \overline{q}_x + q'_x$), each spatial component of $\vec{F}_x$ can be expressed as covariance of $\rho q'_x$ and the turbulent wind velocity in the corresponding direction, e.g.

$$F_{x,3} = \overline{\rho q'_x w'},$$

where w denotes vertical wind velocity. However, since the rapidly varying components of the model variables cannot be easily determined, K-theory is used in the COSMO model to parameterize $\vec{F}_x$ in terms of the prognostic humidity fields (which are in fact the slowly varying components $\overline{q}_x$, but the over-bar is usually omitted). In addition, horizontal turbulent transport is neglected in the current model setup (in principle, it is implemented in the COSMO model for total moisture and might be enabled for tagged/isotope fields in future studies). Altogether, this leads to the following tendency equation:

$$\left(\frac{\partial q_x}{\partial t} \right)_{\text{tur}} = \frac{1}{\rho} \frac{\partial}{\partial z} \left(\rho K_h^v \frac{\partial q_x}{\partial z} \right). \tag{6.2}$$

Here, for simplicity this equation is formulated with the geometrical height z as vertical coordinate, instead of the generalized terrain-following coordinate used in the model. Equation (6.2) has the form of a diffusion equation for the humidity field q_x. The mixing coefficient K_h^v, which corresponds to a classical diffusion coefficient, is calculated in the turbulence parameterization routine of the COSMO model (see again *Doms et al.*, 2005), in the current setup applying a prognostic scheme based on turbulent kinetic energy (TKE). It is the same for moisture and heat transport. In order to retain some numerical smoothing in the vertical also in cases with very little atmospheric turbulence, a lower limit for K_h^v is introduced. In the horizontal, no numerical smoothing of humidity fields is explicitely performed, but the Bott advection scheme introduces some implicit numerical diffusion.

The lower boundary condition of equation (6.2) is given by the surface moisture flux. This surface flux is set to zero for liquid water and ice. For water vapor, in our setup it is determined

based on the principles of Monin-Obukhov similarity theory and applying an algorithm according to *Louis* (1979). This algorithm uses the following parametric equation, which is formally very similar to a discretized form of the parameterization of the atmospheric fluxes with the help of K-theory (cf. equation (6.2)):

$$F_{v,3}^{\mathrm{sfc}} = -\rho C_h^d |\vec{v}| \left(q_v - q_v^{\mathrm{sfc}} \right). \tag{6.3}$$

Here, $F_{v,3}^{\mathrm{sfc}}$ denotes the vertical water vapor flux at the earth's surface, $\vec{v}$ is the horizontal wind velocity on the lowest model level, q_v denotes the specific humidity of vapor on the same level and q_v^{sfc} the humidity at the surface. This surface humidity is determined by the soil model over land, over the ocean it is calculated as the saturation specific humidity at the pre-described sea surface temperature. The bulk transfer coefficient C_h^d, which is again the same as for heat transfer, is calculated within the surface layer parameterization scheme of the COSMO model with the help of a diagnostic TKE-based algorithm.

Second-order accurate finite differences are applied for the spatial discretization of equation (6.2) in the vertical. The time integration of the equation (with equation. (6.3) as lower boundary condition) is performed with the help of an implicit Crank-Nicolson scheme, because this guarantees numerical stability. This scheme requires the solution of a linear tridiagonal equation system for each vertical column of the model domain, for which an algorithm based on Gaussian elimination (also called Thomas algorithm) is used. Within this numerical integration step, also the tendencies due to sub-grid scale clouds and cumulus convection (which have been calculated in other subroutines of the model, following the Marchuk splitting method; see also further below and section 6.2.6) are added to the water vapor and cloud water fields.

For the tagged humidity fields, turbulent transport is parameterized by replacing q_x in equation (6.2) with q_x^t (again, this equation is only applied to tagged vapor, cloud water and cloud ice). Hence, the same mixing coefficients as for total water are used, but the net flux is proportional to the gradient of the tagged field. In this way, the turbulent fluxes of total and tagged water are decoupled with respect to their direction. That is, if the vertical gradients of total and tagged water have opposite signs, total and tagged moisture are effectively transported in opposite directions. This decoupling contrasts the situation for advective transport, for which the wind velocity prescribes the direction of the flux. As lower boundary condition, the surface fluxes of tagged liquid water and ice are set to zero (as for total liquid water and ice). For water vapor, land and ocean points are distinguished: Over land, the surface flux of q_v^t also equals zero, because the land surface scheme has not yet been implemented in our tagging approach, as mentioned above. Over the ocean, equation (6.3) is applied to parameterize the tagged surface flux, with q_v replaced by q_v^t and setting $q_v^{\mathrm{sfc},t} = q_v^{\mathrm{sfc}}$. In this way the ocean is treated as a reservoir of tagged water, and evaporation from the ocean becomes the only source for the parallel tagged water cycle. Numerically, equation (6.2) can be solved analogously for tagged as for total water, with

lower boundary conditions adjusted as described above.

Since the numerical scheme used to parameterize turbulent transport in the COSMO model is not positive definite, occasionally negative humidity values occur after its application. These negative values are not just set to zero, because this would increase the total water mass in the model. Rather, they are filled with moisture from neighboring grid points below. The artificial, unphysical water transport introduced by this procedure (which is called mass flux correction in the following) is supposed to be more tolerable than a violation of mass conservation. For tagged water, the mass flux correction has also been implemented and can be selected with the help of a namelist switch. Its influence on the tagged mass budget is explored in section 6.2.8. It should be noted here that this mass flux correction in fact eliminates the mass budget changes induced by the non-positivity of the turbulence scheme, but that this scheme might still violate mass conservation due to other numerical drawbacks.

In the turbulence parameterization scheme of the COSMO model, in addition to the determination of the turbulent mixing coefficients K_h^v, the influence of sub-grid scale clouds on turbulent transport is evaluated. The modifications of q_v and q_c owing to these clouds are used to calculate adjusted vertical gradients of the moisture fields. These adjustments are translated into residual transport terms, and the corresponding humidity tendencies are calculated. The adjustment procedure has also been mimicked for tagged vapor and cloud water and can be selected via a namelist switch (two alternative schemes have been implemented). However, since its effect on the overall evolution of the tagged humidity fields is small, details of the rather technical description of this procedure are postponed to appendix C. It should just be noted here that the influence on turbulent transport is the only way in which sub-grid scale clouds influence the model's water cycle (besides, they affect the radiation scheme and are used for diagnostic purposes).

6.2.4 Boundary relaxation and Rayleigh damping

At the lateral boundaries of the model domain, the COSMO humidity variables (in the current setup except for rain and snow) are specified by an external data set. In order to avoid numerical problems at the boundaries, which occur e.g. due to the different resolutions of the data and to the reflection of waves at the boundaries, the information from the external data is not just applied at the outmost grid points, but in a relaxation zone covering several grid points. Therefore, a boundary relaxation scheme is used, similar to that introduced by *Davies* (1976). Within the relaxation zone, the following additional forcing is introduced:

$$\left(\frac{\partial q_x}{\partial t}\right)_{\text{bound}} = -\mu_b \left(q_x - q_x^{\text{bound}}\right). \tag{6.4}$$

Here, q_x^{bound} is the boundary field from the external data set, and μ_b denotes a relaxation coefficient, which declines exponentially from the boundary into the model domain. In our model setup, the width of the relaxation zone where equation (6.4) is applied can explicitely be chosen and is set to 50 km. That is, with a spatial resolution of 7 km the boundary relaxation zone covers 8 grid points at each lateral boundary. Equation (6.4) is numerically solved with the help of a forward time step at every grid point within this zone (to which the external data have been interpolated with the help of a preprocessing tool, cf. *Schättler* (2008)).

For the tagged moisture fields, no boundary data are available (cf. section 6.1.2), i.e. $q_x^{t,\text{bound}} = 0$. Thus, equation (6.4) can be simplified to

$$\left(\frac{\partial q_x^t}{\partial t}\right)_{\text{bound}} = -\mu_b q_x^t, \tag{6.5}$$

where the same relaxation factor as for total water is used. In order to consistently treat precipitation (for which also no boundary information can be obtained), equation (6.5) is applied to all tagged humidity fields. Numerically, the equation is solved in the same way as equation (6.4).

In order to prevent wave reflection at the upper boundary of the domain, a damping of the model variables similar to equation (6.4) (called Rayleigh damping) is performed at the uppermost COSMO model layers. In the current setup, all layers above an altitude of 11,000 km are affected by this damping. Since the damping is applied to all non-precipitating moisture fields, it has consistently been introduced for the corresponding tagged fields. An equation similar to (6.5) with μ_b replaced by the Rayleigh coefficient μ_R (cf. *Doms and Schättler*, 2002) is used on the uppermost model layers and solved numerically with the help of an implicit time integration scheme, as for the total humidity fields.

6.2.5 Cloud microphysics

The formation of grid scale clouds and precipitation is characterized by transfer of water mass between the different moisture categories (vapor *v*, cloud water *c* and ice *i*, rain *r* and snow *s*) of the COSMO model. Therefore, several transfer rates S_{xy} between the categories *x* and *y* are parameterized in the model, as shown for the current setup (two-category ice scheme with prognostic precipitation) in Figure 6.2 and summarized in Table 6.1.

Since cloud water and water vapor in warm clouds can be assumed to be in thermodynamic equilibrium, the transfer rate S_{vc}^{c} is determined using a saturation adjustment technique. Therefore, each model grid box is checked for supersaturation with respect to liquid water and subsaturation in the presence of cloud water. If the former occurs, cloud water is formed until saturation is reached. In the case of the latter, cloud water is evaporated until either saturation is attained or no liquid water is left. In both cases, the latent cooling or heating of evaporation or conden-

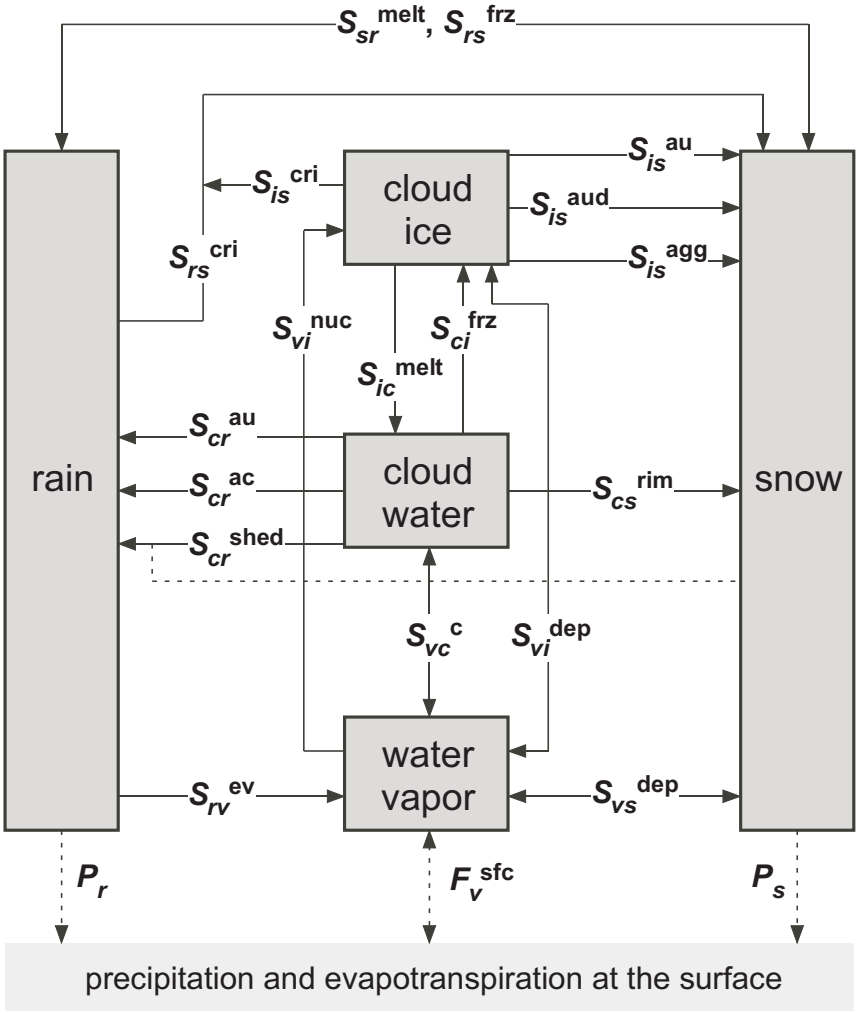

Figure 6.2. *Humidity categories and transfer rates parameterized in the cloud microphysics scheme of the* COSMO *model (adapted from Doms et al., 2005). P_r and P_s denote the precipitation rates of rain and snow at the surface, F_v^{sfc} the evapotranspiration rate. All other transfer rates are explained in Table 6.1.*

sation, respectively, is taken into account (this requires the numerical solution of a transcendent equation with the Newton iteration method). This saturation adjustment is performed several times within one model time step, and q_v and q_c are directly updated in order to make sure that thermodynamic equilibrium with respect to liquid clouds is sustained during the simulation of all atmospheric processes.

For all other transfer rates, no equilibrium assumption can be made. Their parameterization is based on a one-moment bulk water-continuity model, using the specific humidities q_x as dependent variables at each grid point (see again *Doms et al.*, 2005, for details). This parameterization scheme is called once at the end of each model time step. When all transfer rates have been

S_{vc}^{c}	condensation and evaporation of cloud water
S_{cr}^{au}	autoconversion of cloud water to rain
S_{cr}^{ac}	accretion of cloud water by rain drops
S_{rv}^{ev}	evaporation of rain
S_{vi}^{nuc}	heterogeneous nucleation of cloud ice
S_{ci}^{frz}	homogeneous freezing of cloud water
S_{vi}^{dep}	deposition growth and sublimation of ice
S_{ic}^{melt}	melting of cloud ice
S_{is}^{au}	autoconversion of cloud ice to snow (aggregation)
S_{is}^{aud}	autoconversion of cloud ice to snow (deposition)
S_{is}^{agg}	collection of cloud ice by snow (aggregation)
S_{cs}^{rim}	collection of cloud water by snow (riming)
S_{cr}^{shed}	collection of cloud water by wet snow to form rain (shedding)
S_{is}^{cri}	collection of cloud ice by rain to form snow
S_{rs}^{cri}	freezing of rain due to collection of cloud ice
S_{rs}^{frz}	freezing of rain due to heterogeneous nucleation
S_{vs}^{dep}	deposition growth and sublimation of snow
S_{sr}^{melt}	melting of snow

Table 6.1. *Transfer rates between humidity categories parameterized in the cloud microphysics scheme of the* COSMO *model (adapted from Doms et al., 2005).*

specified, the moisture fields are updated according to the following equation:

$$\left(\frac{\partial q_x}{\partial t}\right)_{\text{cloud}} = \begin{cases} \sum_y S_{xy} & , \quad x \in \{v,c,i\} \\ \sum_y S_{xy} + \frac{1}{\rho}\frac{\partial}{\partial z}\left(\rho q_x v_x^{\text{sed}}\right), & x \in \{r,s\}\,. \end{cases} \tag{6.6}$$

Here, a distinction is made between non-precipitating and precipitating humidity categories. For the latter, v_x^{sed} denotes the sedimentation velocity. The time integration of equation (6.6) is based on a simple forward step for vapor, cloud water and ice. For rain and snow, a quasi-implicit, mass conserving Crank-Nicolson scheme is used. Thereby, the equation can be integrated from the top to the bottom of each vertical column of the model domain. The transfer rates S_{xy} are included with the help of a predictor-corrector method. From this integration, also the grid scale precipitation fluxes of rain and snow at the surface are obtained.

The parameterization of tagged mass transfer due to cloud processes mimics the mass transfer of the total humidity fields. For each transfer rate S_{xy}, the donator category x is determined, and the tagged transfer rate is calculated from

$$S_{xy}^{t} = \frac{q_x^t}{q_x} \cdot S_{xy}. \tag{6.7}$$

For example, for cloud water condensation the tagged transfer rate is given by $\frac{q_v^t}{q_v} S_{vc}^{\mathrm{c}}$, for cloud evaporation it is $\frac{q_c^t}{q_c} S_{vc}^{\mathrm{c}}$ (here, the sign of S_{vc}^{c} determines if condensation or evaporation occurs). Afterwards, the tendencies of the tagged moisture fields are obtained by replacing q_x with q_x^t and S_{xy} with S_{xy}^t in equation (6.6). The numerical solution of the equation is again performed analogously as for total water.

For warm cloud processes, the tagged humidity fields are transformed accordingly each time the saturation adjustment routine is called in the model. Therefore, the rate S_{vc}^{c}, which is not explicitely calculated in the adjustment routine, has to be assigned comparing q_v before and after the saturation adjustment. The tagged moisture transfer due to all other cloud processes is calculated within the cloud microphysics parameterization scheme at the end of the model time step. In this final step, also the tagged precipitation fluxes at the surface are obtained from the integration of the tagged version of equation (6.6).

6.2.6 Convection parameterization

In the COSMO model, a mass flux convection scheme following *Tiedtke* (1989) is used to parameterize cumulus convection, which is not explicitely resolved by the model grid (at least not with a horizontal resolution of 7 km as employed in this study). This scheme parameterizes cumulus up- and downdrafts within each vertical column of the model domain applying a simple bulk cloud model. It allows the calculation of convective rain and snow rates at the surface and of three dimensional tendencies for atmospheric water vapor[4]. For the latter, the following equation is used:

$$\left(\frac{\partial q_v}{\partial t}\right)_{\mathrm{conv}} = -\frac{1}{\rho}\frac{\partial}{\partial z}\left(M^u\left(q_v^u - q_v\right) + M^d\left(q_v^d - q_v\right)\right) - S^{\mathrm{cond}} + S^{\mathrm{evap}}. \tag{6.8}$$

Here, M^u and M^d denote the up- and downdraft mass fluxes; q_v^u and q_v^d give the specific humidities of water vapor in updraft and downdraft, respectively. S^{cond} denotes the cloud condensation rate in the updraft and S^{evap} the evaporation rate of cloud water and precipitation. Additional equations are used to parameterize the vertical mass and humidity fluxes based on microphysical transfer rates as well as entrainment and detrainment rates in the up- and downdraft (details are given by *Tiedtke* (1989) and *Doms et al.* (2005)). In order to solve this set of equations, the updraft flux equations are vertically integrated from cloud base to top; the vertical integration of the downdraft equations is performed from the level of free sinking to the surface. Finally, equation (6.8) is applied to determine the convective tendencies of water vapor. For cumulus

[4] In addition, tendencies of temperature and horizontal wind velocity are computed, but these are not considered here, because they do not directly influence the simulated humidity. Tendencies of cloud water are not calculated by the convection scheme; all detrained liquid water is assumed to instantaneously evaporate in the surrounding air.

precipitation, column equilibrium is assumed (rain and snow are not treated as prognostic variables here, contrary to the microphysics scheme). That is, the precipitation tendencies at the surface are calculated from vertically integrating all source and sink terms.

Several closure conditions are necessary for the integration of the up- and downdraft equations described above. With the help of multiple adiabatic ascent calculations of air parcels, it is checked if free convection may occur at a grid point. From these calculations, also the cloud base height and its temperature and humidity are determined. The mass influx at the cloud base, which is the driving mechanism for the convection, is specified in terms of the grid scale variables depending on the type of convection (penetrating, shallow or mid-level). Finally, the downdraft mass flux at the level of free sinking is defined, and the different de- and entrainment rates are expressed in terms of the up- and downdraft mass fluxes and the grid scale variables. The microphysical processes that are taken into account by the bulk cloud model of the convection parameterization are:

- cloud condensation (or deposition on ice for temperatures below the freezing point), for which the same saturation adjustment technique is used as described in section 6.2.5,
- evaporation of detrained cloud water in the environment of the cumulus plume,
- formation of precipitation within the updraft,
- evaporation of precipitation within the downdraft, for which again saturation adjustment is applied (the downdraft is supposed to be at saturation),
- evaporation of precipitation below the cloud base.

Again, the implementation of the secondary water cycle of tagged humidity in the convection parameterization mimics the total moisture water cycle. Equations describing tendencies of tagged vapor, tagged convective precipitation rates and tagged moisture fluxes in up- and downdrafts are obtained by replacing all specific humidities with tagged specific humidities and all microphysical transfer rates with tagged rates in the respective equations for total humidity. These new equations are solved in parallel with those for total water, i.e. tagged humidity has been implemented in all vertical up- and downdraft integrations of the convection parameterization. Therefore, several closure conditions have also been formulated for tagged moisture:

- Tagged humidities at the cloud base are obtained from tracing tagged water in the adiabatic ascent calculations that are used to determine the occurrence of convection. These ascent calculations are initialized using grid scale (tagged) moisture fields.
- Microphysical transfer rates for tagged moisture are calculated in the same way as described in section 6.2.5, i.e. applying equation (6.7). It is important to note that rain and

snow are not treated as prognostic variables here. Thus, the factor q_r^t/q_r that is required for the assignment of the evaporation rate of tagged rain cannot be determined at a single grid point. Instead, it is calculated from the tagged water content of the integral precipitation rate (which is obtained by vertically integrating all source and sink terms above the respective location).

- A critical point for the coupling of the grid scale model fields to the convection scheme is the vertical interpolation of grid scale humidity on half levels of the model grid (see again *Tiedtke*, 1989). Linear interpolation leads to very noisy profiles, hence in the COSMO model half level values are determined by downward extrapolation from the upper full level following a moist adiabat. For tagged water vapor, this is mimicked using the following equation:

$$q^t_{v,k+1/2} = q_{v,k+1/2} \cdot \frac{q^t_{v,k}}{q_{v,k}}.$$

  Here, k denotes the vertical level index, counting from the top of the model domain to the bottom.

For all other closure conditions, e.g. the de- and entrainment rates, the same values as for total humidity are applied. Following this approach, convective tendencies of q_v^t and convective rates of tagged rain and snow can be calculated.

6.2.7 Tracer synchronization and diagnostics

An important issue with respect to the implementation of water tagging in a numerical model is the consistency between the water tracers, which are simulated within an additional water cycle, and the corresponding total moisture fields. Due to numerical errors, the specific humidity of tagged water might become larger than the total water humidity, in particular at locations where large spatial moisture gradients occur, e.g. close to cloud edges. Moreover, the non-positivity of numerical schemes might lead to negative tracer values. In order to avoid these consistency problems, a tracer synchronization is performed for all tagged water categories several times within one COSMO model time step, applying the following equation:

$$0 \leq q_x^t \leq q_x. \tag{6.9}$$

That is, if at a grid point the tagged specific humidity becomes larger than the total humidity, the additional tagged moisture is clipped. Negative tracer values are clipped accordingly. The same synchronization is performed for tagged convective and grid scale precipitation rates at the surface. This synchronization destroys or generates tagged moisture and thus does not conserve mass. However, since the numerical schemes that are used for tracer transport in the COSMO model are relatively accurate (cf. sections 6.2.2 and 6.2.3), these mass changes are supposed to

be small. The total mass balance of tagged water in the model, comprising possible effects of the clipping described here, is explored in section 6.2.8.

Minor inconsistencies between tagged and total humidity are also generated by the output routine that writes the humidity fields on binary files in GRIB format. Such inconsistencies, where q_x^t exceeds q_x by a very small amount, occur at a few grid points, again close to large spatial humidity gradients, and are most probably related to interpolation problems[5]. They are eliminated by applying the same synchronization as given in equation (6.9) to the model output fields during post processing.

In addition to the prognostic tagged humidity fields, several diagnostic quantities related to water tagging have been introduced to the COSMO model and can be added to the model output with the help of namelist parameters (see appendix B). Among these diagnostic variables are the accumulated tagged evaporation flux and accumulated tagged grid scale and convective precipitation at the surface. The former is calculated as temporal integral of the tagged evaporation rate (which is obtained from the adapted version of equation (6.3) as described in section 6.2.3), the latter are computed from the fluxes of tagged rain and snow at the surface (obtained in the microphysics and convection parameterization schemes, cf. sections 6.2.5 and 6.2.6). Furthermore, vertical integrals of the tagged moisture fields are calculated for diagnostic output.

6.2.8 Mass conservation

The studies by *Sodemann* (2006) and *Sodemann et al.* (2009) have shown that in the CHRM model numerical problems can lead to violations of mass conservation of tagged humidity in the order of 10-20% after a few days of simulation. Since one of the major error sources of the CHRM tagging implementation, the inconsistency between the advection schemes of total (Leapfrog) and tagged (MPDATA) humidity, is not present in our water tagging implementation in the COSMO model, there is hope that here tagged water mass is reasonably well conserved. In order to verify this and also to check the general integrity of the tagging realization, the tagged mass budget has been determined for a two-day simulation. Therefore, a special model setup has been necessary, because unlike the study of *Sodemann* (2006), not every source of atmospheric humidity is included in our tagging approach (e.g. moisture inflow from the boundaries and evapotranspiration from land surfaces are not taken into account). An option has been implemented that allows to tag only water evaporating from the ocean surface in a predefined rectangular box (and not from the entire ocean in the model domain). This box can be specified in the namelist in terms of its boundary longitudes and latitudes.

[5] This issue has not yet been completely clarified; however, due to the smallness and scarcity of the deviations, it is regarded as being of minor importance.

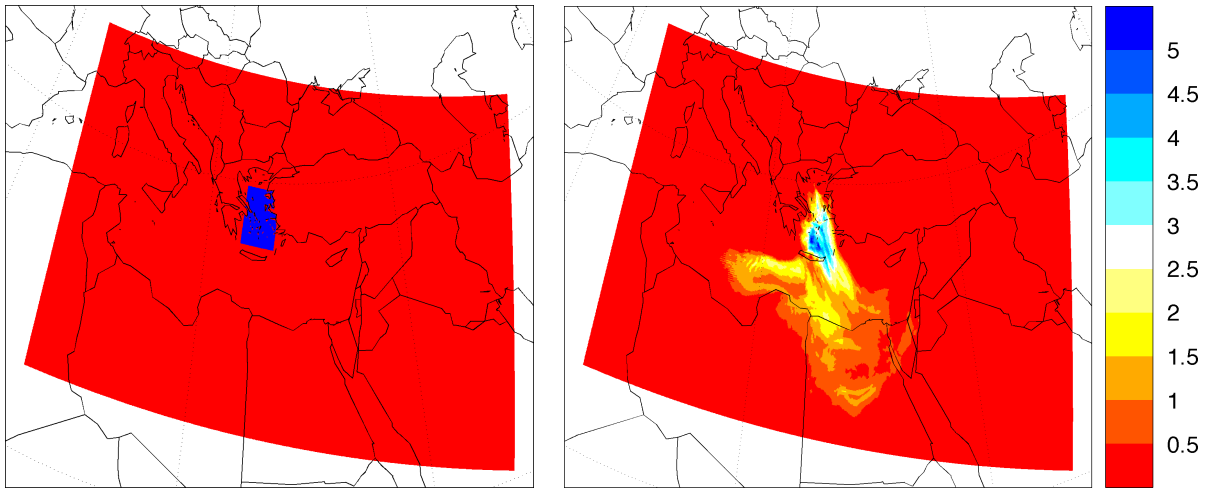

Figure 6.3. *Left: Region of water tagging for mass balance test (blue). The entire model domain is shown in red. Right: Vertically integrated tagged water vapor in* $\mathrm{kg/m^2}$ *at 00 UTC, 2001-11-17. All of this vapor has evaporated from the region shown on the left during a two-day simulation started at 00 UTC, 2001-11-15.*

Figure 6.3 shows the tagging region that is used for the mass conservation test. A rather small area in the center of the model domain has been chosen, because for the determination of the mass budget, it is necessary that no tagged moisture leaves the model domain through its boundaries during the simulation. The vertically integrated tagged water vapor, shown in Figure 6.3 at 00 UTC, 2001-11-17, indicates that this condition is fulfilled for a two-day model run started at 00 UTC, 2001-11-15. For this simulation, the temporal and spatial integral of the tagged evaporation flux has been calculated:

$$F^t_{\mathrm{tot}} = \int_{t_0}^{t_1} dt \int_{\mathrm{dom}} dA\, F_v^{\mathrm{sfc},t}(\vec{y},t),$$

where t_0 and t_1 denote start and end time of the model run, $F_v^{\mathrm{sfc},t}$ is the evaporation flux of tagged moisture (which is different from zero only in the box shown in Figure 6.3), $\int_{\mathrm{dom}} dA$ denotes the horizontal integral over the model domain and $\vec{y}$ gives the horizontal position. This integrated evaporation flux is compared to the sum of all tagged moisture that is present in the model domain at the end of the simulation and that has fallen as precipitation during its progress:

$$q^t_{\mathrm{tot}} = \sum_{x\in\{v,c,i,r,s\}} \int_0^{z_{\mathrm{top}}} dz \int_{\mathrm{dom}} dA\, q^t_x(\vec{y},z,t_1) \quad + \quad \sum_{x\in\{r,s\}} \int_{t_0}^{t_1} dt \int_{\mathrm{dom}} dA\, P^t_x(\vec{y},t).$$

P^t_x denotes the tagged surface flux of (grid scale and convective) rain or snow, and z_{top} is the geometrical height of the top of the model domain. The relative error in tagged mass conservation that is generated by numerical inconsistencies during the simulation can now be obtained as

$$E_{\mathrm{rel}} = \frac{q^t_{\mathrm{tot}} - F^t_{\mathrm{tot}}}{F^t_{\mathrm{tot}}}. \tag{6.10}$$

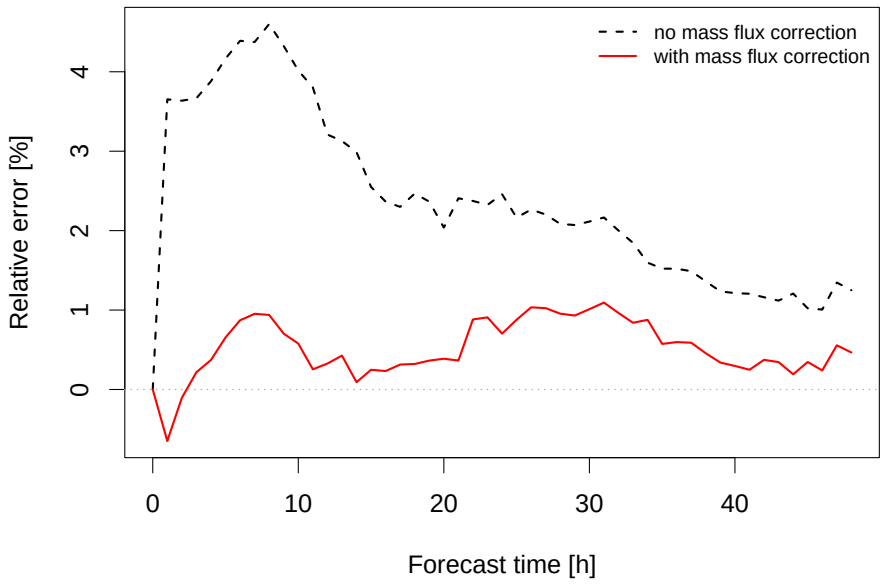

Figure 6.4. *Relative error in tagged mass balance E_{rel}, calculated with equation (6.10) for a* COSMO *simulation started at 00 UTC, 2001-11-15 (cf. Fig. 6.3).*

Figure 6.4 shows E_{rel} for the two-day model run started at 00 UTC, 2001-11-15 as a red line. This error never becomes substantially larger than 1%, and no systematic increase is visible after a forecast time of about 25 hours. Except for the first two hours, E_{rel} is always positive, indicating that slightly more tagged moisture is present in the system than has actually evaporated. The black dashed line shows the relative error for a model run for which the mass flux correction of tagged humidity after the vertical moisture transport (in which negative tracer values are compensated with moisture from neighboring grid boxes, cf. section 6.2.3) has been switched off. In this case, there is a steep increase in E_{rel} during the first hours of the simulation, peeking at 4.6% after 9 hours. Also at later times, the error is more than a factor of two larger than with mass flux correction. This larger error results from the fact that negative tagged humidity values are clipped, whereby tagged moisture is generated. Altogether, this shows that the non-positivity of the vertical transport scheme causes substantial numerical inconsistencies, which are significantly mitigated by the mass flux correction, at least with respect to mass conservation.

The rather small error in the mass budget shown in Fig. 6.4 indicates that the improved numerical schemes and the reduction of discrepancies between the numerical treatment of transport of tagged and total humidity significantly increase the numerical consistency of the water tagging implementation in the COSMO model compared to the CHRM. It should however be noted that the setup that has been used to study the tagged mass conservation here is not completely commensurable to the setup applied by *Sodemann* (2006), since we have not compared the mass of total and tagged humidity, but calculated the budget of tagged moisture and its integrated evaporation flux. Nevertheless, if there were large inconsistencies between between total and

tagged fields, this would also influence the tagged mass budget through the clipping of excessive tagged humidity (cf. section 6.2.7) and would thus lead to an increase in E_{rel}.

Finally, it is important to state that very little clouds and rain occurred in the Mediterranean region during the simulation that has been used to explore the tagged mass balance. The finding of a relatively small error in the tagged mass budget should be valid also in other cases, as numerical problems with mass conservation are mostly related to moisture transport, i.e. primarily to the advection and turbulent transport routines and not to the parameterization of phase transitions in the cloud microphysics scheme. Only the different spectra of cloud water and ice, which are shifted to smaller scales compared to water vapor, might lead to larger errors in the transport routines. Anyway, the total humidity budget in general is dominated by water vapor.

6.3 Isotope fractionation

In this section, the first steps of the implementation of water isotope physics in the COSMO model are described. In particular, some technical details on the prognostic isotope model fields and on the parameterization of fractionation during evaporation from the ocean are given. Except for this fractionation, the heavy water isotopes are treated in the same way as the tagged standard moisture, i.e. their transport and phase transitions are modeled using the same equations as for q_x^t, which have been outlined in the previous sections.

In addition to the five prognostic tagged humidity fields q_x^t (where again x stands for vapor, cloud water, cloud ice, rain or snow) representing the standard light water isotope H_2O, ten prognostic isotope moisture fields have been introduced to the COSMO model that refer to the different categories of the two heavy water isotopes $H_2{}^{18}O$ and HDO. These heavy isotope moisture fields (just denoted isotopes in the following) are represented by their specific humidities ${}^{18}q_x$ and ${}^{2}q_x$, which are scaled with the isotope composition of Vienna standard mean ocean water R_{VSMOW} times the ratio of the molecular weights of the heavy isotope and standard water, j:

$$
\begin{aligned}
{}^{18}q_x &= {}^{18}q_x^* \,/\, \left({}^{18}R_{\mathrm{VSMOW}} \cdot {}^{18}j\right), \\
{}^{2}q_x &= {}^{2}q_x^* \,/\, \left({}^{2}R_{\mathrm{VSMOW}} \cdot {}^{2}j\right).
\end{aligned}
$$

Here, ${}^{18/2}q_x^*$ are the unscaled specific humidities measured in kg/kg, and the ratios of molar weights are ${}^{18}j = 1.11$ and ${}^{2}j = 1.06$. Because of this scaling, the isotope specific humidities are in the same order of magnitude as the standard humidities, and numerical inconsistencies between the fields are minimized. The isotope composition of tagged moisture in usual δ-notation can be calculated from the specific humidity fields via

$$
\begin{aligned}
\left(\delta^{18}\mathrm{O}\right)_x &= \left({}^{18}q_x/q_x^t - 1\right) \cdot 10^3, \\
\left(\delta^{2}\mathrm{H}\right)_x &= \left({}^{2}q_x/q_x^t - 1\right) \cdot 10^3.
\end{aligned}
\tag{6.11}
$$

In the same way as for tagged humidity, isotope precipitation fluxes at the surface are calculated in the model. The isotope composition of accumulated precipitation is obtained from the integrated tagged and isotope fluxes analogously to equation (6.11).

As for the tagged moisture fields, a tracer synchronization is performed for the isotopes. However, owing to the scaling with the VSMOW ratios it is not as straightforward as for tagged humidity to define an upper bound for ${}^N q_x$, $N \in \{2, 18\}$. The following synchronization steps are thus performed:

- Negative isotope ratios are clipped.
- If $q_x^t > q_x$, the isotope specific humidities are reduced in parallel with q_x^t according to

$$\left({}^N q_x\right)_{\text{new}} = \left(\frac{{}^N q_x}{q_x^t}\right)_{\text{old}} \cdot q_x$$

  in order to keep the isotope ratios constant.
- Isotope ratios are limited by a subjectively chosen upper bound: ${}^N q_x / q_x^t < 1.5$.

The first two steps have analogously been implemented for the isotope precipitation fluxes. The synchronization procedure and especially the last step are particularly important in regions of very small tagged humidities, where numerical inconsistencies may lead to unrealistic isotope ratios, which might then introduce an unintended feedback via the evaporation parameterization (see the next paragraph).

In the COSMO model, the parameterization of isotope fractionation during evaporation of water from the ocean is performed in the same way as in the Lagrangian model described in chapter 5. The isotope ratios R_E of the evaporate are obtained from equation (5.1), and isotope surface fluxes are calculated by multiplying these ratios with the standard tagged evaporation flux (which is computed from the tagged version of equation (6.3)). For the application of (5.1), again several parameters have to be specified. The relative humidity h is calculated from equation (5.3), where the specific humidity on the lowermost COSMO model level is used for q_{ll}. Parametric equations for the equilibrium fractionation factor α from *Horita and Wesolowski* (1994) are used, and the isotope ratios of ocean water are set to the same values as given in chapter 5 (the latter can be changed with the help of namelist parameters). For the non-equilibrium fractionation factor k, again two options have been implemented: Either the classical parameterization of *Merlivat and Jouzel* (1979) (with diffusivities from *Merlivat* (1978b), see Figure 5.1) or a wind speed independent parameterization applying equation (5.5) can be chosen via a namelist switch. For the latter, diffusivities from *Cappa et al.* (2003) are used, and the parameter m is set to 0.24 (changeable in the namelist), the value that led to the best agreement between Lagrangian

model results and measurement data in chapter 5. Finally, the atmospheric isotope ratios R_A are specified as follows:

- If the tagged humidity on the lowest COSMO model level at the evaporation site is larger than zero, the atmospheric ratio is calculated from its isotopic composition: ${}^N R_A / {}^N R_{\mathrm{VSMOW}} = {}^N q_v / q_v^t$.
- If $q_v^t = 0$ on the lowest level, there are two options for the definition of R_A that can be chosen in the namelist: Either a global closure assumption applying equation (5.2) or isotope ratios from the historical IsoGSM simulation by *Yoshimura et al.* (2008) can be used (for details see again chapter 5 and further below).

Upper and lower bounds for the isotope ratios in the evaporation flux have been introduced (in the current setting $0.8 < R_E/R_{\mathrm{SMOW}} < 1.2$) in order to prevent unrealistic isotope values for relative humidities h close to 1, for which there is a discontinuity in equation (5.1).

Boundary fields for the COSMO model are obtained from ECMWF analysis data with the help of a preprocessing tool (*Schättler*, 2008), as mentioned above. This tool primarily interpolates the coarser analysis fields to the fine COSMO model grid. Here, the tool can also be used for the preparation of the isotope fields that are required for initializing the atmospheric boundary values for the evaporation parameterization (R_A in equation (5.1)) if the global closure assumption shall not be applied. Therefore, the isotope ratios from the lowest output pressure level of the historical isotope simulation by *Yoshimura et al.* (2008) with the IsoGSM model (version 1) are used. These data are available with a spectral resolution of T62 and are, in a first step, bilinearly interpolated to the horizontal grid of the ECMWF analyses (for which currently a resolution of 0.5° is used). Then, the isotope fields can be read by the preprocessing tool together with all other analysis fields, and they are accordingly interpolated to the COSMO model grid by this tool (again using bilinear interpolation).

Initial tests with the first version of the new $\mathrm{COSMO_{iso}}$ model have shown that some problems with the simulated isotope fields may occur that are related to inconsistencies in the preprocessing of the ECMWF boundary data. In particular, at single grid points over the ocean close to the coast the ECMWF skin temperature, which is employed as SST boundary condition for the COSMO model, sometimes adopts unrealistically high or low values compared to neighboring ocean grid points. This unrealistic SST has a strong influence on the isotope fractionation during evaporation from the ocean and can lead to large spatial gradients in the isotope ratios of water vapor close to the surface in a localized area surrounding the affected grid point. Figure 6.5 shows an example of an ECMWF skin temperature field with such unrealistic variability close to the North African coast. Comparably large inconsistencies occur only at 2 or 3 grid points in the Mediterranean region at a given time (and there are many dates without any inconsistencies). They are most probably related to problems with the interpolation of the analysis

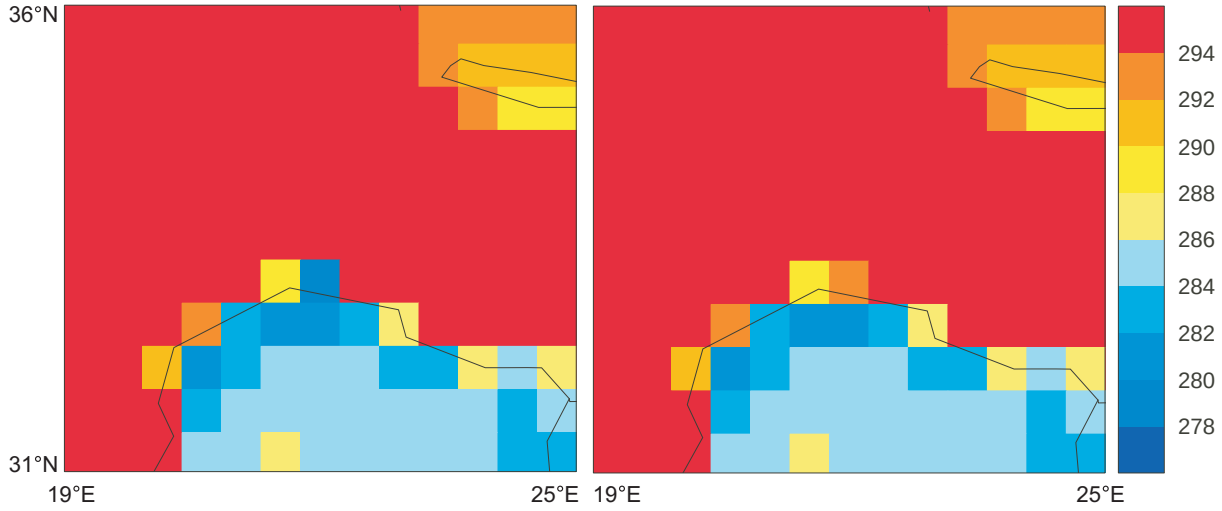

Figure 6.5. *Left: Skin temperature from ECMWF analyses for 2001-11-15, 0 UTC in K. The data has been interpolated on a 0.5° longitude-latitude grid, as used for the* COSMO *model initialization and boundary data. Here, a region between the Libyan coast and Cyprus is exemplarily shown. Right: Filtered skin temperature field for the same date.*

data, which are originally produced as spherical harmonic fields, onto a longitude-latitude grid. Such problems most likely occur in regions of large spatial gradients of the temperature field, e.g. where mountains reach close to the coast[6]. In order to get rid of the unrealistic effects on isotope ratios induced by the SST inconsistencies a smoothing filter is applied to the ECMWF skin temperature before it is used as COSMO boundary condition. The following smoothing algorithm is employed:

- All oceanic ECMWF grid points with exactly one neighboring land point are searched (i.e. the other 3 neighboring points are located over the sea).
- The difference in skin temperature T_{diff} between this coastal point and the oceanic point opposite to the neighboring land point (i.e. in the direction perpendicular to the coast) is calculated.
- If this difference T_{diff} is larger than a subjectively chosen maximum (currently 8 K), the skin temperature at the coastal point is adjusted. The new skin temperature T_{new} is cal-

[6]Similar inconsistencies emerge at the affected grid point if the ECMWF surface geopotential is interpolated to a longitude-latitude grid (not shown). This indicates that the respective problem is not related to the skin temperature alone, but seems to be a general interpolation issue. Increasing the grid resolution does not eliminate the inconsistency.

culated as weighted mean between the skin temperature of the land point T_{land} and the average skin temperature of the three adjacent ocean grid points $\overline{T}_{\mathrm{sea}}$:

$$T_{\mathrm{new}} = 0.1 \cdot T_{\mathrm{land}} + 0.9 \cdot \overline{T}_{\mathrm{sea}}.$$

Here, the weighting factors have also been chosen subjectively.

With the help of this filtering, most of the largest inconsistencies in the simulated isotope fields for the cases explored in this study (see section 6.4) can be eliminated, as shown exemplarily in Fig. 6.5. The temperature threshold for T_{diff} and the whole algorithm have been chosen rather conservatively, that is the changes introduced by the filter are reduced to a minimum. With a more restrictive setting (which could maybe also have changed the temperature at the grid point to the west of the adjusted point in Fig. 6.5), the risk increases that realistically analyzed coastal SST gradients are smoothed out by the algorithm. However, for future case studies it might be necessary to adjust the filter algorithm (and e.g. also consider grid points with more than one neighboring land point) in order to produce satisfying results.

6.4 Case studies

This section describes the first case studies with the newly developed $\mathrm{COSMO}_{\mathrm{iso}}$ model. In its initial version, isotope fractionation is only parameterized for water evaporation from the sea, as mentioned above. The following subsection outlines the selection of cases, the general patterns of moisture transport and cloud occurrence in the Mediterranean region during these cases and the setup of the $\mathrm{COSMO}_{\mathrm{iso}}$ simulations. Subsequently the simulated meteorology is briefly evaluated by comparing it to ECMWF analyses, and results from the water tagging approach are shown. Thereafter, some results for the water isotopes are presented and compared to other data where possible. Finally, two sensitivity experiments are shown that explore the setting of the fractionation parameterization for one particular case study.

6.4.1 Characterization of the example cases and setup of the simulations

Case studies have been performed with $\mathrm{COSMO}_{\mathrm{iso}}$ for four days with isotope measurements in Rehovot. These four days have been selected based on the following two criteria.

- For each of these days, evaporation regions could have been attributed to a large fraction Ra of the sampled water vapor at Rehovot with the Lagrangian moisture source diagnostic described in chapter 4. Such a large value of Ra indicates that moisture sources can principally be detected within a few days before the measurement, and that little clouds and rain

occurred during humidity transport from the evaporation regions to Rehovot (otherwise, the trajectories used in chapter 4 would have been clipped).

- The measured deuterium excess values from the four days cover a large range. In this way, it can be tested if $\text{COSMO}_{\text{iso}}$ is able to reproduce the measured variability in d using a comparably small number of simulations. Due to limited computational resources, the number of case studies is limited. The focus again is on the interpretation of the d-excess because the influence of cloud fractionation processes (which are not simulated with the current version of $\text{COSMO}_{\text{iso}}$) is much smaller on d than on the isotope ratios $\delta^{18}\text{O}$ and $\delta^{2}\text{H}$.

In Table 6.2 the selected days together with the corresponding values of Ra from the Lagrangian diagnostic and the measured d-excess are listed. All values of Ra are greater than or equal 70%, and d varies between 9.3‰ and 41.1‰. Figure 6.6 shows the variation of specific humidity along the 10 day backward trajectories that have been calculated for the source diagnostic in chapter 4. All these trajectories have been clipped at the first point (starting from Rehovot and going backwards in time) where the sum of diagnosed cloud water and ice exceeded 0.1 g/kg or precipitation was larger than 1 mm per 6 hours (see again chapter 4). As can be seen from the Figure, there is some variation in the atmospheric flow patterns by which moisture was transported to Rehovot between these four cases. On the days preceding the 2001-11-18, there was a northerly flow, in which rather strong winds transported very dry air from eastern Europe over the Black Sea to the eastern Mediterranean, where the air took up some moisture before reaching Rehovot. The strong humidity gradient between the dry continental air and the Mediterranean sea surface led to the very large deuterium excess measured on that day. On 2005-04-14, air was transported over the Mediterranean Sea towards Israel in a westerly flow. During the long passage over the ocean, a lot of humidity was taken up by an already moist air mass (in particular the more northern trajectories), leading to a low d-excess. The two other days can be considered as intermediate between these two extremes. Initially relatively dry air masses were transported over the eastern Mediterranean Sea in a north-westerly flow. The period during which the air

Date	Ra from Lagrangian diagnostic [%]	Measured d-excess [‰]
2001-11-18	72	41.1
2003-03-27	84	18.8
2005-04-14	74	9.3
2006-01-29	70	28.1

Table 6.2. *Fraction of water vapor at to which sources have been attributed using the Lagrangian diagnostic described in chapter 4 (*Ra*) and measured d-excess in Rehovot on the days that have been selected for the* $\text{COSMO}_{\text{iso}}$ *case studies.*

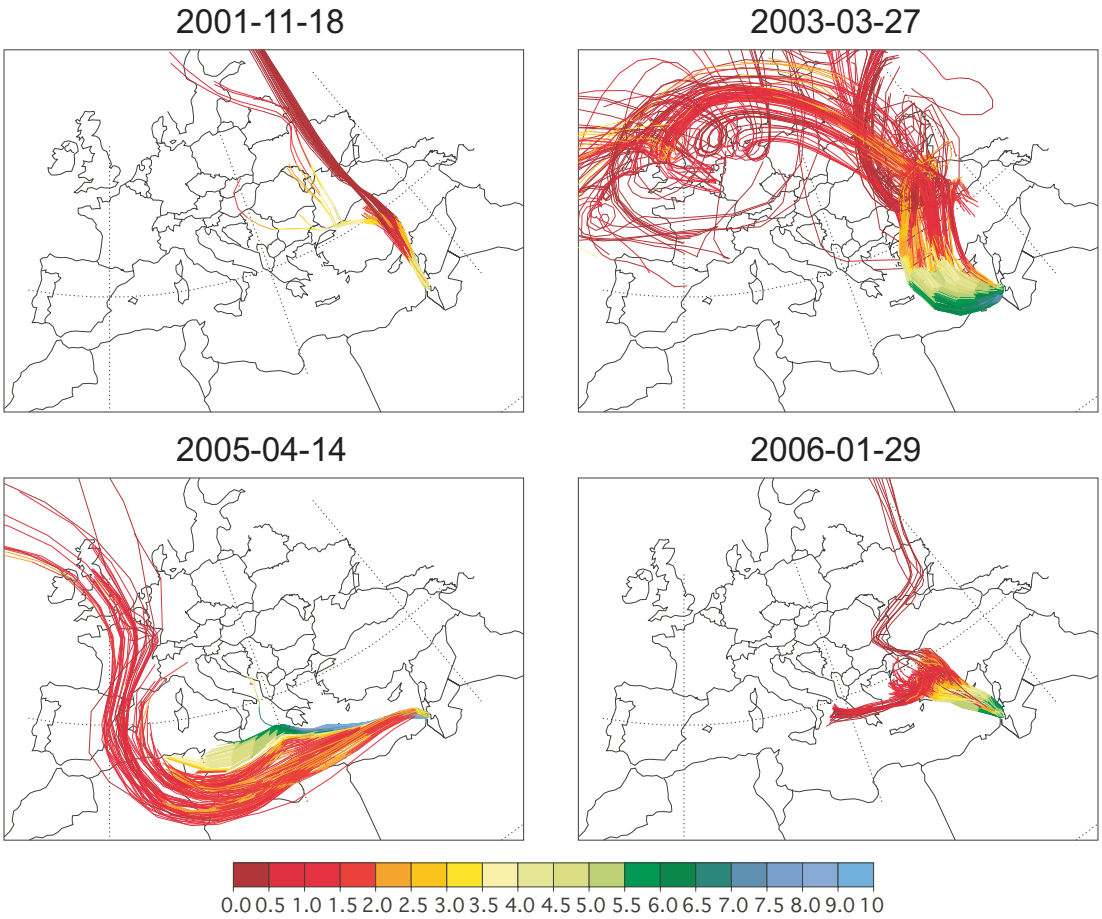

Figure 6.6. *Ten day backward trajectories calculated for the four selected isotope measurement periods at Rehovot. Only parts of the trajectories are shown for which no clouds and no rain from above have been detected. Colors indicate specific humidity in g/kg.*

was in contact with the ocean was a bit longer than for 2001-11-18, resulting in moderately high d values. Another difference between the four flow patterns shown in Fig. 6.6 is indicated by the trajectory clipping: On the one hand, on 2006-01-29 almost all trajectories have been clipped close to the margins of the European continent, indicating that some clouds occurred in that region. Also for the case of 2001-11-18, several trajectories have been clipped over Anatolia. On the other hand, for 2003-03-27 and 2005-04-14 the air parcels could be traced for a long distance without experiencing many clouds or precipitation. This difference also shows up in the satellite pictures displayed in Fig. 6.7, where infrared images from the Meteosat VISSR satellite are shown at 12 UTC on the four measurement days. Several patchy low level clouds can be perceived over the Mediterranean and Turkey for 2001-11-18; on 2003-03-27, the whole region was relatively cloud free, with a few exceptions over eastern Anatolia and the Middle East. Some clouds are visible over Greece and Turkey for 2005-04-14; the Mediterranean Sea

was cloud free on that day. Finally, on 2006-01-29 many high clouds occurred all over the region, in particular over Northern Africa (possibly related to a tropical plume) and the western Mediterranean (where clouds might have been triggered by a cyclonic system). Altogether, the correspondence between the satellite pictures and the trajectories is rather good with respect to the cloud occurrence and trajectory clipping (e.g. on 2006-01-29, moisture uptake occurred in a relatively cloud free area in the eastern Mediterranean and the trajectories did not cross the cloudy regions over the continent). However, the images also show that, although the moisture at Rehovot can be traced back to its evaporation regions without experiencing much cloud formation in between, there is a large variability in the overall cloud occurrence over the Mediterranean region between the four selected days. Hence, isotope model results from $\text{COSMO}_{\text{iso}}$ that do not incorporate fractionation during cloud formation have to be handled with care. In this study, we thus concentrate on the interpretation of d-excess in water vapor, which is less influenced by cloud processes than $\delta^{18}\text{O}$ and $\delta^{2}\text{H}$, as mentioned above. Furthermore, we only analyze vapor isotope fields on the lowest COSMO model level (about 20 meters above ground).

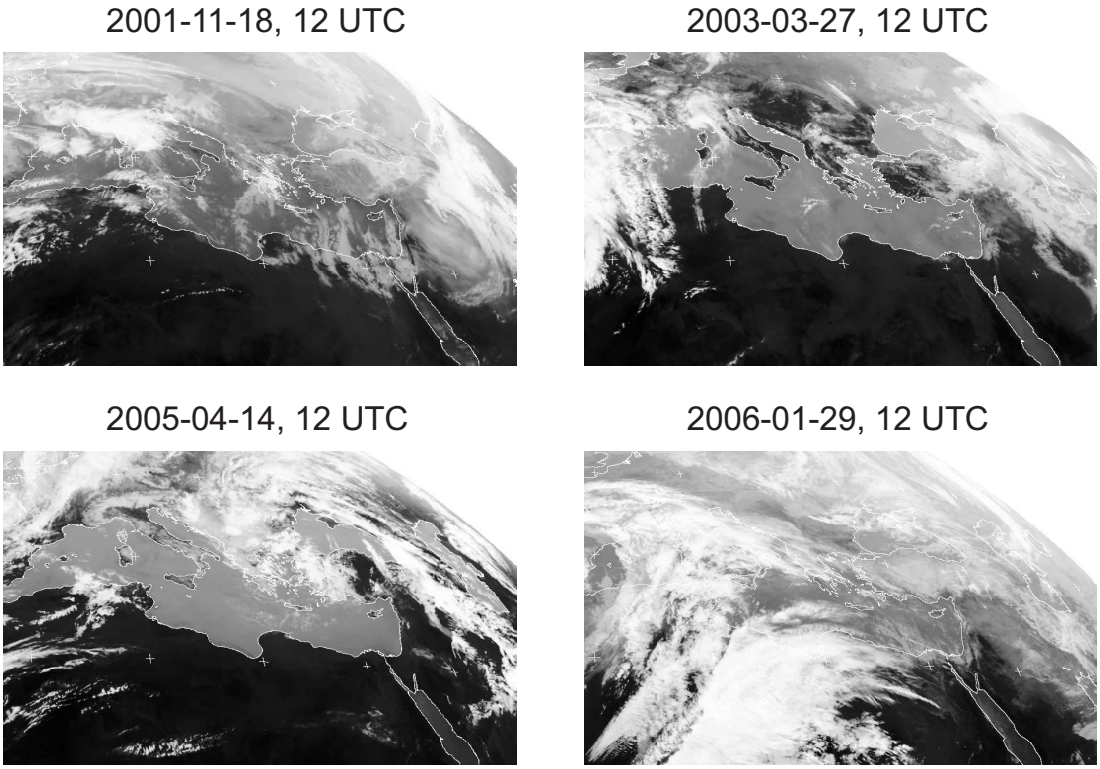

Figure 6.7. *Infrared satellite images of the Mediterranean region from Meteosat VISSR. For each case, a picture is shown at 12 UTC on the measurement day, i.e. 84 hours after the start of the model simulation.*

For the four measurement days listed in Table 6.2, $\text{COSMO}_{\text{iso}}$ simulations have been performed using a model domain that comprises the eastern Mediterranean region (see Fig. 6.1) and a horizontal resolution of 7 km. The (rotated) model grid consists of 600 grid points in the longitudinal times 360 in the latitudinal direction. All simulations have been started at 00 UTC three days before the measurement day (i.e. on 2001-11-15, 2003-03-24, 2005-04-11 and 2006-01-26), and the model has been run for four consecutive days. Hourly output of all relevant meteorological fields has been produced. The main evaluation time, for which most of the maps are shown in the following, is 12 UTC on the measurement day. For comparison with the measurements, the modeled (isotope) specific humidities at the four grid points adjacent to the location of Rehovot have been averaged over the sampling periods (weighted with the simulated specific humidity of total water vapor). In the standard setup that has been applied for all case studies the wind speed independent parameterization of isotope fractionation during evaporation from the ocean has been used (cf. equation 5.5), and the global closure assumption (equation 5.2) has been employed for the initialization of the atmospheric isotope ratios (cf. chapter 5). Two sensitivity experiments exploring these parameterization settings have been performed for one case study (2001-11-18) and will be presented in section 6.4.5.

6.4.2 Simulated meteorology

In order to evaluate the general performance of the COSMO model in simulating the meteorological conditions during the selected cases, several meteorological model output fields have been compared to ECMWF analysis data. Root mean square errors (RMSE) between simulated and analyzed geopotential height of the 500 hPa iso-surface (Z500) and vertically integrated water vapor content (TWV) have been calculated at every 6-hourly analysis time step within a model run. Therefore, the ECMWF analyses have been bilinearly interpolated to the COSMO model grid, and the following equation has been used to calculate the RMSE:

$$\text{RMSE} = \sqrt{\frac{1}{n_{\text{lon}} n_{\text{lat}}} \sum_{i=1}^{n_{\text{lon}}} \sum_{j=1}^{n_{\text{lat}}} \left(\text{Z500}_{\text{COSMO}}(i,j) - \text{Z500}_{\text{ECMWF}}(i,j)\right)^2},$$

where n_{lon} and n_{lat} denote the number of model grid points in longitudinal and latitudinal direction, respectively (the RMSE for TWV has been computed accordingly). In addition, maps of equivalent potential temperature on 850 hPa (THE850) and sea level pressure (SLP) at 12 UTC on the measurement days have been evaluated qualitatively.

Figure 6.8a shows the temporal evolution of the RMSE of Z500 from all model simulations. This field has been chosen for the model evaluation because it represents the large scale circulation in the middle troposphere. Already at the first time step of each model run, there is some difference between the analyses and the COSMO model fields, resulting in a non-zero RMSE.

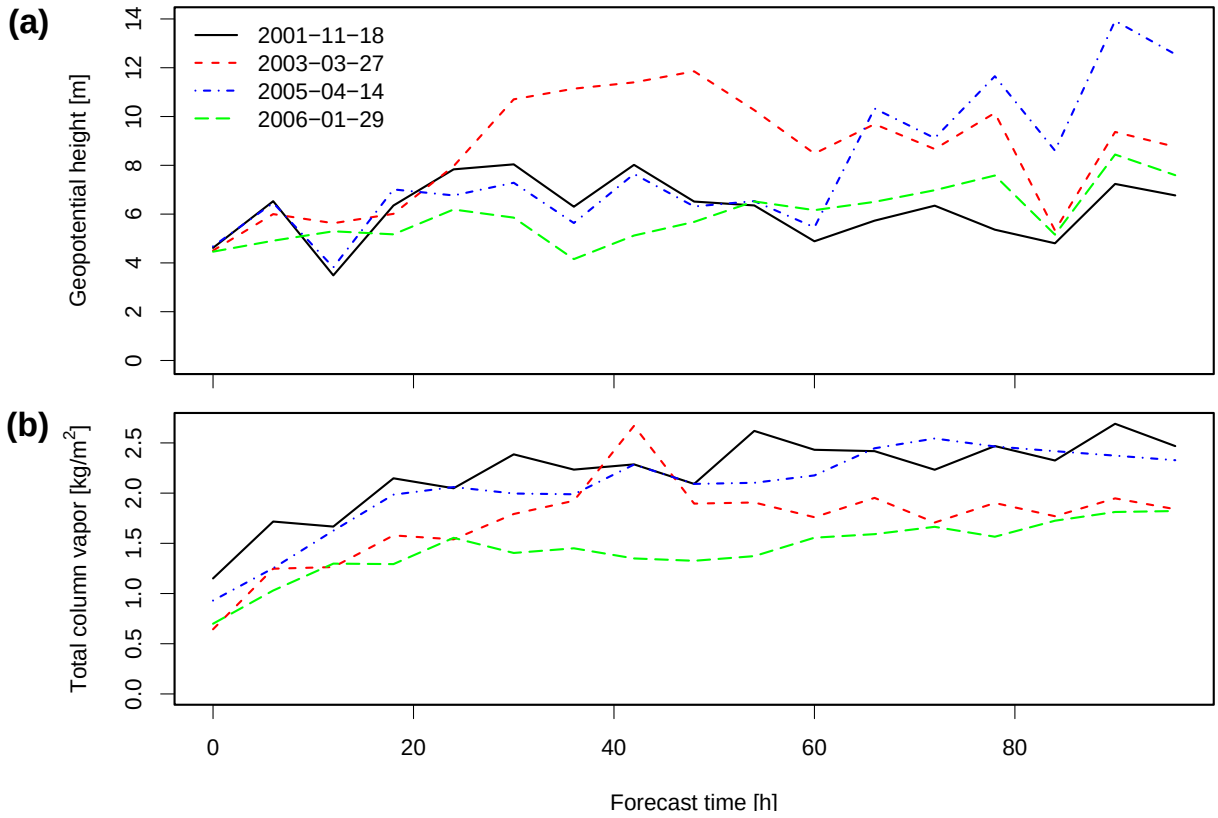

Figure 6.8. *Root mean square errors of* COSMO *simulations (with respect to ECMWF analyses) of 500 hPa geopotential height (a) and vertically integrated water vapor content (b) for the four case studies. The ECMWF analyses have been bilinearly interpolated to the* COSMO *model grid in order to perform this comparison.*

This difference is due to the differing methods used to interpolate the data to the fine COSMO grid: the ECMWF field is a simple bilinear horizontal interpolation of the corresponding coarser analysis, whereas the COSMO model field has been produced by the COSMO pre-processing tool from the same original data (recall that ECMWF analyses are used to initialize the model). This pre-processing tool, in addition to just interpolating the coarse data, takes into account the influence of the varying vertical resolution and the finer model orography. Thereby, some spurious small scale variability is introduced to Z500 that is not present in the original analysis. Hence, the RMSE at the first time step measures the deviation between model and analysis fields that is not related to differing meteorological conditions, but just to the different spatial resolutions of the two data sets. For all four model runs shown in Fig. 6.8a, there is only a moderate increase in the RMSE during the 96 hours of simulation. For the 2003-03-27 case, the RMSE peaks after about 50 hours and decreases again later on. The highest RMSE (about three times the initial value) can be observed at the end of the 2005-04-14 simulation. In the two additional cases, the RMSE does not grow to more than two times the initial value. Keeping in mind that Z500 is in the order of 5000 to 6000 meters, the RMSE from all simulations is around

1-2 per mil. Thus, the large scale tropospheric circulation is very well captured by the COSMO model simulations. This is relatively typical for hindcast simulations, for which analysis data are used to constrain the meteorological fields at the boundaries of the model domain. For the case studies shown here, the result is particularly satisfying because the model domain is rather small and there is no explosive atmospheric development during the simulations.

TWV has been included in the COSMO model evaluation since it is an integral measure of the atmospheric hydrological cycle, whose accurate representation is essential for the water isotope simulation. The RMSE of this field is shown in Fig. 6.8b. Compared to Z500, TWV in general exhibits much more variability on small spatial scales. This fact is reflected in higher relative RMSE values already at the beginning of the simulation (0.6-1.2 $\mathrm{kg/m^2}$, that is in the order of 5-10% of the absolute magnitude of the field), which mainly results from deviations in the continental boundary layer owing to the differing model orographies. Nevertheless, the relative increase of the error is comparable to Z500, i.e. the RMSE never becomes larger than a factor of about four times the initial value. Again, for 2003-03-27 the error peaks in the middle of the simulation. For all other cases, there is a gradual increase in the RMSE; the lowest values are obtained for the 2006-01-29 simulation. Altogether, this shows that the relative contributions of the diverging meteorological conditions between model simulation and analysis to the errors of TWV and Z500 are of comparable magnitude. Thus, the large scale features of the hydrological cycle, just like the large scale tropospheric circulation, are well captured by the COSMO model. This fact is exemplarily illustrated in Fig. 6.9, where maps of TWV from the model simulation and from the interpolated ECMWF analysis are shown at 12 UTC, 2001-11-18. The RMSE for this date is 2.3 $\mathrm{kg/m^2}$. This relatively large RMSE mainly results from deviations on small spatial scales, e.g. over east Anatolia and the Sinai Peninsula, whereas the large scale moisture

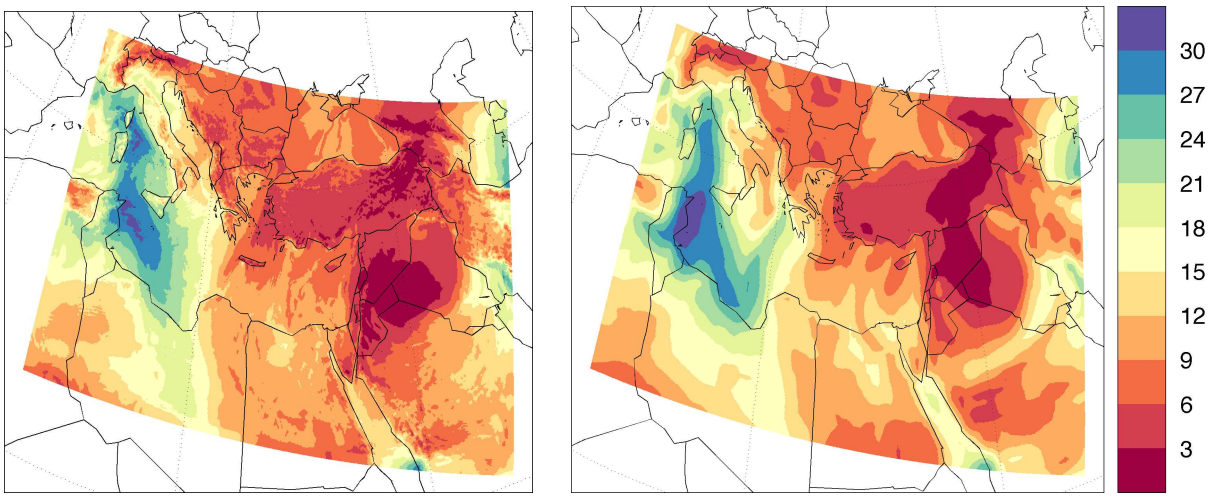

Figure 6.9. *Vertically integrated water vapor content (colors, given in* $\mathrm{kg/m^2}$*) at 12 UTC, 2001-11-18 from* COSMO *model simulation (left) and ECMWF analysis data, bilinearly interpolated on the* COSMO *model grid (right).*

distribution (very dry continental air over Turkey and the Middle east; moist air over the central Mediterranean) is properly represented in the model simulation.

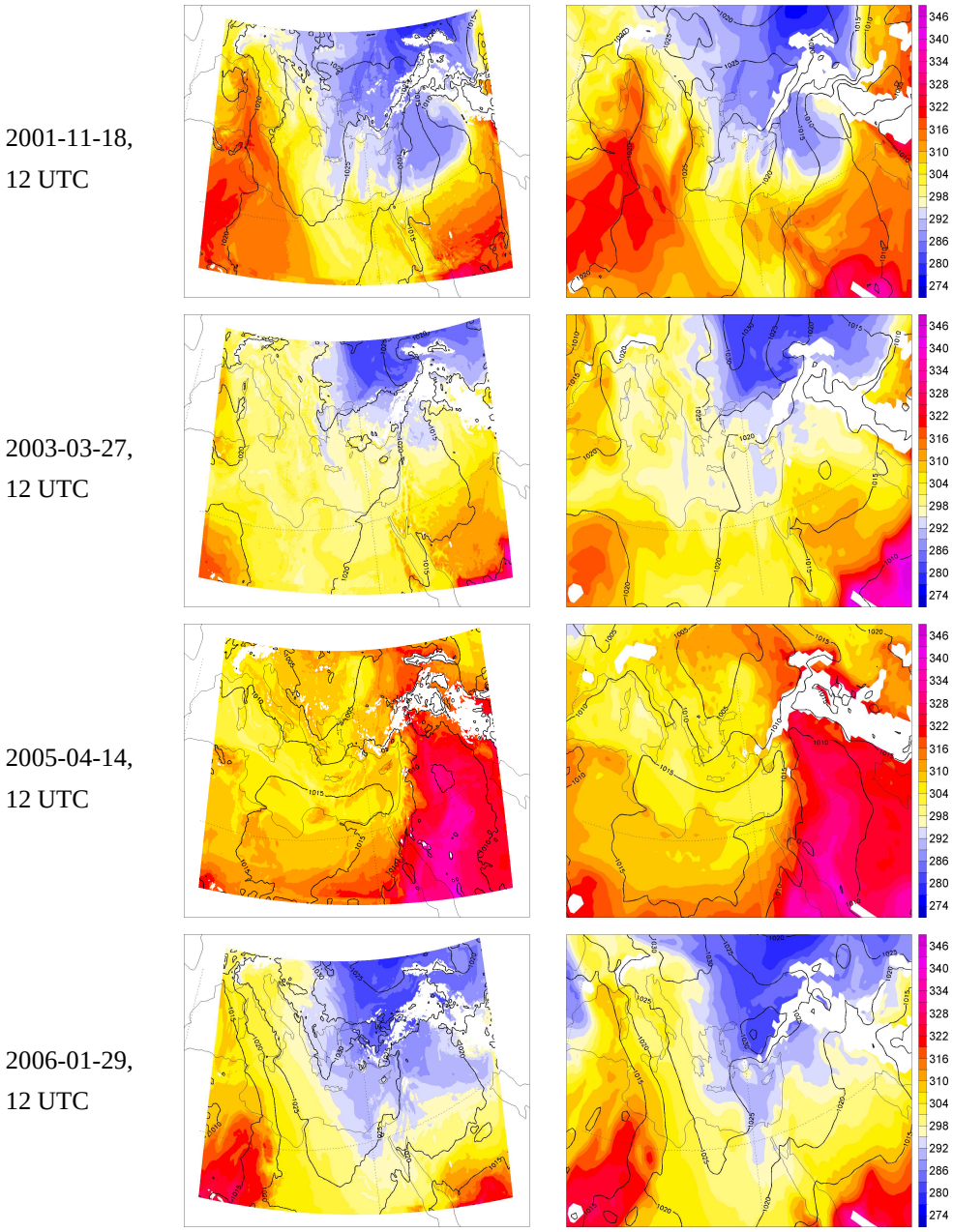

Figure 6.10. *Equivalent potential temperature on 850 hPa in K (colors) and sea level pressure in hPa (thick black contours). For each case study, results from the* COSMO *model simulation (left column) and ECMWF analysis data (right column) are shown at 12 UTC on the measurement day. THE is masked in areas where the 850 hPa surface lies below the orography.*

Figure 6.10 shows maps of THE850 and SLP from COSMO simulations and ECMWF analyses at 12 UTC on the measurement days. THE850 represents the temperature and humidity structure in the lower troposphere, which is an important boundary condition for the isotope fractionation parameterization. The SLP is another integral measure for the tropospheric flow structure and temperature. For THE850, in three of the four cases relatively low values can be found in the north and moderate to high values in the south and in the west of the model domain. An exception is the 2005-04-14 case, for which THE850 is very high in the eastern part and relatively uniform in the rest of the domain. These general patterns are well captured by the COSMO simulations, with some minor deviations on regional scales (e.g., for 2001-11-18 THE850 is a bit too low in the southwesterly part of the domain; for 2003-03-27 somewhat too high values are simulated over the eastern Mediterranean Sea; and on 2006-01-29 THE850 over the Middle East, also over Israel, is too low in the COSMO model). Relatively high SLP values and no large spatial variations in this field occur at the evaluation dates of the four case studies (not taking into account the masked regions of high elevations, where the reduction of surface pressure to sea level introduces some errors). An exception is the SLP gradient over the western Mediterranean Sea on 2006-01-29. Again, these patterns are fairly well simulated by the COSMO model. Small deviations occur e.g. on 2001-11-18 south of Greece, where the simulated high pressure system is too broad compared to the analysis, and on 2006-01-29 in the eastern part of the domain, where modeled SLP values are too large up to about 3 hPa.

Altogether, the comparison performed in this section shows that the COSMO model is well capable of simulating the meteorological conditions in the eastern Mediterranean region during the four selected case studies. Both the general tropospheric circulation and the humidity and temperature structure in the model match the respective conditions in the ECMWF analysis data set, with some minor deviations occurring on regional scales. Nevertheless, it is important to note that the simulated surface conditions over the ocean, which are most important for the parameterization of isotope fractionation during evaporation of water, cannot easily be evaluated, because there are hardly any appropriate observations available to constrain the ECMWF analysis fields in these areas. Thus, we cannot rule out that deficiencies in simulating these surface conditions affect the modeling of isotope ratios in water vapor in $\mathrm{COSMO_{iso}}$.

6.4.3 Water tagging

As already outlined in section 6.1.2, it is essential for the isotope simulation approach pursued in this study that the fraction of tagged humidity $f_x = q_x^t/q_x$ reaches a substantial magnitude at the location and time instant at which modeled isotope fields are to be interpreted, because only the isotope ratios in this fraction of the total moisture are determined in the model. Here, we focus on isotopes in water vapor close to the surface and compare these simulated ratios to measurements at Rehovot. In the following, results are presented for the temporal evolution of

the fraction of tagged water vapor f_v at Rehovot (using average values from the four adjacent grid points for q_x^t and q_x, as mentioned above) and the spatial pattern of this fraction on the lowest COSMO model level at 12 UTC on each measurement day. Furthermore, the vertical distribution of f_v is exemplarily illustrated. The latter is not important for the isotope ratios presented below, but will become interesting for future studies, in particular when investigating stable water isotopes in precipitation.

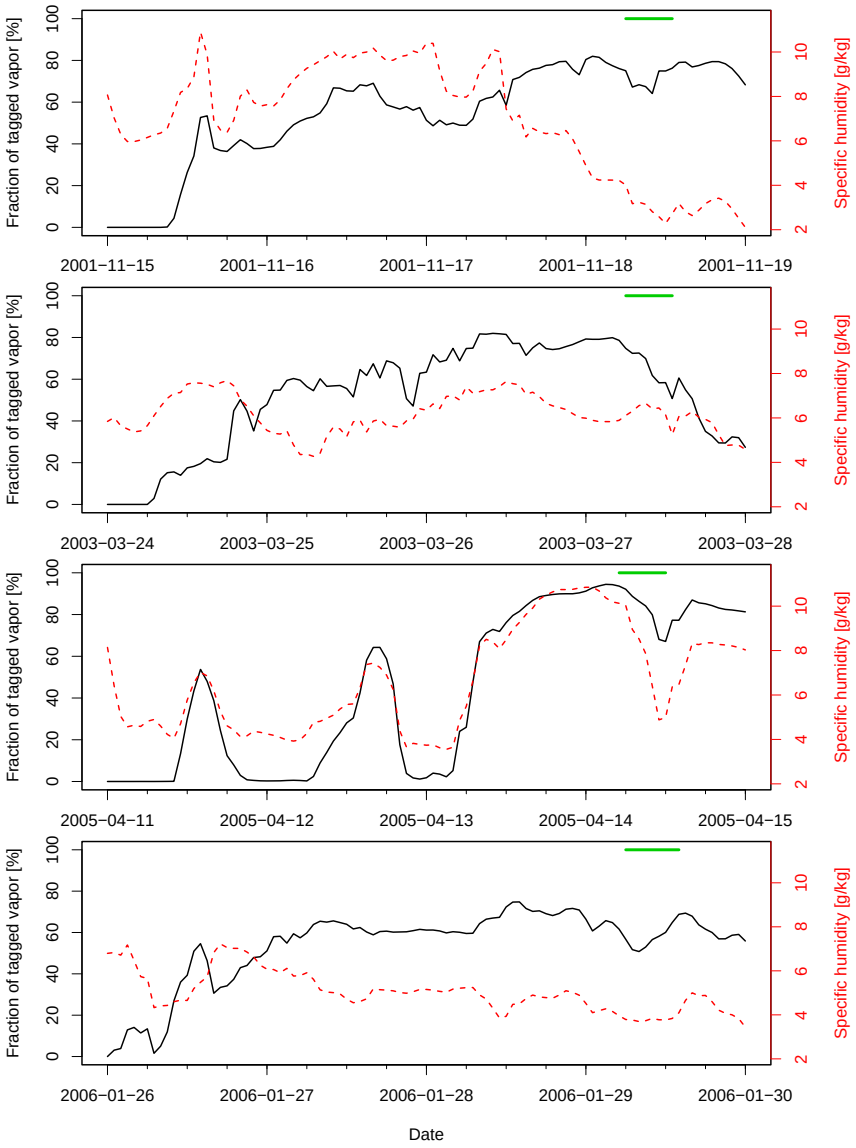

Figure 6.11. *Time series of the fraction of tagged water vapor f_v on the lowest* COSMO *model level at the location of Rehovot (black lines, axes on the left; specific humidities have been averaged over the four adjacent grid points before calculating f_v). The red dashed curves give the corresponding total specific humidity (axes on the right). The green lines at the top indicate the measurement periods.*

Figure 6.11 shows time series of f_v and of the corresponding total specific humidity q_v at Rehovot from the four case study simulations. The tagged vapor fraction grows from zero to values around 50% already during the first day of each simulation, indicating that water that has evaporated from the ocean is transported to Rehovot. Afterwards, larger deviations in the evolution of f_v occur between the four model runs. In the 2005-04-14 case, there is a large variability in f_v, correlated with variations in the specific humidity. Dry, continental air masses containing almost no tagged water alternate with more humid oceanic air, in which f_v is greater than 50%. On the third day, the tagged vapor fraction grows larger than 80% and stays high during the rest of the model run (with a small depression around 12 UTC, 2005-04-14, that is again related to a drop in q_v). In the other three cases, the variability in f_v is smaller, and no substantial correlation to q_v can be observed. During the last one and a half days of the 2001-11-18 simulation, q_v considerably decreases, indicating the approach of a dry continental air mass, which is also visible in Fig. 6.9. Nevertheless, also in this dry air some moisture is present that has evaporated from the sea during the model run, leading to a fairly constant value of f_v. On the contrary, there is a drop in f_v during 2003-03-27 that does not coincide with a major change in q_v. Table 6.3 gives the weighted mean values of f_v at Rehovot for the measurement periods (these periods are shown as green horizontal lines in Fig. 6.11). The temporal means have been calculated bases upon hourly model output, using the simulated total specific humidity as weighting factor. As can be seen from the Table, there are some differences in mean f_v between the cases: A high value is obtained for 2005-04-14; values for 2001-11-18 and 2003-03-27 are moderate, but still fulfill the condition of $f_v > 60\%$[7]; for 2006-01-29, a relatively low f_v smaller than 60% is obtained. Hence, isotope ratios at Rehovot simulated for this last date have to be interpreted more cautiously than for the other days. Note that on 2006-01-29 also more clouds occurred in the Mediterranean region compared to the other three cases (cf. section 6.4.1), making the simulation of isotope ratios (with the current model version) still less reliable.

The spatial pattern of f_v in water vapor close to the earth surface (on the lowest COSMO model level, that is about 20 m above ground) is shown in Figure 6.12 at 12 UTC on each of the four measurement days. As expected, the highest values of f_v, at certain locations more than 90%, occur over the ocean. The pattern over land is very variable, depending on the atmospheric flow conditions. On 2001-11-18, 2003-03-27 and 2006-01-29, f_v values in the order of 60% can be observed over north-eastern Africa and the northern part of the Arabian Peninsula, owing to the mainly north-westerly or northerly flow in the eastern Mediterranean region during the preceding hours (see also Fig. 6.6). On 2005-04-14, the flow was more westerly, leading to lower values over Africa and larger values over Turkey and Syria. In these regions, there is a

[7] A value of 60% is applied as a benchmark for the fraction of tagged water, paralleling the threshold of Ra in chapters 4 and 5.

Date	f_v [%]	d from $\text{COSMO}_{\text{iso}}$ [‰]	d from Lag. model [‰]	Measured d [‰]
2001-11-18	70	37.6	37.4	41.1
2003-03-27	65	21.5	22.5	18.8
2005-04-14	85	7.7	9.4	9.3
2006-01-29	57	28.0	25.4	28.1

Table 6.3. *Simulated tagged water vapor fraction and d-excess at Rehovot from* $\text{COSMO}_{\text{iso}}$ *case studies. Numbers give mean values for the corresponding measurement periods (specific humidities have been averaged over the four adjacent grid points before calculating* f_v *and d for each time step; the temporal averages have been weighted with the simulated specific humidity of total water vapor). The last two columns comprise simulated d-excess using the Lagrangian approach described in chapter 5 and measured d for comparison.*

stronger decrease of f_v further inland (compared e.g. to Egypt on the other days) due to blocking of the low level flow by the more pronounced orography (in particular, the western ridge of the Anatolian mountains is clearly visible in the f_v field, compare with Fig. 6.1). It should be noted here that the wave-like patterns of f_v that emerge over the ocean at 12 UTC, 2003-03-27, can also be observed in the q_v field at this time instance (not shown), indicating that this feature is not an artefact of the tagging implementation.

In order to exemplarily illustrate the vertical distribution of tagged water vapor, Figure 6.13a shows the integral fraction of tagged vapor in the vertical column, calculated as

$$f_v^{\text{int}} = \frac{\int_0^{z_{\text{top}}} q_v^t \, dz}{\int_0^{z_{\text{top}}} q_v \, dz},$$

at 12 UTC, 2001-11-18. Compared to the pattern of f_v on the lowest model level, the influence of the atmospheric flow on f_v^{int} is even larger, since above the boundary layer, surface evaporation and turbulent mixing are no longer important and the distribution of q_v^t is mainly determined by quasi-horizontal advection along (moist) isentropes and, under certain conditions, by deep convection. In general, the values of f_v^{int} are smaller than f_v on the lowest level, because the source of tagged water is located at the surface. In the example shown in Fig. 6.13, only over the south-eastern Mediterranean Sea, the Red Sea and Egypt larger areas with $f_v^{\text{int}} > 60\%$ can be found. Figure 6.13b shows a vertical cross section of f_v along a transect from Tunisia over the eastern Mediterranean Sea, Cyprus and Syria to Iraq. It indicates that over the ocean the tagged water vapor is well mixed within the boundary layer up to a height of ca. 1500-2000 m. This layer is topped by a region of increased vertical stability, as shown by the black isentropes in Fig. 6.13b. Above the boundary layer, almost no tagged vapor can be found, except for one extended structure close to the Greek coast that reaches up to almost 8000 m. This structure

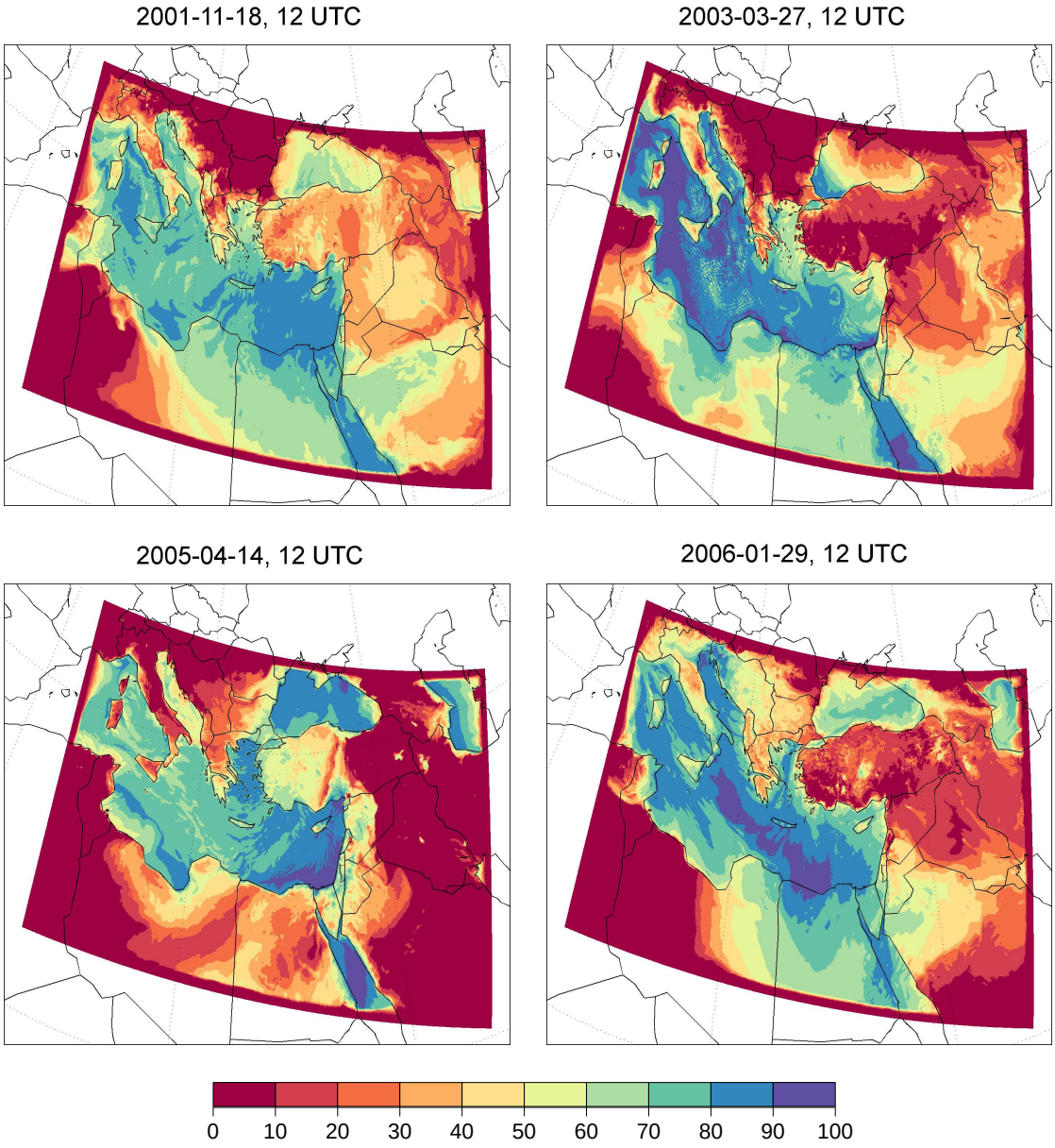

Figure 6.12. *Fraction of tagged water vapor f_v in % on the lowest* COSMO *model level at 12 UTC on each measurement day.*

might result from convective vertical transport of tagged moisture from the boundary layer into the free troposphere. Another mechanism that might lead to the formation of such structures is a strong vertical sloping of isentropes associated with enhanced baroclinity (which is, however, not observable in Fig. 6.13b). Over the Asian continent, f_v is substantially smaller than over the ocean. This fact again is partially related to blocking of the flow from the ocean by the Lebanese coastal mountains, which have about the same height as the oceanic boundary layer. Particularly over the eastern part of the continental domain tagged moisture has been transported to greater

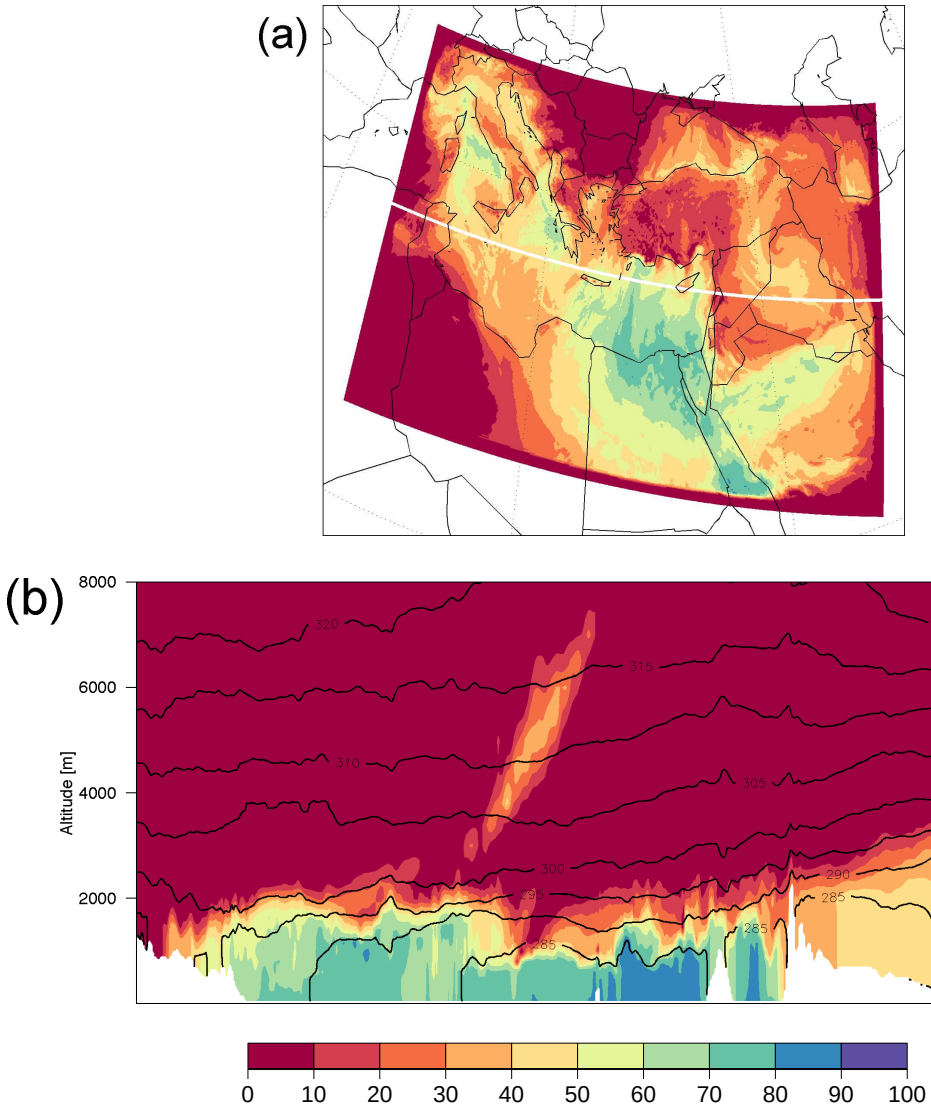

Figure 6.13. *(a) Integral fraction of tagged water vapor in the vertical column f_v^{int} at 12 UTC, 2001-11-18, given in %. (b) Vertical cross section of the tagged water vapor fraction f_v (color) and potential temperature (black contours) along the white line shown in (a). White masked regions indicate the model orography along the cross section.*

altitudes (in comparison to the oceanic atmosphere), probably owing to the reduced vertical stability in this region.

In summary, the results presented in this section show that the approach introduced in this study (combination of water isotope simulation with explicit tagging of moisture that evaporates from the ocean) can principally be applied for the simulation of isotope ratios in water vapor close

to the surface, since a substantial amount of vapor can be tagged within a few days of model simulation. In three of the four selected case studies, the fraction of tagged humidity f_v at Rehovot in the measurement periods is larger than 60%. However, the analyses of the spatial and temporal variability of f_v have shown that the success of the method in a particular case depends on the location where simulated isotope ratios are to be interpreted and on the specific meteorological situation. In general, with the current model version the approach is best suited for the simulation of isotope ratios over the ocean or close to the coast, preferably in downwind direction from the sea. Still, it is important to keep in mind that, also if more than 60% of the moisture has been tagged and its isotope ratios have been simulated, a certain bias might be introduced by the unknown isotopic composition of the remaining humidity (that amounts to 40% or less).

6.4.4 Simulated isotope fields

In this section, isotope ratios in near-surface water vapor are presented that have been simulated with $\text{COSMO}_{\text{iso}}$. In order to minimize the influence of cloud formation on the isotope results (cf. section 6.4.1) and to avoid biases introduced by the moisture fraction that could not be tagged within the simulation (see section 6.4.3 and chapter 5), the focus is again laid on deuterium excess.

Figure 6.14 shows time series of simulated d-excess at Rehovot for the four case studies. These values have been obtained by averaging all specific humidities (of tagged and isotope vapor) from the four adjacent model grid points and applying equation (6.11) for the calculation of isotope ratios. For $1\% < f_v < 60\%$, d is displayed as a gray, for $f_v > 60\%$ as a black line (no values of d are shown for $f_v < 1\%$). As for the tagged water vapor fraction (cf. Fig. 6.11), there are certain differences in the variability of d between the four cases: On the one hand, in the 2006-01-29 run d is fairly constant over more than two days (the fluctuations in the beginning are not very important due to the low value of f_v). On the other hand, for the 2001-11-18 case there is a large increase in d of more than 20‰ within roughly the same time span. This increase correlates with a decrease in specific humidity (see again Fig. 6.11) and is related to the transport of very dry air from the north to Rehovot (cf. Fig. 6.6). The other two cases are intermediate with respect to the variability of d. In the 2003-03-27 simulation d exhibits some short term fluctuations with moderate magnitude; in the 2005-04-14 case there are larger variations during the last one and a half days. The strong fluctuations in the beginning of this model run are related to the alternating oceanic and continental air masses that have also caused the variability in f_v and q_v in this case. However, again the absolute value of f_v is too low to justify confidence in the simulation of d during this initial period, in particular regarding the maxima around 00 UTC, 2005-04-13.

In order to compare these simulations of d to the measurements, the modeled values have been

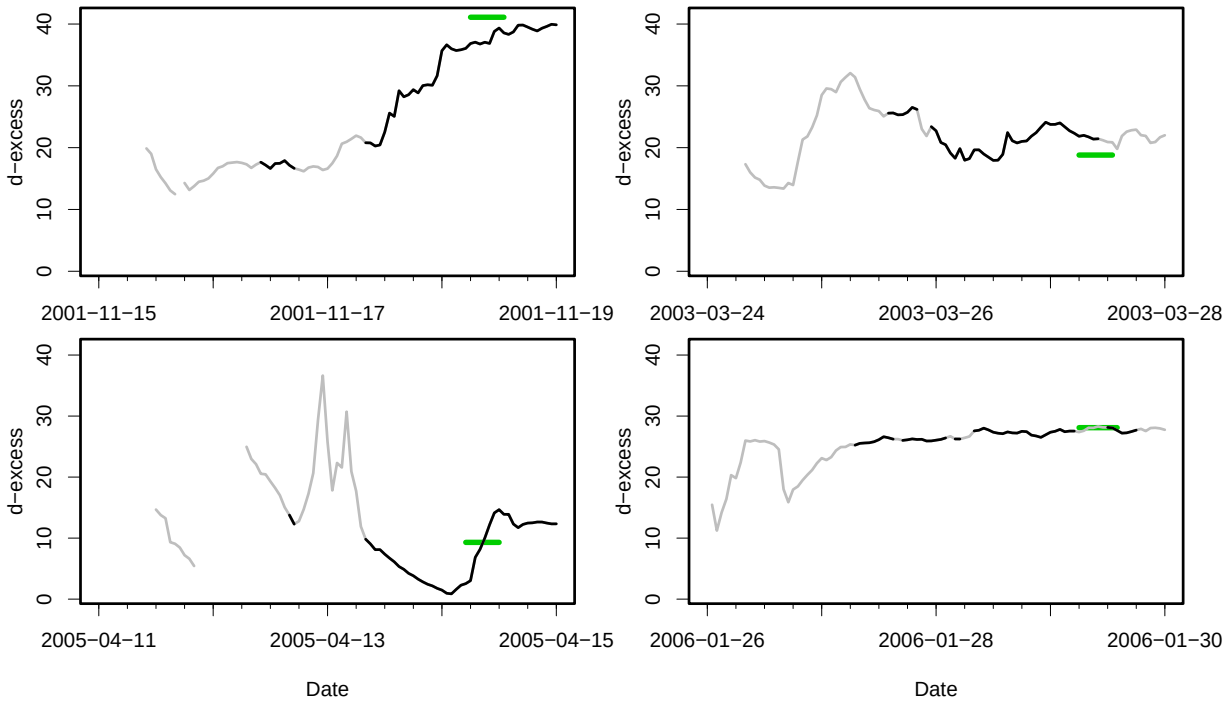

Figure 6.14. *Time series of simulated d-excess (in ‰) at Rehovot from the four* $\text{COSMO}_{\text{iso}}$ *case study simulations. Periods for which the fraction of tagged vapor* f_v *is larger than 60% are highlighted in black. If* $f_v < 1\%$*, no values are shown for d. The green lines indicate the observed values during the measurement periods.*

averaged over the measurement periods, as above weighted with the humidity of total vapor. Table 6.3 shows the resulting values together with the respective results from the Lagrangian model introduced in chapter 5. As can be seen from the Table, the overall variability of the four measurements is pretty well captured by $\text{COSMO}_{\text{iso}}$. The absolute differences between simulated and measured d values $|d_{\text{mod}} - d_{\text{meas}}|$ are always smaller than 4‰, the mean value of these absolute differences is 2.0‰. Moreover, the performance of $\text{COSMO}_{\text{iso}}$ compares well with that of the Lagrangian model (for which the mean absolute deviation from the measurements is 2.5‰). The largest difference between measurement and $\text{COSMO}_{\text{iso}}$ simulation occurs on 2001-11-18, the day with the highest measured d-excess in the whole data set. The underestimation of d in the model might be related to an insufficiency of the fractionation parameterization to represent such an extreme d-excess value[8]. A similar underestimation is obtained from the Lagrangian model, which uses the same parameterization. Another reason might be an improper timing in $\text{COSMO}_{\text{iso}}$: The measurement on 2001-11-18 falls in a period of increasing simulated d-excess (see Fig. 6.14); if in the simulation this increase occurred too late compared to reality, this would

[8]Recall that the parameter settings in this parameterization have been tuned in chapter 5 in order to obtain an optimal consistency between Lagrangian model results and measurements for the whole data set; this does not necessarily imply a proper representation of the extremes.

also explain part of the underestimation of d. Presumably, this timing issue is relevant for the underassessment of d on 2005-04-14 too. Also on this day, the simulated d-excess variation before and during the measurement is very large. A small shift of this variation to earlier times would have a huge impact on the simulated d value during the measurement period. In contrast, the small modeled variability of d on 2006-01-28 is associated with a very good agreement between measurement and $\text{COSMO}_{\text{iso}}$ result. Interestingly, this agreement is neither affected by the low value of f_v nor by the high amount of clouds that occurred on this day (cf. Fig. 6.7). Finally, the overestimation of d on 2003-03-27, which is even stronger in the Lagrangian simulation, can hardly be explained with a simple temporal shift and is probably related to some principal problem in the isotope simulation approach used here. The strong decrease of f_v during the measurement period (cf. Fig. 6.11) indicates an increasing influence of humidity whose isotope ratios cannot be determined within our model run.

Unfortunately, no measurements are available that allow an assessment of the spatial patterns of d-excess in the Mediterranean region for the four case studies. Hence, we compare $\text{COSMO}_{\text{iso}}$ simulations of these patterns with results from the diagnostic trajectory model approach presented in section 4.4.3 (referred to as DTM in the following). This approach uses the purely diagnostic relationship derived in chapter 4 to translate the relative humidity, which is obtained from the moisture sources of each grid box, into d-excess values. Methodologically, it differs more from the $\text{COSMO}_{\text{iso}}$ simulations than the Lagrangian isotope model introduced in chapter 5 (which uses the same parameterization of isotope fractionation as $\text{COSMO}_{\text{iso}}$) and thus is more suitable for an independent comparison. Figure 6.15 presents the simulated d-excess in near-surface vapor from $\text{COSMO}_{\text{iso}}$ and the DTM at 12 UTC, 2001-11-18. Values are only shown at points where the fraction of tagged or attributable water (f_v or Ra, respectively) is larger than 60%. The d-excess fields from both models exhibit a strong spatial gradient with very high values over the eastern part of the Mediterranean and lower values in the west. Apart from this general pattern, also the quantitative agreement between the two simulations is surprisingly good. Only at the western boundary of the COSMO model domain, close to Sardinia and Tunisia, the d values from $\text{COSMO}_{\text{iso}}$ are a little lower than those from the DTM. Also at 12 UTC on the measurement days of the other three case studies, the d-excess fields from $\text{COSMO}_{\text{iso}}$ and DTM, displayed in Figure 6.16, are fairly consistent. One exception is again the westernmost part of the COSMO domain, where $\text{COSMO}_{\text{iso}}$ values are systematically lower. On 2003-03-27 and 2005-04-14, also over the eastern Mediterranean somewhat lower d-values are obtained from $\text{COSMO}_{\text{iso}}$. The agreement in the eastern part is good for the 2006-01-29 case. In the COSMO simulation of this last case, some unrealistic variability occurs close to the northern coast of the Adriatic Sea. A closer examination of this area reveals that this variability is related to inconsistencies in the pre-processing of the ECMWF skin temperature data, as described in section 6.3. In this situation, the relatively simple SST filter introduced in section 6.3 has not been sufficient to overcome these inconsistencies.

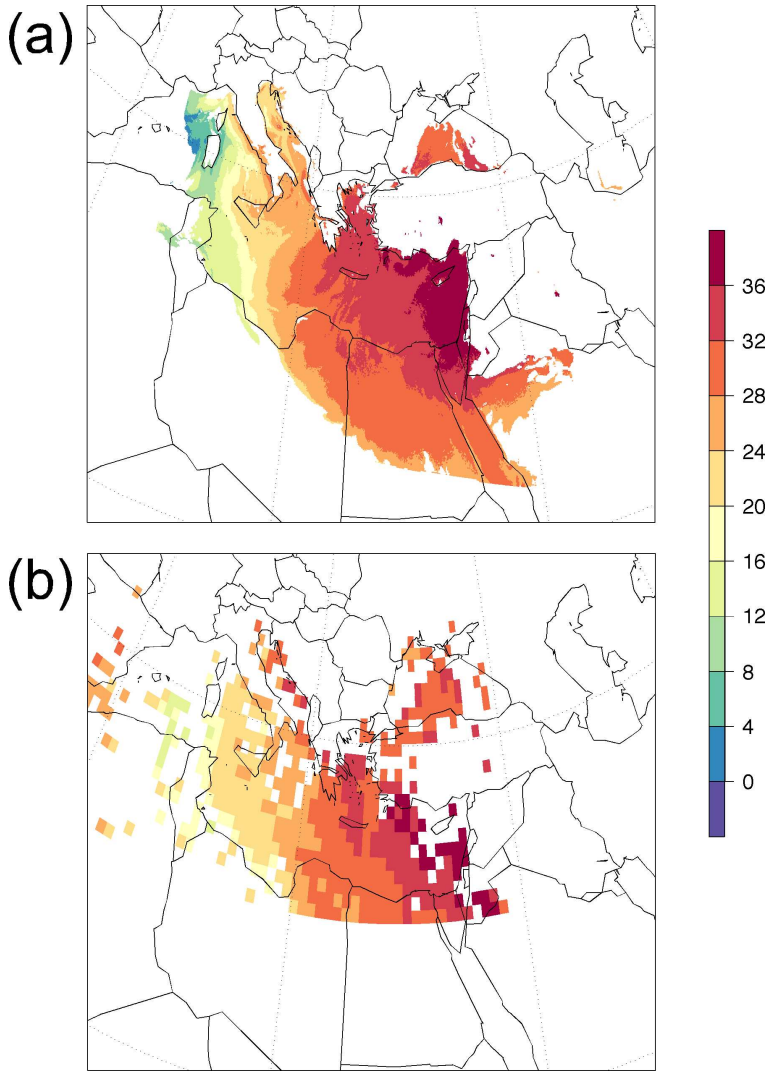

Figure 6.15. *Simulated deuterium excess in water vapor close to the surface, given in ‰, at 12 UTC, 2001-11-18. (a) Results from* $\mathrm{COSMO_{iso}}$ *(on the lowest model level); d is only shown at locations where the tagged vapor fraction* f_v *is larger than 60%. (b) Results from the diagnostic trajectory modeling (DTM) performed in section 4.4.3 (cf. Figure 4.9). Again, only points are shown for which sources could be attributed to more than 60% of the water vapor (*$\mathrm{Ra} > 0.6$*). Note that the* COSMO *model domain extends farther to the south than the domain where the DTM has been applied.*

The systematic difference between d values from $\mathrm{COSMO_{iso}}$ and DTM in the western part of the Mediterranean area most probably results from the proximity of this region to the boundary of the COSMO model domain. Owing to this proximity and the preferably westerly winds, the tagged moisture present in this region (in a $\mathrm{COSMO_{iso}}$ model simulation using the current setup) has mainly been evaporated from local sources. In contrast to that, the DTM has no boundaries

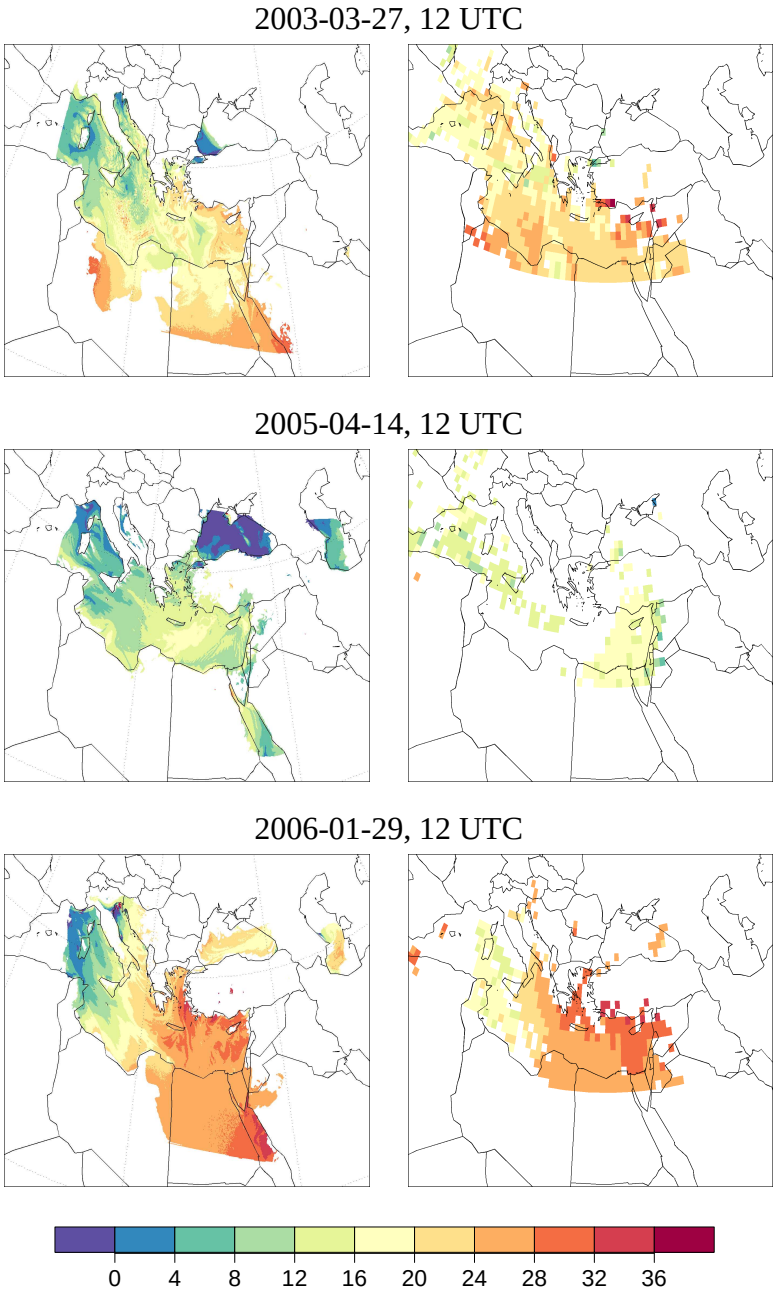

Figure 6.16. *Simulated d-excess in water vapor close to the surface from* $\mathrm{COSMO_{iso}}$ *(left column) and the diagnostic trajectory model DTM (see section 4.4.3; right column) given in ‰, as in Figure 6.15. Points are masked if the fraction of tagged/attributable water (*f_v *or* Ra*, respectively) is lower than 60%.*

and can thus also take more remote moisture sources into account. Since the relative humidity in the Sardinian region is often higher than close to the Spanish coast in the west, these systematic differences in the considered moisture sources are also reflected in a difference in d-excess be-

tween the two models (a lower relative humidity during evaporation leads to a higher *d*-excess, cf. chapter 4). It should however be noted that the sensitivity analysis in section 4.3.3 has shown that local moisture sources might be underestimated by our Lagrangian source analysis (this underestimation might also cause some of the discrepancies over the eastern domain). Therefore, it is not clear which of the two models produces more realistic *d* values in the western Mediterranean. Anyway, it has to be kept in mind that, in order to obtain unbiased isotope ratios from $\text{COSMO}_{\text{iso}}$ model simulations, the main target area should not be located close to the (inflow) boundary of the model domain.

An apparent feature of the $\text{COSMO}_{\text{iso}}$ *d*-excess field at 12 UTC, 2005-04-14 shown in Fig. 6.16 is the extended region with negative values over the Black Sea. Such negative values are rarely observed and sometimes regarded as erroneous in measurements. In the model, basically two processes may generate a negative *d*-excess in water vapor: First, if the ocean is cold and the atmospheric humidity close to, but below the saturation value at the sea surface, the Craig-Gordon parameterization predicts a slightly negative *d* in the evaporation flux[9]. Second, if the atmospheric specific humidity (on the lowest model level) is above the saturation humidity at the ocean surface, a moisture flux from the atmosphere into the ocean occurs. Non-equilibrium fractionation in this flux leads to a relative enrichment of $\delta^{18}\text{O}_{\text{mod}}$ in atmospheric vapor (compared to $\delta^{2}\text{H}_{\text{mod}}$) and thus a decrease of atmospheric *d*-excess. In the case of 2005-04-14, most probably both of these processes contributed to the negative *d* values over the Black Sea. The ocean was very cold in the hours before 12 UTC, and the atmospheric humidity varied around the saturation value. Figure 6.17 exemplarily shows the evaporation flux between 03 and 04 UTC on this day. Over the Black Sea, a region of positive fluxes (i.e. fluxes from the atmosphere into the ocean) has been simulated by the model. In reality, humidity fluxes in this direction have infrequently been observed in the warm sector of extratropical cyclones that moved over a cold ocean (*Neiman et al.*, 1990). The model results presented here suggest that such fluxes may also occur without being enforced by large synoptic disturbances, and that stable water isotopes, in particular the deuterium excess, might be convenient indicators for their occurrence and useful for studying the phenomenon in more detail.

Finally, in addition to the evaluation of simulated deuterium excess, the modeled isotope ratios $\delta^{18}\text{O}_{\text{mod}}$ and $\delta^{2}\text{H}_{\text{mod}}$ are briefly compared to the measurements at Rehovot. The results from $\text{COSMO}_{\text{iso}}$, which have been averaged over the measurement period as described above for *d*-excess, are presented in Table 6.4. As for *d*, the general variability of the measurements is reproduced by $\text{COSMO}_{\text{iso}}$; for both $\delta^{18}\text{O}$ and $\delta^{2}\text{H}$ the rankings of simulated and measured isotope ratios are in perfect agreement (i.e. the highest modeled values correspond to the highest measurements and so on). However, all simulated isotope ratios are positively biased with

[9] In this case, the ratio $\delta^{2}\text{H}_{\text{eq}}/\delta^{18}\text{O}_{\text{eq}}$ is smaller than 8 (cf. section 4.3.1) and the influence of non-equilibrium fractionation is only minor.

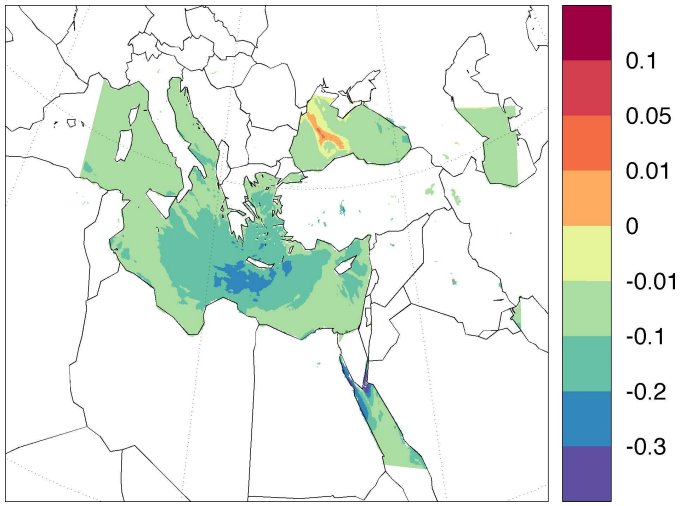

Figure 6.17. *Accumulated evaporation flux from ocean and lakes between 03 and 04 UTC, 2005-04-14, given in* $\mathrm{kg/m^2}$. *Negative values denote fluxes from the surface into the atmosphere, positive fluxes are directed towards the surface.*

Date	$\delta^{18}O_{mod}$ [‰]	$\delta^{18}O_{meas}$ [‰]	$\delta^{2}H_{mod}$ [‰]	$\delta^{2}H_{meas}$ [‰]
2001-11-18	-13.7	-14.6	-72.3	-75.4
2003-03-27	-12.2	-12.5	-76.1	-80.1
2005-04-14	-10.1	-10.9	-72.9	-77.5
2006-01-29	-13.1	-13.8	-77.0	-82.1

Table 6.4. *Simulated ($\delta^{18}O_{mod}$, $\delta^{2}H_{mod}$) and measured ($\delta^{18}O_{meas}$, $\delta^{2}H_{meas}$) isotope ratios at Rehovot.* $COSMO_{iso}$ *model results are mean values for the corresponding measurement periods (specific humidities have been averaged over the four adjacent grid points before calculating δ-values for each time step; the temporal averages have been weighted with the simulated specific humidity of total water vapor).*

respect to the measurements (biases between 0.3‰ and 0.9‰ for $\delta^{18}O$ and between 3.1‰ and 5.1‰ for $\delta^{2}H$, compared to measurement precisions of 0.1‰ and 1‰, respectively). Reasons for these biases are, as mentioned before, the effects of clouds on the isotope ratios (which are not parameterized in the current version of $COSMO_{iso}$) and the presumably more prolonged fractionation history of the untagged water vapor (which is not simulated in the model either). Unfortunately, the number of four data points is too small to allow for a more elaborated statistical analysis of the biases. It is, however, noteable that the biggest deviation between simulated and measured $\delta^{2}H$, for which equilibrium fractionation processes in clouds are thought to play a dominant role (cf. section 4.3.2), has occurred on 2006-01-29, the day with the largest cloud cover in the Mediterranean region (see Fig. 6.7).

6.4.5 Sensitivity experiments

For the 2001-11-18 case study, two sensitivity experiments have been performed in order to investigate the settings of the isotope fractionation parameterization during evaporation from the ocean. In the first of these experiments, isotope ratios from the historical simulation by *Yoshimura et al.* (2008) with the IsoGSM model have been applied for the initialization of the atmospheric vapor in the parameterization routine instead of the global closure assumption (see section 6.3 and chapter 5). The results obtained with this setting are almost entirely identical to those described for the standard setting in section 6.4.4. No changes occur in the simulated isotope ratios at Rehovot and in the spatial pattern of the *d*-excess at 12 UTC, 2001-11-18 (not shown). This indicates that the $COSMO_{iso}$ model results are insensitive to changes in the initialization of atmospheric isotope ratios, which is relevant only at the very first evaporation event in each grid cell (for all subsequent evaporation, the isotope composition of the tagged vapor is applied as boundary condition, see again section 6.3). A similar, but somewhat less pronounced insensitivity has been noted for the Lagrangian model in chapter 5. Consequently, it is not essential to employ external isotope data as boundary condition for the evaporation parameterization in $COSMO_{iso}$. Instead, the global closure assumption can be used. This fact considerably reduces the complexity of data pre-processing necessary for $COSMO_{iso}$ simulations.

In the second sensitivity experiment the parameterization of the non-equilibrium fractionation factor *k* has been altered. Instead of the wind speed independent formulation developed in chapter 5, the classical parameterization by *Merlivat and Jouzel* (1979) has been used. The spatial pattern of the *d*-excess at 12 UTC, 2001-11-18 from this sensitivity run is shown in Fig. 6.18. Comparing this field to the result from the control run shown in Fig. 6.15a, large differences can

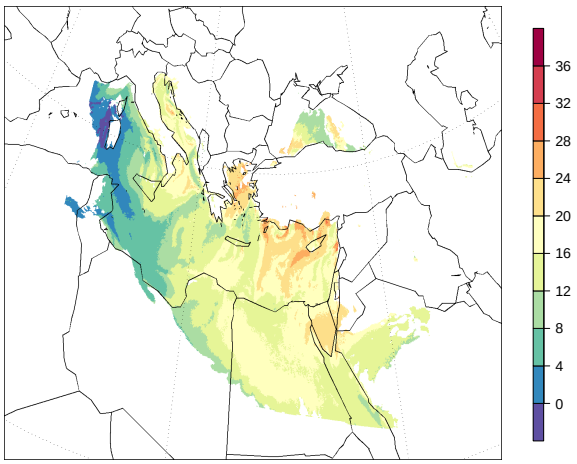

Figure 6.18. *Simulated deuterium excess (in ‰) at 12 UTC, 2001-11-18, as in the upper panel of Figure 6.15, but using the parameterization by Merlivat and Jouzel (1979) for the non-equilibrium fractionation factor k.*

be noticed: *d* is greatly reduced in the sensitivity run, in particular the larger values, leading to a less pronounced spatial gradient over the Mediterranean. The agreement with the DTM model, which does not explicitely calculate non-equilibrium fractionation, is worse for the sensitivity simulation. Also, the *d*-excess value at Rehovot, averaged over the measurement period, which amounts to 18.1‰, is much less consistent with the measured value of 41.1‰ than the result from the control run (37.6‰). Altogether, this indicates that the parameterization of *Merlivat and Jouzel* (1979) leads to similar problems in $COSMO_{iso}$ as in the Lagrangian isotope model (see again chapter 5). In particular, high *d* values are tremendously underestimated. Of course, this conclusion will again have to be confirmed with the help of additional case studies, also from different regions.

6.5 Conclusions

In this chapter, the first steps of the development of a new limited area water isotope model named $COSMO_{iso}$ have been described. A new approach has been introduced that combines the simulation of isotope physics with the implementation of water tracers, which quantify the amount of water that has been evaporated from the ocean during the model run. This new approach allows to simulate all relevant isotope physics within the regional model, without having to rely on external isotope fields (e.g. from a GCM) as boundary condition. Moreover, with the help of the new approach the model can be run in forecast or hindcast mode (making sure that the modeled meteorology is never far from reality, in contrast to default climate simulations) and simulated isotope ratios can directly be compared to measurements on daily to hourly time scales.

With the help of four case studies, it has been demonstrated that our new model approach is principally applicable for the simulation of isotope ratios in water vapor close to the earth's surface. Within three of the four 4-day model runs, it has been possible to simulate the isotope ratios in at least 60% of the water vapor at Rehovot, where isotope measurements have been available, and also over larger areas in the Mediterranean region (primarily over the ocean and near the coast). However, it has also been shown that the actual spatial pattern of tagged moisture strongly depends on the specific meteorological situation. Hence, the success of our approach cannot be a priori guaranteed. Furthermore, it is not yet clear if the method can be applied with comparable success to simulate isotope ratios in cloud water, rain or vapor at higher altitudes (for near-surface vapor, this is relatively easy since it is quite close to the evaporation source). The vertical distribution of tagged vapor that has exemplarily been shown in section 6.4.4 indicates that humidity above the boundary layer may have a much larger residence time than below (at greater heights, the fraction of tagged vapor still is rather small after a 4-day simulation). Of course, this might not be the case in situations characterized by more active weather systems

leading to enhanced vertical moisture transport and precipitation. Altogether, it is well possible that the tagging approach has to be refined to account for more difficult conditions and demands in future applications. One obvious way to do this is the implementation of evapotranspiration from land areas as an additional source for the tagged water cycle. Other possibilities may be to use the COSMO model in nudging mode (that allows to perform more prolonged simulations by nudging the meteorological model fields with observation) or to create an "isotope analysis" with the help of subsequent short term $\text{COSMO}_{\text{iso}}$ forecasts.

The *d*-excess at Rehovot simulated by $\text{COSMO}_{\text{iso}}$ is in very good agreement with the measurements performed there. The variability in the selected measurement data has been properly captured by the model. The performance of $\text{COSMO}_{\text{iso}}$ is comparable to that of the Lagrangian isotope model introduced in chapter 5. Keeping in mind that the latter is based on the meteorological analyses from the ECMWF, whereas in $\text{COSMO}_{\text{iso}}$ also the meteorological conditions in the Mediterranean region are independently simulated, this fact is particularly noteworthy. Also for the isotope ratios $\delta^{18}\text{O}$ and $\delta^{2}\text{H}$, there is a fair agreement between $\text{COSMO}_{\text{iso}}$ simulations and measurements, except for a positive bias of the model results that can be explained with the omission of in-cloud fractionation processes in the model. In order to perform a statistical evaluation of the simulated isotope results with respect to the measurements, the number of four case studies that have been performed so far is not sufficient. Additional simulations will be conducted in the future.

The spatial distribution of $\text{COSMO}_{\text{iso}}$ *d*-excess compares well with the corresponding patterns from the diagnostic trajectory model described in chapter 4. There is a lot of spatial variability in the simulated *d*-excess fields that cannot yet be validated with measurements. Hopefully, this will be possible in the future using additional observations, in particular from satellites. To date, satellite measurements of water isotopes have only been performed for middle and upper tropospheric vapor (e.g. *Worden et al.*, 2007). Also the temporal variability of *d* at Rehovot on sub-daily time scales simulated by $\text{COSMO}_{\text{iso}}$ is often rather large. These short term variations cannot yet be directly verified with measurements[10]. Nevertheless, they give support to the hypothesis that stable isotopes may be used as valuable proxies of the atmospheric hydrological cycle also on very short time scales.

As mentioned before, the implementation of water tagging and isotope physics in the COSMO model performed here primarily serves as a starting point. The model will be completed in future work, and parameterizations for all fractionation processes in the atmospheric water cycle will be included, in particular during the formation of clouds and precipitation and the interaction

[10] Measurements of stable isotopes on hourly basis performed at the Weizmann Institute during the second half of 2008 reveal similar short term variability (Leon Peters, *pers. comm.*). These measurements will be used to evaluate the $\text{COSMO}_{\text{iso}}$ simulations in future work.

of atmospheric moisture with the land surface. With the evaluation performed in this chapter, it has been validated that the first step of the water cycle, evaporation from the ocean, is properly represented in the model.

Chapter 7

Outlook

The main objective of this thesis has been to improve our understanding of physical processes that link climate parameters and proxy data and are thus important for the reconstruction of past climate and weather events. Technically, several methods have been applied in order to address this objective, encompassing statistical data analyses, Lagrangian trajectory calculations and atmospheric simulations using a mesoscale limited-area model. The focus has been on the investigation of two specific types of climate proxies, data from lake sediments and stable water isotopes.

In the first part of this thesis, a comprehensive meteorological data set has been presented and statistically analyzed. In future research, this data set may be applied for exploring correlations between climate parameters and lake sediment data. In this way, new climate proxies, particularly for the reconstruction of extreme weather events, can be established and investigated using statistical calibration methods. A first pilot study, focusing on the calibration of a proxy for extreme windstorms (see chapter 3) demonstrates the feasibility and usefulness of this approach. In this study, a geological hypothesis on the correlation between windstorms and peaks of the quartz grain concentration in a sediment core has been verified with the help of the meteorological data. This correlation may become the basis for the reconstruction of paleo-windstorm records from lake sediments. However, the rather small number of windstorms recovered in the core has not been sufficient to establish a quantitative transfer function, for example in terms of a threshold value of wind velocity whose exceedance leads to the formation of a storm layer in the sediment. This may be achieved in future studies by using data from other suitable lakes. Altogether, in this first part of the thesis the physical processes determining proxy signals have not been studied directly (e.g. by probing the sediment transport in a lake), but a rather general framework has been established for evaluating physically-based hypotheses on these processes through the application of statistical methods to high-quality climatological data sets.
The data and methods introduced in chapters 2 and 3 may also be useful for other investiga-

tions that are not directly related to paleoclimate proxies. For instance, they can be applied for validating climate model simulations with respect to the local climate in the Eifel region. In addition, certain climatological features discovered here might become starting points for further research, like the variability of drought occurrence on decadal time scales (and its potential relation to atmospheric circulation modes) or the contemporaneity of flood events on relatively large spatial scales. Two additional aspects of the meteorological data base that have not been fully addressed in this thesis, but might be important for future research are the temporal homogeneity of the data (which has to be checked in a more thorough way if e.g. temporal trends are investigated) and the issue of interpolating a meteorological parameter to an arbitrary location (for which the simple, linear method applied here might not be sufficient if the interpolated values shall be interpreted more quantitatively).

The second part of this thesis has been concerned with the analysis of stable isotopes in atmospheric water vapor. By focusing on short, synoptic time scales, the physical processes determining these isotope ratios could be directly explored. In particular, quantitative transfer functions have been obtained for the correlation between deuterium excess and environmental conditions during water evaporation from the ocean, and physical parameterizations of the relevant processes have been tested and complemented. Owing to the specific focus of this approach (short time scales, water vapor, evaporation from the ocean), the results are not immediately applicable for the interpretation of proxy data[1]. Nevertheless, the methods developed here may also be used as a basis for the calibration of ice core data in future research. The Lagrangian diagnostic introduced in chapter 4 can be expanded to account for additional processes associated with precipitation formation, and it should be relatively straightforward to use this approach also on longer time scales (cf. *Sodemann et al.*, 2008b). Furthermore, better constraints on specific fractionation processes obtained with the help of the numerical models introduced in chapters 5 and 6 (e.g. the new parameter settings for the Craig-Gordon model) could be important for a more realistic simulation of water isotopes in GCMs. As the results from isotope GCMs are essential for many paleoclimatological applications (e.g. with respect to the non-stationarity of the isotope-temperature relationship in time during different climate regimes), this would have important indirect consequences for the interpretation of proxy records.
Again, several methodological advancements described in the second part of this work are directly helpful for other research areas not immediately related to climate proxies. The setting of the Craig-Gordon parameterization of isotope fractionation during evaporation from the ocean can be adopted for various applications, for instance in hydrology. In addition, this parameterization can be combined with recent trajectory models for fractionation in clouds (*Helsen et al.*, 2007; *Sodemann et al.*, 2008a) in order to obtain an extensive Lagrangian isotope model,

[1] However, the weak correlation between d-excess and SST at least challenges the physical foundation of source temperature reconstructions from ice cores.

which would be suitable for incorporating more realistic boundary conditions than the "classical" Rayleigh models. A progressive development of $COSMO_{iso}$ opens many opportunities for process-oriented investigations on the short term isotope variability in atmospheric waters. In particular, it will be possible to explore isotope signals from specific weather systems, also by directly comparing the simulated isotope ratios to measurements. On the one hand, this will hopefully improve our understanding of different fractionation processes. On the other hand, it might open the way for applying water isotopes as a diagnostic tool also on synoptic time scales. For instance, the isotopes in surface precipitation might carry information on cloud formation temperatures, rain evaporation rates and water origin.

In conclusion, this discussion shows that the present thesis, by focusing on the development of novel methodological approaches, serves as an important starting point for future studies on different aspects of paleoclimate research. Moreover, the process understanding obtained from analyzing present-day climate conditions can also be useful in other areas of atmospheric sciences.

Appendix A

^{210}Pb Measurements from the SMf Core

Table A.1 and Figure A.1 show the ^{210}Pb data that have been used to construct the age model of the SMf sediment core. These data were measured by direct gamma assay in the Liverpool University Environmental Radioactivity Laboratory. Supported ^{210}Pb activity was assumed to be equal to the measured activity of ^{226}Ra.

The overall trend of ^{210}Pb activity closely approximates that of an exponential relation down to a depth of around 20 cm, where equilibrium with supporting ^{226}Ra is reached. However, this trend is punctuated by three layers with greatly reduced activity at 12.5 cm, 15.5 cm and 17.5 cm. These layers are also characterized by reduced ^{226}Ra concentrations and, in two cases, a reduced water content. They most probably have been formed by rearrangement of older material from the periphery of the maar. In the case of the layer at 15.5 cm, this rearrangement may have coincided with the formation of the windstorm layer at 15 cm; the other two layers are not

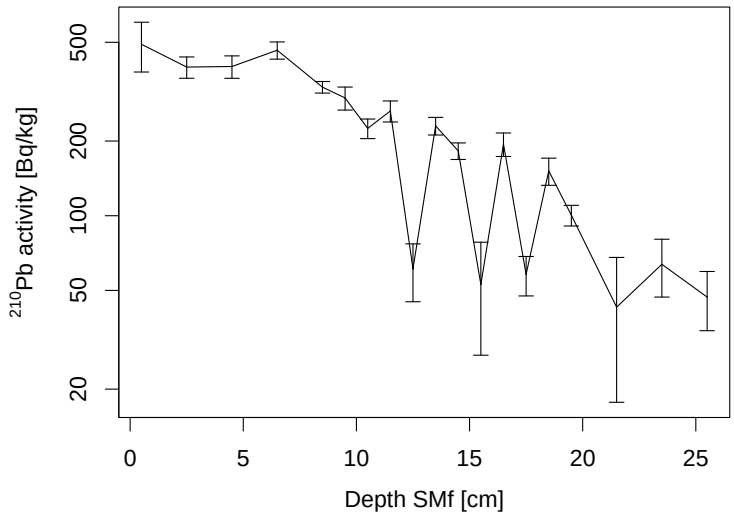

Figure A.1. *Measured total* ^{210}Pb *activity from the SMf core.*

Depth [cm]	^{210}Pb total Bq/kg	^{210}Pb total ±	^{210}Pb supported Bq/kg	^{210}Pb supported ±
0.5	490.9	111.4	79.8	5.7
2.5	397.3	39.2	79.8	5.7
4.5	399.4	41.4	79.7	8.1
6.5	464.6	37.0	88.0	10.3
8.5	329.8	17.7	80.4	5.0
9.5	298.3	31.7	77.5	8.3
10.5	224.9	20.4	61.3	5.4
11.5	264.4	25.7	63.8	6.7
12.5	61.0	16.0	41.3	3.6
13.5	230.3	18.8	62.6	4.4
14.5	182.5	14.0	79.3	4.1
15.5	52.8	25.4	53.2	6.1
16.5	194.4	21.1	82.0	6.6
17.5	58.0	10.5	23.9	2.6
18.5	151.6	19.0	57.2	4.5
19.5	100.5	9.6	58.3	2.3
21.5	42.8	25.1	61.9	5.2
23.5	63.7	16.7	59.0	3.2
25.5	47.0	12.6	59.9	3.9

Table A.1. *Total and supported* ^{210}Pb *activity from the SMf core.*

related to increased silt concentrations. All three layers with reduced ^{210}Pb activity have been excluded from the calculation of the age model. Since the trend in unsupported ^{210}Pb activity suggests that this activity should be above limits of detection down to a depth of around 30 cm, there might be a hiatus in the sediment in a depth of 20 cm (where the measurements indicate equilibrium between ^{210}Pb and ^{226}Ra). This hiatus does not influence the windstorm allocation performed in this study, because we only use data from depths above 20 cm. In order to avoid impacts on the chronology, the final CRS age model has been calculated using the ^{137}Cs/^{210}Pb marker of the 1963 fallout maximum as a reference point.

Appendix B

Technical Remarks on $\mathrm{COSMO}_{\mathrm{iso}}$ Variables and Namelists

This appendix contains two tables that can be helpful for the setup of $\mathrm{COSMO}_{\mathrm{iso}}$ model runs. Table B.1 describes all variables that have been added to the COSMO model as GRIB output fields. These variables are contained in a new GRIB table with table number 206. Table B.2 shows the namelist parameters of the new namelist `ISOCTL` and describes their possible and default settings.

Variable	Code	Level	Unit	Note
QVTAG	1	110	kg/kg	q_v^t
QV18O	2	110	$\mathrm{kg}/(\mathrm{kg}\cdot\mathrm{VSMOW}\cdot j)$	${}^{18}q_v$
QV2H	3	110	$\mathrm{kg}/(\mathrm{kg}\cdot\mathrm{VSMOW}\cdot j)$	${}^{2}q_v$
QCTAG	4	110	kg/kg	q_c^t
QC18O	5	110	$\mathrm{kg}/(\mathrm{kg}\cdot\mathrm{VSMOW}\cdot j)$	${}^{18}q_c$
QC2H	6	110	$\mathrm{kg}/(\mathrm{kg}\cdot\mathrm{VSMOW}\cdot j)$	${}^{2}q_c$
QITAG	7	110	kg/kg	q_i^t
QI18O	8	110	$\mathrm{kg}/(\mathrm{kg}\cdot\mathrm{VSMOW}\cdot j)$	${}^{18}q_i$
QI2H	9	110	$\mathrm{kg}/(\mathrm{kg}\cdot\mathrm{VSMOW}\cdot j)$	${}^{2}q_i$
QRTAG	10	110	kg/kg	q_r^t
QR18O	11	110	$\mathrm{kg}/(\mathrm{kg}\cdot\mathrm{VSMOW}\cdot j)$	${}^{18}q_r$
QR2H	12	110	$\mathrm{kg}/(\mathrm{kg}\cdot\mathrm{VSMOW}\cdot j)$	${}^{2}q_r$
QSTAG	13	110	kg/kg	q_s^t
QS18O	14	110	$\mathrm{kg}/(\mathrm{kg}\cdot\mathrm{VSMOW}\cdot j)$	${}^{18}q_s$
QS2H	15	110	$\mathrm{kg}/(\mathrm{kg}\cdot\mathrm{VSMOW}\cdot j)$	${}^{2}q_s$
PRR_TAG_G	16	1	$\mathrm{kg}/(\mathrm{m}^2\cdot\mathrm{s})$	$P_r^{\mathrm{gsp},t}$
PRR_18O_G	17	1	$\mathrm{kg}/(\mathrm{m}^2\cdot\mathrm{s}\cdot\mathrm{VSMOW}\cdot j)$	${}^{18}P_r^{\mathrm{gsp}}$
PRR_2H_G	18	1	$\mathrm{kg}/(\mathrm{m}^2\cdot\mathrm{s}\cdot\mathrm{VSMOW}\cdot j)$	${}^{2}P_r^{\mathrm{gsp}}$
PRS_TAG_G	19	1	$\mathrm{kg}/(\mathrm{m}^2\cdot\mathrm{s})$	$P_s^{\mathrm{gsp},t}$
PRS_18O_G	20	1	$\mathrm{kg}/(\mathrm{m}^2\cdot\mathrm{s}\cdot\mathrm{VSMOW}\cdot j)$	${}^{18}P_s^{\mathrm{gsp}}$
PRS_2H_G	21	1	$\mathrm{kg}/(\mathrm{m}^2\cdot\mathrm{s}\cdot\mathrm{VSMOW}\cdot j)$	${}^{2}P_s^{\mathrm{gsp}}$
PRR_TAG_C	22	1	$\mathrm{kg}/(\mathrm{m}^2\cdot\mathrm{s})$	$P_r^{\mathrm{con},t}$
PRR_18O_C	23	1	$\mathrm{kg}/(\mathrm{m}^2\cdot\mathrm{s}\cdot\mathrm{VSMOW}\cdot j)$	${}^{18}P_r^{\mathrm{con}}$
PRR_2H_C	24	1	$\mathrm{kg}/(\mathrm{m}^2\cdot\mathrm{s}\cdot\mathrm{VSMOW}\cdot j)$	${}^{2}P_r^{\mathrm{con}}$

Table B.1. *GRIB table that has been introduced for the GRIB output of the new* $\mathrm{COSMO}_{\mathrm{iso}}$ *model variables, describing tagged (index t) and isotope (indices 18 for* $H_2{}^{18}O$ *and 2 for* HDO*) moisture fields. The corresponding GRIB table number is 206. The Level code 110 denotes three-dimensional atmospheric fields, level code 1 denotes 2-d surface fields. VSMOW is the isotopic composition of Vienna Standard Mean Ocean Water (for the respective isotope), j is the ratio of the molecular weights of the heavy isotope and standard water. q denotes specific humidity,* P^{gsp} *and* P^{con} *give the rates of grid scale and convective precipitation at the surface, and* R^{gsp} *and* R^{con} *denote the corresponding accumulated precipitation fluxes.* q^{int} *gives the vertical integral of a moisture field, E denotes the accumulated evaporation flux. Finally, v stands for water vapor, c for cloud water, i for cloud ice, r for rain and s for snow.*

Variable	Code	Level	Unit	Note
PRS_TAG_C	25	1	$\mathrm{kg}/(\mathrm{m}^2 \cdot \mathrm{s})$	$P_s^{\mathrm{con},t}$
PRS_18O_C	26	1	$\mathrm{kg}/(\mathrm{m}^2 \cdot \mathrm{s} \cdot \mathrm{VSMOW} \cdot j)$	${}^{18}P_s^{\mathrm{con}}$
PRS_2H_C	27	1	$\mathrm{kg}/(\mathrm{m}^2 \cdot \mathrm{s} \cdot \mathrm{VSMOW} \cdot j)$	${}^{2}P_s^{\mathrm{con}}$
RAIN_TAG_G	28	1	kg/m^2	$R_r^{\mathrm{gsp},t}$
RAIN_18O_G	29	1	$\mathrm{kg}/(\mathrm{m}^2 \cdot \mathrm{VSMOW} \cdot j)$	${}^{18}R_r^{\mathrm{gsp}}$
RAIN_2H_G	30	1	$\mathrm{kg}/(\mathrm{m}^2 \cdot \mathrm{VSMOW} \cdot j)$	${}^{2}R_r^{\mathrm{gsp}}$
SNOW_TAG_G	31	1	kg/m^2	$R_s^{\mathrm{gsp},t}$
SNOW_18O_G	32	1	$\mathrm{kg}/(\mathrm{m}^2 \cdot \mathrm{VSMOW} \cdot j)$	${}^{18}R_s^{\mathrm{gsp}}$
SNOW_2H_G	33	1	$\mathrm{kg}/(\mathrm{m}^2 \cdot \mathrm{VSMOW} \cdot j)$	${}^{2}R_s^{\mathrm{gsp}}$
RAIN_TAG_C	34	1	kg/m^2	$R_r^{\mathrm{con},t}$
RAIN_18O_C	35	1	$\mathrm{kg}/(\mathrm{m}^2 \cdot \mathrm{VSMOW} \cdot j)$	${}^{18}R_r^{\mathrm{con}}$
RAIN_2H_C	36	1	$\mathrm{kg}/(\mathrm{m}^2 \cdot \mathrm{VSMOW} \cdot j)$	${}^{2}R_r^{\mathrm{con}}$
SNOW_TAG_C	37	1	kg/m^2	$R_s^{\mathrm{con},t}$
SNOW_18O_C	38	1	$\mathrm{kg}/(\mathrm{m}^2 \cdot \mathrm{VSMOW} \cdot j)$	${}^{18}R_s^{\mathrm{con}}$
SNOW_2H_C	39	1	$\mathrm{kg}/(\mathrm{m}^2 \cdot \mathrm{VSMOW} \cdot j)$	${}^{2}R_s^{\mathrm{con}}$
TQVTAG	40	1	kg/m^2	$q_v^{\mathrm{int},t}$
TQCTAG	41	1	kg/m^2	$q_c^{\mathrm{int},t}$
TQITAG	42	1	kg/m^2	$q_i^{\mathrm{int},t}$
TQRTAG	43	1	kg/m^2	$q_r^{\mathrm{int},t}$
TQSTAG	44	1	kg/m^2	$q_s^{\mathrm{int},t}$
EVAPTAG	45	1	kg/m^2	E_v^t
EVAP18O	46	1	$\mathrm{kg}/(\mathrm{m}^2 \cdot \mathrm{VSMOW} \cdot j)$	${}^{18}E_v$
EVAP2H	47	1	$\mathrm{kg}/(\mathrm{m}^2 \cdot \mathrm{VSMOW} \cdot j)$	${}^{2}E_v$

Table B.1. *(continued)*

Name	Type	Description	Default
`liso`	LOG	Main switch for isotope simulation (from namelist `RUNCTL`).	TRUE
`imodturcor_iso`	INT	Type of turbulent transport correction with respect to sub-grid scale clouds (see appendix C); 0: no correction, 1: parameterization with revised liquid water content, 2: parameterization using the fluxes of q_w and θ_w.	1
`ltagreg`	LOG	Water tagging only in a pre-defined region, specified by parameter `regbound`.	FALSE
`regbound`	REAL	Region for water tagging. Four values have to be given, specifying minimum longitude, maximum longitude, minimum latitude and maximum latitude in rotated coordinates.	(0. ,0. ,0. ,0.)
`lmassfcor_iso`	LOG	Mass flux correction of isotope fields after vertical diffusion.	TRUE
`roce_iso`	REAL	Isotope ratios of the ocean water, relative to VSMOW ($^{18}R_L/^{18}R_{\mathrm{VSMOW}}$, $^{2}R_L/^{2}R_{\mathrm{VSMOW}}$).	(1.0017, 1.0082)
`levapext_iso`	LOG	Boundary isotope values of the atmospheric vapor for the evaporation parameterization are provided as external data (R_A at first evaporation event).	FALSE
`imodevap_iso`	INT	Type of parameterization for isotope fractionation during water evaporation from the ocean; 1: classical parameterization after *Merlivat and Jouzel* (1979), 2: new, wind speed independent parameterization from chapter 5.	2
`expk_iso`	REAL	Exponent for non-equilibrium fractionation factor if `imodevap_iso`=2.	0.24

Table B.2. *Namelist parameters from the new namelist* `ISOCTL` *(except for* `liso`*, which belongs to the namelist* `RUNCTL`*).*

Appendix C

Sub-grid Scale Clouds in $\mathrm{COSMO}_{\mathrm{iso}}$

As outlined in section 6.2.3, in the turbulence parameterization routine of the COSMO model two steps are performed that directly or indirectly influence the transport of water species in the model: First, the turbulent transport coefficients are calculated, which are used to parameterize vertical turbulent fluxes and surface layer fluxes. These transport coefficients can be applied for the tagged water species in the same way as for total water, thus no adaptations for water tagging have to be made in this first step. Second, an adjustment of the vertical fluxes of water vapor and cloud water is performed within the turbulence parameterization (by updating the tendencies of q_v and q_c). This adjustment integrates the effects of subgrid-scale cloudiness, using a variant of the statistical cloud condensation scheme by *Sommeria and Deardorff* (1976). In order to develop a fully consistent tagging model, these effects also have to be considered for the tagged water quantities, denoted $q_{v,t}$ and $q_{c,t}$ in this chapter. Therefore, in the following the flux adjustment is described in some detail (referring to an unpublished document by M. Raschendorfer, DWD, and the COSMO Fortran code) and its adaption for the tagged water fields is outlined.

In the warm cloud condensation scheme by *Sommeria and Deardorff* (1976), cloud condensation is assumed to occur at certain, statistically distributed locations within grid boxes that are not entirely saturated. A bivariate Gaussian distribution is assumed for the cloud conservative variables q_w (total water content) and θ_w (liquid water potential temperature) in such a grid box. These variables are defined as follows:

$$q_w = q_v + q_c\,, \tag{C.1}$$

$$\theta_w = \theta - \vartheta_c \cdot q_c\,, \tag{C.2}$$

where θ denotes potential temperature and ϑ_c is given by

$$\vartheta_c = \frac{L_c}{c_{pd} r_p}\,, \tag{C.3}$$

with L_c being the specific heat of condensation, c_{pd} the specific heat capacity of dry air for constant pressure and r_p the Exner factor. This factor is given by

$$r_p = \left(\frac{p}{p_r}\right)^{\frac{R_d}{c_{pd}}} \tag{C.4}$$

with p denoting pressure, R_d the gas constant for dry air and finally $p_r = 1000\,\mathrm{hPa}$ the standard reference pressure. In the following, it is assumed that the Exner factor r_p (and thereby also ϑ_c) can be treated like a constant in a given grid cell. With the help of the scheme of *Sommeria and Deardorff* (1976) and given the assumptions for the statistical distribution of q_w and θ_w mentioned above (bivariate normal, with the variances and correlation of these variables estimated from the previous model time step), a revised liquid water content $\tilde{q}_c$, including the effects of subgrid-scale clouds, and a fractional cloud cover r_c can be calculated for each grid box.
In order to parameterize the additional vertical turbulent transport of the prognostic model variables q_v and q_c emerging from this revision of q_c, the fluxes of these prognostic variables are expressed in terms of the fluxes of q_w and θ_w. Using Reynolds decomposition, e.g. the vertical turbulent flux of q_c is given by $\overline{\rho w' q_c'}$, where ρ is the total density of the air, w the vertical wind velocity, and the over-bar denotes a temporal average. In the saturated part of a grid cell, the following approximation can be applied (q_{vs} denotes saturation humidity):

$$q_v' \approx q_{vs}(T) - q_{vs}(\overline{T}) \approx \frac{\partial q_{vs}}{\partial T} T' \approx \frac{\partial q_{vs}}{\partial T} r_p \theta' \,, \tag{C.5}$$

i.e. the temporal fluctuations of water vapor are related to fluctuations of potential temperature by assuming the temperature dependence of the saturation humidity to be the dominant factor. In the following, the derivative of saturation humidity with respect to temperature, $\alpha := \frac{\partial q_{vs}}{\partial T}$, is also treated as a constant within a grid volume. Applying equations (C.1), (C.2) and the approximation given in (C.5), the vertical flux of q_c in the saturated part of a grid cell can be written as follows:

$$\begin{aligned} \overline{\rho w' q_c'} &= \overline{\rho w' q_w'} - \overline{\rho w' q_v'} \\ &\approx \overline{\rho w' q_w'} - r_p \alpha \overline{\rho w' \theta'} \\ &= \overline{\rho w' q_w'} - r_p \alpha \left(\overline{\rho w' \theta_w'} + \vartheta_c \overline{\rho w' q_c'}\right) . \end{aligned} \tag{C.6}$$

Solving this equation for the flux of q_c yields

$$\overline{\rho w' q_c'} = \frac{1}{1 + r_p \alpha \vartheta_c} \left(\overline{\rho w' q_w'} - r_p \alpha \overline{\rho w' \theta_w'}\right) . \tag{C.7}$$

In an unsaturated part of the grid volume, q_c' and thus $\overline{\rho w' q_c'}$ is zero. In the general case of arbitrary partial cloud cover ($0 \leq r_c \leq 1$), assuming that the average values of q_w and θ_w do not

differ between cloudy and cloud-free subdivisions of the grid cell, linear interpolation between the saturated and the unsaturated solution can be applied:

$$\overline{\rho w' q_c'} = \frac{r_c}{1 + r_p \alpha \vartheta_c} \left(\overline{\rho w' q_w'} - r_p \alpha \overline{\rho w' \theta_w'} \right) . \tag{C.8}$$

From equations (C.1) and (C.8), the vertical turbulent flux of q_v is calculated as follows:

$$\overline{\rho w' q_v'} = \frac{1}{1 + r_p \alpha \vartheta_c} \left((1 + r_p \alpha \vartheta_c - r_c) \overline{\rho w' q_w'} + r_p r_c \alpha \overline{\rho w' \theta_w'} \right) . \tag{C.9}$$

As mentioned above, *K*-theory is applied in the COSMO model, i.e. all vertical fluxes are parameterized to be proportional to the vertical gradients of the corresponding parameters. In the current setup of $\text{COSMO}_{\text{iso}}$, the gradients of the original model variables (i.e. without considering subgrid-scale clouds), which are used to calculate turbulent transport in the dynamical part of the model (see section 6.2.3), are subtracted from the gradients calculated from equations (C.8) and (C.9) in the turbulence parameterization. The diffusion equations using these residual gradients are then solved numerically with an explicit scheme, leading to an additional vertical transport of q_v and q_c.

In order to parameterize an additional transport for the tagged water fields, two alternatives are considered. First, the vertical turbulent fluxes of the tagged fields are also expressed in terms of total water content and liquid water potential temperature. Therefore, the tagged total water content is defined analogously to equation (C.1):

$$q_{w,t} = q_{v,t} + q_{c,t} . \tag{C.10}$$

This tagged water content, as q_w, does not change during cloud condensation. In the saturated part of a grid volume, temporal fluctuations of q_v in first order are related to fluctuations of saturation humidity and, by this, temperature (see equation (C.5)) due to instantaneous condensation and evaporation processes. Analogously to the saturation adjustment routine (see section 6.2.5), the fluctuations in tagged specific humidity are thus proportional to q_v':

$$q_{v,t}' = f_t \cdot q_v' , \tag{C.11}$$

where $f_t = \overline{q}_{c,t} / \overline{q}_c$ for $q_v' > 0$ and $f_t = \overline{q}_{v,t} / \overline{q}_v$ for $q_v' < 0$. In the case of arbitrary short term fluctuations the sign of q_v' is neither known nor necessary constant within one model time step. Hence, f_t cannot be exactly determined. However, due to the stochastic nature of the fluctuations, f_t may be approximated by the fraction of tagged total water in the grid cell (which is conserved during cloud formation):

$$f_t \approx \frac{\overline{q}_{w,t}}{\overline{q}_w} . \tag{C.12}$$

Using equations (C.10) and (C.11), the vertical flux of tagged cloud water in the saturated case is given by

$$\overline{\rho w' q'_{c,t}} = \overline{\rho w' q'_{w,t}} - f_t \cdot \overline{\rho w' q'_v}^{\mathrm{sat}} , \tag{C.13}$$

where the water vapor flux under saturated conditions can be calculated by setting $r_c = 1$ in equation (C.9):

$$\overline{\rho w' q'_v}^{\mathrm{sat}} = \frac{r_p \alpha}{1 + r_p \alpha \vartheta_c} \left(\vartheta_c \overline{\rho w' q'_w} + \overline{\rho w' \theta'_w} \right) . \tag{C.14}$$

In the general case of arbitrary cloud cover r_c, linear interpolation is applied to obtain

$$\overline{\rho w' q'_{c,t}} = r_c \left(\overline{\rho w' q'_{w,t}} - f_t \cdot \overline{\rho w' q'_v}^{\mathrm{sat}} \right) \tag{C.15}$$

and (with equation (C.10))

$$\overline{\rho w' q'_{v,t}} = (1 - r_c) \overline{\rho w' q'_{w,t}} + r_c f_t \cdot \overline{\rho w' q'_v}^{\mathrm{sat}} . \tag{C.16}$$

Equations (C.15) and (C.16) (with the help of (C.12) and (C.14)) give the turbulent fluxes of $q_{c,t}$ and $q_{v,t}$ in terms of q_w, $q_{w,t}$ and θ_w. These equations can now be treated in the same way as equations (C.8) and (C.9) for numerically calculating the additional vertical transport of the tagged water species.

A second, alternative way for applying a vertical transport correction to the tagged water fields is to use the revised liquid water content $\tilde{q}_c$ from the subgrid-scale cloud scheme to calculate the changes in tagged water content due to subgrid-scale cloudiness via

$$\Delta q_{c,t} = f_t \cdot (\tilde{q}_c - q_c) \tag{C.17}$$

$$\Delta q_{v,t} = -\Delta q_{c,t} , \tag{C.18}$$

where f_t is given by

$$f_t = \begin{cases} \frac{q_{v,t}}{q_v} & , \quad (\tilde{q}_c - q_c) \geq 0 \\ \frac{q_{c,t}}{q_c} & , \quad (\tilde{q}_c - q_c) < 0 \end{cases} \tag{C.19}$$

(and thus can be calculated from the prognostic model variables). The vertical gradients of the changes in tagged water content given in equations (C.17) and (C.18) can then be used to parameterize the residual vertical turbulent transport caused by subgrid-scale cloudiness, again applying K-theory (and using an explicit numerical scheme, as for the model variables q_v and q_c in the turbulence parameterization). This second approach on the one hand can be implemented in a more straightforward way than the first one, and it has the advantage that no additional approximations have to be applied (in contrast to equations (C.5) and (C.12), for example). On the other hand, it differs to a greater extent from the parameterization scheme for the total water fields q_v and q_c implemented in the COSMO model, possibly leading to inconsistencies. Moreover, it is an intermediate solution with respect to the physical complexity, because it incorporates only the grid cell average effect of subgrid-scale cloudiness on vertical transport and

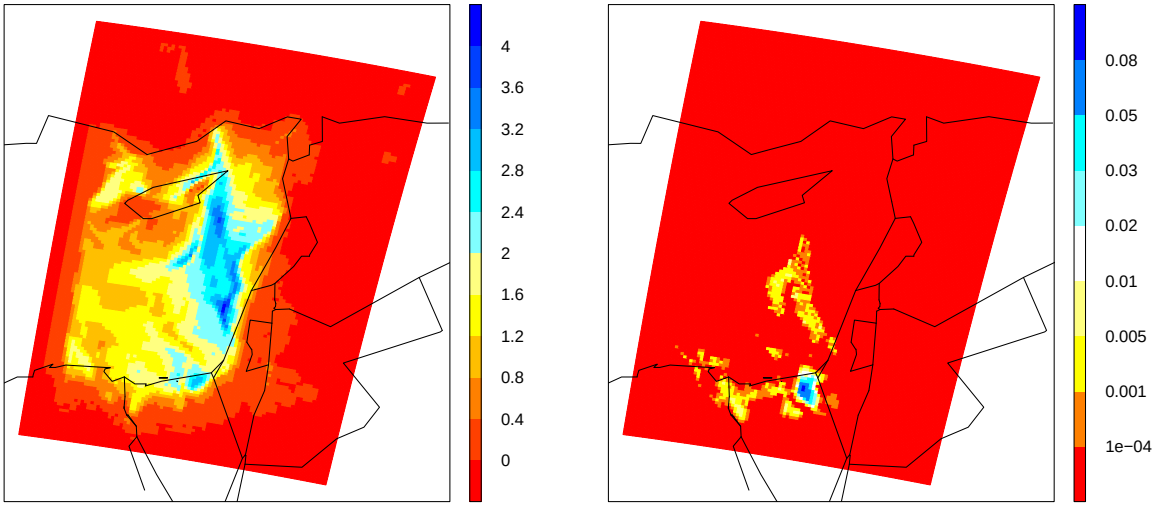

Figure C.1. *Vertically integrated tagged water vapor and liquid water content in* $\frac{g}{m^2}$ *at 9 UTC, 2001-11-18 (control simulation without correction of turbulent transport, started at 6 UTC on the same day).*

does not take into account the subgrid variability of the transport terms.

From this argumentation, it is not obvious which of the two approaches outlined above is more favorable. Hence, both alternatives have been implemented in $\text{COSMO}_{\text{iso}}$, selectable by a namelist switch. Their effect has been explored in two simulations (labeled $S1$ and $S2$). A third control simulation ($S0$) without additional vertical turbulent transport of $q_{v,t}$ and $q_{c,t}$ has also been performed. The simulations have been run in a small model domain covering the Eastern Mediterranean and for an integration time of three hours, starting at 06 UTC, 2001-11-18 (already after such a short integration, the differences between the approaches have become obvious).

Figure C.1 shows the vertical integrals of tagged water vapor $q_{v,t}$ and liquid water content $q_{c,t}$ for the control simulation $S0$. The tagged vapor field is maximal over the ocean, where evaporation occurs, and close to zero almost everywhere over land, because the integration time has not been sufficiently long to allow larger amounts of tagged vapor to be advected over the continents. The amount of tagged liquid water is very small, because few clouds have formed in this simulation and the fraction of tagged vapor in higher altitudes also is small. In Fig. C.2, differences are shown between vertically integrated tagged water vapor (and liquid water content) from the first simulation with correction of turbulent transport ($S1$, parameterization using the fluxes of q_w and θ_w) and from the control simulation $S0$. These differences are supposed to disappear in first order, because the transport correction redistributes tagged water only in the vertical (and such

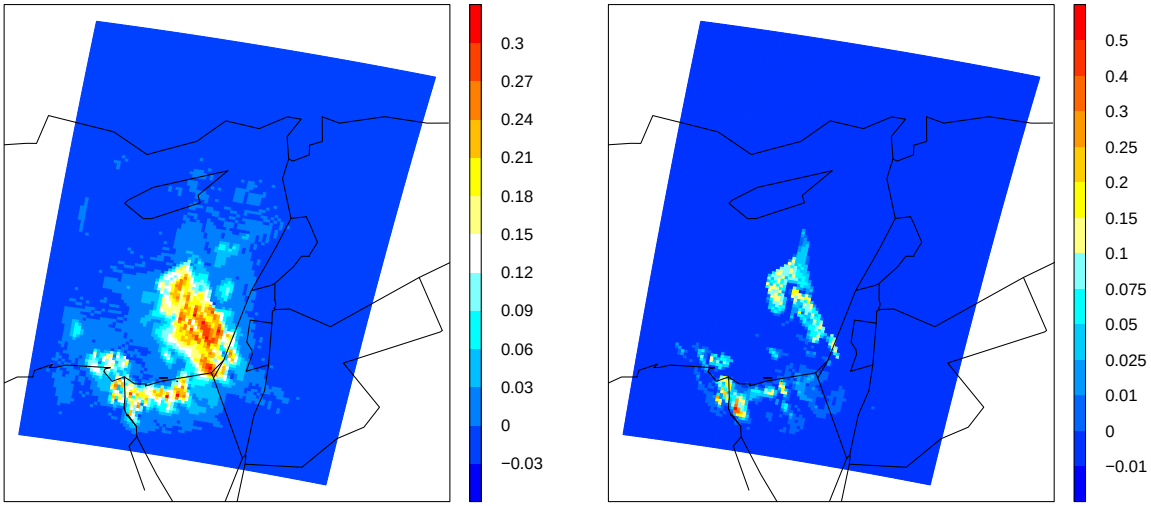

Figure C.2. *Difference between vertically integrated tagged water vapor (left) and liquid water content (right) from simulation with correction of turbulence S*1 *(parameterization with help of the fluxes of* q_w *and* θ_w*) and control simulation S*0 *(as shown in Fig. C.1) in* $\frac{g}{m^2}$.

a redistribution is averaged out by the vertical integration). However, non-vanishing differences may appear through second order effects, caused e.g. by a vertical wind shear. If these second order effects are only due to transport (and cloud transformation processes can be neglected), equal amounts of positive and negative differences are expected. Fig. C.2 shows that the differences between simulation *S*1 and *S*0 are positive almost everywhere in the model domain. In particular, the differences of $q_{c,t}$ are up to one order of magnitude larger than the tagged cloud water from *S*0. This points to an unphysical production of tagged water by the parameterization scheme. Such a production might be due to numerical inconsistencies, e.g. the difference between the implicit scheme used for the vertical transport in the dynamical part of the model and the explicit scheme in the turbulence parameterization. These inconsistencies are particularly important for the transport of tagged water, because the corresponding transport terms (e.g. in the parameterization of equation (C.15)) are extremely small, especially at the beginning of the simulation. In contrast, the differences between the integrated tagged water fields of *S*2 (parameterization with revised liquid water content) and *S*0 shown in Fig. C.3 are of much smaller magnitude, pointing to less numerical errors related to this parameterization, although the sign of the differences also is positive at the majority of the grid points.

Based on this analysis, the parameterization used in simulation *S*2, applying equations (C.17) and (C.18), is thought to be physically more consistent than the one from *S*1. Hence, this pa-

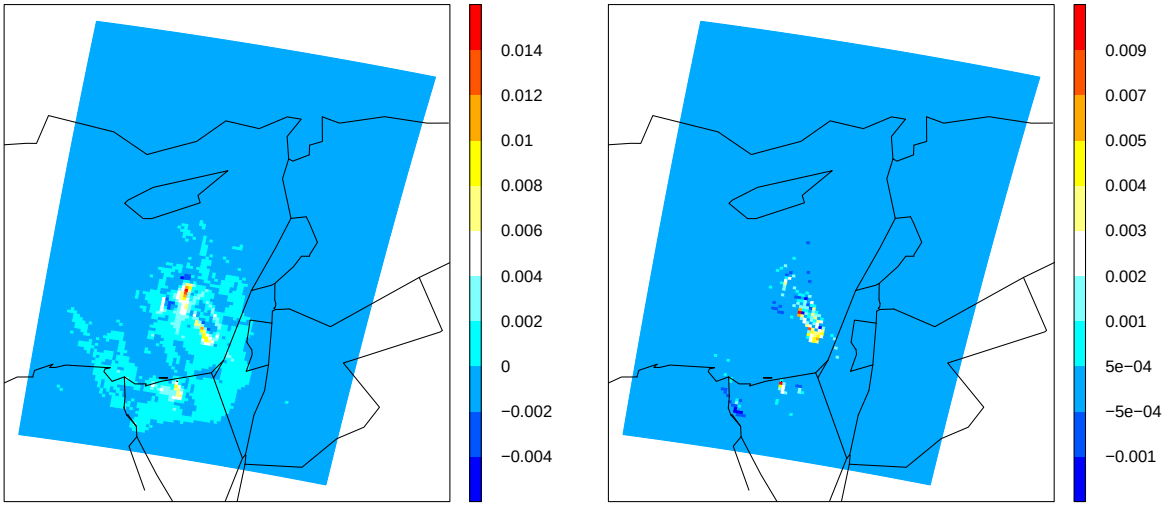

Figure C.3. *Difference between vertically integrated tagged water vapor (left) and liquid water content (right) from simulation with correction of turbulence S2 (parameterization with revised liquid water content) and control simulation S0 (as shown in Fig. C.1) in* $\frac{g}{m^2}$.

rameterization is used for the $\text{COSMO}_{\text{iso}}$ simulations described in this thesis. However, one should keep in mind that numerical errors produced by the discretization, though small in this experiment, might grow larger when the integration time is increased.

Bibliography

Angert, A., J.-E. Lee, and D. Yakir (2008), Seasonal variations in the isotopic composition of near surface water vapor in the Eastern-Mediterranean, *Tellus B*, *60*, 674–684.

Anker, Y., A. Flexer, E. Rosenthal, and E. Ganor (2007), Relationship between the origin of precipitation in the Jordan Rift valley and their geochemical composition, *J. Geophys. Res.*, *112*, D03306, doi:10.1029/2006JD007517.

Appleby, P. G. (2001), Chronostratigraphic techniques in recent sediments, in *Tracking environmental change using lake sediments, Volume 1: basin analysis, coring and chronological techniques*, edited by W. M. Last and J. P. Smol, pp. 171–203, Kluwer Academic, Norwell, USA.

Appleby, P. G., and F. Oldfield (1978), The calculation of ^{210}Pb dates assuming a constant rate of supply of unsupported ^{210}Pb to the sediment, *Catena*, *5*, 1–8.

Araguás-Araguás, L., K. Froehlich, and K. Rozanski (2000), Deuterium and oxygen-18 isotope composition of precipitation and atmospheric moisture, *Hydrol. Process.*, *14*, 1341–1355.

Armengaud, A., R. D. Koster, J. Jouzel, and P. Ciais (1998), Deuterium excess in Greenland snow: Analysis with simple and complex models, *J. Geophys. Res.*, *27*, 8947–8953.

Barkan, E., and B. Luz (2007), Diffusivity fractionations of $H_2^{16}O/H_2^{17}O$ and $H_2^{16}O/H_2^{18}O$ in air and their implications for isotope hydrology, *Rapid Commun. Mass Spectrom.*, *21*, 2999–3005, doi:10.1002/rcm.3180.

Barras, V. J. I., and I. Simmonds (2008), Synoptic controls upon δ^{18}O in southern Tasmanian precipitation, *Geophys. Res. Lett.*, *35*, L02707, doi:10.1029/2007GL031835.

Bärring, L., and H. von Storch (2004), Scandinavian storminess since about 1800, *Geophys. Res. Lett.*, *31*, L20,202.

Besonen, M. R., R. S. Bradley, M. Mudelsee, M. B. Abbott, , and P. Francus (2008), A 1,000-year, annually-resolved record of hurricane activity from Boston, Massachusetts, *Geophys. Res. Lett.*, *35*, L14705, doi:10.1029/2008GL033950.

Bigeleisen, J. (1961), Statistical mechanics of isotope effects on the thermodynamic properties of condensed systems, *J. Chem. Phys.*, *34*, 1485–1493.

Björck, S., and L. B. Clemmensen (2004), Aeolian sediment in raised bog deposits, Halland, SW Sweden: a new proxy record of Holocene winter storminess variation in southern Scandinavia?, *Holocene, 14*, 677–688.

Black, D. E., L. C. Peterson, J. T. Overpeck, A. Kaplan, M. N. Evans, and M. Kashgarian (1999), Eight centuries of North Atlantic ocean atmosphere variability, *Science, 286*, 1709–1713.

Bott, A. (1989), A positive definite advection scheme obtained by nonlinear renormalization of the advective fluxes, *Mon. Weather Rev.*, *117*, 1006–1015.

Bott, A. (1992), Monotone flux limitation in the area-preserving flux-form advection algorithm, *Mon. Weather Rev.*, *120*, 2592–2602.

Brauer, A., G. H. Haug, P. Dulski, D. M. Sigman, and J. F. W. Negendank (2008), An abrupt wind shift in western Europe at the onset of the Younger Dryas cold period, *Nature Geosci.*, *1*, 520–523, doi:10.1038/ngeo263.

Brazdil, R., C. Pfister, H. Wanner, H. von Storch, and J. Luterbacher (2005), Historical climatology in Europe - The state of the art, *Clim. Change, 70*, 363–430, doi:10.1007/s10584-005-5924-1.

Briffa, K. R., T. J. Osborn, and F. H. Schweingruber (2004), Large-scale temperature inferences from tree rings: a review, *Glob. Planet. Change*, *40*, 11–26.

Brutsaert, W. (1975), A theory for local evaporation (or heat transfer) from rough and smooth surfaces at ground level, *Water Resour. Res.*, *11 (4)*, 543–550.

Brutsaert, W. (1982), *Evaporation into the atmosphere*, D. Reidel Publishing Company, Dordrecht, The Netherlands.

Byun, H.-R., and D. A. Wilhite (1999), Objective quantification of drought severity and duration, *J. Climate*, *12 (9)*, 2747–2756.

Cappa, C. D., M. B. Hendricks, D. J. DePaolo, and R. C. Cohen (2003), Isotopic fractionation of water during evaporation, *J. Geophys. Res.*, *108*, 4525, doi:10.1029/2003JD003597.

Ciais, P., J. W. C. White, J. Jouzel, and J. R. Petit (1995), The origin of present-day Antarctic precipitation from surface snow deuterium excess data, *J. Geophys. Res.*, *100*, 18,917–18,927.

Clemmensen, L. B., K. Pye, A. Murray, and J. Heinemeier (2001), Sedimentology, stratigraphy and landscape evolution of a Holocene coastal dune system, Lodbjerg, NW Jutland, Denmark, *Sedimentology*, *48*, 3–27.

Cook, E. R., C. A. Woodhouse, C. M. Eakin, D. M. Meko, and D. W. Stahle (2004), Long-term aridity changes in the western United States, *Science*, *306*, 1015–1018, doi: 10.1126/science.1102586.

Coplen, T. B., P. J. Neiman, A. B. White, J. M. Landwehr, F. M. Ralph, and M. D. Dettinger (2008), Extreme changes in stable hydrogen isotopes and precipitation characteristics in a landfalling Pacific storm, *Geophys. Res. Lett.*, *35*, L21808, doi:10.1029/2008GL035481.

Correge, T. (2006), Sea surface temperature and salinity reconstruction from coral geochemical tracers, *Paleogeogr. Paleoclimatol. Paleoecol.*, *232*, 408–428.

Craig, H. (1961), Isotopic variations in meteoric waters, *Science*, *133*, 1702–1703.

Craig, H., and L. I. Gordon (1965), Deuterium and oxygen 18 variations in the ocean and the marine atmosphere, in *Stable isotopes in oceanographic studies and paleotemperatures*, edited by E. Tongiorgi, pp. 9–130, Lab. Geol. Nucl., Pisa, Italy.

Dansgaard, W. (1964), Stable isotopes in precipitation, *Tellus, 16B*, 436–468.

Dansgaard, W., et al. (1993), Evidence for general instability of past climate from a 250-kyr ice-core record, *Nature*, *364*, 218–220.

Davies, H. C. (1976), A lateral boundary formulation for multi-level prediction models, *Quart. J. R. Meteorol. Soc.*, *102*, 405–418.

de Jong, R., S. Björck, L. Björkman, and L. B. Clemmensen (2006), Storminess variation during the last 6500 years as reconstructed from an ombrotrophic peat bog in Halland, southwest Sweden, *J. Quat. Sci.*, *21*, 905–919.

Delaygue, G., V. Masson, J. Jouzel, R. D. Koster, and R. J. Healy (2000), The origin of Antarctic precipitation: a modelling approach, *Tellus*, *52B*, 19–36.

DiCiccio, T. J., and B. Efron (1996), Bootstrap confidence intervals, *Stat. Sci.*, *11 (3)*, 189–228.

Doms, G., and U. Schättler (2002), *A description of the nonhydrostatic regional model LM. Part I: Dynamics and numerics*, Deutscher Wetterdienst, Offenbach, Germany.

Doms, G., J. Förstner, E. Heise, H.-J. Herzog, M. Raschendorfer, R. Schrodin, T. Reinhardt, and G. Vogel (2005), *A description of the nonhydrostatic regional model LM. Part II: Physical parameterization*, Deutscher Wetterdienst, Offenbach, Germany.

Eden, D. N., and M. J. Page (1998), Palaeoclimatic implications of a storm erosion record from late Holocene lake sediments, North Island, New Zealand, *Palaeogeogr. Palaeoclimatol. Palaeoecol.*, *139*, 37–58.

Elçi, S., P. A. Work, and E. J. Hayter (2007), Influence of stratification and shoreline erosion on reservoir sedimentation patterns, *J. Hydraul. Eng.-ASCE, 133 (3)*, 255–266, doi: 10.1061/(ASCE)0733-9429(2007)133:3(255).

EPICA community members (2004), Eight glacial cycles from an Antarctic ice core, *Nature, 429*, 623–628.

Fairall, C. W., E. F. Bradley, J. E. Hare, A. A. Grachev, and J. B. Edson (2003), Bulk parameterization of air-sea fluxes: Updates and verification for the COARE algorithm, *J. Climate, 16 (4)*, 571–591.

Gat, J. R. (1996), Oxygen and hydrogen isotopes in the hydrological cycle, *Annu. Rev. Earth Planet Sci., 24*, 225–262.

Gat, J. R., and C. Bowser (1991), The heavy isotope enrichment of water in coupled evaporative systems, in *Stable isotope geochemistry: a tribute to Samuel Epstein*, edited by H. P. Taylor, J. R. O'Neil, and I. R. Kaplan, pp. 159–168, The Geochemical Society, Lancaster, UK.

Gat, J. R., and I. Carmi (1970), Evolution of the isotopic composition of atmospheric waters in the Mediterranean Sea area, *J. Geophys. Res., 75*, 3039–3048.

Gat, J. R., I. Carmi, and N. Bauman (1994), The isotopic composition of precipitation at Bet-Dagan, Israel: the "climatic" record (1961-1990), *Israel Meteorological Research Papers, 5*, 10–19.

Gat, J. R., A. Shemesh, E. Tziperman, A. Hecht, D. Georgopoulus, and O. Basturk (1996), The stable isotope composition of waters of the eastern Mediterranean Sea, *J. Geophys. Res., 101*, 6441–6451.

Gat, J. R., B. Klein, Y. Kushnir, W. Roether, H. Wernli, R. Yam, and A. Shemesh (2003), Isotope composition of air moisture over the Mediterranean Sea: an index of air-sea interaction pattern, *Tellus, 55B*, 953–965.

Gedzelman, S. D., and R. Arnold (1994), Modeling the isotopic composition of precipitation, *J. Geophys. Res., 99*, 10,455–10,471.

Gedzelman, S. D., and J. R. Lawrence (1990), The isotopic composition of precipitation from 2 extratropical cyclones, *Mon. Weather Rev., 118*, 495–509.

González-Rouco, J. F., H. Beltrami, E. Zorita, and H. von Storch (2006), Simulation and inversion of borehole temperature profiles in surrogate climates: Spatial distribution and surface coupling, *Geophys. Res. Lett., 33*, L01703, doi:10.1029/2005GL024693.

Halfman, J. D., and T. C. Johnson (1984), Enhanced atmospheric circulation over North America during the early Holocene: evidence from Lake Superior, *Science, 224*, 61–63.

Hambley, G. W., and S. F. Lamoureux (2006), Recent summer climate recorded in complex varved sediments, Nicolay Lake, Cornwall Island, Nunavut, Canada, *J. Paleolimnol., 35*, 629–640.

Hardy, D. R., R. S. Bradley, and B. Zolitschka (1996), The climatic signal in varved sediments from Lake C2, northern Ellesmere Island, Canada, *J. Paleolimnol., 16*, 227–238.

He, H., and R. B. Smith (1999), An advective-diffusive isotopic evaporation-condensation model, *J. Geophys. Res., 104*, 18,619–18,630.

Helsen, M. M., R. S. W. van de Wal, M. R. van den Broeke, E. R. T. Kerstel, V. Masson-Delmotte, H. A. J. Meijer, C. H. Reijmer, and M. P. Scheele (2004), Modeling the isotopic composition of snow using backward trajectories: a particular precipitation event in Dronning Maud Land, Antarctica, *Ann. Glaciol., 39*, 293–299.

Helsen, M. M., R. S. W. van den Wal, M. R. van den Broeke, V. Masson-Delmotte, H. A. J. Meijer, M. P. Scheele, and M. Werner (2006), Modeling the isotopic composition of Antarctic snow using backward trajectories: Simulation of snow pit records, *J. Geophys. Res., 111*, D15109, doi:10.1029/2005JD006524.

Helsen, M. M., R. S. W. van den Wal, and M. R. van den Broeke (2007), The isotopic composition of present-day Antarctic snow in a Lagrangian atmospheric simulation, *J. Climate, 20*, 739–756, doi:10.1175/JCLI4027.1.

Henderson-Sellers, A., K. McGuffie, D. Noone, and P. Irannejad (2004), Using stable water isotopes to evaluate basin-scale simulations of surface water budgets, *J. Hydrometeorol., 5*, 805–822.

Hoffmann, G., M. Werner, and M. Heimann (1998), Water isotope module of the ECHAM atmospheric general circulation model: A study on timescales from days to several years, *J. Geophys. Res., 103*, 16,871–16,896.

Horita, J., and D. J. Wesolowski (1994), Liquid-vapor fractionation of oxygen and hydrogen isotopes of water from the freezing to the critical temperature, *Geochim. Cosmochim. Acta, 58*, 3425–3437.

Horita, J., K. Rozanski, and S. Cohen (2008), Isotope effects in the evaporation of water: a status report of the Craig-Gordon model, *Isot. Environ. Health Stud., 44 (1)*, 23–49, doi: 10.1080/10256010801887174.

Hundecha, Y., and A. Bárdossy (2005), Trends in daily precipitation and temperature extremes across western Germany in the second half of the 20th century, *Int. J. Climatol., 25 (9)*, 1189–1202.

Hyndman, R. J., and Y. N. Fan (1996), Sample quantiles in statistical packages, *Am. Stat., 50*, 361–365.

International Atomic Energy Agency (2005), *Isotopic composition of precipitation in the Mediterranean Basin in relation to air circulation patterns and climate (IAEA-TECDOC-1453)*, Int. Atomic Energy Agency, Vienna, Austria.

Jacob, D., et al. (2007), An inter-comparison of regional climate models for Europe: Model performance in present-day climate, *Clim. Change, 81*, 31–52, doi:10.1007/s10584-006-9213-4.

Johnsen, S. J., W. Dansgaard, and J. W. C. White (1989), The origin of Arctic precipitation under present and glacial conditions, *Tellus, 41B*, 452–468.

Johnsen, S. J., et al. (1992), Irregular glacial interstadials recorded in a new Greenland ice core, *Nature, 359*, 311–313.

Jones, P. D., et al. (2009), High-resolution palaeoclimatology of the last millennium: a review of current status and future prospects, *Holocene, 19*, 3–49, doi:10.1177/0959683608098952.

Joussaume, J., R. Sadourny, and J. Jouzel (1984), A general circulation model of water isotope cycles in the atmosphere, *Nature, 311*, 24–29.

Joussaume, J., R. Sadourny, and C. Vignal (1986), Origin of precipitating water in a numerical simulation of Juli climate, *Ocean-Air Interact., 1*, 43–56.

Jouzel, J., and R. D. Koster (1996), A reconsideration of the initial conditions used for stable water isotope models, *J. Geophys. Res., 101*, 22,933–22,938.

Jouzel, J., and L. Merlivat (1984), Deuterium and oxygen 18 in precipitation, modeling of the isotopic effects during snow formation, *J. Geophys. Res., 89*, 11,749–11,757.

Jouzel, J., G. Hoffmann, R. D. Koster, and V. Masson (2000), Water isotopes in precipitation: data/model comparison for present-day and past climates, *Quat. Sci. Rev., 19*, 363–379.

Jouzel, J., F. Vimeux, N. Caillon, G. Delaygue, G. Hoffmann, V. Masson-Delmotte, and F. Parrenin (2003), Magnitude of isotope/temperature scaling for interpretation of central Antarctic ice cores, *J. Geophys. Res., 108*, 4361, doi:10.1029/2002JD002677.

Jouzel, J., M. Stievenard, S. J. Johnsen, A. Landais, V. Masson-Delmotte, A. Sveinbjörnsdottir, F. Vimeux, U. von Grafenstein, and J. W. C. White (2007), The GRIP deuterium-excess record, *Quat. Sci. Rev., 26*, 1–17.

Jouzel, J., et al. (1997), Validity of the temperature reconstruction from water isotopes in ice cores, *J. Geophys. Res.*, *102*, 26,471–26,487.

Keyantash, J., and J. A. Dracup (2002), The quantification of drought: An evaluation of drought indices, *Bull. Amer. Meteorol. Soc.*, *83 (8)*, 1167–1180.

Klawa, M., and U. Ulbrich (2003), A model for the estimation of storm losses and the identification of severe winter storms in Germany, *Nat. Hazards Earth Syst. Sci.*, *3*, 725–732.

Koster, R., J. Jouzel, R. Souzzo, G. Russel, W. Broecker, D. Rind, and P. Eagleson (1986), Global sources of local precipitation as determined by the NASA/GISS GCM, *Geophys. Res. Lett.*, *13*, 121–124.

Landais, A., E. Barkan, and B. Luz (2008), Record of δ^{18}O and ^{17}O-excess in ice from Vostok Antarctica during the last 150,000 years, *Geophys. Res. Lett.*, *35*, L02709, doi: 10.1029/2007GL032096.

Larsen, C. P. S., and G. M. MacDonald (1993), Lake morphometry, sediment mixing and the selection of sites for fine resolution palaeoecological studies, *Quat. Sci. Rev.*, *12*, 781–792.

Last, W. M., and J. P. Smol (Eds.) (2001), *Tracking Environmental Change Using Lake Sediments. Volume 1: Basin Analysis, Coring and Chronological Techniques*, Academic Publishers, Dordrecht, The Netherlands.

Lawrence, J. R., S. D. Gedzelman, D. Dexheimer, H. K. Cho, G. D. Carrie, R. Gasparini, C. R. Anderson, K. P. Bowman, and M. I. Biggerstaff (2004), Stable isotopic composition of water vapor in the tropics, *J. Geophys. Res.*, *109*, D06115, doi:10.1029/2003JD004046.

Lee, J. E., I. Fung, D. J. DePaolo, and C. C. Henning (2007), Analysis of the global distribution of water isotopes using the NCAR atmospheric general circulation model, *J. Geophys. Res.*, *109*, D16306, doi:10.1029/2006JD007657.

Liu, W. T., K. B. Katsaros, and J. A. Businger (1979), Bulk parameterization of air-sea exchanges of heat and water vapor including the molecular constraints at the interface, *J. Atmos. Sci.*, *36*, 1722–1735.

Louis, J.-F. (1979), A parametric model of vertical eddy fluxes in the atmosphere, *Bound.-Layer Meteor.*, *17*, 187–202.

Lykoudis, S. P., and A. A. Argiriou (2007), Gridded data set of the stable isotopic composition of precipitation over the eastern and central Mediterranean, *J. Geophys. Res.*, *112*, D18107, doi:10.1029/2007JD008472.

Majoube, M. (1971), Fractionnement en oxygén 18 et en deutérium entre l'eau et sa vapeur, *J. Chem. Phys.*, *10*, 1423–1436.

Marti, C. L., and J. Imberger (2008), Exchange between littoral and pelagic waters in a stratified lake due to wind-induced motions: Lake Kinneret, Israel, *Hydrobiologia*, *603*, 25–51, doi: 10.1007/s10750-007-9243-6.

Masson-Delmotte, V., J. Jouzel, A. Landais, M. Stievenard, S. J. Johnsen, J. W. C. White, M. Werner, A. Sveinbjörnsdottir, and K. Fuhrer (2005), GRIP deuterium excess reveals rapid and orbital-scale changes in Greenland moisture origin, *Science*, *309*, 118–121.

Masson-Delmotte, V., et al. (2006), Past temperature reconstructions from deep ice cores: relevance for future climate change, *Clim. Past*, *2*, 145–162.

Merlivat, L. (1978a), The dependence of bulk evaporation coefficients on air-water interfacial conditions as determined by the isotopic method, *J. Geophys. Res.*, *83*, 2977–2980.

Merlivat, L. (1978b), Molecular diffusivities of $H_2{}^{16}O$, $HD^{16}O$ and $H_2{}^{18}O$ in gases, *J. Chem. Phys.*, *69*, 2864–2871.

Merlivat, L., and J. Jouzel (1979), Global climatic interpretation of the deuterium-oxygen 18 relationship for precipitation, *J. Geophys. Res.*, *84*, 5029–5033.

Middleton, G. V. (1966), Experiments on density and turbidity currents, II: Uniform flow of density currents, *Can. J. Earth Sci.*, *3*, 627–637.

Moberg, A., D. M. Sonechkin, K. Holmgren, N. M. Datsenko, and W. Karlen (2005), Highly variable Northern Hemisphere temperatures reconstructed from low- and high-resolution proxy data, *Nature*, *433*, 613–617.

Morid, S., V. Smakhtin, and M. Moghaddasi (2006), Comparison of seven meteorological indices for drought monitoring in Iran, *Int. J. Climatol.*, *26*, 971–985.

Neiman, P. J., M. A. Shapiro, E. G. Donall, and C. W. Kreitzberg (1990), Diabatic modification of an extratropical marine cyclone warm sector by cold underlying water, *Mon. Weather Rev.*, *118*, 1576–1590.

Nesje, A., S. O. Dahl, J. A. Matthews, and M. S. Berrisford (2001), A 4500-yr record of river floods obtained from a sediment core in Lake Atnsjoen, eastern Norway, *J. Paleolimnol.*, *25*, 329–342.

Noone, D., and I. Simmonds (2002), Associations between $\delta^{18}O$ of water and climate parameters in a simulation of atmospheric circulation for 1979-95, *J. Climate*, *15*, 3150–3169.

Noren, A. J., P. R. Bierman, E. J. Steig, A. Lini, and J. Southon (2002), Millennial-scale storminess variability in the notheastern United States during the Holocene epoch, *Nature, 419*, 821–824.

North Greenland Ice Core Project members (2004), High-resolution record of Northern Hemisphere climate extending into the last interglacial period, *Nature, 431*, 147–151.

Payne, V. H., D. Noone, A. Dudhia, C. Piccolo, and R. G. Grainger (2007), Global satellite measurements of HDO and implications for understanding the transport of water vapour into the stratosphere, *Q. J. R. Meteorol. Soc., 133*, 1459–1471, doi:10.1002/qj.127.

Perrie, W., E. L. Andreas, W. Q. Zhang, W. B. Li, J. Gyakum, and R. McTaggart-Cowan (2005), Sea spray impacts on intensifying midlatitude cyclones, *J. Atmos. Sci., 62*, 1867–1883.

Petit, J. R., J. W. C. White, N. W. Young, J. Jouzel, and Y. S. Korotkevich (1991), Deuterium excess in recent Antarctic snow, *J. Geophys. Res., 96*, 5113–5122.

Petit, J. R., et al. (1999), Climate and atmospheric history of the past 420,000 years from the Vostok ice core, Antarctica, *Nature, 399*, 429–436.

Pfahl, S., and H. Wernli (2008), Air parcel trajectory analysis of stable isotopes in water vapor in the eastern Mediterranean, *J. Geophys. Res., 113*, D20104, doi:10.1029/2008JD009839.

Pfahl, S., and H. Wernli (2009), Lagrangian simulations of stable isotopes in water vapor - an evaluation of non-equilibrium fractionation in the Craig-Gordon model, *J. Geophys. Res.*, doi:10.1029/2009JD012054, revised.

Pfahl, S., F. Sirocko, K. Seelos, S. Dietrich, A. Walter, and H. Wernli (2009), A new windstorm proxy from lake sediments - a comparison of geological and meteorological data from western Germany for the period 1965-2001, *J. Geophys. Res.*, doi:10.1029/2008JD011643, accepted for publication.

Pfister, C., R. Weingartner, and J. Luterbacher (2006), Hydrological winter droughts over the last 450 years in the Upper Rhine basin: a methodological approach, *Hydrol. Sci. J., 51 (5)*, 966–985.

Pharo, C. H., and E. C. Carmack (1979), Sedimentation processes in a short residence-time intermontane lake, Kamloops Lake, British-Columbia, *Sedimentology*, *26*(4), 523–541.

Pye, K., and A. Neal (1994), Coastal dune erosion at Formy Point, North Merseyside, England - causes and mechanisms, *Mar. Geol., 119*, 39–56.

Rajagopalan, B., U. Lall, and D. G. Tarboton (1997), Evaluation of kernel density estimation methods for daily precipitation resampling, *Stoch. Hydrol. Hydraul., 11*, 523–547.

Rao, T. N., B. Radhakrishna, R. Srivastava, T. M. Satyanarayana, D. N. Rao, and R. Ramesh (2008), Inferring microphysical processes occurring in mesoscale convective systems from radar measurements and isotopic analysis, *Geophys. Res. Lett.*, *35*, L09813, doi: 10.1029/2008GL033495.

Rindsberger, M., M. Magaritz, I. Carmi, and D. Gilad (1983), The relation between air mass trajectories and the water isotope composition of rain in the Mediterranean Sea area, *Geophys. Res. Lett.*, *10*, 43–46.

Rindsberger, M., S. Jaffe, S. Rahamim, and J. R. Gat (1990), Patterns of the isotopic composition of precipitation in time and space: data from the Israeli storm water collection program, *Tellus, 42B*, 263–271.

Rodbell, D. T., G. O. Seltzer, D. M. Anderson, M. B. Abbott, D. B. Enfield, and J. H. Newman (1999), An 15,000-year record of El Nino-driven alluviation in southwestern Ecuador, *Science*, *283*, 516–520.

Schaber, K., and F. Sirocko (2005), Lithologie und Stratigraphie der spätpleistozänen Trockenmaare der Eifel, *Mainzer geowissenschaftliche Mitteilungen*, *33*, 295–340.

Schär, C., P. L. Vidale, D. Luthi, C. Frei, C. Haberli, M. A. Liniger, and C. Appenzeller (2004), The role of increasing temperature variability in European summer heatwaves, *Nature, 427*, 332–336, doi:10.1038/nature02300.

Schättler, U. (2008), *A description of the nonhydrostatic regional COSMO-Model. Part V: Preprocessing: Initial and boundary data for the COSMO-Model*, Deutscher Wetterdienst, Offenbach, Germany.

Schättler, U., G. Doms, and C. Schraff (2008), *A description of the nonhydrostatic regional COSMO-Model. Part VII: User's guide*, Deutscher Wetterdienst, Offenbach, Germany.

Schmidt, G. A., G. Hoffmann, D. T. Shindell, and Y. Hu (2005), Modeling atmospheric stable water isotopes and the potential for constraining cloud processes and stratosphere-troposphere water exchange, *J. Geophys. Res.*, *110*, D21314, doi:10.1029/2005JD005790.

Schmidt, G. A., A. L. LeGrande, and G. Hoffmann (2007), Water isotope expressions of intrinsic and forced variability in a coupled ocean-atmosphere model, *J. Geophys. Res.*, *112*, D10103, doi:10.1029/2006JD007781.

Schöne, B. R., J. Fiebig, M. Pfeiffer, R. Gless, J. Hickson, A. L. A. Johnson, W. Dreyer, and W. Oschmann (2005), Climate records from a bivalved Methuselah (Arctica islandica, Mollusca; Iceland), *Palaeogeogr. Palaeoclimatol. Palaeoecol.*, *228*, 130–148, doi: 10.1016/j.palaeo.2005.03.049.

Scott, D. W. (1992), *Multivariate density approximation. Theory, practice and visualization*, Wiley, New York, USA.

Seelos, K., and F. Sirocko (2005), RADIUS - rapid particle analysis of digital images by ultra-high resolution scanning of thin sections, *Sedimentology, 52*, 669–681.

Seelos, K., and F. Sirocko (2007), Abrupt cooling events at the very end of the last interglacial, in *The climates of past interglacials. Developments in Quaternary Sciences 7*, edited by F. Sirocko, M. Claussen, M. F. Sànchez Goñi, and T. Litt, pp. 207–220, Elsevier.

Sirocko, F. (Ed.) (2009), *Wetter - Klima - Menschheitsentwicklung. Von der Eiszeit bis ins 21. Jahrhundert*, Wissenschaftliche Buchgesellschaft, Darmstadt, Germany.

Sirocko, F., M. Sarnthein, H. Erlenkeuser, H. Lange, M. Arnold, and J. Duplessy (1993), Century-scale events in monsoonal climate over the past 24,000 years, *Nature, 364*, 322–324.

Sirocko, F., et al. (2005), A late Eemian aridity pulse in central Europe during the last glacial inception, *Nature, 436*, 833–836.

Smith, R. B. (1992), Deuterium in North-Atlantic storm tops, *J. Atmos. Sci., 49*, 2041–2057.

Smolarkiewicz, P. K., and W. W. Grabowski (1990), The multidimensional positive definite advection transport algorithm - nonoscillatory option, *J. Comput. Phys., 86*, 355–375.

Smolarkiewicz, P. K., and L. G. Margolin (1998), MPDATA: A finite-difference solver for geophysical flows., *J. Comput. Phys., 140*, 459–480.

Sodemann, H. (2006), Tropospheric transport of water vapour: Lagrangian and Eulerian perspectives., Ph.D. thesis, ETH Zürich, Diss. ETH No. 16623.

Sodemann, H., V. Masson-Delmotte, C. Schwierz, B. Vinther, and H. Wernli (2008a), Inter-annual variability of Greenland winter precipitation sources. Part II: Effects of North Atlantic Oscillation variability on stable isotopes in precipitation, *J. Geophys. Res., 113*, D12111, doi: 10.1029/2007JD009416.

Sodemann, H., C. Schwierz, and H. Wernli (2008b), Inter-annual variability of Greenland winter precipitation sources. Part I: Lagrangian moisture diagnostic and North Atlantic Oscillation influence, *J. Geophys. Res., 113*, D03107, doi:10.1029/2007JD008503.

Sodemann, H., H. Wernli, and C. Schwierz (2009), Sources of water vapour contributing to the Elbe flood in August 2002 - a tagging study in a mesoscale model, *Quart. J. R. Meteorol. Soc., 135*, 205–223, doi:10.1002/qj.374.

Sommeria, G., and J. W. Deardorff (1976), Subgrid-scale condensation in models of nonprecipitating clouds, *J. Atmos. Sci., 34*, 344–355.

Steppeler, J., G. Doms, U. Schättler, H. W. Bitzer, A. Gassmann, U. Damrath, and G. Gregoric (2003), Meso-gamme scale forecast using the nonhydrostatic model LM, *Meteorol. Atmos. Phys.*, *82*, 75–96.

Stevens, C., and J. Imberger (1996), The initial response of a stratified lake to a surface shear stress, *J. Fluid Mech.*, *312*, 39–66.

Steward, M. K. (1975), Stable isotope fractionation due to evaporation and isotopic exchange of falling waterdrops: applications to atmospheric processes and evaporation of lakes, *J. Geophys. Res.*, *80*, 1133–1146.

Stohl, A., and P. Seibert (1998), Accuracy of trajectories as determined from the conservation of meteorological tracers, *Q. J. R. Meteorol. Soc.*, *124*, 1465–1484.

Stone, C. J., M. H. Hansen, C. Kooperberg, and Y. K. Truong (1997), Polynomial splines and their tensor products in extended linear modeling, *Ann. Stat.*, *25 (4)*, 1371–1425.

Strong, M., Z. D. Sharp, and D. S. Gutzler (2007), Diagnosing moisture transport using D/H ratios of water vapor, *Geophys. Res. Lett.*, *34*, L03404, doi:10.1029/2006GL028307.

Sturm, K., G. Hoffmann, B. Langmann, and W. Stichler (2005), Simulation of delta O-18 in precipitation by the regional circulation model REMOiso, *Hydrol. Process.*, *19*, 3425–3444, doi:10.1002/hyp5979.

Sturm, K., G. Hoffmann, and B. Langmann (2007a), Simulation of the stable water isotopes in precipitation over South America: Comparing regional to global circulation models, *J. Clim.*, *20*, 3730–3750, doi:10.1175/JCLI4194.1.

Sturm, K., F. Vimeux, and G. Krinner (2007b), Intraseasonal variability in South America recorded in stable water isotopes, *J. Geophys. Res.*, *112*, D20118, doi: 10.1029/2006JD008298.

Thompson, L. G., et al. (1998), A 25,000-year tropical climate history from Bolivian ice cores, *Science*, *282*, 1858–1864.

Tian, L., T. Yao, K. MacClune, J. W. C. White, A. Schilla, B. Vaughn, R. Vachon, and K. Ichiyanagi (2007), Stable isotopic variations in west China: A consideration of moisture sources, *J. Geophys. Res.*, *112*, D10112, doi:10.1029/2006JD007718.

Tiedtke, M. (1989), A comprehensive mass flux scheme for cumulus parameterization in large-scale models, *Mon. Weather Rev.*, *117*, 1779–1800.

Trachsel, M., U. Eggenberger, M. Grosjean, A. Blass, and M. Sturm (2008), Mineralogy-based quantitative precipitation and temperature reconstruction from annually laminated lake sediments (Swiss Alps) since AD 1580, *Geophys. Res. Lett.*, *35*, L13707, doi: 10.1029/2008GL034121.

Troen, I., and L. Mahrt (1986), A simple model of the atmospheric boundary-layer - Sensitivity to surface evaporation, *Bound.-Layer Meteor.*, *37*, 129–148.

Uemura, R., N. Yoshida, N. Kurita, M. Nakawo, and O. Watanabe (2004), An observation-based method for reconstructing ocean surface changes using a 340,000-year deuterium excess record from Dome Fuji ice core, Antarctica, *Geophys. Res. Lett.*, *31*, L13216, doi: 10.1029/2004GL019954.

Uemura, R., Y. Matsui, K. Yoshimura, H. Motoyama, and N. Yoshida (2008), Evidence of deuterium excess in water vapor as an indicator of ocean surface conditions, *J. Geophys. Res.*, *113*, D19114, doi:10.1029/2008JD010209.

Uppala, S., et al. (2005), The ERA-40 re-analysis, *Q. J. R. Meteorol. Soc.*, *131*, 2961–3012.

Vimeux, F., V. Masson, J. Jouzel, M. Stievenard, and J. R. Petit (1999), Glacial-interglacial changes in ocean surface conditions in the Southern Hemisphere, *Nature*, *398*, 410–413.

Vimeux, F., V. Masson, J. Jouzel, J. R. Petit, E. J. Steig, M. Stievenard, R. Vaikmae, and J. W. C. White (2001), Holocene hydrological cycle changes in the Southern Hemisphere documented in East Antarctic deuterium excess records, *Clim. Dyn.*, *17*, 503–513.

Vimeux, F., K. M. Cuffey, and J. Jouzel (2002), New insights into Southern Hemisphere temperature changes from Vostok ice cores using deuterium excess correction, *Earth Planet. Sci. Lett.*, *203*, 829–843.

Wackerly, D. D., W. Mendenhall III, and R. L. Scheaffer (2002), *Mathematical statistics with applications*, Duxbury, Pacific Grove, USA.

Walter, A., K. Keuler, D. Jakob, R. Knoche, A. Block, S. Kotlarski, G. Müller-Westermeier, D. Rechid, and W. Ahrens (2006), A high resolution reference data set of German wind velocity 1951-2001 and comparison with regional climate model results, *Meteorol. Z.*, *15 (6)*, 585–596.

WASA-Group (1998), Changing waves and storms in the northeast Atlantic?, *Bull. Am. Meteorol. Soc.*, *79*, 741–760.

Werner, M., M. Heimann, and G. Hoffmann (2001), Isotopic composition and origin of polar precipitation in present and glacial climate simulations, *Tellus*, *53B*, 53–71.

Wernli, H., and H. C. Davies (1997), A Lagrangian-based analysis of extratropical cyclones. I: The method and some applications, *Q. J. R. Meteorol. Soc.*, *123*, 467–489.

Wick, G. A., W. J. Emery, and L. H. Kantha (1996), The behaviour of the bulk-skin sea surface temperature difference under varying wind speed and heat flux, *J. Phys. Oceanogr.*, *26*, 1969–1988.

Wicker, L., and W. Skamarock (1998), A time-splitting scheme for the elastic equations incorporating second-order Runge-Kutta time differencing, *Mon. Weather Rev.*, *126*, 1992–1999.

Wilson, P., J. D. Orford, J. Knight, S. M. Braley, and A. G. Wintle (2001), Late-Holocene (post-4000 years bp) coastal dune development in Northumberland, northeast England, *Holocene*, *11*, 215–229.

Worden, J., D. Noone, K. Bowman, and Tropospheric Emission Spectrometer science team (2007), Importance of rain evaporation and continental convection in the tropical water cycle, *Nature*, *445*, 528–532, doi:10.1038/nature05508.

Worden, J., et al. (2006), Tropospheric emission spectrometer observations of the tropospheric HDO/H_2O ratio: Estimation approach and characterization, *J. Geophys. Res.*, *111*, D16309, doi:10.1029/2005JD006606.

Yamanaka, T., J. Shimada, and K. Miyaoka (2002), Footprint analysis using event-based isotope data for identifying source area of precipitated water, *J. Geophys. Res.*, *107*, 4624, doi:10.1029/2001JD001187.

Yoshimura, K., M. Kanamitsu, D. Noone, and T. Oki (2008), Historical isotope simulation using reanalysis atmospheric data, *J. Geophys. Res.*, *113*, D19108, doi:10.1029/2008JD010074.

Danksagung

Aus datenschutzrechtlichen Gründen kann die Danksagung hier nicht komplett veröffentlicht werden.

Für die Bereitstellung von Daten danke ich dem Institut für Geowissenschaften der Universität Mainz, dem Deutschen Wetterdienst, dem Landesamt für Umwelt, Wasserwirtschaft und Gewerbeaufsicht in Rheinland-Pfalz, dem Bundesamt für Gewässerkunde, dem Global Runoff Data Centre (GRDC) in Koblenz und dem Weizmann Institute of Science.